UNIVERSITÀ DEGLI STUDI DI TRIESTE

XXVIII Ciclo del

Dottorato di Ricerca in Scienze e Tecnologie Chimiche e Farmaceutiche

PhD School in Chemical and Pharmaceutical Sciences and Technologies

FUNCTIONAL CHROMOPHORES FOR LIGHT-HARVESTING APPLICATIONS

PhD Student	**Tanja Miletić**
PhD School Director	**Prof. Mauro Stener**
PhD Supervisor	**Prof. Davide Bonifazi**

ANNO ACCADEMICO 2014 / 2015

UNIVERSITÀ DEGLI STUDI DI TRIESTE

XXVIII CICLO DEL DOTTORATO DI RICERCA IN

SCIENZE E TECNOLOGIE CHIMICHE E FARMACEUTICHE

FUNCTIONAL CHROMOPHORES FOR LIGHT-HARVESTING APPLICATIONS

Settore scientifico-disciplinare: CHIM/06

DOTTORANDA
TANJA MILETIĆ

COORDINATORE
PROF. MAURO STENER

SUPERVISORE DI TESI
PROF. DAVIDE BONIFAZI

ANNO ACCADEMICO 2014 / 2015

Contents

Acknowledgments

…and also this moment arrived. Here I am, trying to write down all the acknowledgments for the wonderful people I met during this experience, those who contributed directly to this manuscript and those who were close to me during this period, hoping I will not forget nobody.

Firstly, I would like to specially thank my supervisor *Prof. Davide Bonifazi* for the opportunity he gave me to start this PhD and to work on different challenging and very interesting projects, for his guidance during these years and for his constant motivation and tremendous enthusiasm.

Many thanks go to *Prof. Maurizio Prato* and Prof. *Tatiana Da Ros* for welcoming me in the big Prato group. I will be always grateful for the opportunity I had to work in such international environment.

I would like to sincerely thank all collaborators that were involved in the FIRB project and made this thesis possible. In particular, many thanks go to *Dr. Eleonora Pavoni*, *Prof. Nicola Armaroli*, *Dr. Mirko Panighel*, *Dr. Giovanni di Santo*, *Prof. Paola Ceroni*, *Dr. Giacomo Bergamini* and *Prof. Giuseppe Brancato* for the collaborative work and help. Moreover, I would also like to thank for their work the people from the University of *Salento, Lecce*, in particular *Dr. Andrea Listorti* and *Dr. Silvia Colella*.

Special thanks go to *Dr. Federica de Leo*, *Dr. Andrea Fermi*, *Prof. Stelios Couris* and *Giannis Orfanos*, for the large amount of work performed for the perylene project even if part of it is not included in this thesis.

The work on carbon nanotubes would not have been realized without the inestimable help of Dr. *Riccardo Marega* and *Dr. Caroline A. Ahad Hadad*. Thank you for being always open to help. Many special thanks are going to *Dr. Nicola Demitri* not only for the X-ray measurements, but also for his great dedication, help and collaboration.

Particular thanks go to *Maria Mercedes Lorenzo Gracia*, *Lou Rocard* and *Dr. Antoine Stopin* for the proofreading of this manuscript and the tremendous help. Moreover, I have to deeply acknowledge *Nicolas Biot* for the precious and inestimable help with the assembling of this thesis. Thanks to all of you for the enormous support. I am not sure I would manage to do it without you.

Sincere thanks go to all the staff members at Department of Pharmaceutical and Chemical Sciences of University of Trieste for their help during these three years.

I would like to thank all the people from *Bonifazi* Group, *Maria*, *Francesco*, *Davide*, *Andrea S.*, *Andrea F.*, *Cataldo*, *Lorenzo*, *Lou*, *Nicolas*, *Alex*, *Antoine* and *Rodolfo*. Thank you for the nice welcome in Cardiff and for creating a very enjoyable working environment. Many thanks go also to the members of the old COMS group. In particular, I would like to thank *Silvia*, *John* and *Dario* for the short collaborative experience we had the opportunity to share. The biggest thanks go to all the people from Prato's Lab, past and present members, for enriching me in these years in so many different ways. In particular, thanks go to *Michela P.* (thank you for managing us in so efficient way), *Caroline, Jose, Marco*, *Dani, Nuria, Cristina, Maribel, Lorenzo, Silvia, Alexa, Federico, Alejandro* (thanks to you, Alex, I will never forget where the Erlenmeyer's are), *Andrea*, *Mimmo*, *Adrian*, *Anirban*, *Francesco*, *Angela, Jeni* (I simply adore you), *Davide* (O Da! Che te devo dire, grazie!*)* and all others from C11 and Pharmacy. Thanks to all for the good time we shared and for the great people you are.

I would like to express my thanks to *Jacopo*. Your scientific enthusiasm, hard motivation together with your well-mannered behavior made me very glad to have the opportunity to work with you, even if for a short period. Undoubtedly, special thanks go to some people who shared with me this experience, who are not only great colleagues but adorable friends. *Arturo* and *Manuel,* you are the best lab mates ever. The time I had in and out the lab with you was simply great; thank you for the nice moments, for the unforgettable support, for your craziness, but above all, thank you for the sincere friendship.

This experience would not be the same without the *chicas* group. The relation between us is difficult to describe. *Ana*, *Maria*, *Vale* and *Agnieszka* thank you simply for being present and for the enormous support, nice moments, discussions, arguments but especially for believing in me when I was not. The folly of our group relies in the peculiar beauty of each of you and for this I particularly thank you. *Agnieszka* thank you twice, you know why! You are my master of life. *Maria,* thank you for always helping and supporting me, this thesis would not be possible without you. *Muchas gracias de corazon*! Very special thanks go to *Giuly*, for the precious friendship and for having been the most unique person I ever met.

Un grande e sentito grazie va a casa Biecheri. *Alice* e *Mariarita* grazie di cuore per il vostro supporto e affetto. Se ora chiamo Trieste casa, è grazie a voi. Semplicemente grazie anche alle mie amiche di sempre. In particolare, *Doris*, *Sandra*, *Ileana*, *Tamara*, *Vok* grazie per avermi sempre supportato ma soprattutto spronato durante questo lungo periodo. *Komšnice*, šta reći nego hvala ti! A special thank goes to my family in law for making me always feel at home. Un ringraziamento speciale lo devo alla mia famiglia per l'incondizionato sostegno

durante questo cammino e per avermi sempre creduto ed affiancato in qualsiasi scelta intrapresa.

At the end of all, there is one last person I need to thank, without whom such effort would have been worth nothing. Thank you *Denis* for being part of my life and for your strong belief in me. Your unconditional support, constant patience and amazing attitude have taught me pretty much about sacrifice and compromise and this is because this thesis is dedicated to you.

List of abbreviations

Å	Angstrom
Abs	Absorption
AFM	Atomic force microscopy
$AlCl_3$	Aluminium chloride
aq.	Aqueous
B_2pin_2	Bis(pinacolato)diboron
BChl	bacteriochlorophylls
BLA	Bond length alternation
BINOL	1,1'-binaphthyl-2-2'-diol
ºC	Degree centigrade (0 ºC = 273.16 K)
calc.	Calculated
CB	Chlorobenzene
Chl	Chlorophylls
CH_2Br_2	Dibromomethane
CH_2Cl_2	Dichloromethane
CH_3CN	Acetonitrile
CH_3SO_3H	Methanesulfonic acid
Cm	Centimeter
CMD	Concerted-metalation-deprotonation
CNTs	Carbon nanotubes
CuO	Copper(II) oxide
$Cu(OAc)_2$	Copper(II) acetate
d%	Doping ratio
DDQ	2,3-dichloro-5,6-dicyano-1,4-benzoquinone
DIPEA	N,N-Diisopropylethylamine
DMF	N,N-Dimethylformamide

DMSO	Dimethylsulfoxide
DNF	Dinaphthofuran
DOS	Density of states
Dtbpy	4,4-di-tert-butyl bipyridine
E_g	Energy bandgap
E_{Int}	Energy due to intermolecular interaction
eq.	Equivalent
E_{Res}	Aromatic stabilization resonance energy
ESI	Electrospray ionisation
E_{sub}	Enery due to the push-pull effect
ET	Electrontransfer
EtOAc	Ethyl Acetate
eV	Electronvolt (1eV = 1.602 x 10^{-19} J)
Fs	Femtoseconds
FG	Functional group
FRET	Förster-type energy-transfer
FTO	Fluorine-doped thin oxide
GNRs	Graphene nanoribbons
H	Hour
H_2SO_4	Sulfuric acid
HDI	Hexarylenebis(dicarboximides)
HLG	HOMO-LUMO gap
HOMO	Highest occupied molecular orbital
HR	High resolution
HTM	Hole Transport Material
Hz	Hertz (s^{-1})
IR	Infrared
*i*PrOH	Isopropanol
IR	Infrared (spectroscopy)

KOH	Potassium hydroxide
LiTFSI	Lithiumbis(trifluoromethanesulfonyl)imide
LUMO	Lowest unoccupied molecular orbital
M	Molar
MALDI	Matrix-assisted laser desorption/ionisation
MeOH	Methanol
MHz	Megaherzt
Min	Minute
MS	Mass spectrometry
MWCNTs	Multi-Walled Carbon nanotubes
Mw	Microwave irradiation
N	Number of units
NMI	Naphtalenemonoimides
NIR	Near infrared
Nm	Nanometer
NMR	Nuclear magnetic resonance
ODCB	*Ortho*-dichlorobenzene
OLED	Organic-light emitting diode
OFET	Organic field-effect transistor
OSC	Organic semiconductor
OTFT	Organic thin-film transistor
PAH	Polycyclic aromatic hydrocarbon
PBIs	Perylene bisimides
Ps	Picosecond
PDI	Perylene diimide
$Pd(OAc)_2$	Palladium(II) acetate
$PC_{71}BM$	phenyl-C_{71}-butyric acid methyl ester
$PhI(OAc)_2$	(Diacetoxyiodo)benzene
PivOH	Pivalic acid

PMI	Perylenemonoimide
PLM	Photoluminescence mapping
PCE	Power conversion efficiency
PPN	Poly(*peri*-naphthalene)
PPV	Poly(*p*-phenylenevinylene)
ppm	Parts per million
PSCs	Perovskite solar cells
P_3OT	poly(3-octylthiophene)
p-TsOH	*p*-Toluenesulfonic acid
PXX	*peri*-xanthenoxanthene
RC	Reaction center
r.t.	Room temperature
$Sc(OTf)_3$	Scandium(III) triflate
SEM	Scanning electron microscopy
SDBS	sodium dodecyl benzene sulfate
Spiro-OMeTAD	Tetrakis(N,N-di-p-methoxyphenylamine)-9,9′-spirobifluorene
SWCNTs	Single walled carbon nanotubes
TAT	Tetra-aza-terrylene
^{t}Bu	*Tert*-Butyl
TCE	Tetrachloroethane
TD	terrylenediimide
Tf_2O	Trifluoromethanesulfonic anhydride
TFA	Trifluoroacetic acid
TGA	Thermogravimetric analysis
THF	Tetrahydrofurane
t.l.c.	Thin layer chromatography
UV-Vis	Ultraviolet-visible
vHS	van Hove singularities
vs.	*versus* (latin)- against

VT	Variable temperature
ZnTPP	Zn (II) tetraphenyl porpyrin
λ	Ultraviolet-visible
ε	Molar extinction coefficient
Φ_{fl}	Fluorescence quantum yield
θ	Dihedral angle
θp	Pyramidalization angles
τ	Fluorescence lifetimes

Abstract

The photosynthetic system is regarded as the most sophisticated nanobiological machine in nature. It deploys a large numbers of pigments in antenna complexes to harvest light and funnel the resulting excited-state energy to the reaction centers. The choice of the light absorbing components is one of the crucial steps in the design of synthetic light-harvesting systems. In this respect, the preparation of new dyes with tunable opto-electronic properties remains a very challenging task for the development of highly efficient light-harvesting materials.

Before addressing the detailed investigations of this thesis work, in *Chapter I,* a briefly introduction on natural and synthetic antennas along with an outlook on the possible types of approaches towards the engineering of the HOMO-LUMO gap for the development of new dyes with unique opto-electronic properties is given to the reader. Moreover, a detailed outline of the manuscript is described.

This dissertation focuses on the design, synthesis and characterization, as well as investigations of the optical properties, of different series of new functional chromophores. Specifically, *Chapter II* addresses the design and synthesis of a series of well-defined oligo (*p*-phenylenevinylenes) bearing styryl units of different π-extension, namely molecules **2-1** and **2-2**. A double *Horner-Wadsworth-Emmons*-type reaction has been exploited for the synthesis of the most π-extended molecule **2-1.** Subsequently, newly prepared chromophores have been used as donor moieties for the preparation of donor-acceptor systems (**f-SWCNT-1** and **f-SWCNT-2**), in which single walled carbon nanotubes (SWCNTs) plays the role of the acceptor unit. The choice of the latter is motivated by the high conductivity, strong mechanical, thermal and environmental resistance that characterize this carbon material. A covalent approach *via* amidation reaction has been exploited to anchor the chromophoric unit to the SWCNT. Eventually, the photophysical properties of the hybrids have been investigated in order to put in evidence the photo-induced processes occurring

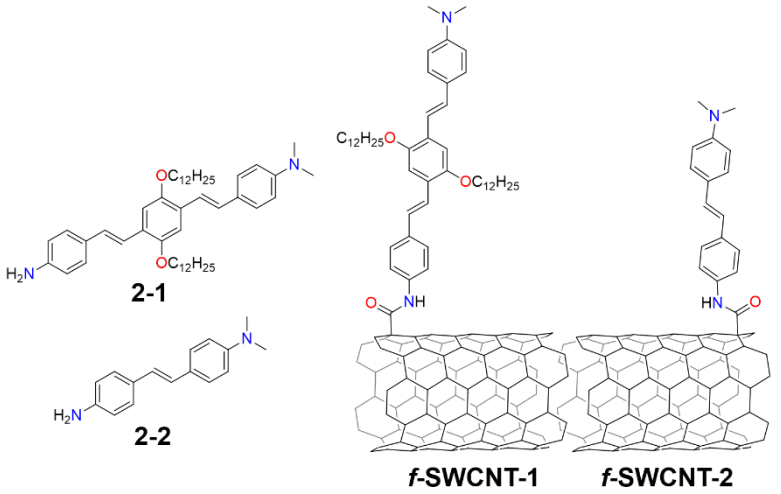

between the individual entities and evaluate their applicability as photoactive material in energy conversion systems.

On the other hand, *Chapter III* describes the synthesis of novel light absorbing molecules based on oxygen-containing π-extended polycyclic aromatic hydrocarbons (PAH), in which two polyaromatic hydrocarbon substructures are bridged through one or two O atoms. The main building block used for this purpose is the perylene molecule. High-yielding ring-closure key steps were exploited for the formation of either furanyl or pyranyl frameworks, depending on the reaction conditions, through intramolecular C-O bond formation. Based on the shape of the aromatic systems and the conjugation of the π fragments, the absorption and emission maxima of newly prepared O-doped π-extended PAH were finely tuned throughout the entire visible region.

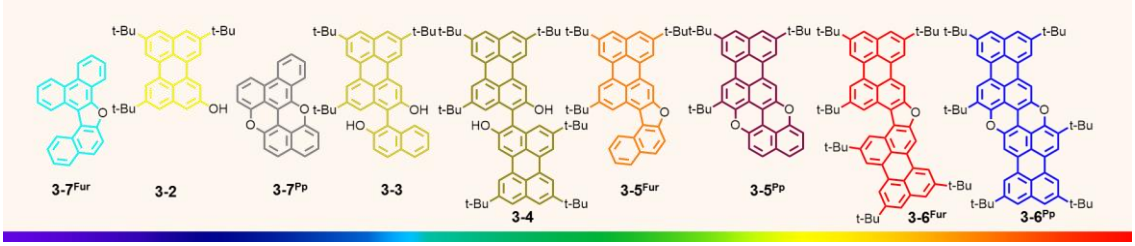

In the second section of this chapter we tackled the development of a second family of O-doped π-extended PAH bearing additional functionalization moieties in order to enhance the solubility and tune energy and optical properties. The last section of the chapter is dedicated to the preparation of a different category of π-conjugates. A new family of biperylene derivatives bearing different dihedral angles between the two perylene moieties, was thus prepared and studied in terms of UV-Vis, fluorescence and XRD spectroscopy.

Riassunto

Il sistema fotosintetico è considerato il sistema "nano"- biologico più sofisticato presente in natura. Utilizza un gran numero di pigmenti, disposti in sistemi antenna, che raccolgono la luce e la trasferiscono a centri di reazione specializzati. La scelta delle componenti che assorbono la luce è uno dei passaggi cruciali nella progettazione di sistemi antenna artificiali. A tale proposito, la sintesi di nuovi cromofori con proprietà optoelettroniche modulabili rimane una delle sfide maggiori per sviluppare materiali che raccolgono la luce con elevata efficienza.

Prima di discutere nel dettaglio la ricerca svolta in questo lavoro di tesi, nel capitolo I, al lettore verrà presentata una breve introduzione riguardante i sistemi antenna naturali e artificiali e i possibili tipi di approccio utilizzati per il *design* di nuovi cromofori dalle uniche proprietà optoelettroniche; in particolare la modifica della differenza di energia fra gli orbitali HOMO e LUMO, detta anche il *bandgap*. Inoltre, questo capitolo riporta anche i punti essenziali dell'intero manoscritto.

Questo lavoro di tesi si concentrerà sulla progettazione, sintesi e caratterizzazione nonché sullo studio foto-fisico di diverse classi di nuovi cromofori funzionali. Più precisamente, il capitolo II descrive il *design* e la sintesi di una serie di composti oligo(*p*-fenilene vinilene) ben definiti, presentanti componenti stiriliche di lunghezze diverse, cioè le molecole **2-1** e **2-2**. A tale proposito, la sintesi della molecola **2-1** è stata realizzata utilizzando la reazione di Horner-Wadsworth-Emmons. Successivamente, tali cromofori sono stati utilizzati come specie donatore per la preparazione di sistemi donatore-accettore (f-SWCNT-1 e f-SWCNT-2), nei quali i nanotubi di carbonio a parete singola (SWCNTs) svolgono il ruolo di accettore. La scelta di quest'ultimi è motivata dall'elevata conducibilità, forte resistenza meccanica, termica ed ambientale che caratterizzano questo materiale carbonioso. Un approccio covalente, che sfrutta una reazione di ammidazione, è stato usato per ancorare l'unità cromoforica alle pareti dei nanotubi SWCNT. Infine, le proprietà foto-

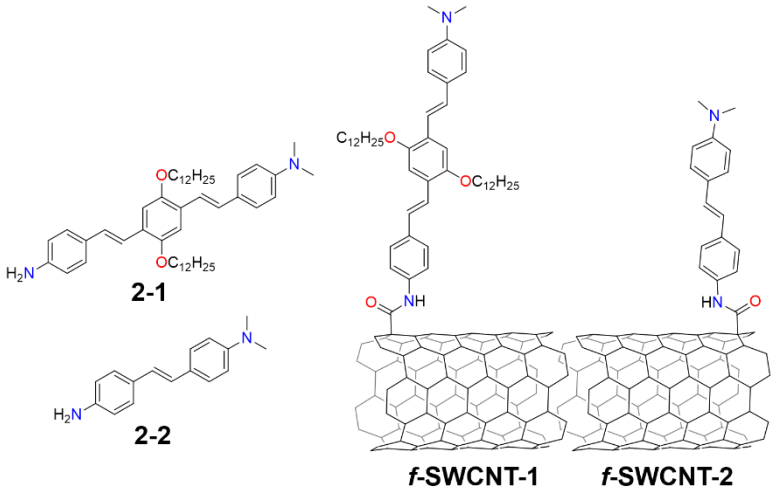

fisiche dei sistemi così preparati sono state studiate allo scopo di evidenziare i processi di trasferimento di energia per risonanza tra le singole componenti e valutarne l'applicabilità come materiale foto-attivo in sistemi di conversione di energia.

Il capitolo III descrive la sintesi di cromofori basati su idrocarburi policiclici aromatici (IPA) dalla superficie aromatica estesa e contenenti atomi di ossigeno, in cui due sottostrutture IPA sono connesse tra loro tramite anelli contenenti uno o due atomi di ossigeno. L'unità principale usata per la sintesi di tali nuovi cromofori è il perilene. Passaggi chiave di ciclizzazione ad elevata resa, basati su condizioni di reazione diverse, sono stati utilizzati al fine di preparare anelli furanici e piranici, tramite formazione di legami C-O intramolecolari. In base alla forma del sistema aromatico e la coniugazione dei vari frammenti contenenti atomi di ossigeno, i valori massimi di assorbimento e di emissione dei nuovi cromofori sono stati finemente regolati attraverso tutto lo spettro del visibile.

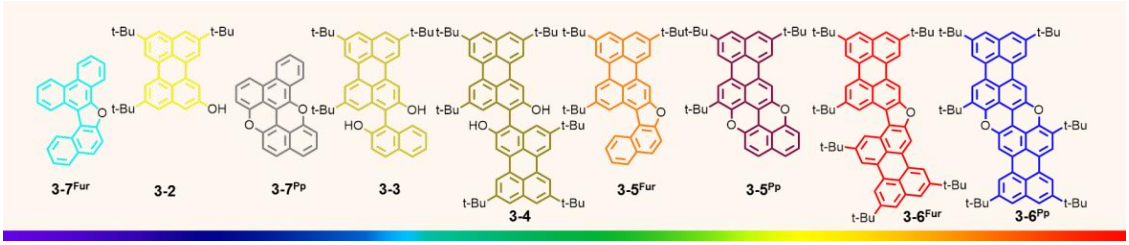

Nella seconda sezione di questo capitolo abbiamo affrontato la preparazione di una seconda famiglia di IPA contenenti ossigeno che presentano gruppi funzionali aggiuntivi con lo scopo di aumentarne la solubilità e poter modulare le proprietà opto-elettroniche. L'ultima sezione del capitolo, invece, è dedicata alla sintesi di un'ulteriore categoria di IPA. Più in specifico è stata preparata una nuova classe di composti biperilenici caratterizzati da angoli diedri diversi tra le due porzioni perileniche e studiata in termini di UV-Vis, fluorescenza e spettroscopia raggi X.

1. General introduction

Energy is the most important issue of the 21st century.[1] The world's current energy requirements are far from being satisfied, and the solar energy represents the most abundant renewable energy resource available to us. There is a huge gap between the present use of solar energy and its enormous potential.[2] This potential is demonstrated by the high efficiency of natural photosynthesis, which provides the necessary chemical energy for almost all life on Earth and this since more than two billion years.[3]

Photosynthesis literally means "synthesis with light" and it is the process used by plants, algae and certain bacteria to harness energy from sunlight into chemical energy.[4] The photosynthetic process begins with the absorption of sunlight by specialized pigment-protein complexes (known as light harvesting complexes), that function as antennae for incident energy. This is followed by the funneling of the excitation energy within the antenna assembly to special sites called the reaction centers (RCs), in which the captured energy is converted into chemical energy by means of electron-transfer reactions (Figure 1.1.).

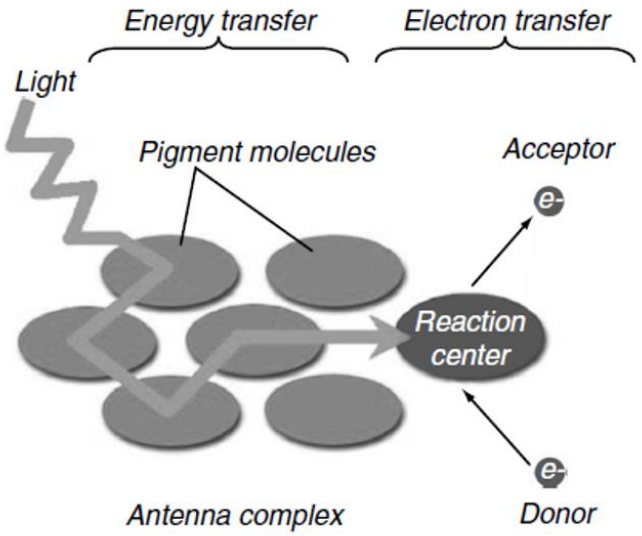

Figure 1.1. Schematic representation of antennas and reaction centers in photosynthetic systems. Antenna pigments collect the light and energy transfer processes deliver the excited state to the reaction center where electron transfer reactions store the energy.[5]

Astonishing features of photosynthesis are its remarkable efficiency and adaptability. At low light intensities, the fact that almost every captured photon reaches the RCs triggering the charge separation process emphasizes the near 100% energy transfer efficiency. That efficiency relies on a particular organization and ratio of selected chromophores (with

distinct optical and redox properties) that enables maximum light absorption and energy conversion.[3,6]

The photoinduced energy transfer processes in most photosynthetic antennas are occurring by Förster resonance energy transfer (FRET) mechanism.

$$D + h\nu \rightarrow D^*$$

$$D^* + A \rightarrow D + A^*$$

$$A^* \rightarrow A + h\nu'$$

FRET is a distance-dependent interaction between the electronic excited states of two pigment molecules in which the excitation is transferred from a donor (D) molecule to an acceptor (A) molecule in a non-radiative fashion through long-range dipole-dipole interactions. In the process of FRET, initially a donor (D) fluorophore is excited by a photon and then relaxes to the lowest excited state, S_1. The energy released when the electron returns to the ground state (S_0) may simultaneously be transferred to a nearby chromophore, the acceptor (A). After excitation, the excited acceptor emits a photon and return to the ground state, if another quenching state do not exist. (Figure 1.2) The theory supporting energy transfer is based on the concept of treating an excited fluorophore as an oscillating dipole that can undergo an energy exchange with a second dipole having a similar resonance frequency.

Few criteria must be satisfied in order for FRET to occur: *(i)* the fluorescence emission spectrum of the donor molecule must overlap the absorption or excitation spectrum of the acceptor chromophore; *(ii)* the two chromophores (donor and acceptor) must be in the close proximity one to the other (typically 1 to 10 nanometer); *(iii)* the transition dipole orientation of the donor and acceptor must be approximately parallel to each other; *(iv)* the fluorescence lifetime of the donor molecule must be of sufficient duration to permit the FRET to occur.[7]

The rate of FRET between two chromophores exhibiting dipole-dipole interactions is expressed by the following equation:[8]

$$k_{FRET} = \frac{1}{\tau_D} \frac{9000(\ln 10)k^2 \Phi_D I}{128\pi^5 N n^4} \frac{1}{R^6}$$

Where k is the orientation factor associated with the dipole-dipole interaction between the D and A, n is the refractive index of the medium, N is Avogadro's number, ϕ_D is the fluorescence quantum yield and τ_D is the excited state lifetime of the donor. R describes the center-to-center separation of donor and acceptor and the FRET is typically observed in the range of 1-10 nm. The Förster spectral overlap I is referred to the spectral overlap between the donor emission spectrum and acceptor absorption spectrum.

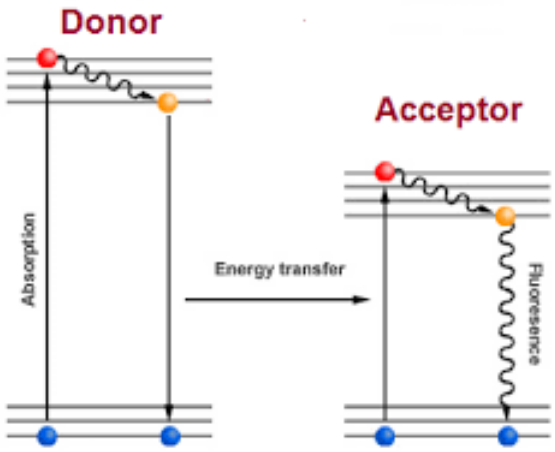

Figure 1.2. Jablonski diagram of FRET.[7]

1.1 From natural to artificial light-harvesting complexes

There is a wide variety of light-harvesting complexes in nature. They differ in the arrangements of chromophores, chromophore types (*e.g.* chlorophyll, bilins and carotenoids) and optical properties. Some major examples of photosynthetic antennas are the green sulfur bacterial chlorosome,[9] cyanobacterial phycobilisomes,[10] dinoflagellate peridinin-chlorophyll protein, [11] the Pcb protein (Prochlorococcus chlorophyll a_2/b_2),[12] light-harvesting complex II (LHCII) in green plants[13] and the purple bacterial light-harvesting complexes 1 (LH1) and 2 (LH2).[14]

Figure 1.3**.** displays structures of some of the main classes of photosynthetic antenna complexes. All these antennas are membrane proteins containing a network of interacting chromophores. Even though they show structural diversity, all antenna complexes are able to convert the photogenerated excitations to charge separation with very high efficiency.[15]

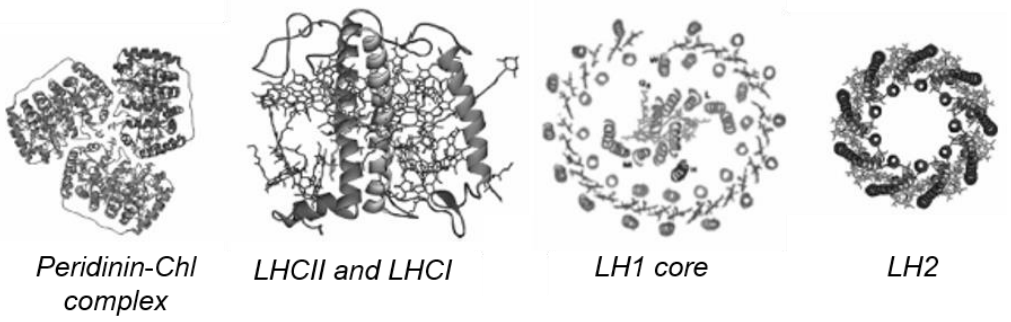

Figure 1.2. Some examples of photosynthetic light-harvesting antenna complexes. From left: dinoflagellate peridinin-chlorophyll protein,[11] light-harvesting complex II in green plants[13] and the purple bacterial light-harvesting complexes 1 (LH1) and 2 (LH2).[14]

The chromophores used for photosynthetic light harvesting include chlorophylls, linear tetrapyrroles, and carotenoids such as β-carotene and lutein in plants, or bacteriochlorophylls

in bacteria. The unique biological and chemical functions of those molecules are determined by their molecular structures, containing highly delocalized conjugated molecular orbitals. The absorption properties of these chromophores are highly tunable and vary owing to the extent of the conjugation and the number and nature of the substitutions, creating a "rainbow" of colors that covers the visible and the near infrared regions of the solar spectrum (Figure 1.4).[16]

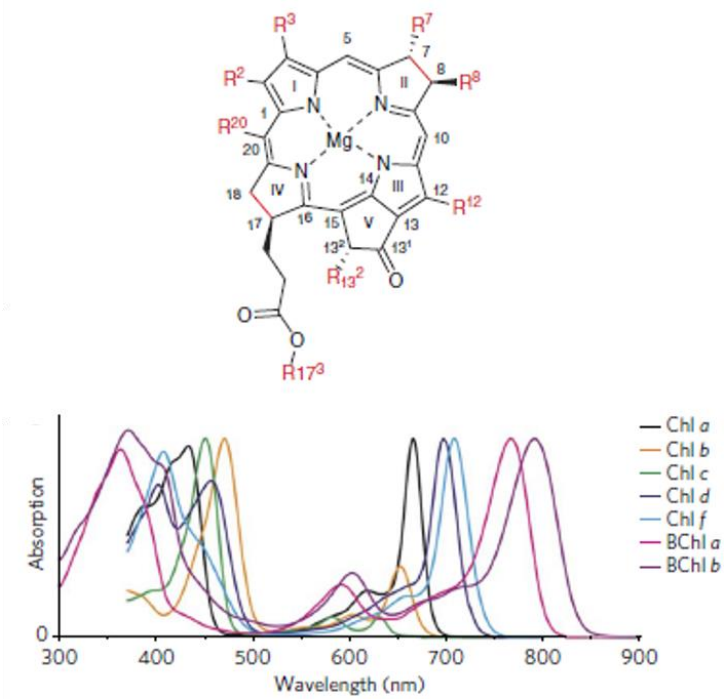

Figure 1.3. Top: General structure of the main pigments used in natural light harvesting chlorophylls (Chl) and bacteriochlorophylls (BChl), which are differently substituted tetrapyrroles. Bottom: Absorption spectra of photosynthetic pigments in various solvents.[17]

Key parameters that characterize antennas are the absorption cross-section of the solar energy, as well as its conversion efficiency and rate. Chromophores must strongly absorb visible or near infrared light (characteristic $\varepsilon \sim 100{,}000\ M^{-1}cm^{-1}$),[3] and the excited states generated by this absorption must be sufficiently long lived. The efficiency is determined by the fraction of the absorbed energy that reaches the reaction center and can be described by the quantum yield. Commonly, natural antennas present very high quantum yields, not lower than 95%.[4,18] Moreover, they are relatively stable supramolecules and are arranged in a controlled and precise way that provides paths for excitons to migrate to the reaction centers. The fast energy transfer between single chromophores (characteristic times vary from 100 to 1000 fs)[19] should be combined with the relatively slow (tens of picoseconds) electron transfer from the antenna to the reaction center to avoid the over-loading of the latter. They

present also ways of deactivating potentially destructive side products such as triplet states and singlet $0_2^{\bullet}$.

The controlled organization of functional chromophores into highly ordered self-assembled arrays mimicking the characteristics of natural photosynthetic systems have polarized a great interest in material science for various applications.[20–22] In this respect, supramolecular assemblies of spatially well-organized dyes can facilitate excitation energy transfer and are fundamental to the realization of efficient artificial antennas.

First of all, the most important requirement for a light-harvesting system is its capacity to absorb light, the absorption spectrum of its components should cover a substantial part of the visible spectral region. In this respect, the most important step in the design of an artificial antenna system is the selection of the chromophores.

The chromophore is the simplest unit of the light-harvesting complex, but no single chromophore is capable of efficiently powering artificial photosynthesis. For instance, Zn (II) tetraphenyl porpyrin (ZnTPP) has a very high extinction coefficient (500×10^3 M^{-1} cm^{-1}),[23] but it covers only a narrow region of the solar spectrum (maximum absorbance peak at 424 nm). This problem can be overcome by working with dye aggregates,[24] which owing to excitonic couplings can have much broader absorption ranges. On the other hands, perylene bisimides (PBIs) have much wider spectral coverage, but present lower molar extinction coefficient than ZnTPP (95×10^3 M^{-1} cm^{-1} for unsubstituted perylene bisimide).[23] Hence, the incorporation of different chromophores into an organized spatial arrangement that enables efficient energy transfer between them is the second key step for the creation of artificial antenna. For the assembly of the chromophores, covalent and non-covalent strategies have been envisaged allowing to obtain an unlimited number of artificial antennas structurally organized as dendrimers,[25–29] macrocycles,[30,31] supramolecular polymers,[32] nanostructures[33–36] or assembled using biomaterials such as proteins[37,38] or nucleic acids,[39,40] having unique photophysical and optical properties.

An example of covalently linked light-harvesting assembly is presented in Figure 1.4. It is a dendrimer macromolecule in which the peripheral chromophores are the primary light absorbers as in the natural antenna. Dendrimers are well-defined, tree-like macromolecules with a high degree of order and the possibility to contain selected chromophoric units in predetermined sites of their structure and have attracted great attention as novel nanoscopic light-harvesting molecules.[41] *Müllen* and co-workers reported an example of naphthaleneimide-peryleneimide-terrylenediimide-based dendrimer (Figure 1.4). This

multichromophoric rigid polyphenylenic dendrimer bearing a terrylenediimide (TD) as a core, perylenemonoimide (PMI) chromophores in the scaffold and naphtalenemonoimides (NMI) at the rim absorbs light over the whole visible range of the spectrum and emits mainly in the red region due to unidirectional FRET from NMI and PMI donors to TD. [42] In fact, the spatial positioning of these chromophores within the triad and their respective spectral properties make this multichromophoric system an efficient light collector. It is possible to design and synthesize dendrimers containing a large variety of chromophoric groups organized in the dimensions of time, energy and space in order to obtain efficient light-harvesting devices.[41]

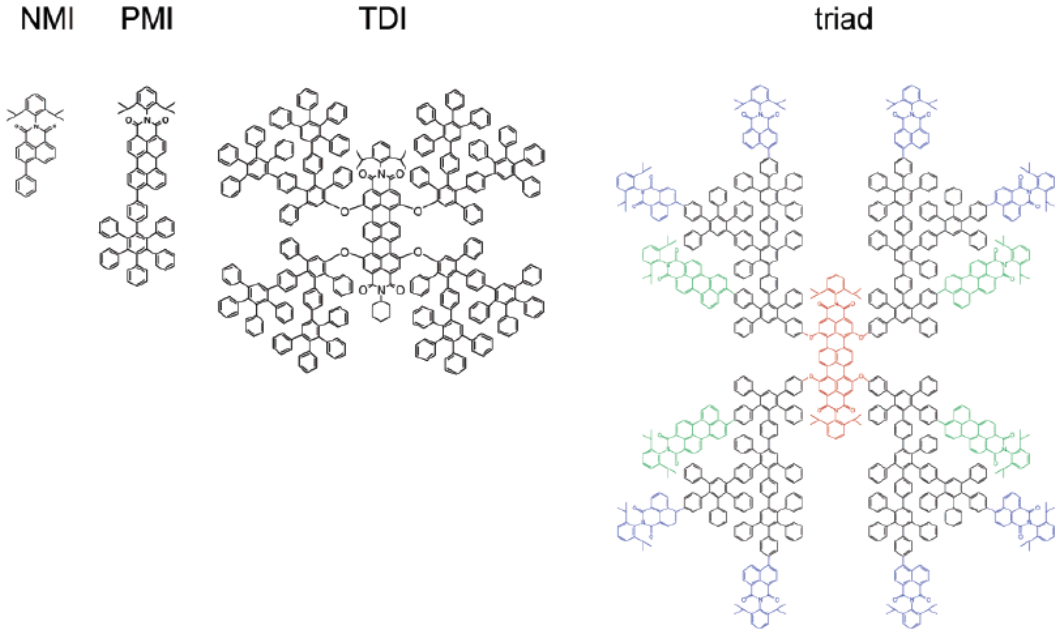

Figure 1.4. Example of a polyphenylene dendrimer with multiple peripheral peryleneimide, naphtalenemonoimides (NMI) at the rim and a central terrylenediimide chromophore.[42]

On the other hands, based on non-covalent chromophore assembly, *Kobuke* and co-workers described the first example of a cyclic hexamer of phorphyrins prepared by connecting slipped-cofacial dimer units via coordination from the imidazolyl arm to the central Zn ion (Figure 1.5).[30] Phorphyrins are ideal chromophores for artificial light harvesting because they are structurally similar to photosynthetic pigments and have advantageous photophysical properties, such as photo-stability, visible-light absorption,[43] long-lived excited states, rapid excitation energy exchange,[44] and high molar extinction coefficients, which can be easily tuned by metal coordination.[45] In the porphyrin cyclic hexamer macroring, the porphyrin−porphyrin arrangement is very similar to those of the light-harvesting complexes in photosynthetic bacteria in term of relative orientation and overall structure.

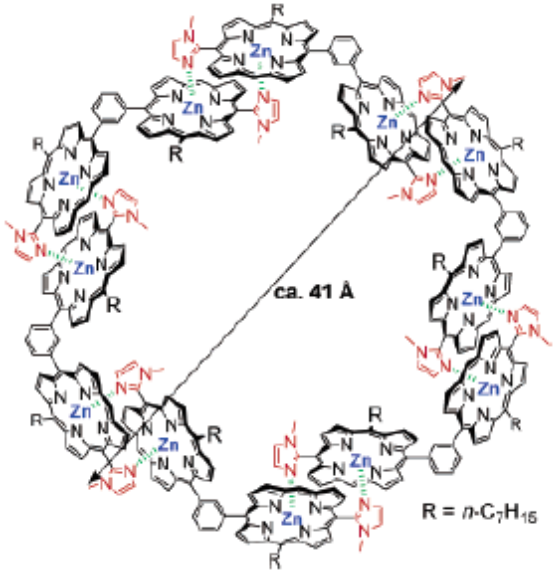

Figure 1.5. A structural model of the target porphyrin hexameric macroring.

In summary, the choice of the chromophores and the way to assembly them remain the two important steps for the creation of artificial antennas. Even though natural pigments offer us a large panel of photophysical and optical properties, the preparation of new dyes with tunable colors remains a very challenging task for the development of highly efficient light-harvesting materials.

1.2 Tuning the colors of molecules by tuning the HOMO-LUMO gap (HLG)

The design of functional material through band gap and energy level tuning is crucial in developing new dyes with unique photophysical and optical properties. In this respect, various structural variables have to be mastered in order to control the HOMO-LUMO gap of π-conjugated systems. In this section we will briefly introduce the key parameters that have to be taken in consideration to design functional organic chromophores with tunable opto-electronic properties.

The band gap of a material (E_g) derived from a linear π-conjugated system can be defined by the sum of five contributions as described by the following equation, demonstrating that the structural feature of π-conjugates is crucial on the control of the HOMO-LUMO gap.[46,47]

$$E_g = E_{BLA} + E_{Res} + E_{Sub} + E_{\theta} + E_{\mathrm{Int}}$$

One of the main features that influence the magnitude of the energy gap is explained by the *Peierls* instability, which depends on the degree of Bond length alternation (BLA) in the conjugated path. Specifically, E_{BLA} is related to the difference between single and double bond lengths. Synthetic modifications leading to structural changes resulting in a reduced BLA can be expected to decrease the HOMO-LUMO gap (HLG).[46] For instance, in aromatic systems like poly(p-phenylene), poly(pyrrole) or polythiophene (Figure 1.6), that have a non-degenerated ground state, the two limiting mesomeric forms (aromatic *vs* quinoid) obtained by the flip of the double bonds are not energetically equivalent. In most cases the quinoid form is characterized by a smaller E_g.[48]

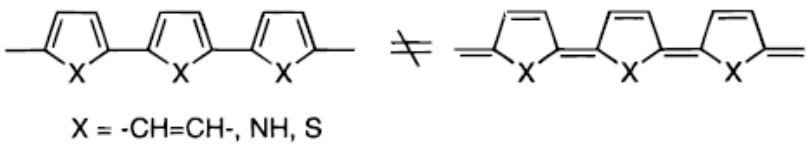

X = -CH=CH-, NH, S

Figure 1.6. Schematic representation of the two limiting mesomeric forms obtained by the flip of double bonds for poly(p-phenylene), poly(pyrrole) or polythiophene .[46]

Another important contribution to take into account is the resonance energy of the monomeric unit. The aromaticity results in competition between the confinement of π-electron within the rings and delocalization along the chain. In fact, the energy needed to switch from the aromatic form to the quinoid one directly depends on the aromatic stabilization resonance energy (E_{Res}) of the aromatic moiety. This effect thus contributes to the HOMO-LUMO gap (E_g) by a quantity of E_{Res}, and may be affected for instance by insertion of heteroatoms or by the bridging group between the two aromatic cycles. Particularly in the case of polyaromatic systems, another aspect that has to be considered is the rotational disorder around carbon-carbon bond of two cycles. In this respect, the planarity in a π-conjugated molecule is defined by E_θ, where θ is the dihedral angle between consecutive units and can affect the overlap between the orbitals and thus increase E_g by a quantity of E_θ. Among all, the most direct way to tune the HOMO and LUMO energy levels of a π-electron system involves the introduction of electron-withdrawing or electron-donating substituents that will respectively increase the HOMO or decrease the LUMO level. The influence of the so called "push-pull" effect on the energy gap of a π-conjugated structure can be expressed as E_{Sub}.[46,47] All four structural factors contribute to the tuning of the HOMO-LUMO gap and are essential for the design of synthetic approaches for the engineering of the HLG of an isolated conjugated system. However, in some cases, when assembling individual molecules into a material, a fifth contribution, E_{Int}, related to the

intermolecular interactions can affect the magnitude of the band gap. The described structural factors that determine the band gap of linear π-conjugated systems are summarized in Figure 1.7.

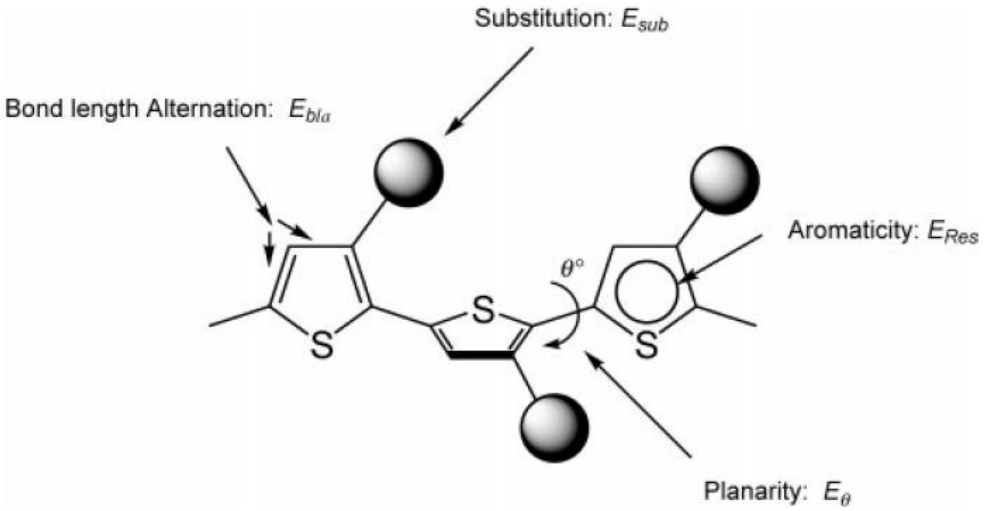

Figure 1.7. Representation of the structural factors that influence the band gap of materials derived from π-conjugated systems.[47]

In the present work we will discuss in detail the use of different synthetic tools related to one or several structural contributions discussed above to finely tune the HOMO-LUMO gap of π-conjugates. In particular, an approach to control the energy band gap that involves the elongation of the aromatic surface along with planarization and rigidification of the conjugated system will be employed.

1.3 Outline of the dissertation

In this doctoral work, our research activities were directed toward the different aspects of the preparation of single chromophoric constituents presenting unique opto-electronic properties. In this respect, we wanted to provide an insight view on the relationship between structure and properties of different classes of π-conjugated structures. Accordingly, the work here presented is divided into two main chapters and schematically represented in Figure 1.8.

Figure 1.8. Schematic representation of the outline of this doctoral dissertation

Chapter II describes the design and the synthesis of a novel oligo (p-phenylenevinylenes) chromophore for the functionalization of single walled carbon nanotubes (SWCNTs). Since photoinduced processes attracted much interest because of their relevance to solar energy conversion systems, we will present the preparation and the photophysical characterizations of new systems made of electron-accepting single chirality enriched SWCNTs and electron-donating dimethylamino distyrylbenzene derivatives. A covalent approach *via* amidation reaction has been exploited to anchor the chromophoric unit to the SWCNT.

On the other hand, concerning the choice of light-absorbing components for the preparation of synthetic light-harvesting systems *Chapter III* addresses the design and synthesis of oxygen-containing π-extended conjugated systems as new chromophoric entities. The main conjugated skeleton considered is the perylene. In particular, starting from perylene we developed different classes of compounds bearing different structural features (such as aromatic elongation, torsion angle and doping ratio). An intramolecular acid-catalyzed cyclization and a Cu(I)-mediated C-H activation/C-O cyclization were exploited to prepare the furanyl and pyranyl frameworks, respectively. Photophysical measurements showed that the molecules feature tunable absorption properties and high emission yields. Simultaneously, we tackled the development of a second family of O-doped π-extended conjugated systems bearing additional functionalization sites for anchoring different functional groups or moieties. This strategy will allow the incorporation of the newly prepared chromophores into more complex systems and their exploitation as light-harvesting materials. The preliminary results toward their synthesis are presented. The last section of the chapter provides an overview on the relationship between the interplanar angle and the optical properties of π-extended PAHs, aiming to the preparation of new material with tunable opto-electronic properties.

1.4 Bibliography

[1] N. Armaroli, V. Balzani, *Angew. Chemie - Int. Ed.* **2007**, *46*, 52–66.

[2] N. S. Lewis, *MRS Bull.* **2007**, *32*, 808–820.

[3] G. D. Scholes, G. R. Fleming, A. Olaya-Castro, R. van Grondelle, *Nat. Chem.* **2011**, *3*, 763–774.

[4] B. Green R., W. Parson, *Advances in Photosynthesis and Respiration - Light-Harversitng Antennas in Photosynthesis.*, **2003**.

[5] S.-S. Sun, N. S. Sariciftci, *Organic Photovoltaics*, Taylor & Francis, **2005**.

[6] D. Gust, T. A. Moore, A. L. Moore, *Acc. Chem. Res.* **1993**, *26*, 198–205.

[7] S. A. Hussain, *Energy* **2009**, *132*, 1–4.

[8] G. D. Scholes, *Annu. Rev. Phys. Chem.* **2003**, *54*, 57–87.

[9] J. Pšenčík, T. P. Ikonen, P. Laurinmäki, M. C. Merckel, S. J. Butcher, R. E. Serimaa, R. Tuma, *Biophys. J.* **2004**, *87*, 1165–1172.

[10] N. Adir, *Photosynth. Res.* **2005**, *85*, 15–32.

[11] T. Larkum, *Trends Plant Sci.* **1996**, *1*, 247–248.

[12] C. S. Ting, G. Rocap, J. King, S. W. Chisholm, *Trends Microbiol.* **2002**, *10*, 134–142.

[13] Z. Liu, H. Yan, K. Wang, T. Kuang, J. Zhang, L. Gui, X. An, W. Chang, *Nature* **2004**, *428*, 287–292.

[14] R. Van Grondelle, V. Novoderezhkin, *Biochemistry* **2001**, *40*, 15057–15068.

[15] R. J. Cogdell, A. T. Gardiner, H. Hashimoto, T. H. P. Brotosudarmo, *Photochem. Photobiol. Sci.* **2008**, *7*, 1150–8.

[16] T. Szabó, M. Magyar, K. Hajdu, M. Dorogi, E. Nyerki, T. Tóth, M. Lingvay, G. Garab, K. Hernádi, L. Nagy, *Nanoscale Res. Lett.* **2015**, *10*, 458.

[17] R. Croce, H. van Amerongen, *Nat. Chem. Biol.* **2014**, *10*, 492–501.

[18] T. Pullerits, V. Sundström, *Acc. Chem. Res.* **1996**, *29*, 381–389.

[19] T. Ritz, S. Park, K. Schulten, *J. Phys. Chem. B* **2001**, *105*, 8259–8267.

[20] G. M. Whitesides, J. P. Mathias, T. Seto, Christoph, *Science.* **1991**, *254*, 1312.

[21] D. Philp, J. F. Stoddart, *Angew. Chem. Ed. Engl.* **1996**, *35*, 1154–1196.

[22] L. Maggini, D. Bonifazi, *Chem. Soc. Rev.* **2012**, *41*, 211.

[23] P. D. Frischmann, K. Mahata, F. Würthner, *Chem. Soc. Rev.* **2013**, *42*, 1847–70.

[24] Z. Chen, A. Lohr, C. R. Saha-Möller, F. Würthner, *Chem. Soc. Rev.* **2009**, *38*, 564–584.

[25] M. S. Choi, T. Yamazaki, I. Yamazaki, T. Aida, *Angew. Chem. Int. Ed.* **2004**, *43*, 150–158.

[26] M.-S. Choi, T. Yamazaki, I. Yamazaki, T. Aida, *Angew. Chem.* **2004**, *116*, 152–160.

[27] S. Hecht, J. M. J. Frechet, *Angew. Chem. Int. Ed.* **2001**, *40*, 74–91.

[28] U. Hahn, M. Gorka, F. Vögtle, V. Vicinelli, P. Ceroni, M. Maestri, V. Balzani, *Angew. Chem. Int. Ed.* **2002**, *41*, 3595–3598.

[29] V. Balzani, G. Bergamini, P. Ceroni, E. Marchi, *New J. Chem.* **2011**, *35*, 1944–1954.

[30] R. Takahashi, Y. Kobuke, *J. Am. Chem. Soc.* **2003**, *125*, 2372–2373.

[31] P. Parkinson, C. E. I. Knappke, N. Kamonsutthipaijit, K. Sirithip, J. D. Matichak, H. L. Anderson, L. M. Herz, *J. Am. Chem. Soc.* **2014**, *136*, 8217–8220.

[32] R. Abbel, C. Grenier, M. J. Pouderoijen, J. W. Stouwdam, P. E. L. G. Lecle, R. P. Sijbesma, E. W. Meijer, A. P. H. J. Schenning, *J. Am. Chem. Soc* **2009**, *131*, 833–843.

[33] T. E. Kaiser, H. Wang, V. Stepanenko, F. Würthner, *Angew. Chem. Int. Ed.* **2007**, *46*, 5541–5544.

[34] A. Lohr, F. Würthner, *Angew. Chem. Int. Ed.* **2008**, *47*, 1232–1236.

[35] A. Ajayaghosh, V. K. Praveen, C. Vijayakumar, S. J. George, *Angew. Chem. Int. Ed.* **2007**, *46*, 6260–6265.

[36] A. Ajayaghosh, C. Vijayakumar, V. K. Praveen, S. S. Babu, R. Varghese, *J. Am. Chem. Soc.* **2006**, *128*, 7174–7175.

[37] R. A. Miller, A. D. Presley, M. B. Francis, *J. Am. Chem. Soc.* **2007**, *129*, 3104–3109.

[38] M. Endo, M. Fujitsuka, T. Majima, *Chem. A Eur. J.* **2007**, *13*, 8660–8666.

[39] P. K. Dutta, R. Varghese, J. Nangreave, S. Lin, H. Yan, Y. Liu, *J. Am. Chem. Soc.* **2011**, *133*, 11985–11993.

[40] J. G. Woller, J. K. Hannestad, B. Albinsson, *J. Am. Chem. Soc.* **2013**, *135*, 2759–2768.

[41] V. Balzani, P. Ceroni, M. Maestri, V. Vicinelli, *Curr. Opin. Chem. Biol.* **2003**, *7*, 657–665.

[42] M. Cotlet, T. Vosch, S. Habuchi, T. Weil, K. Müllen, J. Hofkens, F. De Schryver, *J. Am. Chem. Soc.* **2005**, *127*, 9760–9768.

[43] S. Prathapan, T. E. Johnson, J. S. Lindsey, *J. Am. Chem. Soc.* **1993**, *115*, 7519–7520.

[44] Y. Terazono, G. Kodis, K. Bhushan, J. Zaks, C. Madden, A. L. Moore, T. A. Moore, G. R. Fleming, D. Gust, *J. Am. Chem. Soc.* **2011**, *133*, 2916–2922.

[45] K. Tomizaki, R. S. Loewe, C. Kirimaier, J. Schwartz, J. Retsek, F. Bocian D, D. Holten, S. J. Lindsey, *J. Org. Chem.* **2002**, *67*, 6519–6534.

[46] J. Roncali, *Chem. Rev.* **1997**, *97*, 173–206.

[47] J. Roncali, *Macromol. Rapid Commun.* **2007**, *28*, 1761–1775.

[48] J. L. Brédas, *J. Chem. Phys.* **1985**, *82*, 3808.

2. Oligo(*p*-phenylene vinylene) chromophores: from the synthesis to the functionalization of SWCNTs for photovoltaic applications

This chapter describes the preparation and physical characterization of oligo(*p*-phenylene vinylene)-derived single-walled carbon nanotubes (SWCNTs). The first part addresses the synthesis and characterization of oligo(*p*-phenylene vinylenes) (OPV) modules and the covalent functionalization of SWCNTs enriched in (7, 6) chirality. The second part sets out the photophysical properties of OPV functionalized carbon nanotubes and the understand of photo-induced interactions between SWCNTs and selected molecular system.

The chapter is divided in three main sections: *i) section 2.1* includes a general introduction on carbon nanotubes giving an overview on their chemistry and properties, along with a brief overview about organic photovoltaics, *ii) section 2.2* deals with the design of OPV-based donor-acceptor systems for photovoltaic devices and describes the synthesis of the targeted OPV-functionalized carbon nanotubes; *iii) section 2.3* describes the absorption and emission properties of OPV decorated SWCNT, while *iv*) *section 2.4* describes the characterization of OPV-SWNT as doping agents for spiro-OMeTAD in a flat $CH_3NH_3PbI_3$-based solar cell.

The research work in *section 2.3* has been carried out jointly with *Eleonora Pavoni* from the group of *Prof. Nicola Armaroli* at the *Istituto per la Sintesi Organica e la Fotoreattività* (*CNR - ISOF*), *Bologna*, Italy. The research described in *sections 3.4* was performed by *Vanira Trifiletti*, *Aurora Rizzo*, *Dr. Andrea Listorti* and *Dr. Silvia Colella* from the group of *Dr. Gianluca Accorsi* at the *Istituto di Nanotecnologie (CNR-Nanotec)* and *Università del Salento,* Lecce, Italy.

The X-ray analysis presented in this chapter was performed by *Nicola Demitri* (*Elettra – Sincrotrone Trieste*). Furthermore, *Dr. Riccardo Marega from* University of Namur, *Belgium*, *Dr. Caroline A. Ahad-Hadad, Agnieszka Gajewska and Luka Đorđević* from *University of Trieste, Italy,* are kindly acknowledged for their collaboration.

2.1 General introduction on Oligo(*p*-phenylene vinylene) based Donor-Acceptor Systems for Photovoltaic Devices

The unique, nanosized, three-dimensional structure of natural photosynthetic systems and the functions of solar-energy conversion have incited the scientific community to mimic such processes in artificially organized systems. Since, the reaction centers of photosynthetic organisms can be assumed as photovoltaic devices at the molecular level, donor and acceptor molecules have been organized onto electrode surfaces to obtain details on the relationship between the surface structure and the photo-electrochemical properties.[1] In this respect, recent studies have used carbon nanotubes (CNTs) as nanoplatforms to attach molecules, providing hybrid systems that can be designed for specific applications, including light-harvesting devices.[2] CNTs present outstanding properties such as high conductivity, strong mechanical, thermal and environmental stability.[3] Despite these unique properties of CNTs, one of the major drawbacks is that they are often produced with metal catalyst and amorphous carbon impurities. Since these impurities can obscure the properties of CNTs, they need to be removed, nitric acid treatment and Air/HCl treatment being the most commonly used purification procedures.[4,5] These treatments have been shown to create oxygen-containing functional groups on the CNT surfaces that can be used as reaction sites for a further chemical derivatization.[6,7] The covalent attachment of molecules to CNTs broadens the range of potential applications of CNT systems and allows the tailoring of the properties of modified CNTs. In the recent years a lot of attention has been addressed to the preparation of multicomponent systems and nanohybrids exploiting the covalent attachment of electron donors such as ferrocene,[8] phthalocyanines[9] or porphyrins[10,11] onto nanocarbon materials. For example, adducts of single walled carbon nanotubes (SWCNTs) with pyrene or porphyrin exhibit fast electron transfer, leading to long-lived charge separated states.[12]

In this chapter we reported the design and preparation of SWCNTs based donor-acceptor system for the construction of molecular photovoltaic devices. The acceptor moiety is represented by SWCNTs enriched in 7, 6 chirality, while for the donor moiety a π-conjugated oligo(*p*-phenylene vinylene) has been chosen. The choice of the latter is motivated by the stability, high luminescent efficiency, and ease of synthesis of those compounds.[13,14] The first sections of this chapter are dedicated to a general introduction on organic photovoltaics, followed by an overview on carbon nanotubes structure, properties and chemistry as well as their application in organic photovoltaics.

2.1.1 General Introduction on Organic Photovoltaic Cells

The ever-increasing quest for sustainable and renewable sources of energy promoted enormous interest in the solar cell technology. Solar energy is the most abundant, inexhaustible and clean source of energy till date. The power from the sun intercepted by the earth is many times larger than the present rate of the world energy consumption.[15] In this respect, solar photovoltaic technology represents one of the finest ways to harness the solar power. Photovoltaic devices deal with the conversion of sunlight into electrical energy. They belong to three main classes: organic (*e.g.*, heterojunction cells), photoelectrochemical cells (*e.g.*, dye sensitized solar cells) and inorganic (*e.g.* silicon), the latter being used in the majority of the solar cells in the market today. Such solar cells have been highly optimized and show efficiencies greater than 15 %.[16] Nevertheless, their high manufacturing costs, difficulties in tailoring the cells to various applications and the inherent physical rigidity of silicon hamper their widespread use as solar-based power. On the other hand, solar cells, such as dye-sensitized solar cells (DSSCs)[17,18] and bulk heterojunction cells (BHJs)[19–21] are promising for inexpensive and large-scale solar energy conversion.

The study of such devices started by the discovery of the *photovoltaic effect* by the French Scientist *E. Bequerel* in 1839[22] who observed an electric potential between two electrodes attached to a solid or liquid system upon light irradiation. This breakthrough has been the base for a variety of concept to convert solar radiation into electricity, paving the way for new alternative energy generation.

The main processes of converting light into electric current in all organic photovoltaic cells are *(i) absorption* of a photons leading to the formation of an excited state, the electron-hole pair (exciton generation), *(ii) Exciton diffusion* to a region, where *(iii) charge separation* occurs. Finally *(iv)* the *charge transport* to the anode (holes) and cathode (electrons) to supply a direct current for the consumer load.[23] The organic photovoltaic cells can be constructed in a variety of ways, including single layer, bilayer heterojunction and bulk heterojunction cells[24] (Figure 2.1). In spite of the different device architectures, the principles of their operation are substantially the same.[25]

Generally, in a single layer cell, the photovoltaic material is sandwiched between two conductive contacts (electrodes) with different work functions (homojunction devices); one layer consists of an electron-donor, while another of an electron-acceptor material (heterojunction devices, Figure 2.1 a) or a bulk-mixture of both (bulk-heterojunction devices, Figure 2.1 c). The donor and the acceptor in an organic photovoltaic cell are

completely different materials. Each material has a characteristic HOMO and LUMO energy, with the HOMO and LUMO of the donor being higher in energy than their respective counterparts in the acceptor. The gap between the HOMO and the LUMO is referred as the optical band-gap and determines the minimum wavelength of light required for excitation in each material.

The schematic energy-band diagram of a donor–acceptor heterojunction is reported in Figure 2.1 b. In order to allow the interaction of light with the photovoltaic material, the device is constructed onto a transparent substrate (glass, plastic film) and one of the conducting contacts is also transparent, so the material can absorb the incident sunlight photons and generate excitons. An exciton is an excited state corresponding to a bound state of an electron, e^-, and an imaginary particle called an electron hole, h^+. Upon irradiation, an electron excitation from the HOMO to the LUMO of the donor generates an exciton, leaving behind a hole of opposite charge (process 1 in Figure 2.1 b). Since the promoted electron and the hole have opposite electric charges, both remain bounded by a Coulomb force, making this state slightly more stable than a dissociated free electron and a hole. It is noteworthy to indicate that only photons higher in energy than the band gap ($h\nu \geq E_g$) lead to the photogeneration and that the energy transferred to the exciton increases with E_g (*i.e.*, higher is the energy content of the photon, higher is the energy of the exciton generated).

The exciton is then dissociated into charges of different sign (process 2 in Figure 2.1 b) generating an electron lying in the LUMO of the acceptor material and a hole in the HOMO of the donor material. [23] The overall electric field between the two electrodes drives separated charge carriers towards the respective contacts (*charge transport*). This light triggered transfer of one electron from a molecule to another is regarded as photoinduced electron transfer. At the end, the charges migrate through the material and are collected at the electrodes (process 3 in Figure 2.1 b) to generate an electric current. Hence, the flow of absorbed photons is converted into a usable flow of direct current (DC) power by the illuminated cell.

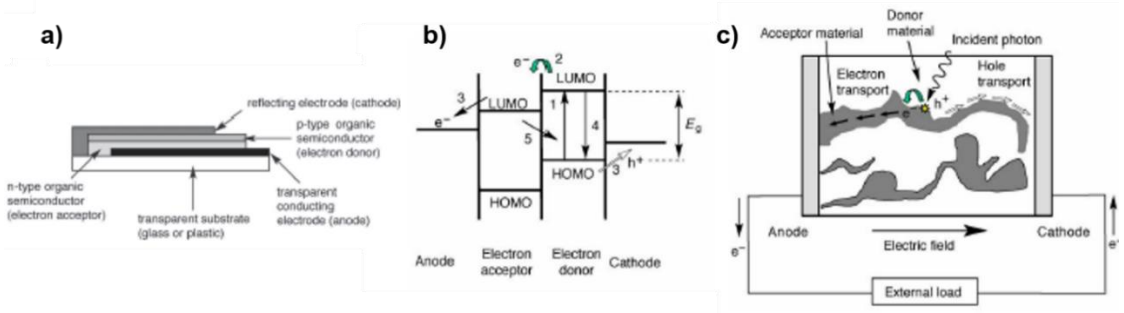

Figure 2.1 (a) Typical heterojunction organic solar cell architecture; (b) schematic energy-band diagram of a donor–acceptor heterojunction. (c) schematic bulk-heterojunction solar cell. Donor and acceptor materials are intimately mixed together to form a dispersed heterojunction.[23]

While in homojunction devices exciton dissociation usually takes place at the junction with the electrodes, in heterojunction and bulk-heterojunction devices it takes place much more efficiently at the donor–acceptor interface, leading to a free electron in the acceptor material and a free hole in the donor. Since donor materials are more likely to conduct holes and acceptor materials electrons, the bulk-heterojunction architecture ensures the transport of charge carriers to the electrodes with only a small chance to recombine with their counterpart (*e.g.* bumping into each other, process 5 in Figure 2.1 b) as they do not have to diffuse through the same material (in contrary to homojunction devices), and connect with the correct electrode. To increase the close contact between the donor and the acceptor materials and to provide complete transport of excitons to the donor-acceptor interface and thus exciton dissociation, the bulk-heterojunction architecture was developed.[23]

The first significant reports regarding organic photovoltaic cells date back to beginning of the 20th century. In 1959, *Kallaman and Pope*[26] reported on photovoltaic measurements on thin (10 μm) anthracene single crystals cell. The anthracene crystal was positioned between two NaCl solutions, which acted as transparent electrical contacts and were further connected to silver electrodes. They reported an efficiency of only 2 x 10^{-6} %. Later, the same authors also observed a photovoltaic effect in a tetracene water system.[27] Eventually, in 1978 *Fishman* and co-workers reported on organic solar cells based on merocyanine dyes that exhibited sunlight efficiencies in excess of 1 %.[28] However, these single layer cells have been mostly abandoned and replaced by heterojunction solar cells for the reasons described above. While in a bilayer device, the junction between donor and acceptor materials is planar, in a bulk heterojunction device, attempts have been made to maximize/optimize the interface between phases. Generally, bulk heterojunctions may be achieved by co-deposition of donor and acceptor dyes[29–31] or solution casting of either

polymer/polymer,[32,33] polymer/dye[34–36] or dye/dye[37,38]donor-acceptor blends. One of the most promising examples concerns the fabrication of cells composed of thieno[3,4-b] thienyl- and benzodithienyl-based polymers (PTBs) as donor specie and fullerene phenyl-C_{71}-butyric acid methyl ester ($PC_{71}BM$) as acceptor, yielding above 7.4 % power conversion efficiency under ambient conditions.[39]

The design and the choice of the donor and acceptor molecules represented one of the most important steps in the construction of photovoltaic devices. The selected molecules must be characterized by optical band-gaps that are small enough to be excited efficiently by the solar radiation. Moreover, the donor molecule has to stabilize the hole transport, while the acceptor must favor the electron transport. The combination of the two must also be chosen to allow for the proper offset between their HOMO and LUMOs. Finally, the molecules must be properly functionalized in order to be solubilized for processing.

Based on all that, the development in the mid-1990 of solar cells based mainly on photoactive organic materials, has offered the prospect to make solar power affordable for far broader uses. Donor-acceptor based organic solar cells are currently showing power conversion of more than 9 %.[40] Nevertheless, efficiencies of these organic devices have not yet reached those of their inorganic counterparts (10-25 %).[40] Despite this, organic photovoltaic technology presents some great advantages: *i)* the use of low quantities of materials; and *ii)* the possibility of tuning the optoelectronic properties of the organic molecules involved by chemical modification; *iii)* the composition based on handy materials and the fact that the fabrication process does not need high temperatures, allowing the generation of very flexible thin films with plastic substrates.

In order to reach higher efficiencies, innovative materials such as carbon nanotubes (CNTs) have been integrated in organic photovoltaic cells.[41] CNTs are one-dimensional nanostructures characterized by a ballisitic charge transport along their axis. In addition, their band-gap can be tuned by employing different radii and chiralities, allowing a precise band engineering. In addition, thanks to their high surface area (about 1600 $m^2\ g^{-1}$) and their electron-accepting properties, CNTs can be considered as a wide conductive network offering a tremendous opportunity for exciton dissociation. For these reasons, CNTs have been widely studied in electro- and photo-active nanocomposites in association with semi-conducting materials.[42,43]

Accordingly, initial reports revealed appreciable success in integrating CNTs as an electron accepting material together with electron-donating conjugated polymer, such as poly(3-

octylthiophene) (P_3OT),[43] or poly(*p*-phenylenevinylenes) (PPV),[44] into ITO based photovoltaic devices. However, CNTs present different drawbacks that limit their effectiveness in multifunctional CNTs-based nanoconjugates and/or nano-hybrid photovoltaic systems. Key issues are addressed to the lack of a reliable and reproducible control of the surface chemistry and their organization within the active layer due to their particular intermolecular cohesive forces (0.5 eV nm^{-1}). In fact, CNTs tend to strongly aggregate both in the solid state and in solution, forming bundled structures that impair the reproducibility of the conducting properties and display a reduced threshold of a few percent. An efficient strategy to bypass this and create easy-to-process CNT-based materials employs their chemical derivatization,[45] either in a covalent[46–49] or non-covalent[50–53] fashion. Specifically, the incorporation of photoactive antenna chromophores (displaying high extinction coefficient in the visible region of the solar spectrum) such as porphyrins[1] emerged as one of the most suitable routes to engineer charge-separation and photovoltaic conversion.

2.1.2 General Account on Carbon Nanotubes

Carbon structures can exhibit multiple allotropic forms, with very diverse properties from the soft and conductive graphite to the hard and insulating diamond. Fullerenes, are molecules composed entirely of carbon arranged in hexagonal and pentagonal rings assuming the form of a hollow sphere. Carbon nanotubes (CNTs) are another allotropic form of carbon and, when synthesized, are often capped by a half fullerene at the end.[54] The discoveries of C_{60} in 1985 by *Kroto et al.*[55] and carbon nanotubes in 1991 by *Ijima* and co-workers[56] have inspired a new interdisciplinary era in material science and technology. Both fullerene and carbon nanotubes (CNTs)[57] display unique structures that bring with them remarkable mechanical, thermal, and optical properties that are extremely promising for applications in electronics, advanced materials and medicinal chemistry.[58,59]

2.1.2.1 CNTs structure and electronic/optical properties

At the structural level, a carbon nanotube can be imagined as a rolled up sheet of graphene (see Figure 2.2), with a planar-hexagonal arrangement of sp^2 carbon atoms distributed in a honeycomb lattice.[45]

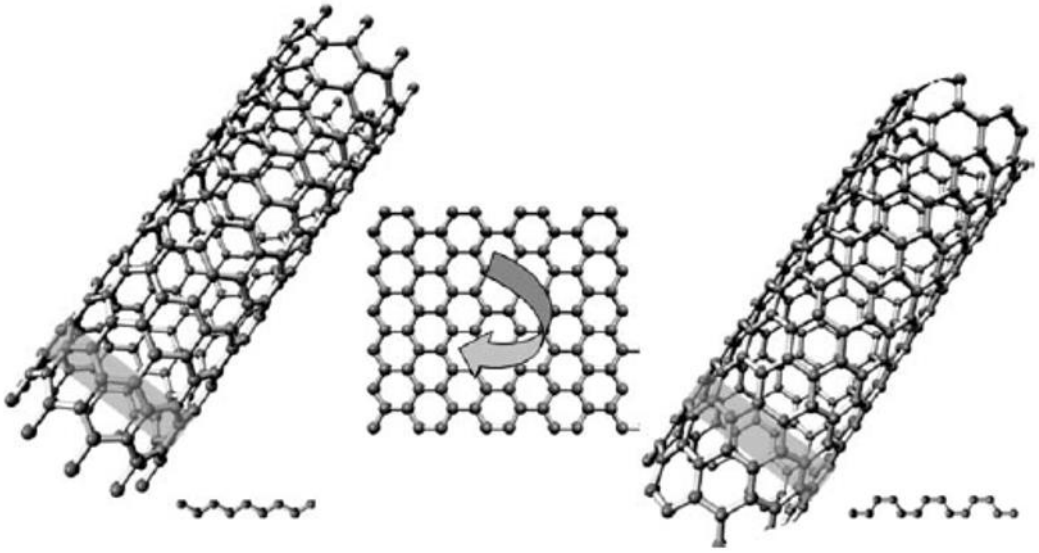

Figure 2.2 Representation of single walled carbon nanotube (SWCNTs). It can be pictured as a rolled graphene sheet and according to the rolling direction can be classified as zigzag, armchair or chiral.[45]

There are two main types of carbon nanotubes presenting high structural perfection: Single-Walled Carbon Nanotubes (SWCNTs) that consists of a single graphite sheet seamlessly wrapped into a cylindrical tube (Figure 2.2) and Multi-Walled Carbon nanotubes (MWCNTs) that comprise an array of single walled nanotubes concentrically nested reaching diameters of up to 100 nm.[6]

Most SWCNTs present a diameter about 0.4 to 4 nm, with a tube length that can be many millions of times longer, and due to the high ratio between the two dimensions they are virtually considered mono-dimensional (1D) objects. Despite structural similarity to a single sheet of graphite, which is a semiconductor with zero band gap, SWCNTs may be either metallic or semiconducting, depending on the rolling direction of the graphene sheet (Figure 2.3).[60] Thus, nanotubes have different structures, which can be described by the chiral vector (*n, m*), where the integers *n* and *m* represent the number of unit vectors along two directions in the honeycomb crystal lattice of graphene and are described by the equation: $C_h = na_1 + ma_2$. The chiral vector is determined by the diagram in Figure 2.3. The *(n,m)* indices fully define the SWCNT radius and chirality and determine its electronic structure. If m = 0, the nanotubes are called ‘‘zigzag’’. If n = m, the nanotubes are called ‘‘armchair’’. Otherwise, they are called ‘‘chiral’’.

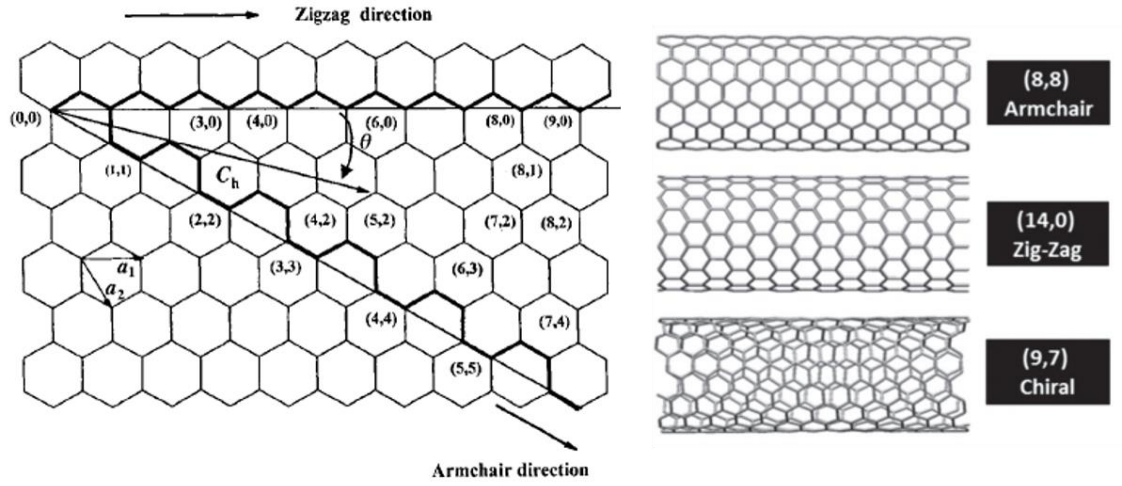

Figure 2.3. A 2D graphene sheet showing chiral vector C_h and chiral angle θ,[58] (left) that give rise to armchair, zig–zag and chiral nanotube structures with metallic or semi-conducting electronic character (right).[61]

All armchair SWCNTs are metallic ($|n\text{-}m| = 3q$), while those with $|n\text{-}m| \neq 3q$, where q is a nonzero integer, are semiconductors with a tiny band gap. All the others are semiconductors with a band gap that inversely depends on the nanotube diameter.[62] Usually, without chirality control, we obtain one third metallic and two thirds semiconducting SWCNTs.

Eventually, we can underline that the chiral vector, (n, m), determines both the diameter of a SWCNT and its opto-electronic properties. In fact, the three SWCNTs depicted in Figure 2.3 have approximately the same tube diameter, but they dramatically differ for their opto-electronic properties. The electronic density of states (DOS) of a SWCNT (Figure 2.4) consists of distinctive levels known as van Hove singularities (vHS) defined by circumferential wave vectors. As already mentioned, all armchair SWCNTs are metallic with a continuous DOS near the Fermi level (EF) (which is highlighted by the dashed blue line in Figure 2.4), while the DOS of the semiconducting SWCNTs show a significant band gap on the order of 500 meV that varies inversely with diameter. Metallic SWCNTs are characterized by higher dielectric constants ($\varepsilon > 1000$) than the semiconducting one ($\varepsilon < 10$).[63] On the other hand, larger diameter SWCNTs present larger dielectric constants than smaller ones. The position of the Fermi level, as well as the reduction and oxidation potentials, also vary as a function of diameter.

Generally, SWCNTs possess extraordinary mechanical properties such as a high Young modulus (estimated to be 1–5 TPa), high tensile strength (50–200 GPa), high elasticity and resilience, thermal conductivity and large aspect ratio (length to diameter).[58]

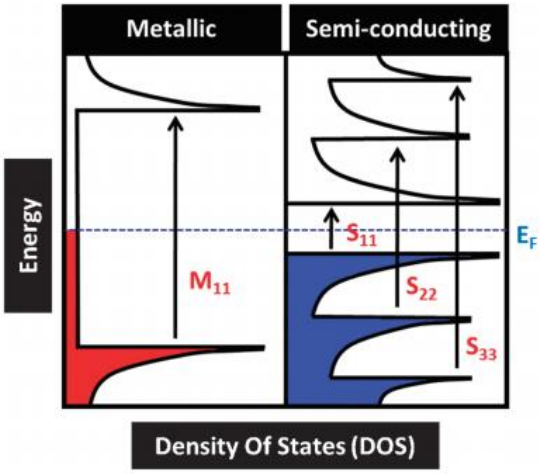

Figure 2.4 Schematic view of the electronic density of states (DOS) of metallic and semiconducting SWCNTs.[61]

A SWCNT is considered perfectly crystalline *i.e.* without defects if the graphene sheet has no alteration in the hexagonal aromatic structure of the carbon atoms along the tube. However, CNTs are not absolutely perfect due to the presence of certain defects. They can be mainly classified into four groups: *i)* topological defects, corresponding to the presence of rings other than hexagons, for example pentagon/heptagon pairs[64] *ii)* rehybridization (chemical treating defects consisting of atoms/groups covalently attached to the carbon lattice of the tube); *iii)* incomplete bonding defects (vacancies, dislocations, *etc*); *iv)* doping with other elements than carbon. Either they can be strategically inserted, for instance treating CNTs with very harsh acidic conditions,[65] either they can be inevitably formed during the growth of CNTs. In any way, their presence in the carbon network can lead to attractive properties and new potential nano-devices. Defects are also key factor in the covalent chemistry of CNTs because they can serve as anchor groups for further functionalization.

Carbon nanotubes can be produced using several different techniques while new routes are continuously being developed. Commonly used methods exploit the catalytic decomposition of certain hydrocarbons as source of carbon on small metal particles (*e.i.* Fe, Co, Ni) under a certain applied energy. The diameter of so prepared nanotubes is governed by that of the catalyst particles responsible for their growth. The most common methods are: arc discharge of graphite, laser ablation of carbon and chemical vapor deposition techniques,[54] that produce nanotubes of mixed electronic character (metallic and semi-conducting types), length, diameter and helicity; and of different degrees of contamination with metal catalyst, graphitic nanoparticles, and amorphous carbon.

2.1.2.2 Chemistry of Carbon Nanotubes

As discussed before, SWCNTs tend to form bundles due to the presence of strong van der Walls interactions (0.5 eV nm^{-1}) between tube-to-tube contacts. This feature results in scarce solubility in almost all organic solvents and aqueous solutions, which is an obstacle for the full exploitation of their properties. For these reasons, to be used into any type of devices, an appropriate modification has to be undertaken in order to render them dispersible and thus processable. Several protocols have been described in the literature to exfoliate and functionalize SWCNTs in order to obtain individuals and/or small bundles of carbon nanotubes.[7] They can be chemically modified mainly by the following strategies: *(i)* functionalization of the defect located on the sidewall and the rims; *(ii)* non-covalent interactions; (*iii*) sidewall covalent functionalization and (*iv*) endohedral inclusion.[66]

The covalent functionalization of nanotubes is more robust and better controllable compared to functionalization based on non-covalent method, and therefore will be adopted in this research work. Carbon nanotubes structure can be divided into two main regions: the end caps and the side wall. The end caps of a carbon nanotube resemble a hemispherical fullerene and its reactivity. In fact, the reactivity of the fullerenes is primarily driven by the enormous strain generated by their spherical geometry as reflected in the pyramidalization angles (θp) of the carbon atoms (Figure 2.5 a).[67] For an sp^2-hybridized (trigonal) carbon atom, planarity is strongly preferred, and this implies a pyramidalization angle of 0°, while in contrast an sp^3-hybridized (tetrahedral) carbon atom requires an angle of 19.5°. In the case of fullerene all carbon atoms have an angle of 11.6°, indicating that their geometry is more appropriate for tetrahedral than trigonal hybridization. Thus, the chemical conversion of any trivalent carbon atom in C_{60} to tetravalent carbon is accelerated by the strain relief that strongly favors the addition chemistry on fullerene molecules.[67] The side wall, instead, presents carbon atoms with a lower pyramidalization angle, but with the p-orbital misalignment as major source of strain in that region. In fact, a carbon nanotube with the same radius as C_{60} exhibits a less distorted π-framework but a great deviation of the π-orbitals alignment. This misalignment is the origin of torsional strain in nanotubes and the driving force for chemical functionalization.

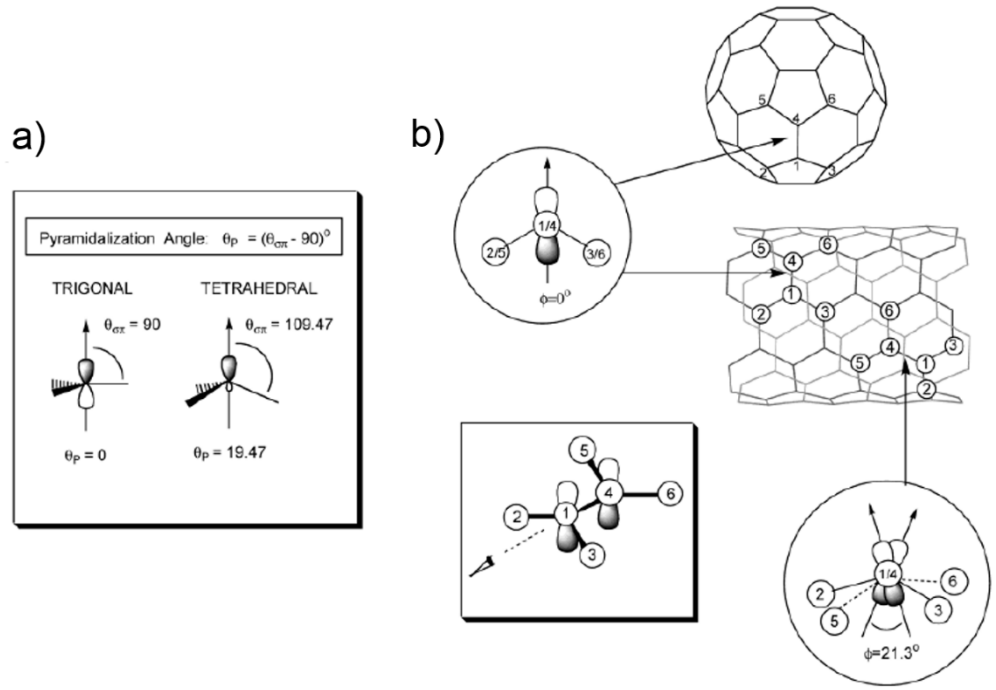

Figure 2.5. (a) pyramidalization angle (θ_P), and (b) the π-orbital misalignment angles along the C1-C4 in the (5,5) SWNT and its capping fullerene, C_{60}.[67]

The reactivity of carbon nanotubes can be rationalized in terms of curvature-induced pyramidalization angle and misalignment (ϕ) of the π-orbitals in comparison with the graphene structure. Both factors induce a local strain, leading to CNTs generally more reactive than a flat graphene sheet. Furthermore, on the bases of the carbon nanotubes structure there is a correlation between tube diameter and reactivity. Both pyramidalization angles and p-orbital misalignment are inversely proportional to the tube diameter, then smaller carbon nanotubes are expected to be more reactive than larger nanotubes. Moreover, the CNTs reactivity depends also on the chirality of the system as reported by *Li* and co-workers[68] and *Kataura* and co-workers.[69,70] Considering SWCNTs with the same diameter: the zig-zag carbon nanotubes are less reactive than armchairs that are less reactive than the chiral tubes.

Two main approaches have been developed for the covalent functionalization of carbon nanotubes: *(i)* the addition chemistry to SWCNTs; and *(ii)* amidation and esterification of oxidized SWCNTs.[7] The direct functionalization of pristine SWCNTs can be obtained via electrophilic, nucleophilic or radical additions using highly reactive species. Several reviews have been reported on the chemistry of SWCNTs describing exhaustive or representative examples of addition reactions.[59,71,72] On the other hand, the treatment of CNTs under strong acidic and oxidative conditions, such as sonication in a mixture of concentrated nitric

and sulfuric acid, or heating in a mixture of sulfuric acid and hydrogen peroxide, results in the formation of short and opened tubes bearing oxygenated functions such as carbonyl, carboxyl, hydroxyl groups. These functional groups can then serve as anchor point for further functionalization. For instance, the acid functions can easily react with alcohols or amines to give ester or amide derivatives.[7]

Amidation or esterification reactions can be carried out on oxidized SWCNTs by standard methods, either using acid chlorides as intermediates or carbodiimide-based coupling reagents. This approach offers the possibility of attaching many organic fragments and synthesizing a great variety of CNT derivatives. *Haddon* and coworkers[73] first reported different functionalization strategies leading to soluble SWCNTs *via* amidation reactions between oxidized nanotubes and octadecylamine (Figure 2.6, **2-12**) and 4-tetradecylaniline through the formation of an acyl chloride intermediate. The octadecylamine groups present on the nanotubes increased the solubility of the material in most of organic solvents, assisting its characterization and facilitating the achievement of highly purified SWCNT that are suitable for physical properties measurements.

This approach has been widely exploited to afford a large variety of functionalized CNTs and the most significant results have been collected in a variety of outstanding review papers.[7,66,71,72] Herein we report some examples where this approach has been used for combining the SWCNT properties with those of other interesting materials. For instance, coupling SWCNTs with C_{60} fullerene create unique structures that have been studied for charge-transfer properties. In 2007, *Langa* and co-workers described the first synthesis of hybrid conjugated SWCNT–C_{60} materials **2-13** (Figure 2.6). The authors decorated the SWCNTs with fragments of N-anilinopyrazolino C_{60} fullerene, by an amidation reaction with the SWCNT acyl chloride. Similarly, a grapevine nanostructure (**2-14**) was prepared, based on SWCNT covalently functionalized with C_{60} *via* amidation reaction.[74] This hybrid material was investigated by means of Electron Spin Resonance (ESR) spectroscopy revealing the presence of an electron transfer process between the SWCNT and the fullerene. Using the same synthetic methodology, *Bonifazi et al*. reported the synthesis of several hybrid fullerene derivatives–SWCNT materials that combined C_{60} fullerenes with appended photoactive ferrocene or porphyrin functionalities and SWCNTs (**2-15**, Figure 2.6). X-Ray Photoelectron Spectroscopy (XPS) analysis has been used to prove the presence of C_{60} fullerene derivatives around the exo-surface of the oxidized SWCNT walls, through the

appearance of the characteristic photoelectron N 1s emission peak at 400.3 eV, typical of amide groups.

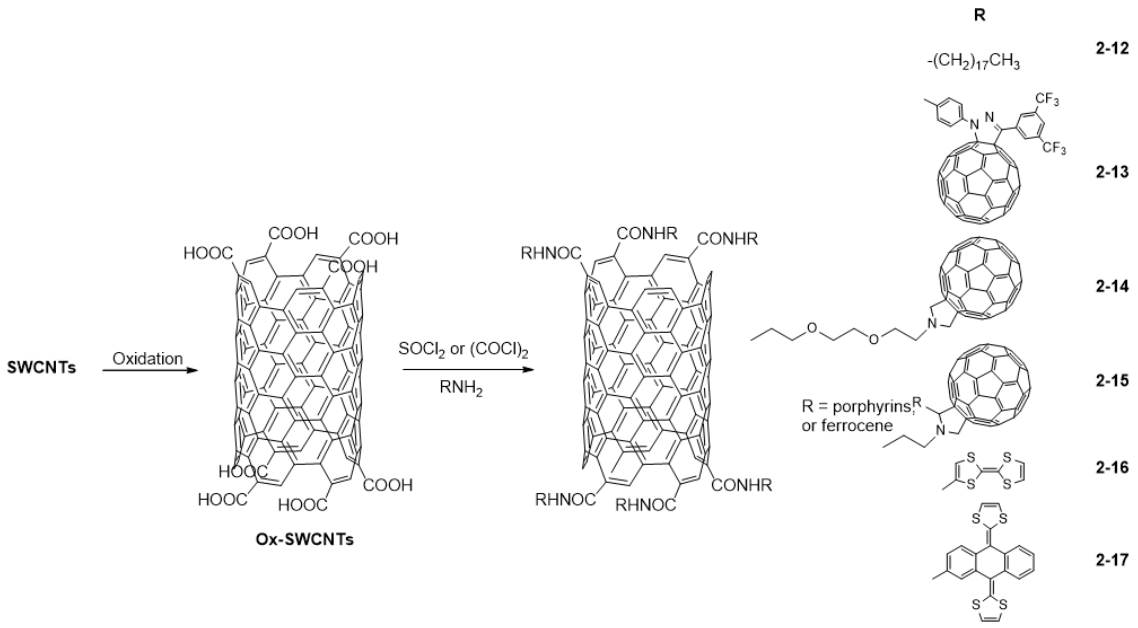

Figure 2.6 Derivatization reactions of acid-cut nanotubes *via* amidation reaction.

Martin, *Prato*, *Guldi* et al.[75] also described the functionalization of SWCNTs with the strong electron donor tetrathiafulvalene (TTF) (**2-16**, Figure 2.6) or its π-extended analogs (exTTF) (**2-17**), through esterification or amidation reactions. This work reports the preparation of the first TTF–SWCNT donor–acceptor systems, to evaluate the possible use of CNTs in solar energy conversion systems. The functionalization was confirmed by different analytical, spectroscopic and microscopic techniques. Photophysical analysis by time resolved spectroscopy revealed the presence of radical species indicating the existence of an efficient photoinduced electron transfer, a critical point for photovoltaic devices.

The covalent functionalization of SWCNTs *via* amidation reaction will be exploited for the prupose of this research work and the decisive synthetic strategy adopted for the functionalization of SWCNTs with small chromophoric molecules is reported in the following *section 2.2.*

2.1.3 Aim of the project

As already discussed, the preparation of molecular donor-acceptor hybrids is crucial in the engineering of organic photovoltaic cells to convert sunlight into electrical energy. In this respect, a lot of attention has been paid in the last two decades to the design, synthesis and characterization of a wide range of molecular and supramolecular assemblies which can undergo inter-component processes (i.e. electron and/or energy transfer) upon absorption of

light.[76] For example the efficient use of metallo-phthalocyanins, porphyrins,[77] conjugated polymers and nanoparticulate materials in photo-responsive applications have been already reported. Such materials, are characterized by a large light absorption cross section in the visible range of the solar spectrum and present the ability to effectively separate and utilize the charges, thus transferring the energy over long distances. Using functional building blocks that efficiently harvest sunlight and integrating them with a suitable electron acceptor entity facilitate the charge-separation and the formation of the electrical current.

As introduced before, SWCNTs present tremendous advantages and will be used as acceptor moiety in the development of novel donor-acceptor devices. Similarly, π-conjugated oligomers, are prime choices as donor moieties in such systems. First, investigated as model compounds for conjugated polymers, they have been widely studied for optoelectronic devices because of their well-defined chemical structure that facilitates the tuning of electronic properties and their potential ability to form well-ordered molecular assemblies.[78–83] Indeed, their opto-electronic properties can be easily modulated by either changing the length of the conjugated backbone or introducing various substituents. In particular, oligo(*p*-phenylene vinylene)s (OPVs) are being investigated to be utilized in solar cells and light emitting diodes (LEDs) due to their stability, high luminescent efficiency, and ease of synthesis.[13,14] OPVs with solubilizing substituents combine the low-cost, solution-based processing of conjugated polymers with the improved structural control inherent to oligomers.[14,83] Such examples of donor-acceptor systems, reported in the literature, describe the energy and electron transfer from donor OPVs and analogous poly(phenylenevinylene)s (PPVs) to acceptors, such as C_{60},[84,85] phenanthroline,[86] and doped organic dyes.[87,88] A representative example is reported by *Armaroli* and co-workers. They described the synthesis and photophysical characterization of C_{60}– OPV dyads, F-D1 and F-D2, which exhibit different conjugation length of the OPV fragments (Figure 2.7). Transient absorption measurements confirmed the photo-induced electron transfer in F-D1 and F-D2. A charge-separated state is formed within 100 ps and decays in less than 5 ns.

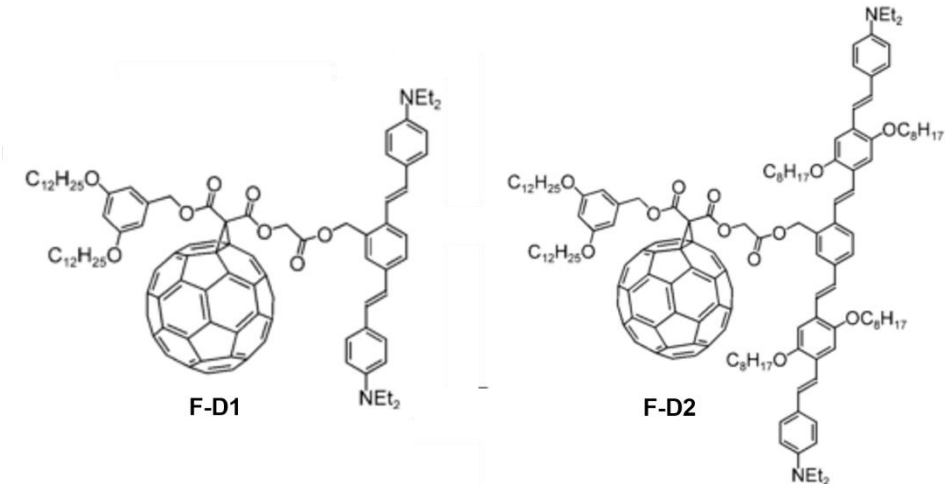

Figure 2.7 Chemical structures of acceptor-donor dyad based on diethylamino-substituted oligophenylenevinylene (OPV) bearing different conjugation length and fullerene C_{60} described by *Armaroli* and co-workers.

Following the observation of electron transfer from conducting oligomers and/or polymers derived from PPVs,[19,89,90] and the successful preparation of photovoltaic cells from such bulk heterojunction materials,[91] in this chapter we will describe the preparation and characterization of novel donor-acceptor systems based on OPV and SWCNT. In order to enhance the properties of such material in development, we decided to use SWCNTs enriched in 7, 6 chirality. This will allow us to benefit from well-defined properties of structurally controlled SWCNTs (all semiconducting). In this way, we will address the problem of achieving monodispersity in terms of length, diameter and most important helicity. To evaluate the interaction between the two components of the system we prepared two OPVs with different lengths, allowing us to study the influence of the resulting tuning in the HOMO-LUMO gap onto the efficiency of the system.

The chemical structures of SWCNT-OPV conjugates and electron-donating oligo(*p*-phenylene vinylene) derivatives **2-1** and **2-2** utilized in this study are depicted in Figure 2.8. To permit a closer contact between the two active materials aiming to avoid formation of bundles of carbon nanotubes aggregates, we grafted OPV molecules **2-1** and **2-2** on the external walls of nanotubes *via* amidation reaction.

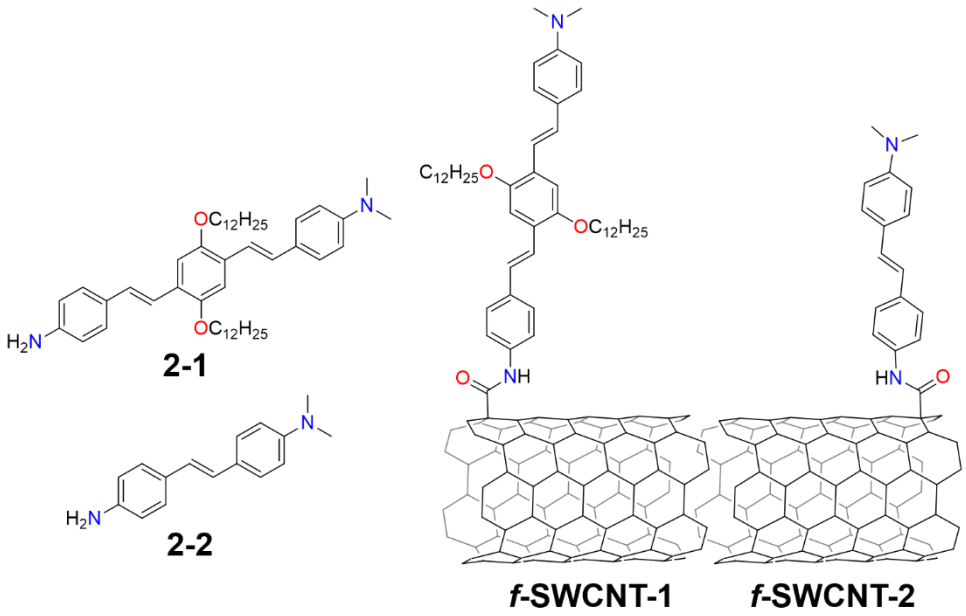

Figure 2.8 Molecules **2-1** and **2-2** used for this study and OPV-decorated SWCNTs enriched in (7,6) chirality**.**

2.2 Synthesis and characterization of oligo(p-phenylene vinylene) chromophores for SWCNT functionalization

This section addresses the preparation and physical characterization of new hybrid systems composed of *(i)* electron-accepting single chirality enriched SWCNTs and *(ii)* electron-donating oligo(*p*-phenylene vinylene) derivatives **2-1** and **2-2.**

2.2.1. Synthesis of oligo(p-phenylene vinylene) chromophores for functionalization of SWCNT (7, 6)

The synthesis of a series of well-defined dimethylamine derivatives containing styryl units of different π-extension will be described. In this respect, any reaction that allows the formation of new carbon–carbon bonds concomitant to either preservation or creation of a double bond, is suitable to synthesize OPVs. Among all synthetic approaches adopted for the preparation of arylene vinylenes, the Knoevenagel condensations[92] or more prominent palladium-catalyzed cross-coupling reactions,[93] namely the *Heck*, the *Stille* and the *Suzuki* reactions were extensively used for the synthesis of a large variety of OPV derivatives.[94] However, till now one of the most common synthetic routes concerns the Wittig and the Horner–Wadsworth–Emmons (HWE) reactions, which have been extensively studied.[95] In this respect, aldehyde compounds are very versatile and easily accessible precursors for such reactions. In HWE polycondensation, the reaction of aldehydes with stabilized phosphorus ylides leads to olefins with excellent trans selectivity. The reaction can be carried out in the

presence of various substituents on the aromatic rings, thus allowing the synthesis of different materials with improved solubility, and different characteristics. For the preparation of OPV derivatives **2-1** and **2-2** the classical Horner–Wadsworth–Emmons reaction was thus employed.

In this study, long chain alkoxy groups have been introduced in the chromophore structure to enhance the solubility of the final π-conjugated system. The syntheses of compound **2-1** and **OPV-SWCNTs (7, 6)** conjugates are outlined in schemes 2.1 and 2.4, respectively. The synthesis of trimeric OPV **2-1** bearing alkoxy groups in the center aromatic ring was effectively achieved following a six steps route as shown in scheme 2.1, while compound **2-2** was synthesized according to a previously reported synthetic protocol.[96]

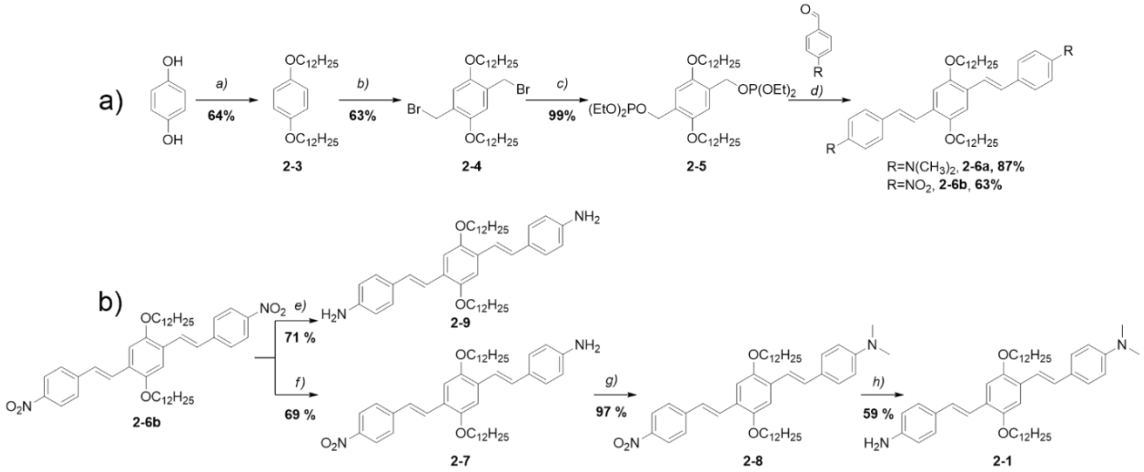

Scheme 2.1 Synthetic pathway undertaken for the synthesis of OPV **2-1**. Reagents and conditions: a) 1-bromododecane, K_2CO_3, DMF, 60 °C, 24 h, b) (HCHO)*n*, HBr (33 wt% AcOH), ACOH, 5h; c) $P(OEt)_3$, 160 °C, 5h; d) *t*-BuONa, DMF, overnight, r.t. ,e)f) Na_2S aq. sol., pyridine, 90 °C, 30 min; g) $(HCHO)_n$, $NaCNBH_3$, AcOH, overnight, r.t.; h) $SnCl_2$, EtOAc, overnight, reflux.

First, commercially available hydroquinone was treated with 1-bromododecane in the presence of K_2CO_3 and DMF to afford the bisdodecyloxybenzene **2-3** in 64% yield.[97] A subsequent bromomethylation reaction[98,99] of 1,4-bis(dodecyloxy)benzene in presence of a mixture of paraformaldehyde and HBr in acetic acid followed by a Michaelis-Arbuzov reaction yielded bisphosphonate compound **2-5** in quantitative yield.[100] The crucial step was the following HWE reaction, which has proven to be a powerful tool for the synthesis of OPV derivatives as the trans olefines are selectively produced.[101] As depicted in scheme 2.2 a first attempt to synthesize unsymmetric target **2-8** by stepwise addition of one equivalent of *t*-BuONa and 4-dimethylaminobenzaldehyde to **2-5** followed by the addition of an excess of 4-nitrobenzaldehyde was carried out. A complex mixture of compounds was obtained and only a scarce quantity of **2-8** has been collected after purification by column

chromatography. For a better understanding of non-symmetric HWE reaction outcome and in order to investigate the reactivity of the two components employed (*p*-nitrobenzaldehyde and *p*-dimethylaminobenzaldehyde), double HWE reaction was performed starting from bisphosphonate derivative **2-5**.[102] Thus, **2-5** has been reacted separately, in the presence of *t*-BuONa in DMF, with dimethylaminobenzaldehyde and with *p*-nitrobenzaldehyde affording the desired products **2-6a** and **2-6b**, in 87% and 63% yield, respectively. The high yield and purity of the product obtained by double Horner-Emmons route are noteworthy, so a classical synthetic approach consisting on a six step reaction protocol has been followed for the preparation of target molecule **2-1** as initially described in scheme 2.1.

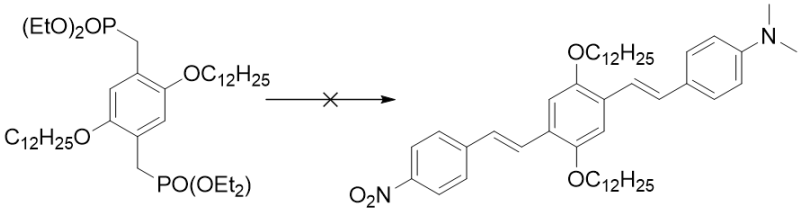

2-5 **2-8**

Scheme 2.2 Attempted stepwise synthesis of unsymmetrical **2-8**. Reagents and conditions: 1. *p*-dimethylaminobenzaldehyde, *t*-BuONa, THF, 1h, r.t.; 2. *p*-nitrobenzaldehyde, overnight, r.t.

Upon slow diffusion of MeOH into a solution of **2-6a** in CH_2Cl_2 intense yellow crystals suitable for X-ray diffraction were obtained. Figure 2.9 shows the ORTEP image of the crystal structure, which is arranged according to the spatial group *P* -1 (essential crystal and refinement data are reported in *appendix*).

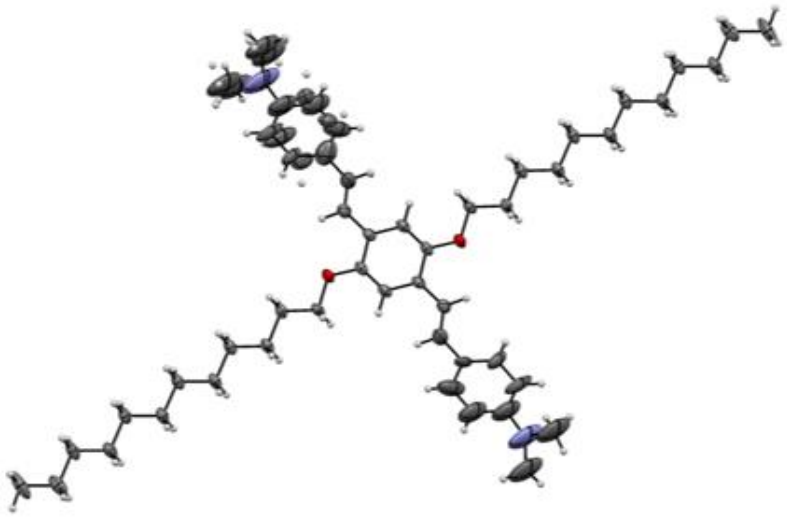

Figure 2.9 X-ray structure of **2-6a** (50% probability ellipsoids). The N,N-dimethylaniline moiety appears disordered in two conformations almost equally populated (55% : 45%).

Once the dinitro derivative **2-6b** has been prepared (scheme 2.1b), a selective mono-reduction reaction in presence of a NaS_2 aq. sol. has been exploited to obtain amino-nitro derivative **2-7** in 69% yield. The selective reduction of one nitro group was realized following a procedure used for the preparation of similar π-extended systems reported in literature.[103] The synthesis of compound **2-7** highlights the fact that the development of a mono-reduction reaction of a symmetric dinitro compound is very useful in the preparation of extended asymmetric π-conjugated chromophores, as it provides a nitro-amino compound that can be hereinafter selectively protected. It is noteworthy to indicate that the same reaction can be pushed toward the formation of compound **2-9** using a larger amount of reducing agent. To prepare compound **2-8**, compound **2-7** was treated with $(CHO)_n$ and $NaBH_3CN$, in AcOH[104] and the dimethylamino compound **2-8** was obtained in 97% yield. Final reduction of nitro group in presence of $SnCl_2$ [105] yielded target compound **2-1** in 59% yield. Compound **2-1** along with other synthesized intermediates were fully characterized by melting point, ^{1}H-, ^{13}C-NMR, IR spectroscopy and ESI-HRMS spectrometry (*Chapter IV*). The ^{1}H-NMR spectrum of compound **2-1** is reported in Figure 2.10 and shows an asymmetric pattern of the aromatic signals in the region between 7.4 and 6.6 ppm. The signals corresponding to the olefinic protons appear as doublets at 7.26, 7.06 and 7.04 ppm with J value of 16.5 Hz, which indicates trans geometric isomerism.

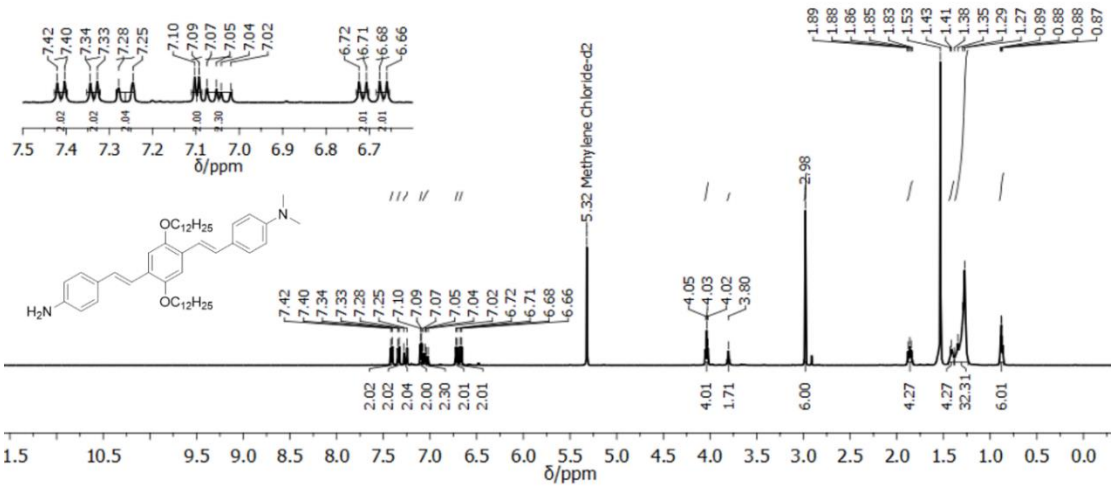

Figure 2.10 ^{1}H-NMR spectrum of final trimeric OPV **2-1** in CD_2Cl_2 at r.t.

Lastly, as a test reaction, to prove the reactivity of synthesized compounds toward amidation reaction, compounds **2-2** and **2-1** were reacted with benzoyl chloride in presence of Et_3N in

acetone to obtain compounds **2-10** and **2-11** respectively. The amidation reaction worked in high yields and short reaction time. The synthetic details are reported in Scheme 2.3.

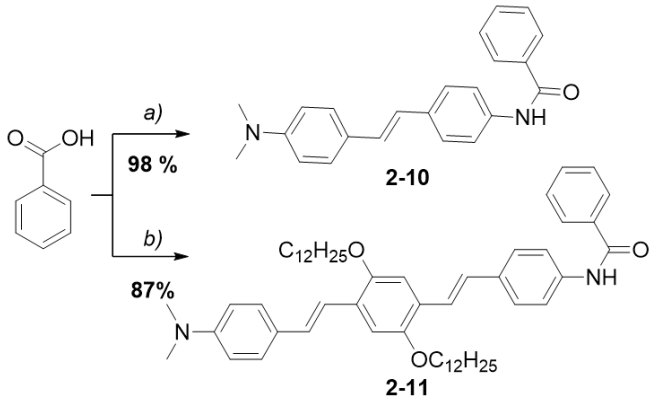

Scheme 2.3 Synthesis of compounds **2-10** and **2-11**. Reagents and conditions a) **2-2**, Et_3N, acetone, 2h, r.t.; b) **2-1**, Et_3N, acetone, 2h, r.t

2.2.2 Functionalization of SWCNTs

The preparation of OPV functionalized materials **f-SWCNT-1** and **f-SWCNT-2** was accomplished by covalent attachment of trimeric OPV **2-1** and compound **2-2**, respectively onto the surface of previously oxidized SWCNTs (7, 6) by amidation reaction and it is reported in Scheme 2.4. The extensive covalent functionalization of CNTs can disrupt the conjugated π-system of the tube thus affecting the optical and electronic properties of the material. In this respect, the use of milder functionalization methodologies is needed to retain the nanotube properties. In fact, oxidized SWCNTs (**ox-SWNTs)** were obtained by reaction of high purity pristine CoMoCat SWNTs (7, 6) with a 3:1 aq. solution of 3 M H_2SO_4 : 3 M HNO_3 at 80° C for 2 h, following a modified protocol described in literature.[106] The resulting oxidized material was treated with $SOCl_2$ to give a SWCNT-acid chloride intermediate[107] that was allowed to react with aminostyryl **2-1** and **2-2** in the presence of Et_3N in DMF to give OPV decorated SWCNTs enriched in (7, 6) chirality.

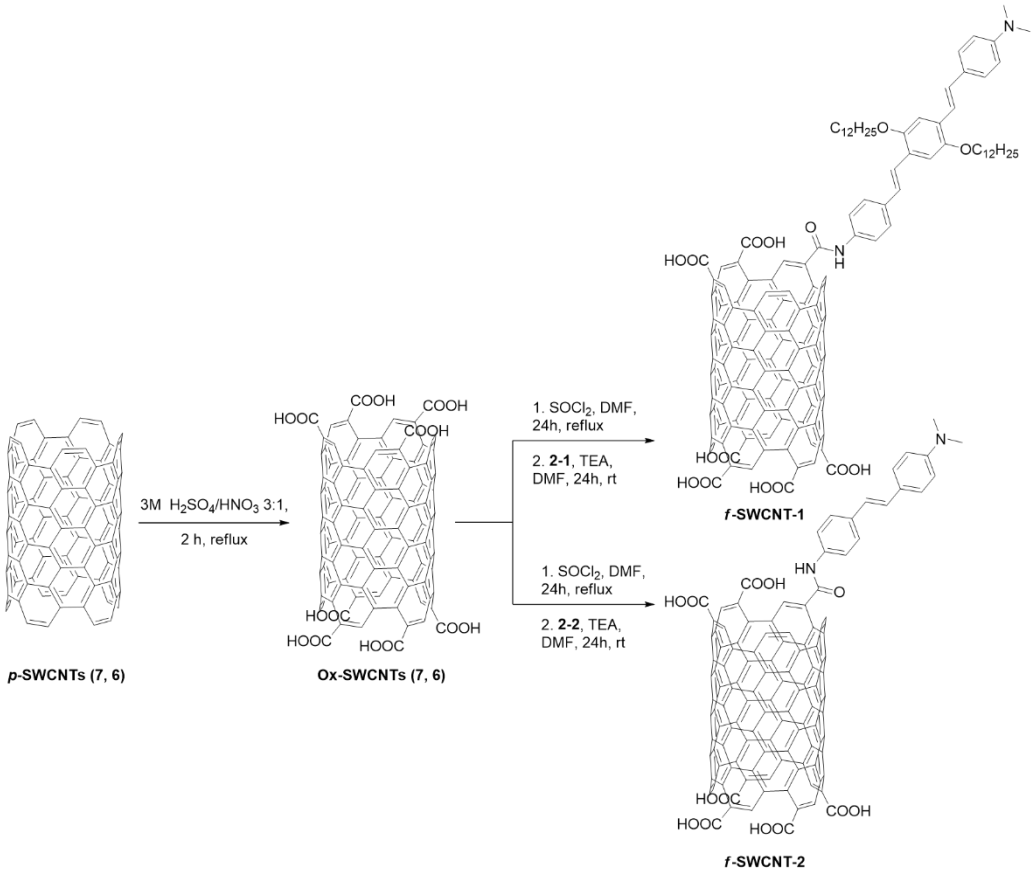

Scheme 2.4 Functionalization pathways toward the preparation of OPV-decorated SWNTs (7,6).

OPV-SWCNTs hybrids were characterized by UV-Vis-NIR spectroscopy, photoluminescence spectroscopy for chirality determination, Raman spectroscopy, X-ray photoelectron spectroscopy (XPS), thermogravimetric analysis (TGA) and transmission electron microscopy (TEM).

2.2.3 Characterization of OPV-functionalized material

In order to investigate the degree of functionalization, XPS and TGA measurements were carried out under N_2. The comparison of TGA profiles of pristine (**p–SWCNTs**), oxidized (**Ox-SWCNTs**) and functionalized SWCNTs gave a first evidence of the sidewall functionalization of the nanotubes (Figure 2.11). The weight-loss plots relative to **p–SWCNTs** and **Ox–SWCNTs** display the pyrolytic step of oxygenated functionalities in the range between 100 and ~ 500 °C with a weight loss of 4.5 % for **Ox-SWCNTs** in respect to **p-SWCNTs** (calculated at 500 °C). A mass content of 1000 μmol of –COOH per g of nanotube is estimated. An additional 5.0% weight loss is observed for **f-SWCNT-1**, and 4.4 % for **f-SWCNT-2,** resulting in one group of OPV **2-1** approximatively each 914 carbon

atoms for **f-SWCNT-1** (corresponding to 71 µmol of **2-1** per g of nanotube) and one group of compound **2-2** around each 383 carbon atoms for **f-SWCNTs-2** (corresponding to 184.6 µmol of **2-2** per g of nanotube).

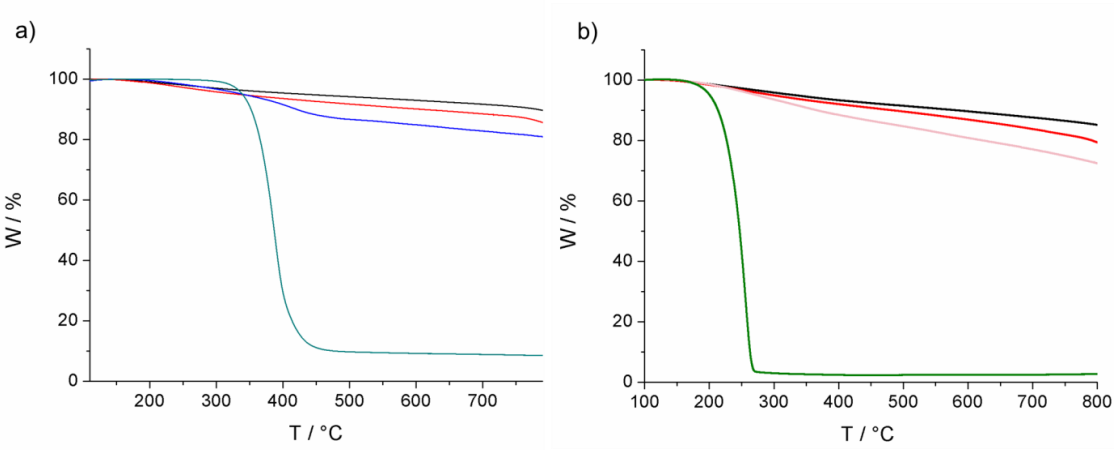

Figure 2.11. TGA profiles recorded at 10°C/min under N_2 for (a) p-SWCNTs (black), Ox-SWCNTs (red), ***f*-SWCNTs-1** (blue), OPV derivative **2-1** (cyan); and (b) **p-SWCNTs** (black), **Ox-SWCNTs** (red), ***f*-SWCNTs-2** (pink) and compound 2-2 (olive).

XPS studies showed an increase of O at% content in the oxidized sample (9.27 at% for O 1s at 532.7 eV meaning a 2.52 at% increase with respect to p-SWCNTs). Compositional data obtained from XPS analysis of analyzed SWCNTs materials are reported in Table 2.1. As expected, the introduction of dimethylamino derivatives groups onto the SWCNTs surface lead to the presence of N signature in **f-SWCNT-1** and **f-SWCNT-2** (1.83 at % for N1s at 400.1 eV and 1.80 at % for N1s at 400.1 eV, respectively). Surprisingly a minimal presence of N was detected also in the **Ox-SWCNTs** (0.54 at % for N1s at 400 eV) which introduction can be attributed to the sulfo-nitric treatment adopted for the oxidation reaction.

Table 2.1. Compositional data obtained from XPS analysis of ox-, p- and functionalized SWCNTs derivatives.

Sample	C at%	N at%	O at%
p-SWCNT (7,6)	92.82±0.24	-	6.74 ±0.27
Ox-SWCNT (7,6)	89.31±0.71	0.54±0.12	9.266±0.47
f-SWCNT-1	86.73±0.45	1.83±0.22	8.004±0.42
f-SWCNT-2	84.48±0.71	1.8±0.14	11.07± 0.45

Raman spectroscopy was used as additional technique to confirm the SWCNTs functionalization. Raman spectrum of the **Ox-SWCNT** sample (λ_{exc}=532 nm), reveals an increased D band around 1330 cm^{-1} (I_D/I_G = 0.21) in comparison with pristine SWCNTs where the defect band is very low in intensity (I_D/I_G = 0.086) The amidation reaction exploited for the attachment of derivatives **2-1** and **2-2** onto ox-SWCNTs surface does not modify significantly the intensity of the D band (Figure 2.12), where the I_D/I_G ratio for **f-SWCNT-1** and **f-SWCNT-2** is 0.22 and 0.23, respectively. The appearance of a new band around 1160 cm^{-1} was also observed and can be attributed to the presence of functionalized moieties.

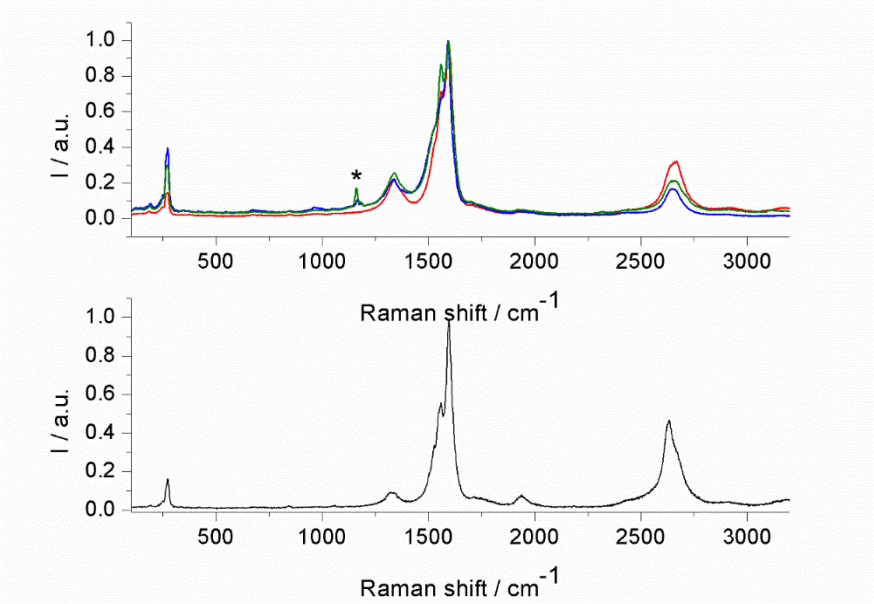

Figure2.12 Top: superimposed Raman spectra of **Ox-SWCNTs** (red), **f-SWCNT-1** (blue), **f-SWCNT-2** (olive). Bottom: Raman spectra of **pristine SWCNTs** (black); at 532 nm excitation. All spectra are normalized with respect to the G band intensity.

Moreover, the functionalized SWCNT samples were analyzed by TEM (see *Chapter IV*). For the analysis, a small droplet of the sample solution was deposited on a carbon-coated copper grid, followed by the evaporation of the solvent. Usually, the length and dispersion state of CNTs can be assessed by TEM at low magnification. Figure 2.13 shows the TEM images for the functionalized ***f*-SWCNTs-1** which provides the most direct evidence that the soluble samples contain carbon nanotubes. Moreover, as comparison we also recovered TEM images of compound **2-1.**

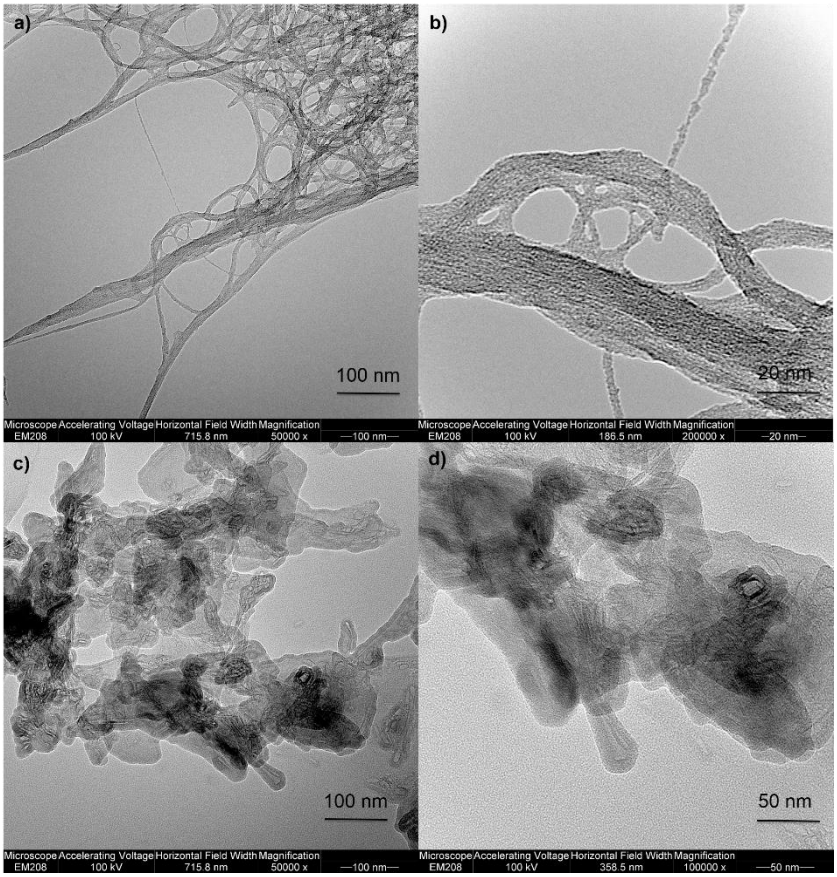

Figure 2.13 TEM images of 1 mg/mL dispersion of (a, b) ***f*-SWCNT-1** and (c, d) molecule **2-1** deposited on a carbon-coated copper grid.

2.3 Spectroscopic investigation of pristine and functionalized SWCNTs (7, 6)

As already discussed, the electronic and optical properties of SWCNTs are closely linked to their structure, which is defined by the chiral indices (*n,m*).[62] As the absorption (E_{22}) and emission (E_{11}) strongly depends on the chirality, every CNT species have a specific combination of E_{22} and E_{11} as a fingerprint. These distinct electronic absorption and emission transitions for different semiconducting nanotubes isolated in aqueous surfactant suspensions can be revealed through spectrofluorimetric measurements.[108] In this respect, Photoluminescence (PL) spectroscopy has become a very powerful tool for the investigation of semiconducting SWNTs because the E_{11} PL peaks of different type of SWNTs are observed individually by the excitation of E_{22} depending on their electronic structures. The photoluminescence mapping (PLM) is the most used approach and it provides emission spectra recorded as a function of the excitation wavelength.[109] The resulting three-dimensional plot shows the emission intensity maps as a number of excitation wavelengths, all across the visible spectral range. Every region of the map represents the signal of a given (*n,m*) species. For the purpose of this work, SWCNTs enriched in (7, 6) chirality has been

purchased from Sigma Aldrich. In collaboration with the group of *Prof. Nicola Armaroli* from *ISOF-CNR, Bologna,* initially the enrichment of the specific (7, 6) chirality in our SWCNTs sample was checked by recording the absorption spectra and the photoluminescence map.

SWCNTs (7,6) present two characteristic optical absorption features at 648 nm and 1122 nm, that correspond to the transitions E_{22} and E_{11}, respectively as reported in the literature[110]

In order to have a SWCNTs dispersion suitable for the photophysical characterization, the sample was dispersed through sonication (30 min) in water in the presence of sodium dodecyl benzene sulfate (SDBS) as surfactant. The experimental absorption spectrum reported in Figure 2.14 a shows the presence of other species in the sample. In fact, the sample used is only enriched in (7, 6) chirality, which is undoubtedly confirmed by the absorption peak at around 650 nm, while the second transition (expected around 1120 nm), is less evident. This can be attributed to the overlapping of bands from other species that absorb light in the same region.[111]

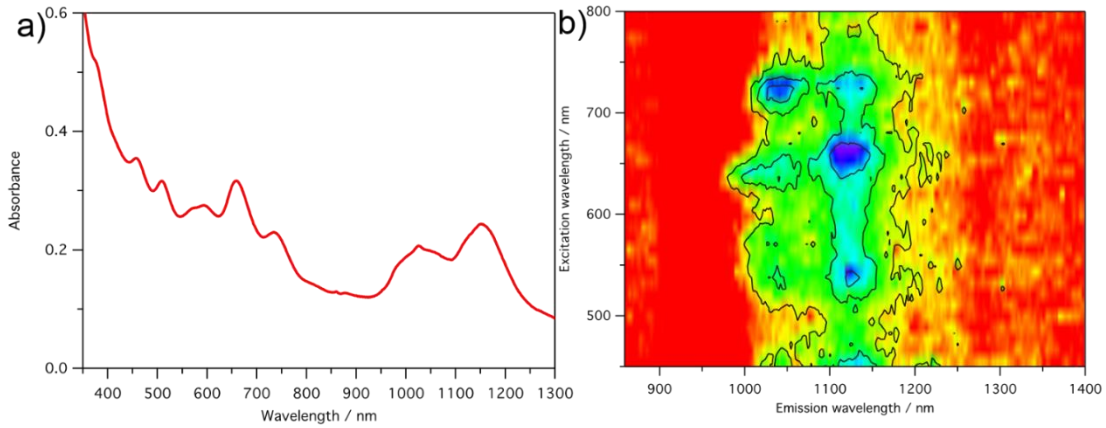

Figure 2.14 (a) Absorption spectrum and (b) photoluminescence mapping of a sample of SWCNTs enriched in the (7,6) chirality dispersed in water with SDBS.

On the other hand, the PLM of the SWCNT sample, depicted in Figure 2.14 b, displays emission features with different intensity, but, the highest at around 650 nm in excitation and 1120 nm in emission, can be clearly assigned to SWCNTs (7,6).

The situation completely changes after the chemical treatment of the SWCNTs (7, 6), which do not show any more detectable luminescence. In fact, after oxidation (reported in *Section 2.2.2*) the electronic features of the investigated nanotubes are considerably altered due to a rehybridization from sp^2 to sp^3 leading to a loss of conjugation. For such reason, the sample of **Ox-SWCNTs** (7,6), dispersed in DMF through sonication, does not exhibit any luminescence.

In order to study the photophysical behavior of hybrids **f-SWCNT-1** and **f-SWCNT-2**, the UV-Vis-NIR absorption and luminescence spectra were recorded and the excited state lifetimes have been measured. The two prepared dyads, **f-SWCNT-1** and **f-SWCNT-2**, presented different solubility and two different solvents were exploited for the measurements. In fact, compounds **2-1** and **f-SWCNT-1** were dispersed in DMF, whereas **2-2** and **f-SWCNT-2**, in 1,2 dichlorobenzene (ODCB), in order to have a well dispersed f-SWCNTs solution suitable for the photophysical analysis. The recorded electronic absorption spectra are reported in Figure 2.15. The calculation of the molar extinction coefficients was possible only for the organic compounds **2-1** and **2-2**. Compound **2-1** is characterized by two absorption maxima at 467 nm (ε = 57000 M^{-1} cm^{-1}) and 381 nm (ε = 20000 M^{-1} cm^{-1}), while **2-2** exhibits an absorption peak at 363 nm (ε = 31000 M^{-1} cm^{-1}), with a shoulder on the higher energy side. The increment of the π-conjugation length in **2-1** resulted in a shift of the maximum absorption peak of 104 nm toward the red in comparison to **2-2**. As shown in Figure 2.15, the absorption spectra of the dyads, **f-SWCNT-1** and **f-SWCNT-2,** result to be featureless and it was not possible to discriminate the UV–Vis absorption bands of the OPV molecules linked, probably due to an overwhelming absorption of **Ox-SWCNTs** in the same spectral region. Moreover, the absence of marked features of SWCNTs is attributable to the functionalization. Even if, milder oxidation conditions have been used the electronic structure of SWCNTs has been substantially modified and E_{11} and E_{22} transitions can be probably discerned only at low densities of covalent functionalization.[112]

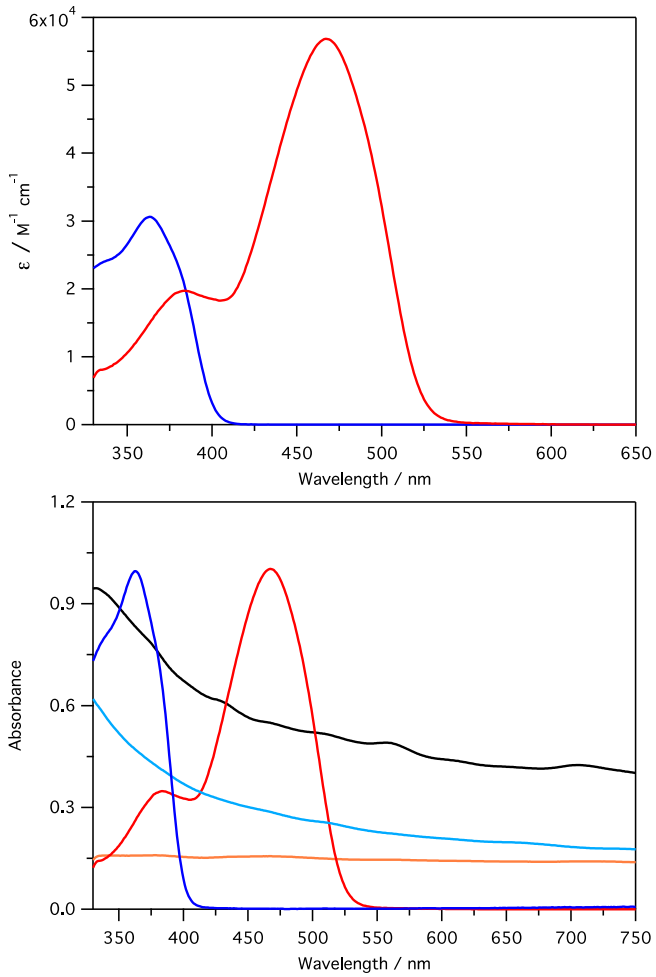

Figure 2.15. Top: Absorption spectra of **2-1** (red) in DMF and **2-2** (blue) in ODCB. Bottom: Absorption spectra of **2-1** (red), **f-SWCNT-1** (orange), **ox-SWCNT (7,6)** (black) in DMF and of **2-2** (blue) and **f-SWCNT-2** (light blue) in ODCB.

In order to evaluate the presence of photoinduced processes between the carbon nanotube and the OPV fragments, luminescence studies were performed for **f-SWCNT-1** using DMF as solvent and for **f-SWCNT-2** in ODCB, and compared with the reference materials **2-1** and **2-2**. Recoded spectra are depicted in Figure 2.16 and key data are collected in Table 2.2. It is noteworthy to mention that, typically, photophysical studies of samples containing SWCNTs are affected by high uncertainty. Particularly, it is difficult to determine absorbance values and, accordingly, to make quantitative luminescence assessments. This is ascribable to the nanometric nature of the SWCNTs causing extensive light scattering and to their tendency to self-aggregate and form bundles due to the poor solubility in the most common solvents. However, we found that **f-SWCNT-1** and **f-SWCNT-2** form stable and optically transparent dispersions in DMF and ODCB, respectively, allowing comparative studies with the OPV compounds and quantitative luminescence assessments. The extension

of the π-bridge of the planar molecular framework of OPVs results as a positive structural factor in enhancing the molecular fluorescent properties. The reference compound **2-1** shows an emission spectrum with a maximum at 510 nm and a fluorescence quantum yield above 38%, while the spectrum of **f-SWCNT-1** exhibits an emission maximum at 530 nm and a fluorescence quantum yield below 0.1%. Such strongly quenched emission (estimated to be over 99 % in **f-SWCNT-1** compared to **2-1**) indicates a substantial electronic interaction between the nanotubes and the anchored organic π-conjugated moiety. Compound **2-2** exhibits an emission spectrum with a maximum at 430 nm and an emission quantum yield of 12.8%. The fluorescence band of **f-SWCNT-2** is substantially hypsochromically shifted compared to that of the reference compound **2-2** (Δ_λ = 30 nm). The estimated fluorescence quantum yield for this system is less than 0.3%, indicating a quenching of above 97 % compared to compound **2-2**.

Table 2.2. Luminescence band maxima, fluorescence quantum yields and excited state lifetimes of **2-1**, **1-SWCNTs** (in DMF) and of **2-2** and **2-SWCNTs** (in ODCB).

Sample	λ_{max} (nm)	Φ_{FL} (%)	τ (ns)
2-1	510	38.5	1.37
f-SWCNT-1	530	[a]	1.51
2-2	430	12.8	0.61
f-SWCNT-2	400	[a]	0.68 (72%) 3.31 (28%)

[a]Φ_{FL} of the hybrid materials could not be determined as the light partitioning among the OPV and CNT moieties is not known. However, the quenching of the luminescence intensity of solutions of **f-SWCNT-1** and **f-SWCNT-2** *vs.*, respectively, **2-1** and **2-2** is above 99 and 97 % respectively. The excitation wavelengths used in these experiments corresponded to the absorption maxima of **2-1** (467 nm) and **2-2** (363 nm).

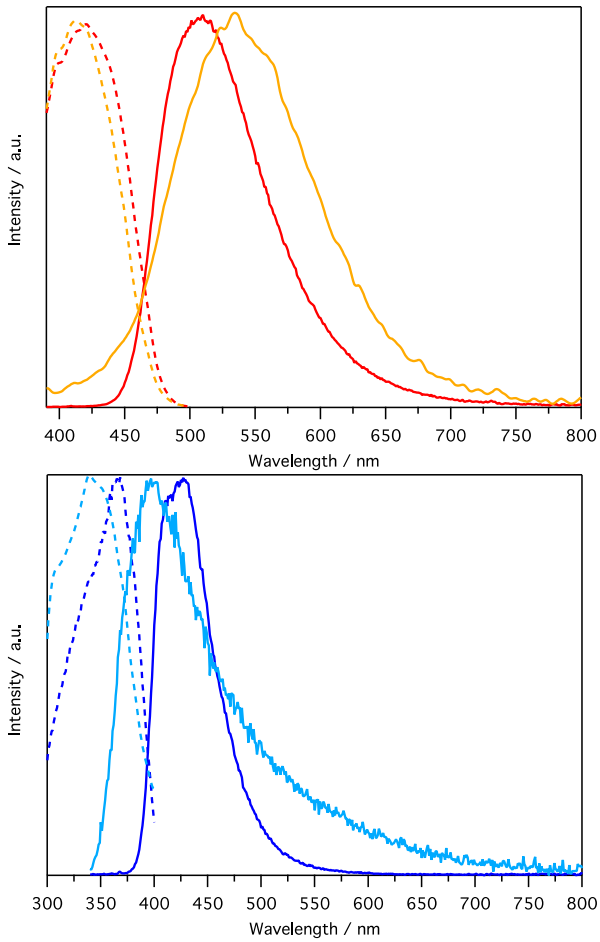

Figure 2.16. Top: Normalized excitation spectra at λ_{em} = 520 nm (dashed line) and emission spectra at λ_{ex} = 350 nm (full line) of **2-1** (red) and **f-SWCNT-1** (orange) in DMF. Bottom: Excitation spectra at λ_{em} = 420 nm (dashed line) and emission spectra at λ_{ex} = 330 nm (full line) of **2-2** (blue) and **f-SWCNT-2** (light blue) in ODCB.

The emission decay profiles of **2-1** and **f-SWCNT-1** are fitted monoexponentially, yielding singlet lifetimes of 1.3 and 1.5 ns, respectively. The latter value suggests that probably there is the presence of very small amounts of free **2-1** in the **f-SWCNT-1** dyad. Using a single photon counting spectrometer, which has a time resolution of 40 ps, no shorter lifetimes were detected for **f-SWCNT-1**. Therefore, intercomponent photo-induced processes (*i.e.* energy or electron transfer processes) must take place within 40 ps. The emission lifetime of **2-2** is mono-exponential and results to be 0.61 ns, while sample **f-SWCNT-2** showed a bi-exponential fluorescence decay with a prevalent component of 0.68 ns (72%) and a minor contribution of 3.31 ns (28%). The former could be easily attributed to the presence of a small amount of unbounded **2-2** in the dyad (less than 2%), while in contrast, the longest lifetime is more difficult to assign. A possible hypothesis could be that it might reflect the interaction between neighboring fluorophores covalently bounded onto the surface of the

SWCNT.

Moreover, thanks to the peculiarity of **f-SWCNT-1** and **f-SWCNT-2** to form stable and optical transparent dispersions in DMF and ODCB, respectively, it was possible to carry out sub-picosecond time-resolved measurements with the aim to clarify the nature of the photo-induced processes. Unfortunately, attempts to determine the quenched OPV lifetimes of **f-SWCNT-1** and **f-SWCNT-2** at shorter time scales with a streak camera apparatus (1 ps resolution) did not afford convincing results, as the OPV moieties most probably undergoes photodegradation upon intensive irradiation with a titanium-sapphire (Ti:Sa) ultrafast laser.

The absence of significant photoluminescence for **f-SWCNT-1** and **f-SWCNT-2** combined with the results we obtained in lifetime experiments showed no convincing proofs to determine the occurring processes (*i.e*., electron or energy transfer interactions). In light of these results, we decided, in collaboration with *Dr. Andrea Listorti* from the research group of the *University of Salento, (Lecce, Italy)*, to expand the use of newly synthesized materials and exploit them in hybrid organic/inorganic derivatives based on perovskites.

2.4. Extension of the use of f-SWCNTs-1 in perovskite solar cells

2.4.1 General Introduction on Perovskite solar cells

In the past few years has been seen the rapid emergence of a new class of solar cells based on mixed organic–inorganic halide perovskites. The ease of fabrication, strong solar absorption, low non-radiative carrier recombination rates for such simply prepared materials, and reasonably high carrier mobility make perovskites attractive for a number of applications such as lasing, lightening and, particularly photovoltaics.[113,114] The structure and physical properties of organo-metal halide $CH_3NH_3MX_3$ (M = Pb or Sn, X = Cl, Br or I), which is the key material of perovskite solar cells, were reported for the first time by *Weber* in 1978.[115] The interest in this material benefit from recent investigations of related thin-film transistors and light-emitting diodes (LEDs) by *Mitzi* and co-workers.[116,117] *Miyasaka et al.* were the first to report photovoltaic results for perovskites and showed a photovoltaic function of the perovskite nanocrystalline particles self-organized on TiO_2 as n-type semiconductors of dye-sensitized cells.[114,118] Since this preliminary work, the power conversion efficiency (PCE) of solar cells based on methylammonium lead halide ($CH_3NH_3PbX_3$ where X can be I, Br or Cl) has increased drastically from the initial 3.9% to more than 20 % in less than 6 years.[118,119] Numerous device structures[113,120–123] have thus been explored, differing both for the photovoltaic performances and for the morphological and structural properties of the

deposited perovskite material.[124–126] In fact, the device performance of perovskite solar cells is highly dependent on their architecture. Two major examples of perovskite solar cells have been developed so far, *i.e.*, mesoscopic and planar architectures (Figure 2.17)[113] In the mesoscopic structure the perovskite can either be introduced as a thin layer covering the oxide scaffold with the pores in the scaffold infiltrated with charge transporting material or it can form an overlayer on top of the completely infiltrated oxide scaffold as shown in Figure 2.17 a and b, respectively. On the other side, the planar architecture can exist in two different configurations, conventional (Figure 2.17 c) or inverted (Figure 2.17 d) depending on the direction of electric current.[113] The conventional solar cell architecture presents a sandwich-like design with a hybrid halide perovskite layer, typically $CH_3NH_3PbI_3$, acting as light harvesting material between a semiconducting oxide and organic Hole Transport Material (HTM). The semiconducting oxide, typically titanium dioxide (TiO_2), is deposited onto a conductive glass (fluorine-doped thin oxide, FTO) and act as electron transporting layer, while the HTM extracts the generated holes from the active $CH_3NH_3PbI_3$ layer. The solar cell is completed with the evaporation of a metal anode (silver or gold) on top of the HTM.[113]

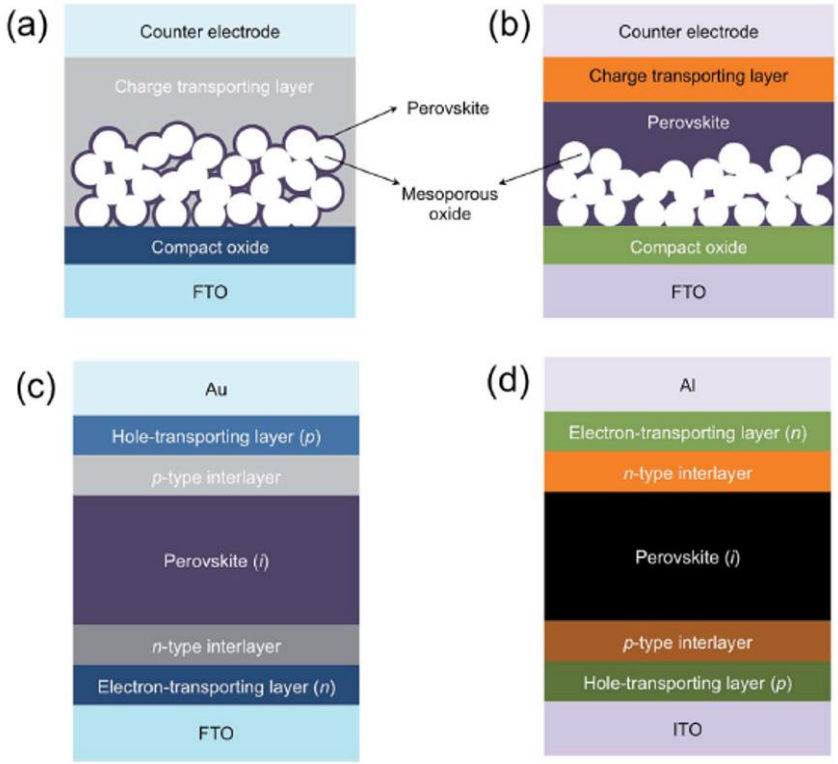

Figure 2.17. Schematic representation of mesoscopic heterojunction solar cells (a) no perovskite overlayer and (b) with perovskite overlayer; and planar heterojunction solar cells with (c) conventional "n–i–p" and (d) inverted "p–i–n" configurations.[113]

Organic molecules are often employed as a hole-transporting material for both mesoscopic- and planar-structured perovskite solar cells. Among the investigated HTMs, 2,2′,7,7′-Tetrakis(N,N-di-p-methoxyphenylamine)-9,9′-spirobifluorene (Spiro-OMeTAD), a non-polymeric small-molecule hole conductor, is the most popular choice for conventional planar perovskite solar cells. It has been largely the most exploited material, leading to the highest photovoltaic performances.[17,127] The chemical structure of Spiro-OMeTAD is reported in Figure 2.18. It has been introduced by *Park*, *Grätzel* and co-workers[128] and initially developed for organic LEDs[129] and lately found to be effective in solid-state dye cells.[17] However, SpiroOMeTAD can only be prepared through a complicated synthetic route, resulting in high costs and its intrinsic hole-mobility and -conductivity are low and for these reasons it has to be doped before integration in a device.[130]

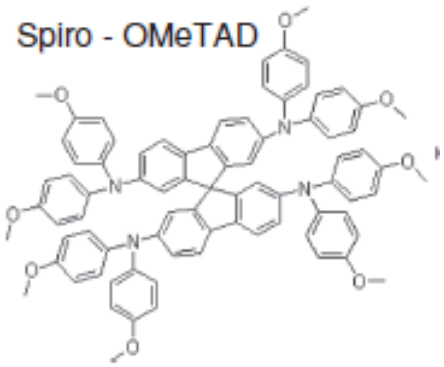

Figure 2.18 Chemical structure of SpiroOMeTAD HTM.

In this respect, the most common way to enhance charge mobility in a molecular hole transporting material is *via* addition of p-dopant species. Chemical dopants such as $N(PhBr)_3SbCl_6$ were first introduced to oxidize, and thus p-dope spiro-OMeTAD, but were rapidly replaced by the more effective additive lithiumbis(trifluoromethanesulfonyl)imide (LiTFSI)[17,131]. In contrary to chemical oxidants, LiTFSI does not oxidize directly the spiro-OMeTAD but promotes the oxidative reaction between spiro-OMeTAD and oxygen in the presence of either light or thermal excitation.[132,133] Unfortunately, the oxidation process is not easy to control and the variability of oxidized Spiro-OMeTAD concentration can dramatically affect the performance, reproducibility, and stability of the device.[134] To solve this problem several molecular complexes have been explored recently as alternative doping agents,[135–137] including carbon nanomaterials such as nanotubes. Indeed, MWCNTs and SWCNTs, thanks to their impressive charge transporting properties, have been investigated as p-type dopants or stand-alone hole transporting materials in PSCs.[121,138–141] Successful application of carbon nanomaterials in PSCs has been reported in only few studies. Last year

Lee et al. reported on the hierarchically structured hole transport layers of Spiro-OMeTAD and MWCNTs for PSCs. They have embedded MWCNTs in Spiro-OMeTAD in a HTM double layer consisting of a tiny film of pristine Spiro-OMeTAD and an overlying layer of a mixture of Spiro-OMeTAD and MWNTs, leading to an increase of the PCE from 12.8 % to 15.1 % as the nanotube concentration increases from 0 to 2 wt%.[142]

Based on these findings and our work described before, we report here that the functionalized single-wall carbon nanotubes (**f-SWCNT-1**) can also act as conductive nanofillers in a Spiro-OMeTAD layer used as HTM for hybrid PSCs based on $CH_3NH_3PbI_3$, thus aiming to provide better performances and longer time stabilities to the device. A schematic representation of the device is reported in Figure 2.19. In addition, we expect that the anchored **2-1** OPV bearing long alkoxy chains in the central aromatic ring and amine residues at the extremity could improve the compatibility with Spiro-OMeTAD in comparison with **Ox-SWCNTs** and enhance the affinity of the HTM mixture for the perovskite layer at the interface, thanks to the presence of the terminal amine groups.

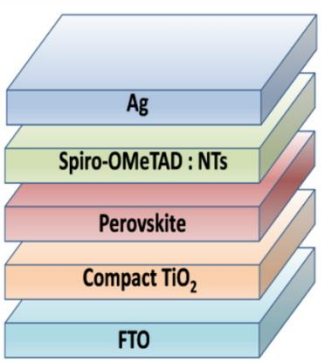

Figure 2.19 Schematic representation of the photovoltaic device containing **f-SWCNTs-1** as dopant for the Spiro-OMeTAD layer.

2.4.2. Characterization of f-SWCNT-1 as doping agent for spiro-OMeTAD in a flat $CH_3NH_3PbI_3$-based solar cell

In this section we report the characterization of **f-SWCNT-1** as doping agent for spiro-OMeTAD in a hybrid PSCs based on $CH_3NH_3PbI_3$. As reference material for this study the corresponding non-functionalized **Ox-SWCNTs** were used. Initially, **Ox-SWNTs** and functionalized **f-SWCNT-1** were dispersed in chlorobenzene (CB) through sonication and the clear dispersion has been used to prepare several solutions of Spiro-OMeTAD at different concentrations. This has been performed in order to test: *i)* the optimal Spiro-OMeTAD thickness and *ii)* the best degree of doping with SWCNTs samples. In this respect, different concentrations of the Spiro-OMeTAD (*i.e*. 45 mg/mL, 63 mg/mL and 90 mg/mL) and **f-**

SWCNT-1 as dopant (*i.e.* 0.4 mg/mL and 0.8 mg/mL) in CB have been investigated. The characteristic curves and photovoltaic parameters recorded for the best performing devices, varying the Spiro-OMeTAD concentration and the amount of **f-SWNTs-1**, are reported in the *appendix*. These tests show that the optimal Spiro-OMeTAD thickness is achieved using a concentration of 63 mg/mL, while the best doping degree is obtained with a concentration of 0.4 mg/mL of SWCNTs in CB. These concentrations of HTM and doping agent will be exploited for our study. Moreover, all the **f-SWCNT-1** doped devices have been compared with undoped (HTM) and conventionally doped devices with LiTFSI using comparable spiro-OMeTAD concentration and the best characteristic curves recorded for the fabricated devices are reported in Figure 2.20. The corresponding photovoltaic parameters are collected in Table 2.3.

Table 2.3. PV parameters of the best performing devices (average and standard error in bracket).

Device	PCE (%)	FF	V_{oc} (V)	J_{sc} (mA cm^{-2})
HTM	7.1	0.53	1.02	13.1
	(6.5 ± 0.5)	(0.47 ± 0.04)	(1.00 ± 0.03)	(13.8 ± 1)
HTM + **f-SWCNT-1**	9.6	0.58	1.00	16.6
	(7.9 ± 1.3)	(0.48 ± 0.08)	(0.99 ± 0.01)	(16.6 ± 0.4)
HTM + **Ox-SWCNTs**	9.0	0.52	0.97	17.7
	(6.4 ± 1.8)	(0.41 ± 0.08)	(0.94 ± 0.04)	(16.4 ± 2.0)
HTM + LiTFSI	10.9	0.65	1.03	16.3
	(9.8 ± 0.8)	(0.63 ± 0.07)	(1.04 ± 0.03)	(15.2 ± 1.3)

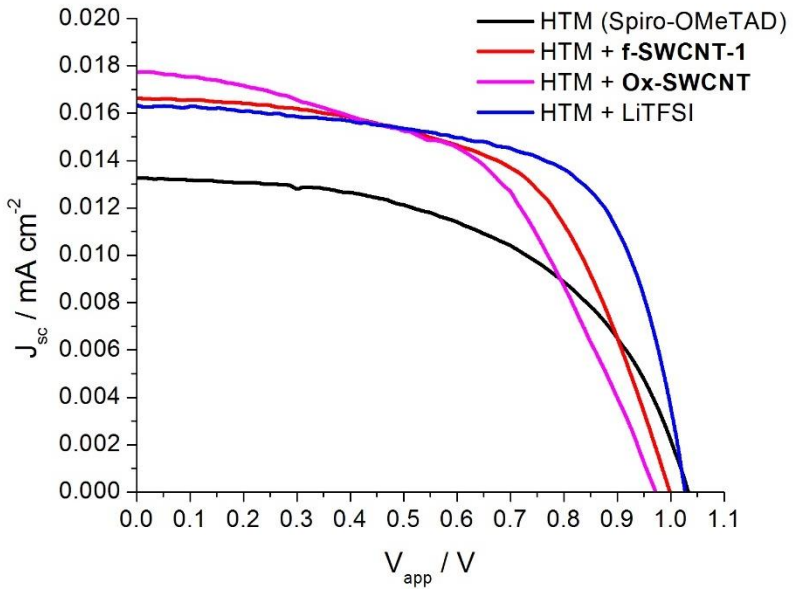

Figure 2.20. Characteristic curves of the best performing devices: device based on undoped Spiro-OMeTAD (black line), Spiro-OMeTAD doped with **f-SWCNTs-1** (red line) and **Ox-SWCNTs** (magenta line), and Spiro-OMeTAD conventionally doped with LiTFSI (blue line).

Comparing the PV results obtained with the undoped Spiro-OMeTAD, the carbon nanotube doping significantly enhances the short-circuit current, clearly indicating a higher conductivity of the hole transporting layer and a better charge extraction at the electrode.[138] In fact, a maximum PCE of 9.6% was achieved for the device containing **f-SWNT-1**, with respect to 7.1% of the undoped spiro-OMeTAD. Devices including **Ox-SWNTs** as dopant of the HTM show an extremely broad statistical distribution of the short-circuit current, and likewise scattered PCE, that can be attributed to a non-homogenous distribution of nanotubes within the film. Considerably, the HTM doped with **f-SWCNT-1** allows the achievement of slightly lower, but mainly comparable, performances with respect to the spiro-OMeTAD standardly doped with LiTFSI, both in terms of efficiency (9.6% for **f-SWNT-1** doped HTM *vs* 10.9% for LiTFSI doped HTM) and in terms of statistical distribution. This demonstrates the suitability of this carbon material as valid doping agent for spiro-OMeTAD, as alternative to the conventional chemical dopants. In addition, the comparison between the use of functionalized **f-SWNT-1** and non-functionalized **Ox-SWNTs** as HTM dopants, would permit to unravel the role of the organic functionalization present on **f-SWNT-1**, since better and more reproducible photovoltaic performances are recorder using the sample bearing the OPV moieties.

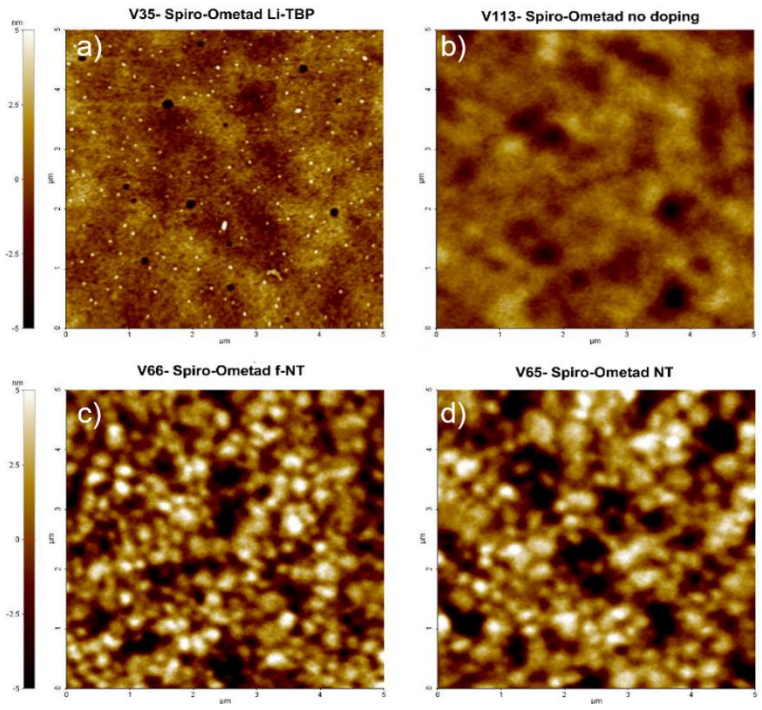

Figure 2.21. AFM characterization of HTM layers used for the solar cell fabrication. Spiro-OMeTAD (a) doped with conventional Li-salt, (b) undoped, (c) doped with **f-SWCNT-1** and (d) doped with **Ox-SWCNT**.

The morphology and thus the uniformity of the hole transported layers (undoped, conventionally doped and doped with SWCNTs) employed for the solar cell fabrication were investigated by means of Atomic Force Microscopy (AFM) and the recorded AFM images are reported in Figure 2.21. The pristine spiro-OMeTAD coated surface appears to be very smooth and homogeneous with the root mean square roughness (Rq) of 1.1 nm, whereas the addition of LiTFSI to the spiro-OMeTAD results in the formation of aggregates and pinholes in the film that are ascribable to the poor solubility of the Li salt. In contrast, the doping of the HTM layer with SWCNTs increase the spiro-OMeTAD roughness maintaining a homogeneous films morphology if compared to the LiTFSI doping. The **Ox-SWNT** and **f-SWCNT-1** doped samples present a roughness of Rq=2.6 nm and Rq=2.2 nm, respectively; suggesting that a more homogeneous dispersion of **f-SWCNT-1** in the spiro-OMeTAD matrix could be conferred by the organic chromophore covalently attached. In fact, the functionalization allows a better dispersion of SWCNTs within the HTM, allowing more reproducible photovoltaic performances. Evidently, the photo-conversion efficiency achieved by **f-SWCNT-1** doping is comparable with the standard Li-salt doping, demonstrating the suitability of those material as valid alternative for the spiro-OMeTAD doping in perovskite-based solar cells.

2.5 Conclusions

This chapter focused on the preparation and characterization of novel donor-acceptor systems based on OPV bearing different π-conjugated lengths and SWCNT. SWCNT enriched in 7,6 chirality have been used in order to enhance the properties of the material in development and benefit from the well-defined properties of structurally controlled SWCNTs. Chrmophoric molecules **2-1** and **2-2** have been successfully synthesized exploiting a classical Horner–Wadsworth–Emmons and fully characterized in terms of melting point, ^{1}H-, ^{13}C-NMR, IR spectroscopy and ESI-HRMS spectrometry. Two dyads, **f-SWCNT-1** and **f -SWCNT-2,** have been prepared linking chromophores **2-1** and **2-2**, respectively, on SWCNTs following a covalent functionalization route *via* amidation reaction. The structural properties of the OPV-SWCNTs conjugates were fully investigated *via* thermogravimetric analysis (TGA), X-ray photoelectron spectroscopy (XPS), transmission electron microscopy (TEM) and raman spectroscopy. The photophysical properties of the OPV-CNTs derivatives were investigated through steady state absorption and emission spectroscopy and trough time resolved fluorescence. The photophysical characterization revealed strong electronic interactions between the different components in both dyads. However, definitive experimental evidences could not be obtained for supporting photo-induced electron and/or energy transfer processes involving the OPV chromophores and the CNTs wall. This problem encountered could be addressed by optimizing the functionalization strategy of SWCNTs introducing more functional groups or using other chromophore candidates with longer emission lifetimes.

However, thanks to the peculiarity of these systems to form stable and optical transparent dispersions, we were able to extend their application in perovskite based solar cells. In this respect, **f-SWCNT-1** was implemented as p-type dopant in a Spiro-OMeTAD layer as HTM for hybrid PSCs based on $CH_3NH_3PbI_3$. As a result, the HTM doped with **f-SWCNT-1** allows a comparable, but slightly lower performances with respect to the standardly doped spiro-OMeTAD, both in terms of efficiency (9.6% vs 10.9%) and in terms of statistical distribution, demonstrating the suitability of this material as valid doping agent for spiro-OMeTAD, as alternative to the conventional LiTDS. Despite the fact that the presence of the chromophore onto SWCNTs did not present the photoactive response we expected, the implementation of OPV-SWCNT dyad in perovskite solar cell allowed us to obtain a more homogeneous dispersion in the spiro-OMeTAD matrix. In this way, these results

demonstrate that the functionalization allowing a better dispersion of SWCNTs within the HTM, could lead to more reproducible photovoltaic performances.

2.6 Bibliography

[1] H. Imahori, S. Fukuzumi, *Adv. Funct. Mater.* **2004**, *14*, 525–536.

[2] C.-Y. Yen, Y.-F. Lin, S.-H. Liao, C.-C. Weng, C.-C. Huang, Y.-H. Hsiao, C.-C. M. Ma, M.-C. Chang, H. Shao, M.-C. Tsai, et al., *Nanotechnology* **2008**, *19*, 1–9.

[3] M. Terrones, *Annu. Rev. Mater. Res.* **2003**, *33*, 419–501.

[4] I. W. Chiang, B. E. Brinson, R. E. Smalley, J. L. Margrave, R. H. Hauge, *J. Phys. Chem. B* **2001**, *105*, 1157–1161.

[5] C. Bower, A. Kleinhammes, Y. Wu, O. Zhou, *Chem. Phys. Lett.* **1998**, *288*, 481–486.

[6] R. H. Baughman, A. a Zakhidov, W. a de Heer, *Science* **2002**, *297*, 787–92.

[7] P. Singh, S. Campidelli, S. Giordani, D. Bonifazi, A. Bianco, M. Prato, *Chem. Soc. Rev.* **2009**, *38*, 2214–2230.

[8] D. M. Guldi, M. Marcaccio, D. Paolucci, F. Paolucci, N. Tagmatarchis, D. Tasis, E. V??zquez, M. Prato, *Angew. Chemie - Int. Ed.* **2003**, *42*, 4206–4209.

[9] B. Ballesteros, G. D. La Torre, C. Ehli, G. M. A. Rahman, F. Agulló-Rueda, D. M. Guldi, T. Torres, *J. Am. Chem. Soc.* **2007**, *129*, 5061–5068.

[10] D. Baskaran, J. W. Mays, X. P. Zhang, M. S. Bratcher, *J. Am. Chem. Soc.* **2005**, *127*, 6916–6917.

[11] C. Aurisicchio, R. Marega, V. Corvaglia, J. Mohanraj, R. Delamare, D. A. Vlad, C. Kusko, C. A. Dutu, A. Minoia, G. Deshayes, et al., *Adv. Funct. Mater.* **2012**, *22*, 3209–3222.

[12] A. J. Ferguson, J. L. Blackburn, N. Kopidakis, *Mater. Lett.* **2013**, *90*, 115–125.

[13] I. G. C. Coutts, H. R. Goldschmid, C. Musgrave, I. C. S. C, *Adv. Mater.* **1997**, *9*, 639–643.

[14] Y. Tao, A. Donat-bouillud, M. D. Iorio, J. Lam, T. C. Gorjanc, C. Py, M. S. Wong, Z. H. Li, *Thin Solid Films* **2000**, *363*, 298–301.

[15] N. Armaroli, V. Balzani, *Angew. Chem. Int. Ed.* **2007**, *46*, 52–66.

[16] A. M. Bagher, *Int. J. Renew. Sustain. Energy* **2014**, *3*, 53–58.

[17] U. Bach, D. Lupo, P. Comte, J. E. Moser, F. Weissörtel, J. Salbeck, H. Spreitzer, M. Grätzel, *Nature* **1998**, *395*, 583–585.

[18] B. O'Regan, D. T. Schwartz, S. M. Zakeeruddin, M. Grätzel, *Adv. Mater.* **2000**, *12*, 1263–1267.

[19] N. S. Sariciftci, L. Smilowitz, a J. Heeger, F. Wudi, *Science (80-.).* **1992**, *258*, 1474–1476.

[20] M. W. Rowell, M. A. Topinka, M. D. McGehee, H. J. Prall, G. Dennler, N. S. Sariciftci, L. Hu, G. Gruner, *Appl. Phys. Lett.* **2006**, *88*, 86–89.

[21] W. U. Huynh, *Science (80-.).* **2002**, *295*, 2425–2427.

[22] E. Becquerel, *C. R. Acad. Sci.* **1839**, 561.

[23] R. Gómez, J. L. Segura, *J. Chem. Educ.* **2007**, *84*, 253.

[24] H. Hoppe, N. Sariciftci, *J. Mater. Res.* **2004**, *19*, 1924–1945.

[25] J.-M. C. R. Nunzi, *Physique* **2002**, 532.

[26] H. Kallmann, M. Pope, *J. Chem. Phys* **1959**, *30*, 585–586.

[27] N. Geacintov, M. Pope, H. Kallman, *J. Phys. Chem.* **1966**, *45*, 2639–2649.

[28] D. L. Morel, A. K. Ghosh, T. Feng, E. L. Stogryn, P. E. Purwin, R. F. Shaw, C. Fishman, *Appl. Phys. Lett.* **1978**, *32*, 495.

[29] M. Hiramoto, H. Fujiwara, M. Yokoyama, *Appl. Phys. Lett.* **1991**, *58*, 1062.

[30] W. Geens, T. Aernouts, J. Poortmans, G. Hadziioannou, *Thin Solid Films* **2002**, *403*, 438–443.

[31] P. Peumans, S. Uchida, S. R. Forrest, *Nature* **2003**, *425*, 158–162.

[32] G. Yu, A. J. Heeger, *J. Appl. Phys.* **1995**, *78*, 4510.

[33] K. Tada, K. Hosoda, M. Hirohata, R. Hidayat, T. Kawai, M. Onoda, M. Teraguchi, T. Masuda, A. A. Zakhidov, K. Yoshino, *Synth. Met.* **1997**, *85*, 1305–1306.

[34] J. J. M. Halls, R. H. Friend, *Synth. Met.* **1997**, *85*, 1307–1308.

[35] J. J. Dittmer, E. A. Marseglia, R. H. Friend, *Adv. Mater.* **2000**, *12*, 1270–1274.

[36] C. Y. Yang, A. J. Heeger, *Synth. Met.* **1996**, *83*, 85–88.

[37] K. Petritsch, J. . Dittmer, E. . Marseglia, R. . Friend, A. Lux, G. . Rozenberg, S. . Moratti, A. . Holmes, *Sol. Energy Mater. Sol. Cells* **2000**, *61*, 63–72.

[38] L. Schmidt-Mende, A. Fechtenkotter, K. Mullen, E. Moons, R. H. Friend, J. D. MacKenzie, *Science* **2001**, *293*, 1119–1122.

[39] Y. Liang, Z. Xu, J. Xia, S. T. Tsai, Y. Wu, G. Li, C. Ray, L. Yu, *Adv. Mater.* **2010**, *22*, 135–138.

[40] M. A. Green, K. Emery, Y. Hishikawa, W. Warta, E. D. Dunlop, *Prog. Photovoltaics Res. Appl.* **2015**, *23*, 1–9.

[41] S. Cataldo, P. Salice, E. Menna, B. Pignataro, *Energy Environ. Sci.* **2012**, *5*, 5919–5940.

[42] H. Ago, K. Petritsch, M. S. P. Shaffer, A. H. Windle, R. H. Friend, *Adv. Mater.* **1999**,

11, 1281–1285.

[43] E. Kymakis, G. A. J. Amaratunga, *Appl. Phys. Lett.* **2002**, *80*, 112.

[44] T. Umeyama, N. Kadota, N. Tezuka, Y. Matano, H. Imahori, *Chem. Phys. Lett.* **2007**, *444*, 263–267.

[45] D. M. Guldi, N. Martin, *Carbon Nanotubes and Related Structures: Synthesis, Characterization, Functionalization, and Applications*, Wiley-VCH Verlag GmbH & Co. KGaA, **2010**.

[46] D. Baskaran, J. W. Mays, X. P. Zhang, M. S. Bratcher, *J. Am. Chem. Soc.* **2005**, *127*, 6916–6917.

[47] S. Campidelli, C. Sooambar, E. Lozano Diz, C. Ehli, D. M. Guldi, M. Prato, *J. Am. Chem. Soc.* **2006**, *128*, 12544–12552.

[48] J. Jin, Z. Dong, J. He, R. Li, J. Ma, *Nanoscale Res. Lett.* **2009**, *4*, 578–583.

[49] H. Li, R. B. Martin, B. A. Harruff, R. A. Carino, L. F. Allard, Y.-P. Sun, *Adv. Mater.* **2004**, *16*, 896–900.

[50] D. M. Guldi, G. M. A. Rahman, M. Prato, N. Jux, S. Qin, W. Ford, *Angew. Chem.* **2005**, *117*, 2051–2054.

[51] C. Ehli, G. M. A. Rahman, N. Jux, D. Balbinot, D. M. Guldi, F. Paolucci, M. Marcaccio, D. Paolucci, M. Melle-Franco, F. Zerbetto, et al., *J. Am. Chem. Soc.* **2006**, *128*, 11222–11231.

[52] H. Li, B. Zhou, Y. Lin, L. Gu, W. Wang, K. A. S. Fernando, S. Kumar, L. F. Allard, Y.-P. Sun, *J. Am. Chem. Soc.* **2004**, *126*, 1014–1015.

[53] J. Chen, C. P. Collier, *J. Phys. Chem. B* **2005**, *109*, 7605–7609.

[54] G. D. Nessim, *Nanoscale* **2010**, *2*, 1306–1323.

[55] Kroto, HW, J. Heath, S. O'Brien, R. Curl, R. Smalley, *Nature* **1985**, *318*, 162–3.

[56] S. Iijima, *Nature* **1991**, *354*, 56–58.

[57] R. C. Haddon, *Acc. Chem. Res.* **1992**, *25*, 127–133.

[58] C. N. Rao, B. C. Satishkumar, A. Govindaraj, M. Nath, *Chemphyschem* **2001**, *2*, 78–105.

[59] M. Prato, K. Kostarelos, *Acc. Chem. Res.* **2008**, *41*.

[60] J. W. G. Wilder, L. C. Venema, A. G. Rinzler, R. E. Smalley, C. Dekker, *Nature* **1998**, *391*, 59–62.

[61] S. a. Hodge, M. K. Bayazit, K. S. Coleman, M. S. P. Shaffer, *Chem. Soc. Rev.* **2012**, *41*, 4409.

[62] R. Saito, M. Fujita, G. Dresselhaus, M. S. Dresselhaus, *Appl. Phys. Lett.* **1992**, *60*,

2204.

[63] R. Krupke, *Science (80-.).* **2003**, *301*, 344–347.

[64] A. J. Stone, D. J. Wales, *Chem. Phys. Lett.* **1986**, *128*, 501–503.

[65] J. Liu, A. G. Rinzler, H. Dai, J. H. Hafner, R. K. Bradley, P. J. Boul, A. Lu, T. Iverson, K. Shelimov, C. B. Huffman, et al., *Science* **1998**, *280*, 1253 –1256.

[66] J. L. Delgado, M. Herranz, N. Martín, *J. Mater. Chem.* **2008**, *18*, 1417.

[67] S. Niyogi, M. a. Hamon, H. Hu, B. Zhao, P. Bhowmik, R. Sen, M. E. Itkis, R. C. Haddon, *Acc. Chem. Res.* **2002**, *35*, 1105–1113.

[68] J. Li, G. Jia, Y. Zhang, Y. Chen, *Chem. Mater.* **2006**, *18*, 3579–3584.

[69] Y. Sato, K. Yanagi, Y. Miyata, K. Suenaga, H. Kataura, S. Iijima, *Nano Lett.* **2008**, *8*, 3151–3154.

[70] Y. Miyata, T. Kawai, Y. Miyamoto, K. Yanagi, Y. Maniwa, H. Kataura, *J. Phys. Chem. C* **2007**, *111*, 9671–9677.

[71] D. Tasis, N. Tagmatarchis, A. Bianco, M. Prato, *Chem. Rev.* **2006**, *106*, 1105–36.

[72] A. Hirsch, *Angew. Chemie Int. Ed.* **2002**, *41*, 1853–1859.

[73] J. Chen, *Science* **1998**, *282*, 95–98.

[74] W. Wu, H. Zhu, L. Fan, S. Yang, *Chem. - A Eur. J.* **2008**, *14*, 5981–5987.

[75] M. A. Herranz, N. Martin, S. Campidelli, M. Prato, G. Brehm, D. M. Guldi, *Angew. Chem. - Int. Ed.* **2006**, *45*, 4478–4482.

[76] N. Armaroli, *Photochem. Photobiol. Sci.* **2003**, *2*, 73–87.

[77] M. G. Walter, A. B. Rudine, C. C. Wamser, *J. Porphyr. Phthalocyanines* **2010**, *14*, 759–792.

[78] T.-Q. Nguyen, R. Y. Yee, B. J. Schwartz, *J. Photochem. Photobiol. A Chem.* **2001**, *144*, 21–30.

[79] P. F. Van Hutten, V. V. Krasnikov, G. Hadziioannou, *Acc. Chem. Res.* **1999**, *32*, 257–265.

[80] H. E. Katz, S. F. Bent, L. W. William, M. L. Schilling, S. B. Ungashet, *J. Am. Chem. Soc.* **1994**, *116*, 6631–6635.

[81] A. P. H. J. Schenning, P. Jonkheijm, E. Peeters, E. W. Meijer, *J. Am. Chem. Soc.* **2001**, *123*, 409–416.

[82] A. . Fallis, *J. Chem. Inf. Model.* **2013**, *53*, 1689–1699.

[83] J. F. Hulvat, M. Sofos, K. Tajima, S. I. Stupp, *J. Am. Chem. Soc.* **2005**, *127*, 366–372.

[84] N. Armaroli, F. Barigelletti, P. Ceroni, J.-F. Eckert, J.-F. Nicoud, J.-F. Nierengarten, *Chem.Commun.* **2000**, *7*, 599–600.

[85] J.-F. Eckert, J.-F. Nicoud, J.-F. Nierengarten, S.-G. Liu, L. Echegoyen, F. Barigelletti, N. Armaroli, L. Ouali, V. Krasnikov, G. Hadziioannou, *J. Am. Chem. Soc.* **2000**, *122*, 7467–7479.

[86] N. Armaroli, J.-F. Eckert, J.-F. Nierengarten, *Chem. Commun.* **2000**, 2105–2106.

[87] J. Morgado, F. Cacialli, R. Iqbal, S. Moratti, A. Holmes, G. Yahioglu, L. Milgrom, R. Friend, *J. Mater. Chem.* **2001**, *11*, 278–283.

[88] K. Brunner, J. A. E. H. Van Haare, B. M. W. Langeveld-voss, H. F. M. Schoo, J. W. Hofstraat, A. Van Dijken, **2007**, 1–8.

[89] R. A. J. Janssen, J. C. Hummelen, K. Lee, K. Pakbaz, N. S. Sariciftci, A. J. Heeger, F. Wudl, *J. Chem. Phys.* **1995**, *103*, 788–793.

[90] J. N. Clifford, T. Gu, J.-F. Nierengarten, N. Armaroli, *Photochem. Photobiol. Sci.* **2006**, *5*, 1165–72.

[91] L. Ouali, V. V. Krasnikov, U. Stalmach, G. Hadziioannou, *Adv. Mater.* **1999**, *11*, 1515–1518.

[92] N. C. Greenham, S. C. Moratti, D. D. C. Bradley, R. H. Friend, A. B. Holmes, *Nature* **1993**, *365*, 628–630.

[93] F. Babudri, S. R. Cicco, G. M. Farinola, F. Naso, A. Bolognesi, W. Porzio, *Macromol. Rapid Commun.* **1996**, *17*, 905–911.

[94] N. Drolet, Y. Tao, M. Leclerc, S. Inge, *Synthesis (Stuttg).* **2004**, 4619–4626.

[95] A. P. Davey, A. Drury, S. Maier, H. J. Byrne, W. J. Blau, *Synth. Met.* **1999**, *103*, 2478–2479.

[96] C. Wu, J. Wei, D. Tian, Y. Feng, R. H. Miller, Y. Wang, *J. Med. Chem.* **2008**, *51*, 6682–6688.

[97] A. Llanes-Pallas, C. Palma, L. Piot, A. Belbakra, A. Listorti, M. Prato, P. Samori, N. Armaroli, D. Bonifazi, *J. Am. Chem. Soc.* **2009**, *131*, 509–520.

[98] B. Wang, M. R. Wasielewski, *J. Am. Chem. Soc.* **1997**, *119*, 12–21.

[99] Z. K. Chen, H. Meng, Y. H. Lai, W. Huang, *Macromolecules* **1999**, *32*, 4351–4358.

[100] D. A. M. Egbe, H. Tillmann, E. Birckner, E. Klemm, *Macromol. Chem. Phys.* **2001**, *202*, 2712–2726.

[101] K. Mullen, G. Wegner, *Electronic Materials: The Oligomer Approach*, **1998**.

[102] T. Jiu, Y. Li, H. Liu, J. Ye, X. Liu, L. Jiang, M. Yuan, J. Li, C. Li, S. Wang, et al., *Tetrahedron* **2007**, *63*, 3168–3172.

[103] U. Caruso, M. Casalboni, A. Fort, M. Fusco, B. Panunzi, A. Quatela, A. Roviello, F. Sarcinelli, *Opt. Mater.* **2005**, *27*, 1800–1810.

[104] W. Zhang, S. Oya, M.-P. Kung, C. Hou, D. L. Maier, H. F. Kung, *J. Med. Chem.* **2005**, *48*, 5980–8.

[105] C. Lu, Y. Guo, J. Yan, Z. Luo, H. Luo, M. Yan, L. Huang, X. Li, *J. Med. Chem.* **2013**, *56*, 5843–5859.

[106] A. Gasnier, J. M. Gonzalez-Dominguez, A. Anson-Casaos, J. Hernandez-Ferrer, M. L. Pedano, M. D. Rubianes, M. T. Martinez, G. Rivas, *Electroanalysis* **2014**, *26*, 1676–1683.

[107] C.-H. Andersson, H. Grennberg, *European J. Org. Chem.* **2009**, 4421–4428.

[108] S. M. Bachilo, M. S. Strano, C. Kittrell, R. H. Hauge, R. E. Smalley, R. B. Weisman, M. O'Connell, T. W. Odom, J.-L. Huang, P. Kim, et al., *Science (80-.).* **2002**, *298*, 2361–2366.

[109] S. M. Bachilo, *Science* **2002**, *298*, 2361–2366.

[110] R. B. Weisman, S. M. Bachilo, *Nano Lett.* **2003**, *3*, 1235–1238.

[111] A. V Naumov, S. Ghosh, D. A. Tsyboulski, S. M. Bachilo, R. B. Weisman, *ACS Nano* **2011**, *5*, 1639–1648.

[112] M. J. O. Connell, *Science* **2002**, *297*, 593–597.

[113] T. Salim, S. Sun, Y. Abe, A. Krishna, A. C. Grimsdale, Y. M. Lam, *J. Mater. Chem. A Mater. energy Sustain.* **2015**, *3*, 8943–8969.

[114] M. A. Green, A. Ho-Baillie, H. J. Snaith, *Nat Phot.* **2014**, *8*, 506–514.

[115] D. Weber, *Z. Naturforsch* **1978**, *33*, 1443–1445.

[116] D. B. Mitzi, S. Wang, C. A. Feild, C. A. Chess, A. M. Guloy, *Science (80-.).* **1995**, *267*, 1473–1476.

[117] D. B. Mitzi, K. Chondroudis, C. R. Kagan, *IBM J. Res. Dev.* **2001**, *45*, 29–45.

[118] A. Kojima, K. Teshima, Y. Shirai, T. Miyasaka, *J. Am. Chem. Soc.* **2009**, *131*, 6050–6051.

[119] M. A. Green, K. Emery, Y. Hishikawa, W. Warta, E. D. Dunlop, *Prog. Photovoltaics Res. Appl.* **2015**, *23*, 1–9.

[120] J. Burschka, N. Pellet, S.-J. Moon, R. Humphry-Baker, P. Gao, M. K. Nazeeruddin, M. Grätzel, *Nature* **2013**, *499*, 316–320.

[121] W. Zhang, M. Saliba, D. T. Moore, S. K. Pathak, M. T. Horantner, T. Stergiopoulos, S. D. Stranks, G. E. Eperon, J. A. Alexander-Webber, A. Abate, et al., *Nat Commun* **2015**, *6*, 6142.

[122] W. Chen, Y. Wu, J. Liu, C. Qin, X. Yang, A. Islam, Y.-B. Cheng, L. Han, *Energy Environ. Sci.* **2015**, *8*, 629–640.

[123] V. Trifiletti, V. Roiati, S. Colella, R. Giannuzzi, L. De Marco, A. Rizzo, M. Manca, A. Listorti, G. Gigli, *ACS Appl. Mater. Interfaces* **2015**, *7*, 4283–4289.

[124] A. Listorti, E. J. Juarez-Perez, C. Frontera, V. Roiati, L. Garcia-Andrade, S. Colella, A. Rizzo, P. Ortiz, I. Mora-Sero, *J. Phys. Chem. Lett.* **2015**, *6*, 1628–1637.

[125] G. Pellegrino, S. Colella, I. Deretzis, G. G. Condorelli, E. Smecca, G. Gigli, A. La Magna, A. Alberti, *J. Phys. Chem. C* **2015**, 150807063606009.

[126] V. L. P. Guerra, D. Altamura, V. Trifiletti, S. Colella, A. Listorti, R. Giannuzzi, G. Pellegrino, G. G. Condorelli, C. Giannini, G. Gigli, et al., *J. Mater. Chem. A* **2015**, 20811–20818.

[127] Y. Shirota, H. Kageyama, *Chem. Rev.* **2007**, *107*, 953–1010.

[128] H.-S. Kim, C.-R. Lee, J.-H. Im, K.-B. Lee, T. Moehl, A. Marchioro, S.-J. Moon, R. Humphry-Baker, J.-H. Yum, J. E. Moser, et al., *Sci. Rep.* **2012**, *2*, 591.

[129] J. Salbeck, N. Yu, J. Bauer, F. Weissörtel, H. Bestgen, *Synth. Met.* **1997**, *91*, 209–215.

[130] T. Leijtens, J. Lim, J. Teuscher, T. Park, H. J. Snaith, *Adv. Mater.* **2013**, *25*, 3227–3233.

[131] H. J. Snaith, M. Grätzel, *Appl. Phys. Lett.* **2006**, *89*, 2004–2007.

[132] A. Abate, T. Leijtens, S. Pathak, J. Teuscher, R. Avolio, M. E. Errico, J. Kirkpatrik, J. M. Ball, P. Docampo, I. McPherson, et al., *Phys. Chem. Chem. Phys.* **2013**, *15*, 2572–2579.

[133] U. Cappel, T. Daeneke, U. Bach, *Nano Lett.* **2012**, 18–21.

[134] W. H. Nguyen, C. D. Bailie, E. L. Unger, M. D. McGehee, *J. Am. Chem. Soc.* **2014**, *136*, 10996–11001.

[135] J. Burschka, A. Dualeh, F. Kessler, E. Baranoff, N.-L. Cevey-Ha, C. Yi, M. K. Nazeeruddin, M. Grätzel, *J. Am. Chem. Soc.* **2011**, *133*, 18042–5.

[136] N. J. Jeon, J. Lee, J. H. Noh, M. K. Nazeeruddin, M. Grätzel, S. Il Seok, *J. Am. Chem. Soc.* **2013**, *135*, 19087–19090.

[137] M.-C. Jung, S. R. Raga, L. K. Ono, Y. Qi, *Sci. Rep.* **2015**, *5*, 9863.

[138] H. Chen, X. Pan, W. Liu, M. Cai, D. Kou, Z. Huo, X. Fang, S. Dai, *Chem. Commun.* **2013**, *49*, 7277–9.

[139] P. Solar, Z. Li, S. a Kulkarni, P. P. Boix, E. Shi, A. Cao, K. Fu, S. K. Batabyal, *ACS Nano* **2014**, *8*, 6797–6804.

[140] S. N. Habisreutinger, T. Leijtens, G. E. Eperon, S. D. Stranks, R. J. Nicholas, H. J. Snaith, *Nano Lett.* **2014**, *14*, 5561–5568.

[141] S. N. Habisreutinger, T. Leijtens, G. E. Eperon, S. D. Stranks, R. J. Nicholas, H. J. Snaith, *J. Phys. Chem. Lett.* **2014**, *5*, 4207–4212.

[142] J. Lee, M. M. Menamparambath, J.-Y. Hwang, S. Baik, *ChemSusChem* **2015**, *8*, 2358–2362.

3. Design and synthesis of π -extended O-doped polycyclic aromatic hydrocarbons

In this chapter, the design, synthesis and photophysical properties of a novel series of *O*-doped polyaromatic hydrocarbons, in which two PAH substructures are bridged through one or two O atoms are described. The first part addresses the synthesis and characterization of oxygen-doped perylene-based systems presenting a rainbow of colors and tunable spectroscopic and electrochemical properties. The second part describes the synthetic strategy adopted for the preparation of a second family of *O*-doped nanoribbons bearing additional functionalization sites for anchoring different functional groups or moieties.

The chapter is divided into six main sections: *i) section 3.1* includes a general introduction on perylene-based functional chromophores; *ii) section 3.2* introduces the oxygen doped π-extended PAH; *iii) section 3.3* gives an overview on intramolecular C-O bond formation through transition metal-catalyzed reaction and acid-based cyclization; *iv) section 3.4* collects the results obtained with the design and synthesis of π-extended new scaffolds based on perylene systems and examines their photophysical properties; *v) section 3.5* deals with the design and synthesis of *O*-doped nanoribbons bearing additional functionalization sites and *vi) section 3.6* reports the synthesis and characterization of biperylene-compounds bearing different dihedral angles, highlighting the planarization effects on the optical properties of the system.

The X-ray analyses presented in this chapter were performed by *Nicola De*mitri (*Elettra – Sincrotrone Trieste*), the fluorescence lifetimes and fluorescence quantum yield measurements by *Dr. Giacomo Bergamini,* from *Prof. Paola Ceroni's* group (*Università di Bologna*) and the preliminary DFT calculations by *Giuseppe Brancato* (*Scuola Normale Superiore di Pisa*). Furthermore, *Francesca Vita* from University of Trieste is kindly acknowledged for SEM imaging.

3.1 General introduction on perylene-based functional chromophores

3.1.1. Polycyclic aromatic hydrocarbons (PAH)

The design and synthesis of low band gap polycyclic aromatic compounds are of great interest owing to their potential applications as semiconductors in organic field effect transistors (OFETs),[1] as light-harvesting dyes in organic solar cells,[2] as near infrared (NIR) fluorescent probes in high resolution bio-imaging and bio-sensing, and as chromophores in non-linear optics.[3–5] PAH is a common name connected to aromatic hydrocarbons in which more than two unsubstituted fused benzene rings are present. They are precursors of extended carbon networks and their carbon skeletons can be viewed as small pieces of graphene. Accordingly, large PAHs having size of 1-5 nm are defined by the term graphene molecule, while nanographene can be termed a graphene fragment ranging from 1-100 nm in size. For sizes over 100 nm, they can be directly regarded as graphene (Figure 3.1.1).[6,7] The benzenoid PAHs can be seen as model compounds to understand the fundamental structure-property relationship of graphene. Such material can be thought as highly conductive polymer and its smaller sections, depending on the size and arrangement of the fused hydrocarbon, can have a range of properties from conducting to insulating.[3,6,8]

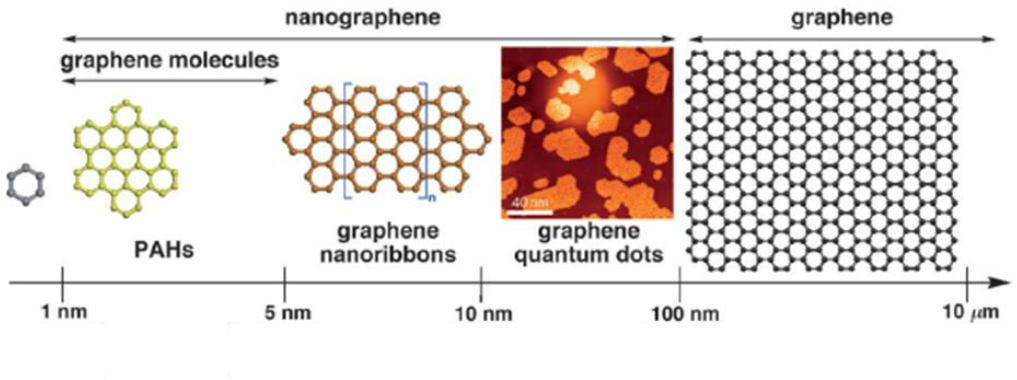

Figure 3.1.1. Schematic representation of graphene terminology defined according to their size scale.[6]

Nano-sized graphene fragments can be prepared by two distinct strategies, namely the "bottom up" and "the top down" methods (Figure 3.1.2). Top-down approaches typically include hydrothermal[9] or lithiographic[10] cutting of graphene without a control over the size distribution, shape and edges structure of the resulting nanographenes. On the other hand, "bottom up" chemical synthesis provides access to monodisperse nanographenes with control over their chemical and physical structures, with the advantage of reproducibility.[11]

In this context, the atomically precise synthesis of nanographene has been extensively explored.[6]

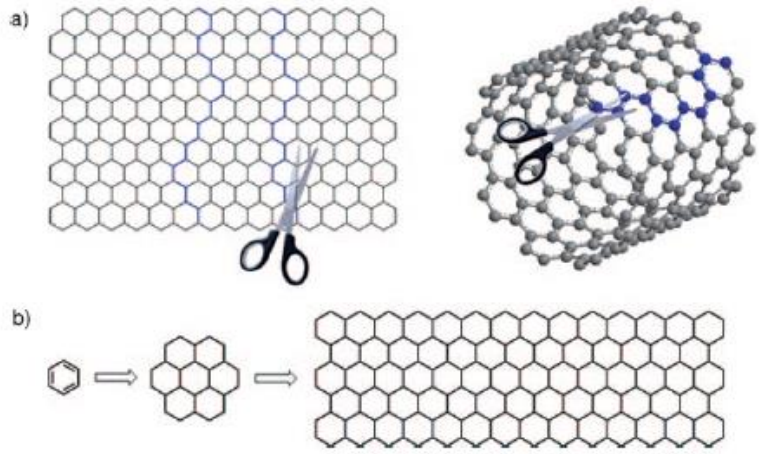

Figure 3.1.2. Schematic representation of the a) top-down and b) bottom-up fabrication of GNRs.[12]

The chemical syntheses of polycyclic aromatic hydrocarbons (PAHs) were pioneered by *Scholl*[13] and *Clar*[14] in the first half of the 20th century. They achieved the preparation of numerous polyaromatics under drastic conditions at high temperatures in strongly oxidizing reactions melt. Later on, the progress of modern synthetic methods and analytical techniques has allowed the efficient synthesis of a wide variety of π-extended PAHs under milder condition.[15–17] In particular, the high efficient synthesis of hexa-*peri*-haxabenzocoronene (Figure 3.1.3) accomplished by planarization of hexaphenylbenzene **3-31** *via* intramolecular cyclodehydrogenation reaction developed by *Müllen***,** paved the way for the preparation of a large variety of well-defined PAH by employing tailor-made oligophenylenes as percursors.[4] Similarly to graphene, unsubstituted graphene molecules are only barely soluble in common organic solvents and despite the appeal of accessing increasingly large structurally well-defined models of graphene, the planarization of large oligophenylene precursors reaches its limits in solution.

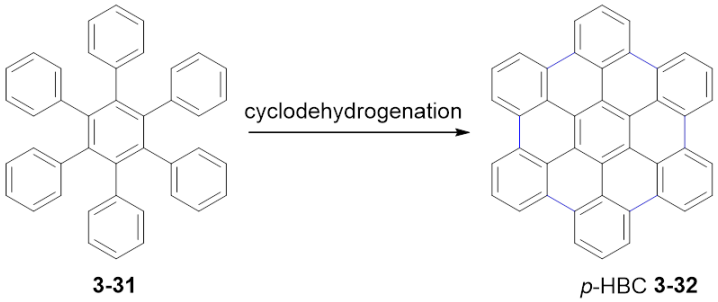

Figure 3.1.3. Synthesis of hexa-*peri*-hexabenzocoronene (*p*-HBC **3-32**) through intramolecular oxidative cyclodehydrogenation

If we then exam a graphene sheet (Figure 3.1.4), different molecular subunits could be readily picked out. Thus, 1-D oligophenylene **3-34**, all-benzenoid PAH such as **3-32**, and perylene **3-33** can be thought as molecular subunits of graphite,[18] and since graphite is a conductor and strongly absorbs light, those molecular subunits often possess exploitable properties for optoelectronic[19] and dyestuff chemistry.[15]

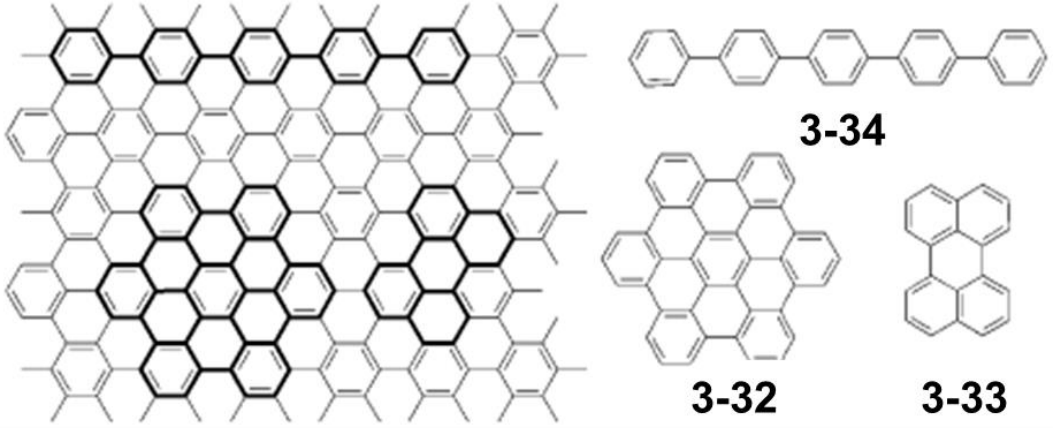

Figure 3.1.4. Polyphenylens and rylenes structures as subunit of graphite.[18]

In this work, we will focus our attention on a particular type of graphene nanoribbon, the polyrylenes, also called poly-*peri* naphthalene. This low band gap PAHs with both armchair and zigzag edges represent PAHs with two or more naphthalene units fused in the *peri* position. Smaller sections of this polymer are called oligorylens, according to their nomenclature that was introduced by *Clar*.[20] On the basis of the number of fused naphthalenes, they can be termed perylene, terrylene, quaterrylene and so on (figure 3.1.5). Perylene dyes are key chromophores in dye chemistry. In fact, this is a class of extensively studied materials that have received a great deal of attention due their exceptional optical properties (high extinction coefficients and long-wavelength absorption/emission) and outstanding chemical, thermal, photochemical and photophysical stability.[21] Within the field of oligorylenes, rylene imides (Figure 3.1.5 b) were largely explored in dye chemistry, supramlecular assemblies,[22–24] optoelectronic applications and photovoltaics.[25–27]

.

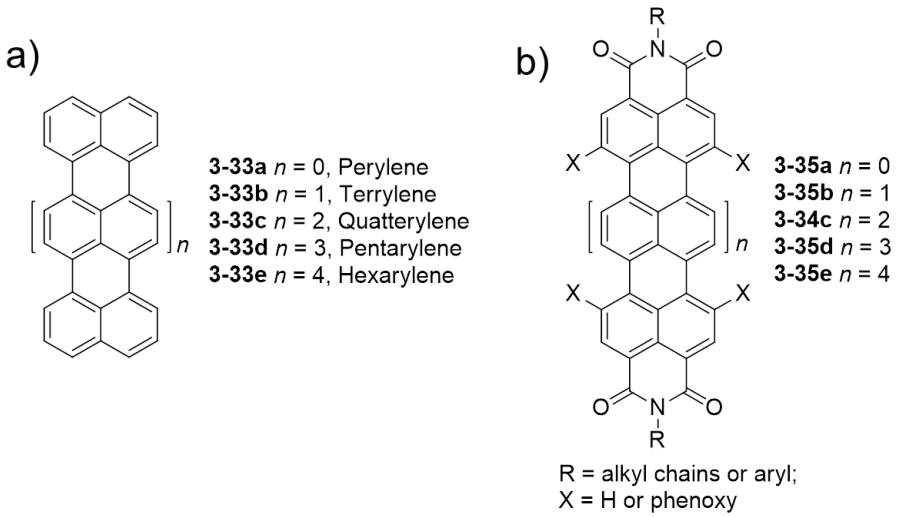

Figure 3.1.5 General structures of (a) rylenes and (b) rylene bisimides.

3.1.2 Perylene and oligorylenes

Perylene is a polycyclic aromatic molecule constituted of five rings and can be naturally found in coal tar. It has been synthesized for the first time in laboratory in 1910 by *Scholl* and co-workers, by oxidative coupling of two naphthalene units in *peri*-positions with anhydrous $AlCl_3$. Indeed, this condensation of aromatic rings has been named after its inventor as the "Scholl reaction".[19,28] Perylene can be considered as two fused naphthalene units that have partial connection of their π-systems, making the π-electrons not fully delocalized over the entire molecular skeleton. Perylene, with its 20 π-electrons would be classified as antiaromatic considering the *Hückel* rule, but from its reactivity (undergoes electrophilic aromatic substitutions) and ^{1}H NMR spectroscopy (proton signals in the aromatic region around 7-8 ppm), can be clearly gathered that perylene is aromatic.[29] Similar to polymers, the perylene core could be elongated to poly(*peri*naphthalenes), which represent the so-called rylene dyes. Accordingly, perylene can be viewed as the smallest but most important homolog of this class of compounds. It is characterized by a relative small HOMO-LUMO gap[30] when compared to hydrocarbons of similar molecular weight, and undergoes reversible reduction and oxidation ($E_{1/2}$ = -2.139 for reduction and 0.609 eV for oxidation), resulting as an electron donor.[29]

Perylene has a characteristic strong absorption in the UV-Vis region with a molar absorptivity of ε = 38 500 M^{-1} cm^{-1} at 434 nm. Moreover, it presents small Stokes shift and high fluorescence quantum yield (ϕ_{fl} = 0.98). Those optical properties make perylene one of the most attractive precursors for pigments, dyes and organic photovoltaic applications.[29]

The perylene core presents twelve positions that can be functionalized, known as *peri*- (3,4,9,10 positions), *bay*- (1, 6, 7, 12) and *ortho*- (2, 5, 8, 11) positions (figure 3.1.6).

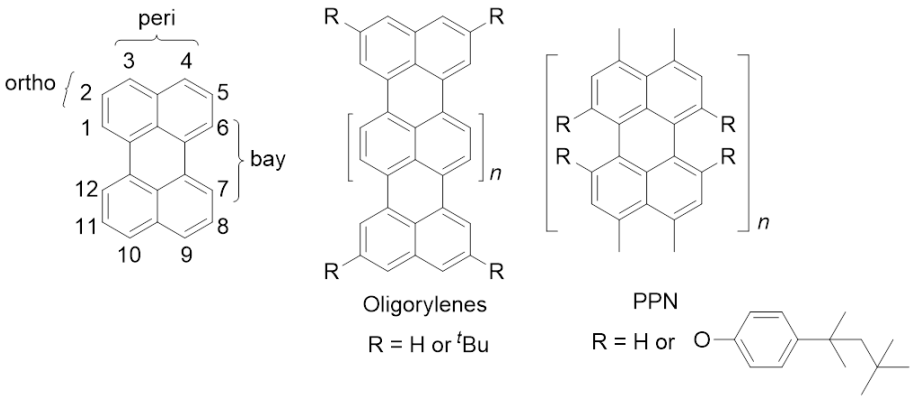

Figure 3.1.6. Chemical structures of unsubstituted perylene, oligorylene and poly(*peri*-naphthalene) PPN.

Extending the aromatic π-surface of perylene in *peri* positions two new classes of compounds have been reported, olygorylenes and poly(peri-naphthalene) PPN polymers (Figure 3.1.6). Theoretical works predicted a very small HOMO-LUMO gap for poly(*peri*-naphthalene) (PPN) polymers, thus making this class of molecules suitable as electrical conductors. This behavior can be attributed to the nature of the ladder-type conjugates structure that leads to a more rigid skeleton than those of other electro-active conjugated polymers such as poly(*p*-phenylenevinylene) (PPV) or poly(p-phenylene) PPP.[31] Indeed, the band gap decreases increasing the chain length from 2.8 eV for unsubstituted perylene to a theoretical optical bandgap of 0.93-0.98 eV for the polymer PPN.

From a synthetic point of view, it is very challenging to prepare higher order rylenes especially because of their expected insolubility that can be attributed to the rigidity of the backbone. The introduction of solubilizing groups permits the preparation and characterization of more soluble materials. Quatterylene compound ($n = 4$, figure 3.1.6), was first described by *Clar*[20] in 1948, and the preparation of its soluble *tert*-butyl derivative was reported by *Müllen* and co-workers in 1990.[32] The best current synthetic routes still follow classic Scholl conditions that are suitable only for small scale production. Those long-chain rylenes possess outstanding electronic properties, a distinct bathochromic shift in the longest wavelength absorption is reached increasing *n* (naphthalene unit), making them extremely interesting because their emission colors can be tuned from blue to near-infrared by extending the chain length. Indeed, the most π-extended synthesized *tert*-butyl pentarylene ($n = 5$, Figure 3.1.6) absorbs in the near infrared region, but due to the scarce solubility the

determination of its molar extinction coefficient was limited. Usually, higher order rylenes are characterized by low fluorescence quantum yields, contrary to the parent perylene (*n* = 0; Figure 3.1.6) and terrylene (*n* = 1) which present high quantum yields of 0.94 and 0.74, respectively. In the case of quatterylene (*n* = 1) there is a crossover to a dipole-forbidden transition between the ground and the lowest excited states, causing the fluorescence to be very small (ϕ_{fl} = 0.05).[33,34] This is a serious problem in the design of efficient luminescent red and infrared materials. Moreover, to date, hexarylene and the higher order homologues continue to be elusive targets for chemists due to the lack of suitable building blocks, effective synthetic protocols for the long-range π-extension and due to their unprocessability caused by their very poor solubility.[32]

Some substantial examples of more soluble higher order polyrylens are reported in literature and illustrated in Figure 3.1.7. Polymer **3-36** presents solubilizing octylphenoxy groups throughout the backbone that are responsible for the twisting of the molecule and inhibition of strong π- π interactions. *Wang* and co-workers developed a new efficient synthetic method toward processable bis-N-annulated quaterrylene **3-37a** exploiting an oxidative coupling and ring closure reaction in presence of DDQ and $Sc(OTf)_3$ from easily available N-annulated perylene derivatives.[35–37] The introduction of pyrrole ring into the poly(*peri*-naphthalene) backbone results in a bathochromic shifted absorption band (13 nm, λ_{abs} = 673 nm) in comparison with *tert*-butyl quatterylene, and in an increased fluorescence quantum yield ($\phi_{fl.}$ = 0.26).[36] Subsequently, the same synthetic approach was successfully extended to the synthesis of hexarylene derivative **3-37b** The authors reported a maximum absorption band around 840 nm in THF at r.t for this molecule.[35] In this way, *Wang* and co-workers were able to prepare for the first time tri-N-annulated hexarylenes containing three space demanding, branched alkyl chains and different end-cap pending groups to guarantee their good processability. This approach represents a new way toward the rational synthesis of N-doped graphene nanoribbons with well-defined edges.[34,35]

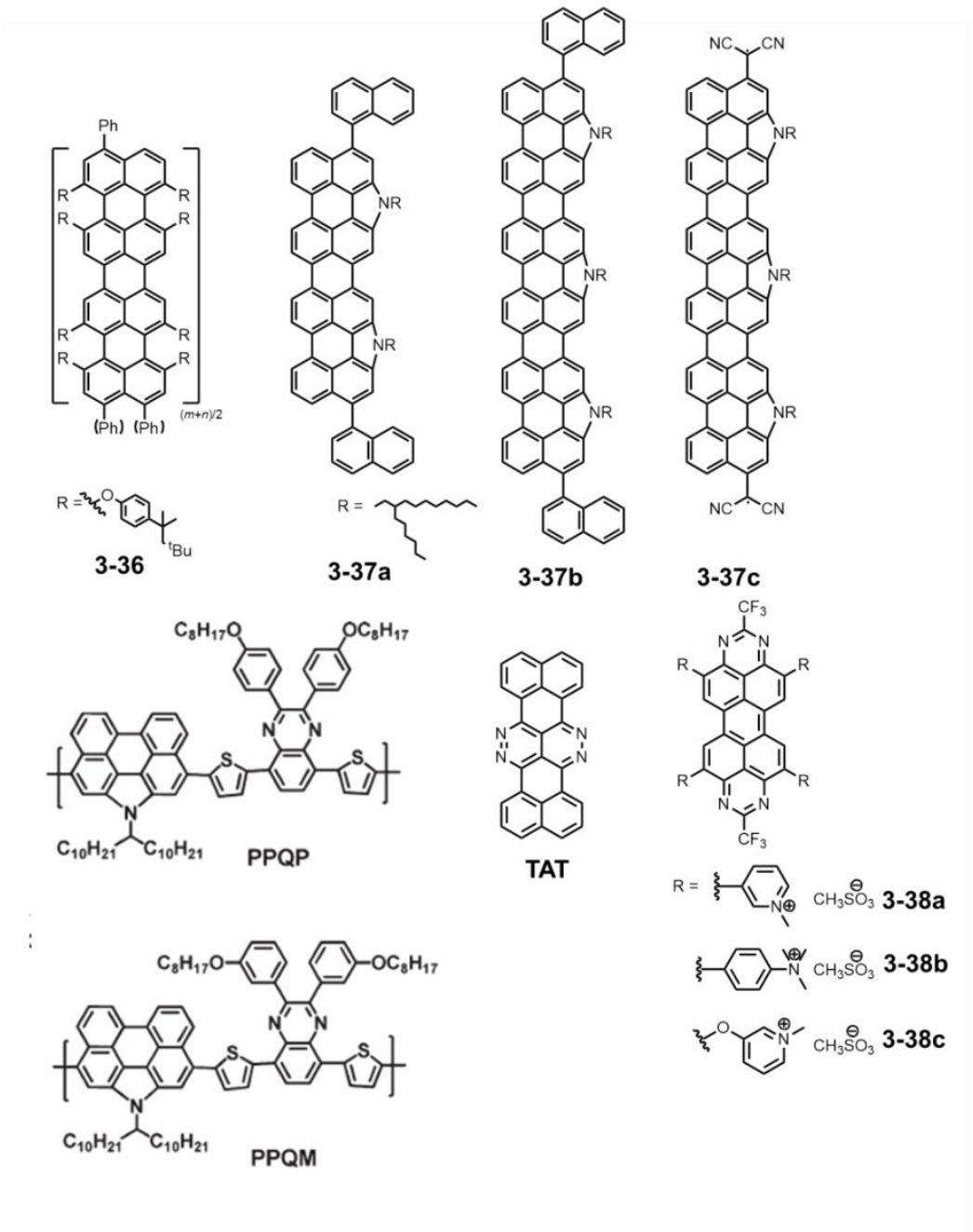

Figure 3.1.7. Chemical structures of higher order rylene compounds and other peryleno-based chromophores.[29]

Further progress in the synthesis of N-doped extended rylenes has been achieved with the preparation of stable tetracyano-oligo(N-annulated perylene)quinodimethanes (*i.e.* **3-37c**). Such molecules with tunable ground states are promising candidates for nonlinear optics and ambipolar field effect transistors.[38] Some examples of perylene-based material that have found practical application are depicted in Figure 3.1.7 and described below.

Wise et al. explored the possibility to use small-molecule acceptor, as the tetra-aza-terrylene (TAT). Single-crystals can be grown oriented along the c-axis crystallographic direction,

and over-coated with pentacene to form a highly ordered donor/acceptor interface in organic photovoltaic devices.[39] Facile synthesized pyrroloperylene moiety was incorporated in push-pull polymers (PPQP, PPQM) for organic solar cells applications as well.[40] While, highly emissive water soluble perylene derivatives **3-38** (a-c) were synthesized and used as fluorescent markers to study biological systems. This class of compounds displayed remarkable absorption and emission properties with fluorescence quantum yields up to 82% in water.[41]

However, most of the applications of perylenes, rylenes and azarylenes have been realized in homologue *peri*-imide systems (Figure 3.1.8). The chemistry of rylene imides starts with perylene diimide (PDI), first prepared in 1913.[42] PDIs are very attractive building blocks for multichromophore systems because they are not only excellent colorants and present high fluorescence quantum yields, but possess outstanding chemical, thermal, photochemical and photo-physical stability. They persist against molten KOH at 220 °C, concentrated H_2SO_4 at 220 °C and concentrated bleach, and have a thermal stability up to 550 °C.[43] Moreover, this class of rylene dyes exhibit electron transport behavior and present the ability to finely tune their electronic properties through chemical modification. As already discussed the major drawback of higher order rylenes is their poor solubility and processability that usually comes with the extension of the aromatic scaffold. However, the large π-conjugated systems of rylene dyes provide a versatile synthetic basis for further functionalization. The type of the substituents as well as the position of functionalization (at the *peri* and at the *bay* positions - Figure 3.1.8) of rylene core has a strong influence on the resulting solubility as well as the optical properties, such as band gap energies, absorption wavelengths, and the spatial properties of the molecular orbitals.[18,27,43]

The aromatic scaffold can be extended along the molecular axis as well as along the equatorial axis, resulting in a bathochromic shift of the absorption and emission properties. With those modifications, the rylene series can cover the broad region of visible (400–760) and NIR (760–1200 nm) absorption.

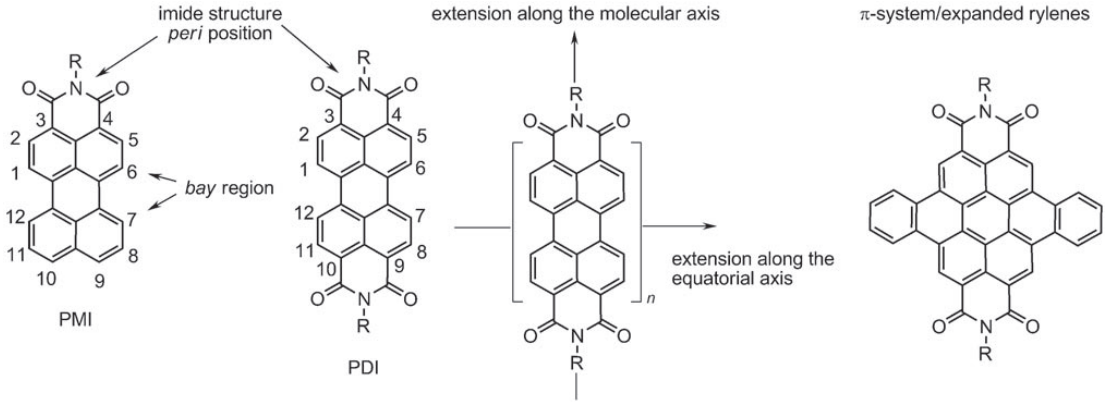

Figure 3.1.8. Chemical structures of unsubstituted peryleneimide chromophores: Perylene-3,4-dicarboximide (PMI) and perylenebis(dicarboximide) (PDI), illustration of the bay, peri positions, as well as the concept of achieving higher order rylenes by elongation of the aromatic scaffold.[27]

One descriptive example has been described by *Müllen* and co-workers through the synthesis of a series of rylene dyes going from perylenebis(dicarboximide) to hexarylene-bis(dicarboximide) as shown in Figure 3.1.9.[21] They reported a bathochromic shift of ca.100 nm per each additional naphthalene unit going up to 950 nm for the more extended hexarylenebis(dicarboximides) HDI. As a result of the extension of the aromatic π system along the molecular axis, the molar absorptivities are also increased, with a maximum of ε = 293 000 M^{-1} cm^{-1} for the hexarylenediimide HDI (Figure 3.1.9).

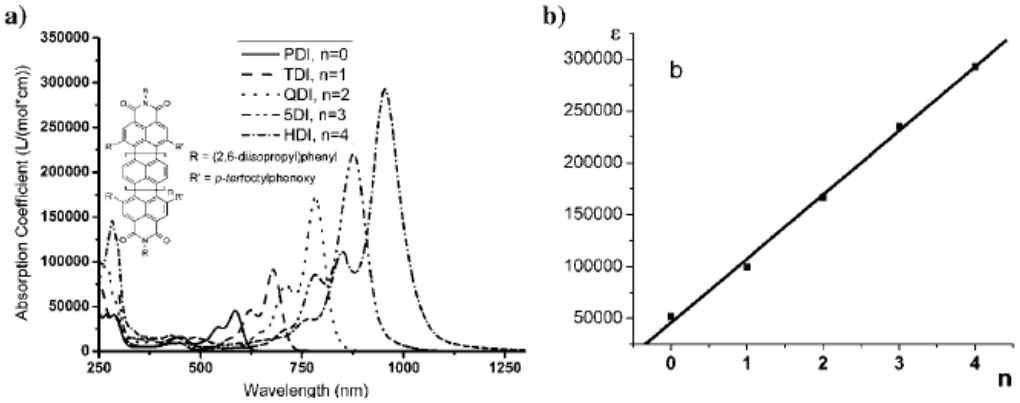

Figure 3.1.9 (a) absorption specra of rylene diimides and (b) dependence between the numbers of naphthalene units.[43]

In this way, the chemical modification of rylene diimides offers access to a large portfolio of tailored functional rylene chromophores, which can be functionalized for the desired application. Indeed, functionalized rylene derivatives were explored for demanding applications such as optoelectronic [44] and photovoltaic[26,45,46] devices, energy-transfer cascades,[47] light-emitting diodes,[48] near-infrared-absorbing systems[49] and single-molecule investigations of energy and electron-transfer processes. [18]

3.2 Oxygen-doped PAH

Replacing the carbon atoms with other heteroatoms at defined positions,[8] is also emerging as a versatile functionalization strategy to control the chemical, charge-carrier and self-assembly behaviors of PAHs.[50] Accordingly, graphene molecules with a precise doping pattern can be prepared with the use of heteroatom-bearing monomeric precursors through bottom-up covalent synthesis following protocols in solution[51] and on surfaces.[52] To the best of our knowledges, up to now there are no reports on precise oxygen-doping of π-extended conjugated systems, while precise doping with nitrogen atoms has been achieved.[8] In this regard, organic semiconductor *peri*-xanthenoxanthene (PXX) **3-8^{Pp}** (Figure 3.2.1 a), can be viewed as the first member of a potential family of O-doped aromatic hydrocarbons. This oxygen doped equivalent of anthanthrene is characterized by excellent carrier transport and injection properties, good processability, chemical and high-thermal stability and has shown exceptional performance as active organic semiconductor (OSC) in transistors for rollable OLEDs (Figure 3.2.1 b).[53] The outstanding properties of PXX derivatives [54,55] are achieved thanks to the large π-conjugated system which is expected to enhance the overlap of molecular orbitals and to the introduction of heteroatoms (oxygen) into the π-system that stabilizes the reactive sites against oxidation improving its environmental stability.

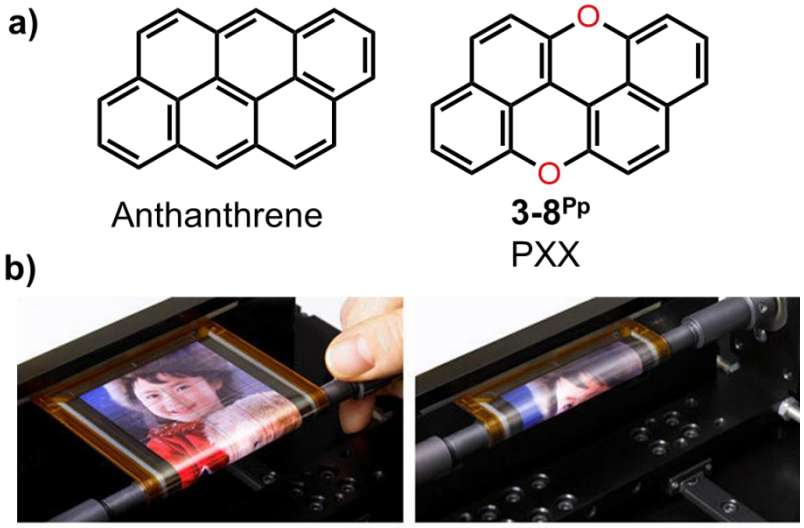

Figure 3.2.1. (a) Molecular Structures of and PXX of hexacyclic PAH Anthanthrene and *O*-doped analogue PXX and (b) photo of rollable OTFT-driven OLED display wrapped around a Pencil, based on PXX derivative.[1]

[1] Photo taken from http://www.sony.net/SonyInfo/News/Press/201005/10-070E/

Nevertheless, so far the elongation of PXX into larger O-doped frameworks has been not explored. Understanding and controlling the O-doping ratio could provide the conceptual basis to design new families of organic semiconductors with tunable optoelectronic properties.[56] In this regard, our group made a great progress in the development of oxygen-doped π-extended PXX systems (Figure 3.2.2). *Stassen et al.*[57,58] reported the synthesis of O-doped benzorylenes, presenting armchair-type edges, like pentaphenopentaphene (**3-40**) and napthotetraphenopyranthrene (**3-41**). X-ray diffraction revealed that derivative **3-41** undergoes strong π-stacking at the solid state forming lamellar-like microstructures. The tendency of this class of molecules to form well-defined architectures make them ideal prospective candidates for the use in optoelectronic devices.[56,59]

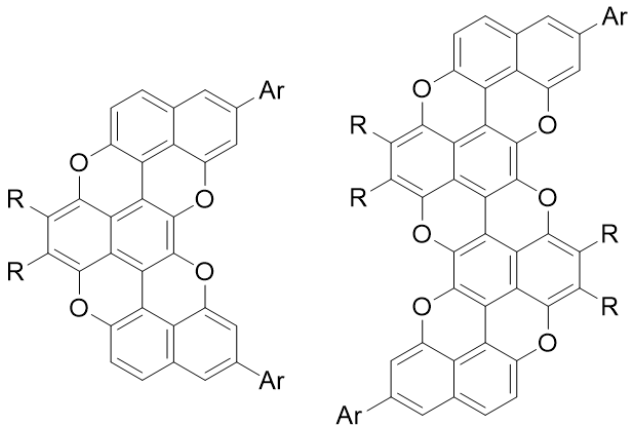

Figure 3.2.2 Heteroatom-doped benzorylenes developed by our group.[59]

From the other hand, polycyclic aromatic compounds containing furan moieties are expected to provide relatively high HOMO levels and offer utility in electronic devices, such as OLED,[60] OFETs[61] and organic photovoltaics.[62] Only few reports that describe the synthesis of structurally well-defined oligonaphtofuranes with controlled doping pattern are described in literature. *Tsubaki et al* have reported a pivotal example of oxygen-containing oligoaromatic compounds with tunable opto-electronic properties. They described the synthesis of a series of fan-shaped oligonaphthofurans with narrowed dihedral angles composed of alternating naphthalene and furan rings using a bottom up approach. The largest molecule that has been prepared contains eight naphthalene and seven furan units (Figure 3.2.3 a). The maximum absorbance and emission wavelengths were steadily red-shifted as the number of aromatic rings of the oligonaphthofurane was increased.[63] In parallel, the

same authors reported the synthesis and properties of butterfly-shaped expanded naphthofuran derivatives, analyzing the effect of the dihedral angle on the optical properties of the system (Figure 3.2.3 b).[64] Photophysical measurements showed that the molecules feature high emission yield and tunable absorption UV-Vis properties.

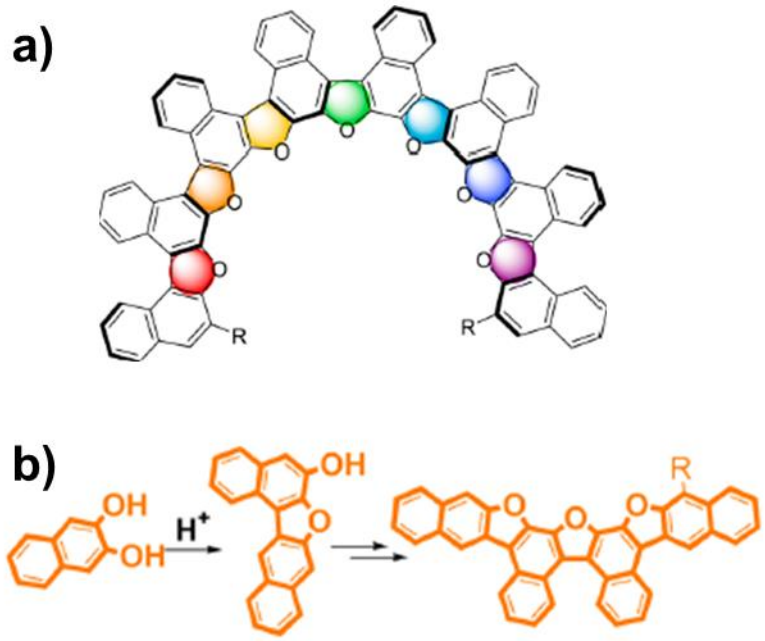

Figure 3.2.3. Oligonaphthofuran structures reported by Nakanishi *et al*.(a) fan-shaped oligonaphthofurans (up to 8 naphthalene units) and (b) butterfly-shaped expanded dinaphthofuranes (DNF).

3.3 General account on intramolecular C-O bond formation

Aryl ethers and oxygen heterocycles are common structures in many pharmaceutically and agriculturally important compounds,[65–69] as well as in materials and catalytic science.[70] Traditional methods for the preparation of these compounds include the Williamson ether synthesis,[71] direct nucleophilic substitution reactions,[72] transition metal mediated Buchwald-Hartwig reaction and Ullman-type couplings of alkoxides with aryl halides.[73]

3.3.1 Five membered ring intramolecular C-O bond formation

Among the numberless C-O bond formation reaction provided by organic synthesis, we focused our attention on the formation of intramolecular diaryl ether linkage. Several approaches were considered for this type of reaction among which cross-coupling reaction between an aryl halide with an organometallic reagent are commonly the most reported.[74–76] Recently, the direct cyclization of tethered heteroatoms onto adjacent C-H bonds emerged as an attractive and efficient method for ring forming reactions (scheme 3.3.1).[77] This

approach treats the C-H bond as functional group (in analogy to a carbon-metal or carbon-halogen bond), thus the use of pre-functionalized substrates is not needed.

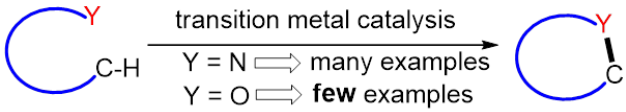

Scheme 3.3.1 General strategy for transition-metal-catalyzed etherification of unactivated C-H bonds.[77,78]

While the intramolecular C-H activation/C-N cyclization reaction for the synthesis of azaheterocycles has been largely studied and reported,[79–82] much less achievements have been addressed to the preparation of oxaheterocycles *via* the same protocol.[78] The following section gets in detail on the different studies reporting synthetic methodologies involving the intramolecular alkoxylation reaction for the formation of benzofuran rings.

In 2010, *Yu et al*. described the first example of a dihydrobenzofuran synthesis that involves a tertiary aliphatic alcohol-directed cycloetherification process that is catalyzed by $Pd(OAc)_2$ and $PhI(OAc)_2$ as the oxidant (scheme 3.3.2).[83] This Palladium-catalyzed etherification of $C(sp^2)$-H bonds could be extended to compounds containing a variety of different functional groups, including electro-donating and electron-withdrawing groups. Remarkably, this reaction could also be applied for the synthesis of natural products and drug molecules containing spirocyclic dihydrobenzofurans,

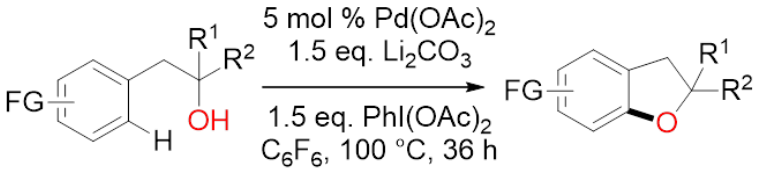

Scheme 3.3.2. Pd-catalysed C-H activation/C-O cyclization reported by Yu.[83]

Interestingly in 2011, *Liu* and co-workers reported a phenol-directed C-H activation/C-O cyclization for the synthesis of dibenzofurans via a Pd(0)/Pd(II) catalytic cycle using air as the oxidant (scheme 3.3.3).[77]

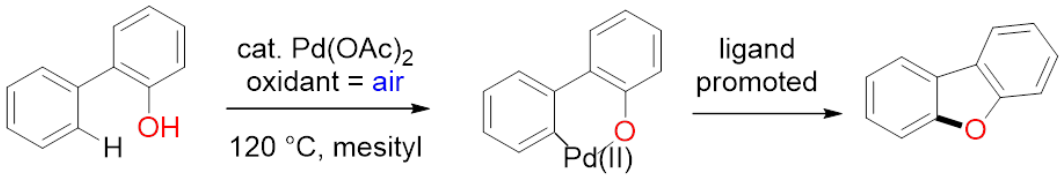

Scheme 3.3.3. Phenol-directed cyclization through a Pd(II)/Pd(0) cycle.[77]

The authors describe that the C-O bond formation reaction was significantly improved by the addition of sodium pivalate. The latter seems to act as an anionic ligand that, coordinated to Pd(II), promotes C-H activation by acting as proton shuttle. Moreover, heating the reaction at higher temperatures increased significantly the reaction yields (Figure 3.3.1), suggesting the C-O reductive elimination as the turnover-limiting step instead of the C-H activation. Different ligands and additives were used to improve the reductive elimination step and 4,5-diazafluoren-9-one ligand results to be a suitable candidate to help the aerobic oxidation of Pd(0) to regenerate Pd(II). This approach to functionalized ethers could be extended to a large variety of differently substituted dibenzofurans. The use of air as oxidant is very appealing from economic and environmental points of views, and the high tolerance towards functional groups makes this methodology highly attractive.

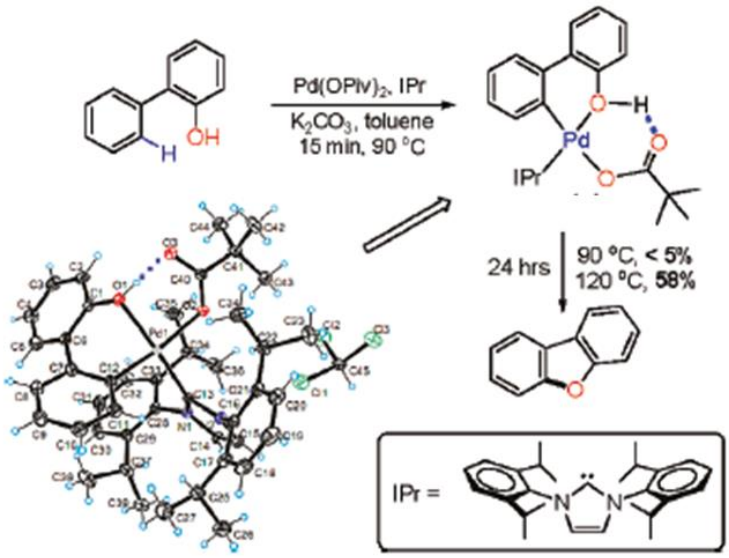

Figure 3.3.1. Phenol-directed cyclization through a Pd(II)/Pd(0) cycle for formation of four coordinate Pd(II) complex.[77]

Shortly after, *Yoshikai* and co-workers, described a similar transformation, under palladium catalysis, in the presence of 3-nitropyridine as ligand and *tert*-butyl peroxybenzoateas as oxidant (scheme 3.3.4). In this case, kinetic isotope effect experiments indicated that the C-H bond cleavage is the rate-limiting step of the reaction. Thus, the authors proposed that the

reaction most likely proceed through a Pd(II)/Pd(IV) catalytic cycle.[84] The use of a quite simple catalytic system allows the synthesis of a wide range of dibenzofuran derivatives.

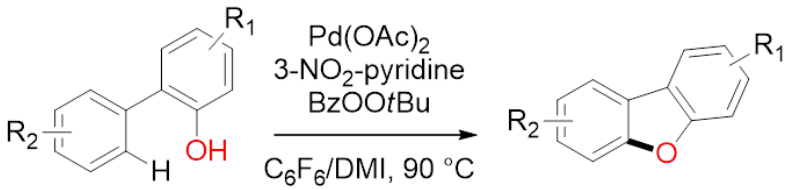

Scheme 3.3.4. Palladium catalysedC-H activation/C-O cyclization reported by *Yoshikai* and co-workers.[84]

More recently, *Zhu et al.* reported the use of inexpensive copper catalysis for the preparation of similar molecular systems.[85,86] Copper-catalyzed etherification of unactivated C-H bonds was achieved in the presence of additives, like PivOH under open air conditions (scheme 3.3.5). Lower reaction efficiency was recorded when the process is performed under argon, supporting the key role of O_2. Preliminary studies revealed that an irreversible, rate-limiting concerted-metalation-deprotonation (CMD) process is most likely involved in this reaction. Although an electron-withdrawing group at the para-position relative to the phenolic OH is required to prevent direct oxidation of the substrate, the methodology relies on a simple reaction system and inexpensive Cu salts. This synthetic methodology not only serves as an alternative approach for the synthesis of dibenzofurans but also broadens the application of Cu-catalyzed C-H activation/C-O cyclization reactions in the preparation of oxygen-containing heterocycles.

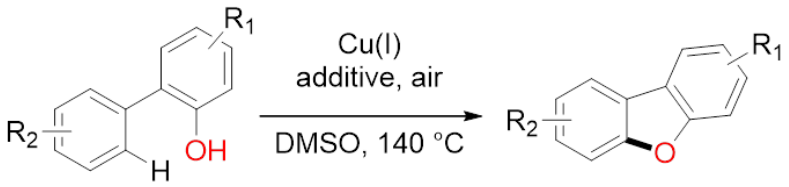

Scheme 3.3.5 Approach toward dibenzofurans developed by *Zhu et al.* (R1 = electron-withdrawing groups such as
NO_2, CN, CHO).[85]

From the other hand, over the last years the acid-catalyzed ether bond-formation has re-emerged as very versatile and clean synthetic route for the preparation of diarylfuran frameworks.[63,64] The transformation of dihydroxy biaryl to corresponding diarylfurans, using various acid catalysts, protic or Lewis acid has been studied for a long time.[57,58] Herein, we report the most exploited synthetic methodologies.

In 1991, *Yamato et al.* report an efficient procedure for the ring closure of 2,2'-dihydroxybiphenyls in the presence of the solid superacid, Nafion-H (a solid perfluorinated

resinsulfonic acid) to afford dibenzofuran derivatives in good to moderate yields (scheme 3.3.6).[87]

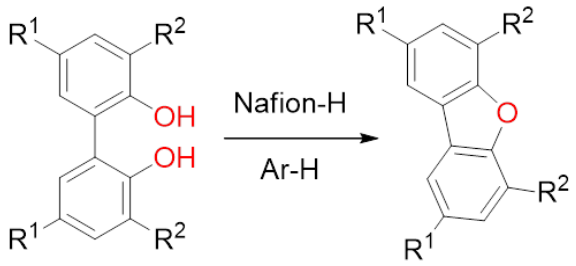

Scheme 3.3.6. Synthesis of dibenzofuran compounds described by *Yamato et al.*

Afterwards, in 2004, *Kotani* and co-workers developed a simple method for the ring closure of 2, 2'-binaphthol to the dinaphthofurane framework in the presence of $SnCl_4$ as Lewis acid.[88] Moreover, ring closure reaction on functionalized binaphthol derivatives has been accomplished in satisfactory yields by the treatment with concentrated sulfuric acid[89] and zeolite catalysts in *o*-dichlorobenzene at high temperature.[90,91]

Similarly, *Areephong et al.* reported a practical procedure for the preparation of functionalized 7-oxa-[5]-helicenes from 2,7-dihydroxynaphthalene in the presence of *p*-TsOH acid in toluene under reflux in good to high yields.[92] The authors reported that the cyclization step occurs *via* an intramolecular nucleophilic addition through the formation of a cyclic hemiacetal, which upon dehydration yields desired naphthofuran (scheme 3.3.7). This straightforward synthetic approach was then exploited for the preparation of numerous naphthofuran derivatives including the fan-shaped oligonaphthofuranes described by *Nakanishi.* [63]

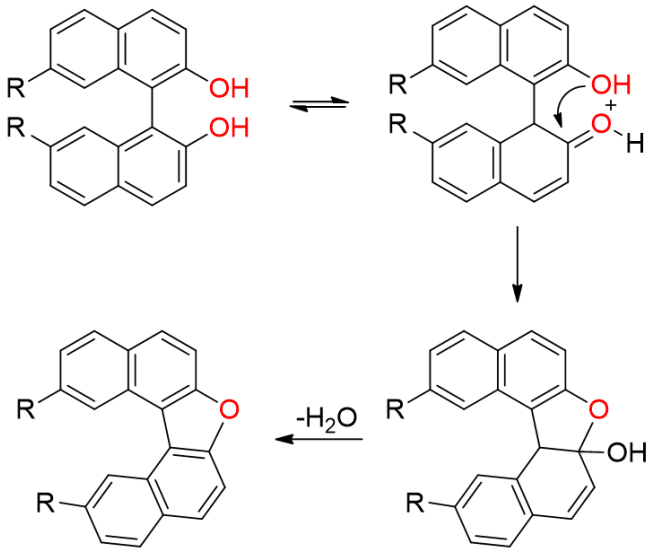

Scheme 3.3.7. Proposed mechanism for the cyclization reaction in presence of *p*-TsOH.[92]

3.3.2. Six membered ring intramolecular C-O bond formation

One of the most relevant examples of oxygen-containing compounds bearing a pyranyl motif is *peri*-xanthenoxanthene (PXX) **3-8^{Pp}**. This molecule has been known since the beginning of the last century[93] and used as pigments[94] and in charge transfer complexes.[95] Only lately, PXX and its derivatives have been investigated by *Merck* and *Sony* as organic semiconductors due to their outstanding carrier transport capacity, chemical inertness and high-thermal stability.[54,96]

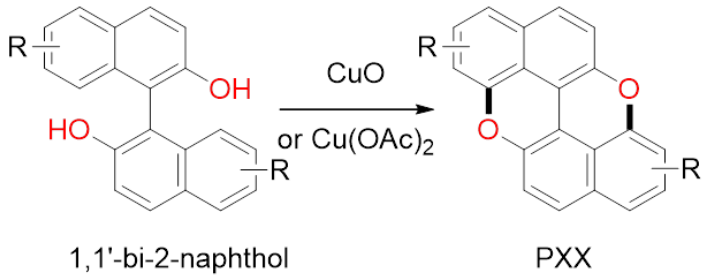

Scheme 3.3.8. General representation of PXX synthesis.

PXX was synthesized for the first time in 1905[97] by *Bünzly* and *Decker* through oxidation of binaphthols with potassium ferrocyanide, affording PXX together with unidentified oxidized by-products.[59] After that, different synthetic protocols describing the use of $Cu(OAc)_2$[95,98] or transition metals oxides *i.e.* MnO_2 or CuO[93,99] under air at elevated temperatures were reported (scheme 3.3.8). In 2007, *Wetherby* and co-workers proposed an alternative approach to prepare substituted derivatives of PXX starting from 3,3'-disubstituted-1,1'-bi-2-naphthols with a stoichiometric amount of mercury(II) amide complex $Hg[N(SiMe_3)_2]_2$.[100] The authors reported that the mechanism of this reaction proceeds *via* an intramolecular electrophilic aromatic substitution. In parallel, a synthetic approach exploiting electrochemistry for preparation of thiophene PXX-doped copolymers was described.[101] Recently, *Cui* and co-workers described the preparation of three types of alkylated PXX *via* microwave assisted cyclization reaction in the presence of $Cu(OAc)_2$ in *o*-dichlorobenzene at 190 °C.[96] However, the synthetic methodologies above reported present limited applications and are not easily extended to others organic compounds due to the drastic conditions (high temperatures) and generally low yields. Therefore, there is the need to develop new synthetic methodology for the preparation of six-membered ether rings in an intramolecular fashion, by employing generally milder reaction conditions.

In this respect, the reaction conditions for the preparation of PXX derivatives were investigated and optimized by our group.[59] Starting from the protocol reported by *Pummerer* with CuO,[93] binaphthol was transformed into PXX in 42% yield, while the use of CuOAc and other transition metals such as $Pd(OAc)_2$, $NiCl_2$, etc. gave low yields or no conversion.[59] Interestingly, when the most recent C-H activation methodology described by *Zhu et al.*[85,86] for five membered ring formation with the use of inexpensive copper in the presence of PivOH was applied, the yield was exceptionally improved to 94%.[59] This reaction results to be very appealing because it does not require an inert atmosphere (can be carried out under open air condition) and neither long reaction times (between 15 min and 1 h). Based on this achievements, *Stassen et al.* reported the synthesis of unprecedented O-doped benzorylenes using CuI in the presence of PivOH in DMSO (scheme 3.3.9).[56]

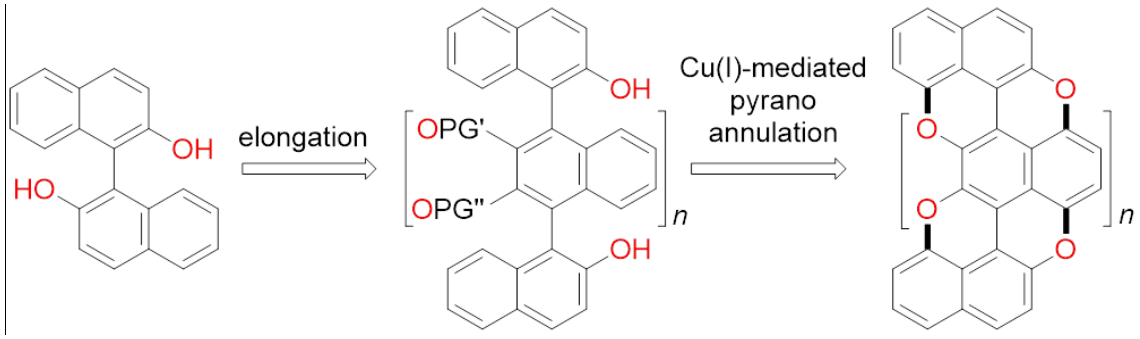

Scheme 3.3.7 Synthetic strategy toward the O-doped benzorylenes.[59]

One of the aim of this dissertation is to apply such optimized conditions for the synthesis of future oxygen-containing π-extended PAH, in which, based on the different reaction conditions either furanyl and pyranyl ring will be formed.

3.4 Synthesis, band-gap tuning, optical investigation of new emissive O-doped π-conjugated scaffoldings

3.4.1 Aim of the project

In this dissertation, the author intends to apply the intramolecular metal- or acid-catalyzed C-O bond formation as key reaction for the synthesis of novel oxygen containing π-extended PAH using perylene as staring building block.

Inspired by the outstanding properties of PXX and driven by the recent achievements in the synthesis of O-doped benzorylenes we decided to design a novel class of O-doped π-extended PAH with controlled doping patterns through a precise bottom up approach. In

particular, the intention is to study the relationships that exist between the molecular structure and optical properties of the system. To this end, different synthetic tools will be adopted to control the energy band gap of π-conjugates that involves the elongation of the aromatic surface along with planarization and rigidification of the conjugated system. As depicted in Figure 3.4.1 three main classes of compounds were considered: BINOL, PXX and DNF derivatives in which the aromatic scaffold has been extended along the molecular axis. Such elongation is meant to induce a narrowing of the HOMO–LUMO gap within the same family, thereby causing a bathochromic shift in the absorption and emission spectrum.

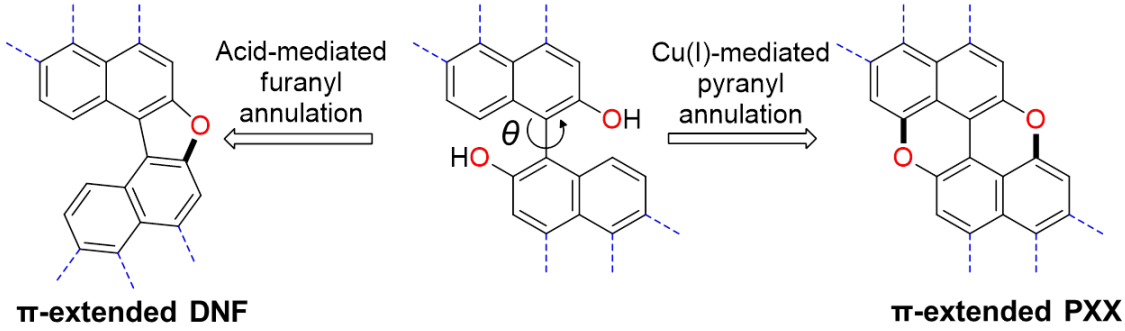

Figure 3.4.1 The furanyl and pyranyl cyclization strategies for the synthesis of dinaphthofuran (DNF) and peri-xanthenoxanthene (PXX) derivatives. The dashed lines indicate the possible substitutions patterns of the C-sp^2 aromatic core.

The first series of π-extended O-doped aromatic hydrocarbons considered in this section is represented in Figure 3.4.2. It consists of novel O-doped equivalents of anthrabenzopentacene (**3-5^{Pp}**) and anthrabenzonaphthohexaphene (**3-6^{Pp}**). The PXX core was extended with one, three and six aromatic units to get **3-7^{Pp}**, **3-5^{Pp}** and **3-6^{Pp}**, respectively. The impact of the aromatic elongation on the optical properties of the molecules has been thus studied in detail.

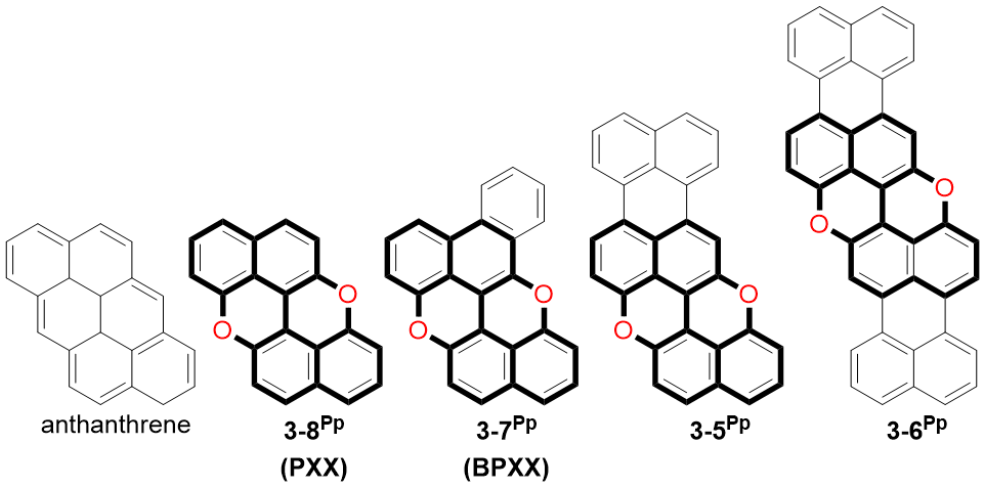

Figure 3.4.2. Molecular structures of anthanthrene, its O-doped analogue PXX (**3-8^{Pp}**), and π-extended PXX derivatives **3-7^{Pp}**, **3-5^{Pp}** and **3-6^{Pp}**, where the chromophore core was extended with one, three and six aromatic units, respectively.

In parallel, we will present the preparation of highly emissive oligonaphthofuran derivatives (Figure 3.4.3), in which the key synthetic step includes an acid-catalyzed dehydration of biperylenol. Analogously to the PXX derivatives, the π-surface has been extended in respect to the less conjugated dinaphtofuran (**3-8^{Fur}**) for one, three and six aromatic units.

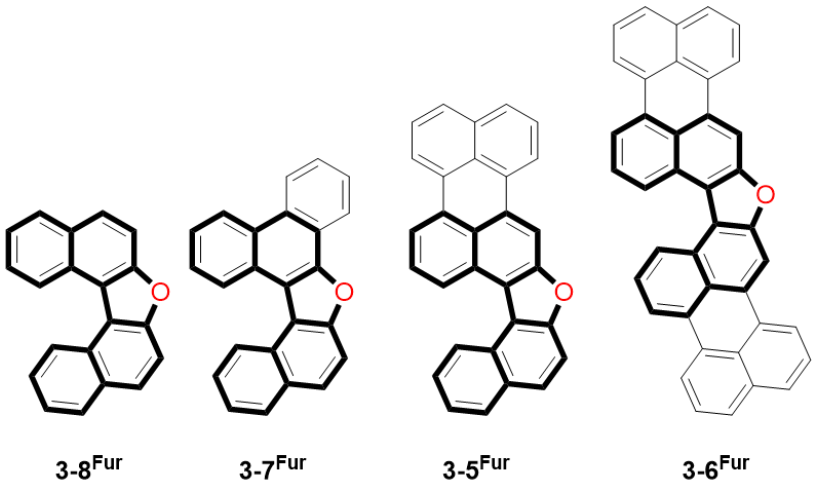

Figure 3.4.3. Furanyl generation of O-doped hydrocarbons investigated in this thesis. The DNF (**3-8^{Fur}**) core was extended with one, three and six aromatic units.

In this regard, we propose the synthesis of two main families of compounds: *(i)* the *biperylene* family in which an oxidative C-C coupling was exploited for the linkage of two perylenol units and the *(ii) naphthalene-perylene* family in which a naphthol unit was coupled to a perylenol unit following the same mild oxidative coupling conditions. As reference molecules for our study a third class of compounds was developed, *naphthalene-phenanthrene*, where the BINOL core was increased by only one benzene unit.

3.4.2 Synthesis of biperylene drivatives 3-6^{Fur} and 3-6^{Pp}

In order to increase the solubility of the final large polycyclic aromatic hydrocarbons we decided to introduce *tert*-butyl substituents on perylene *ortho* positions.

The general retrosynthetic strategy adopted for the preparation of biperylene-derivatives **3-6^{Fur}** and **3-6^{Pp}** is depicted in scheme 3.4.1. It involves *(i)* a Friedel-Crafts alkylation of perylene followed by iridium-catalyzed borylation, *(ii)* an oxidative replacement of boron to give the corresponding hydroxyl derivative and *(iii)* a Cu (II)- catalyzed C-C coupling reaction between two perylenol units. *(iv)* A final Cu (I) mediated C-O intramolecular cyclization reaction for the preparation of pyranyl derivatives will be adopted while *(v)* an acid-mediated C-O cyclization will be exploited for the formation of furanyl compounds.

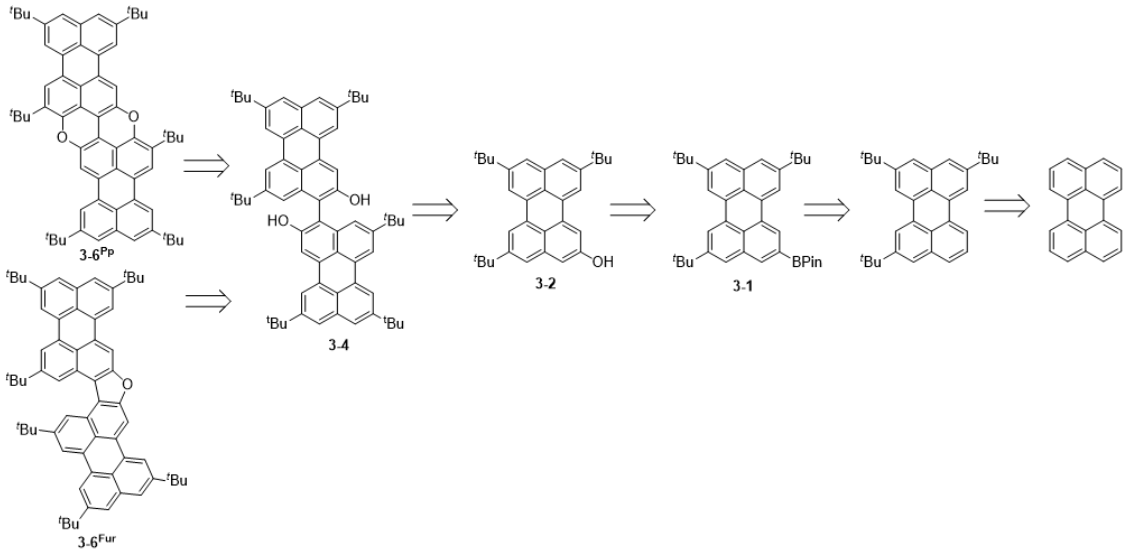

Scheme 3.4.1 Retrosynthetic approach adopted for the synthesis of biperylene derivatives **3-6^{Fur}** and **3-6^{Pp}**.

Accordingly, first step in the realization of proposed synthesis is the *tert*-butylation of commercially available perylene in positions 2, 5, and 8. The treatment of perylene with 3.3 eq. of *t*-BuCl under Friedel-Craft conditions following a slightly modified procedure reported in literature[102] lead to the formation of 2-*tert*-butylperylene (**3-39**) in 45 % yield as reported in scheme 3.4.2. Only a minor aliquot of a mixture of di- and tri-*tert*-butylperylene was detected but not isolated.

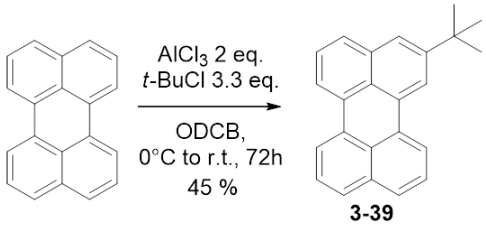

Scheme 3.4.2. *tert*-butylation reaction in presence of 3.3 equivalents of *t*-BuCl.

Under the mentioned conditions, no tetra-*tert*-butyl derivative was formed and 49 % of starting material was recovered as unreacted. A second attempt maintaining the same reaction conditions and using 6.6 eq. of *t*-BuCl leaded, once more, to **3-39** as major product. Therefore, to prepare 2,5,8-tri-*tert*-butylperylene needed for our propose we decided to follow the conditions reported by *Pillow. et al*. in their patent published in 2010.[103] Accordingly, perylene was treated with a large excess of *t*-BuCl under Friedel-Craft conditions to achieve a mixture of di-, tri- and tetra substituted *t*-Bu-perylene, which was subsequently submitted to selective C-H borylation reaction in the presence of 10 mol% Ir-catalyst and 20 mol% of dtbpy and B_2pin_2 in *n*-hexane at 80 °C for 24 h (scheme 3.4.3). The approach allowed us to isolate tetra-*tert*-butylperylene **3-10** in 30-33% yield, **3-11** in 30 %

yield and target compound **3-1** in 20-25 % yield, by column chromatography. While the synthesis and characterization of compound **3-10** is well described in literature, [102,104,105] synthesis of compounds **3-1** and **3-11** opens an easy and controlled way for selective functionalization of perylene *ortho* positions. Indeed, to the best of our knowledges, only few examples are reported regarding the direct substitution at 2, 5, 8, 11 positions of perylene core. *Coventry at al*. reported in 2005 the selective Ir-catalyzed borylation of polycyclic aromatic hydrocabons including perylene to achieve 2, 5, 8, 11-tetra-substituted derivative.[106] For compound **3-11** single crystal suitable for X-ray diffraction was obtained. Intense yellow crystals of the investigated compound were grown by slow diffusion from a CH_2Cl_2/MeOH solution. Inset in scheme 3.4.3 shows the ORTEP image of the crystal structure, belonging to the spatial group R-3 (essential crystal and refinement data are reported in *appendix*).

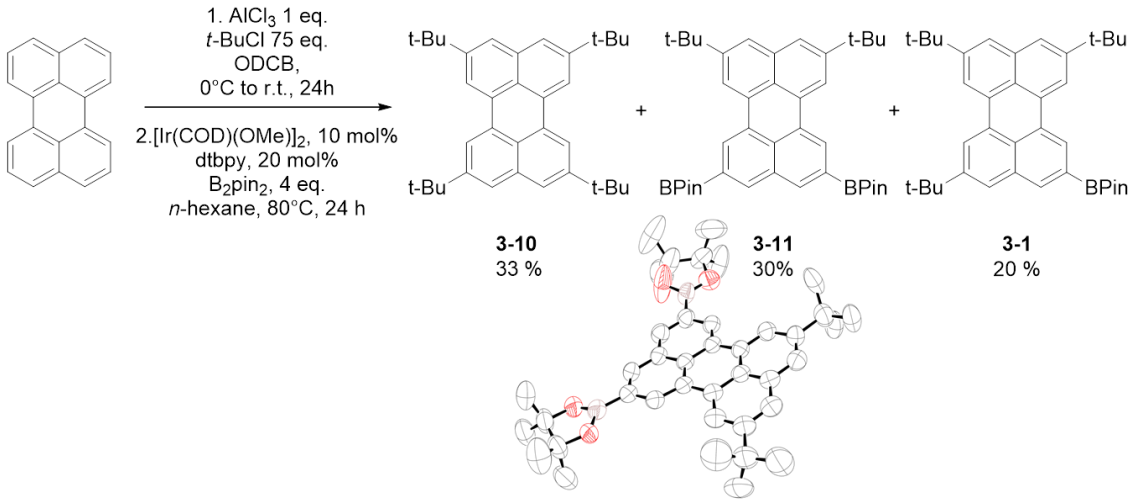

Scheme 3.4.3. Synthetic protocol adopted for the preparation of **3-1** and ORTEP representation of a single molecule of **3-11** (50% probability ellipsoids). Coordinated solvent molecules and hydrogen atoms omitted for clarity. Solvent for crystallization: CH_2Cl_2/MeOH (space group *R* -3).

The next step towards our synthetic protocol was the oxidation of **3-1,** which was achieved applying the reaction conditions described by *Crawford et al.* for pyrene derivatives,[107] to our system using aq. 35 wt% H_2O_2 and NaOH for 2 h in THF at r.t. Indeed, perylenol derivative **3-2** was obtained in 80-85 % yield (Scheme 3.4.4).

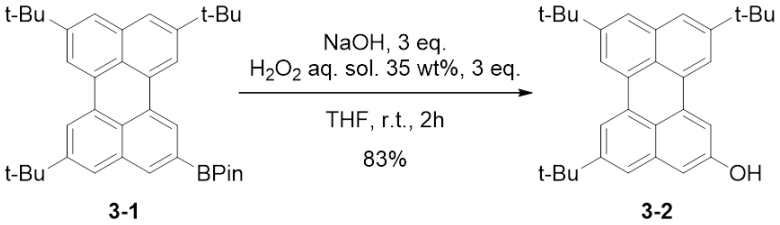

Scheme 3.4.4. Oxidation reaction for the preparation of compound **3-2**.

Compound **3-4** was synthesized exploiting racemic and achiral coupling protocol reported in literature for naphthol derivatives.[59,108] Herein, we describe different attempts of preparation of racemic *tert*-butyl-biperylenediol **3-4** (BIPOL) (table 3.4.1). The first route undertaken for the synthesis of BIPOL consists in the oxidative C-C coupling reaction in the presence of racemic phenylethylamine and $CuCl_2$ following a protocol previously developed in our group. Surprisingly, the formation of compound **3-4** was accompanied by the formation of pyranopyranyl derivative **3-6^{Pp}**.

Table 3.4.1 Synthetic attempts for preparation of **3-4.**

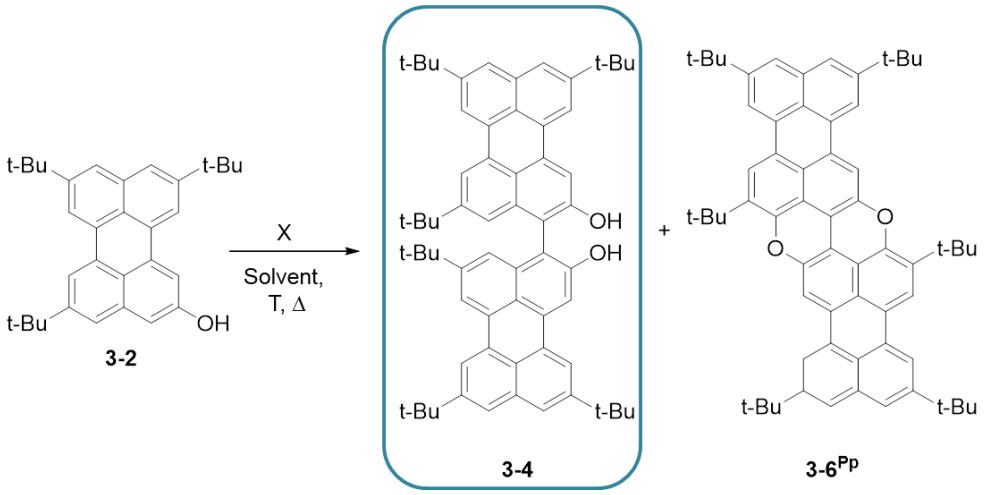

Entry	Reagents (X)	Solvent	°C/time	Yield (%)
1	$CuCl_2$ 2 eq. 2-PhEtNH$_2$ 2.5 Eq.	CH_2Cl_2:CH_3CN [2:1]	0°C to r.t., 24 h[a]	**3-4** (27 %) **3-2** (35%)
2	$CuCl_2$ 3 eq. 2-PhEtNH$_2$ 2.5 Eq.	CH_2Cl_2:CH_3CN [2:1]	0°C to r.t., 24 h[ab]	**3-4** (0 - 62 %) **3-6^{Pp}** (41-62 %)
3	$CuCl_2$ 4 eq. 2-PhEtNH$_2$ 2.5 eq.	CH_2Cl_2:CH_3CN [2:1]	0°C to r.t., 24 h[a]	**3-4** (29 %) **3-6^{Pp}** (28 %)
4	[Cu(OH)(Cl)TMEDA]$_{cat}$/air	CH_2Cl_2	1 h, 20°C[b]	**3-4** (71%) traces of **3-6^{Pp}**

[a] Oxygen free reaction
[b] open air conditions

Using two equivalents of $CuCl_2$ in the presence of phenylethylamine in a 2:1 mixture of CH_2Cl_2 and CH_3CN as solvent we were able to synthesize for the first time the BIPOL compound. In this attempt, part of the starting material was recovered and desired compound **3-4** was obtained in 27 % yield as yellow solid (entry 1, table 3.4.1). Increasing to three

equivalents the loading of $CuCl_2$ allowed us to prepare compound **3-4** in 62% yield (entry 2, table 3.4.1). Unfortunately, the reaction revealed to have a lack of reproducibility, and the yields for isolated BIPOL **3-4** were in the range of 0–62%. Moreover, the reaction proceeds strongly toward the formation of pyranopyranyl derivative **3-6^{Pp}** which was isolated in 41-62 % yield. Such outcome indicates that in oxidative conditions in the presence of copper BIPOL is easily undergoing further oxidation giving compound **3-6^{Pp}**. Performing the reaction with or without air provided similar reaction efficiency. For the lack of reproducibility, a milder oxidative coupling protocol was explored. A highly efficient process of aerobic oxidative coupling of 2-naphthol derivatives catalyzed by 1 mol % of Cu-TMEDA catalyst has been developed by *Nakajima* and co-workers[109] and applied for dimerization reaction of hydroxyl perylene **3-2** into desired BIPOL.[109,110]

With this synthetic methodology, the coupling reaction between two hydroxyl perylene units was achieved successfully using Cu(OH)ClTMEDA catalyst in catalytic amount, between 1-2 mol % giving good yields under open air conditions and short reaction times (entry 4, table 3.4.1). Indeed, compound **3-4** was synthesized in 71 % yield in the presence of less than 2 mol% Cu-catalyst in 1 h under air at 20 °C using CH_2Cl_2 as solvent. We obtained BIPOL **3-4** reproducibly in higher yield than with the reactions performed using $CuCl_2$ in the presence of phenylethyl amine. Moreover, applied protocol emerged as very clean and easy of purification. We found that compound **3-4** is soluble in a large variety of organic solvents, such as EtOAc, acetone, MeOH, $CHCl_3$, CH_2Cl_2, toluene and hexane. The chemical structure of BIPOL **3-4** was confirmed by melting point, IR, ^1H and ^{13}C NMR spectroscopy (*chapter IV*) and ESI-HRMS through detection of the peak corresponding to the mass at m/z 870.5360 ([M], for $C_{64}H_{70}O_2$, calc.: 870.5370). Furthermore, crystals of **3-4** suitable for single-crystal X-ray analysis were grown by slow diffusion from a CH_2Br_2/MeOH solution. One crystallographically independent molecule is present in the asymmetric unit (Figure 3.4.4). Weak hydrophobic interactions keep molecules packed. Solvent cavities have been found parallel to *a* cell axis, where molecule **3-4** hydroxyl groups are exposed and interact with methanol molecules (four disordered solvent molecules have been modeled). The dihedral angle (θ) between the two perylene moieties is 62.8° and the two hydroxyl groups adopt a *syn*- conformation. This torsion angle is quite high because the rotation around the bond 1,1' is restricted only by sterical hindrance of hydroxyl and proximal *tert*-butyl groups.

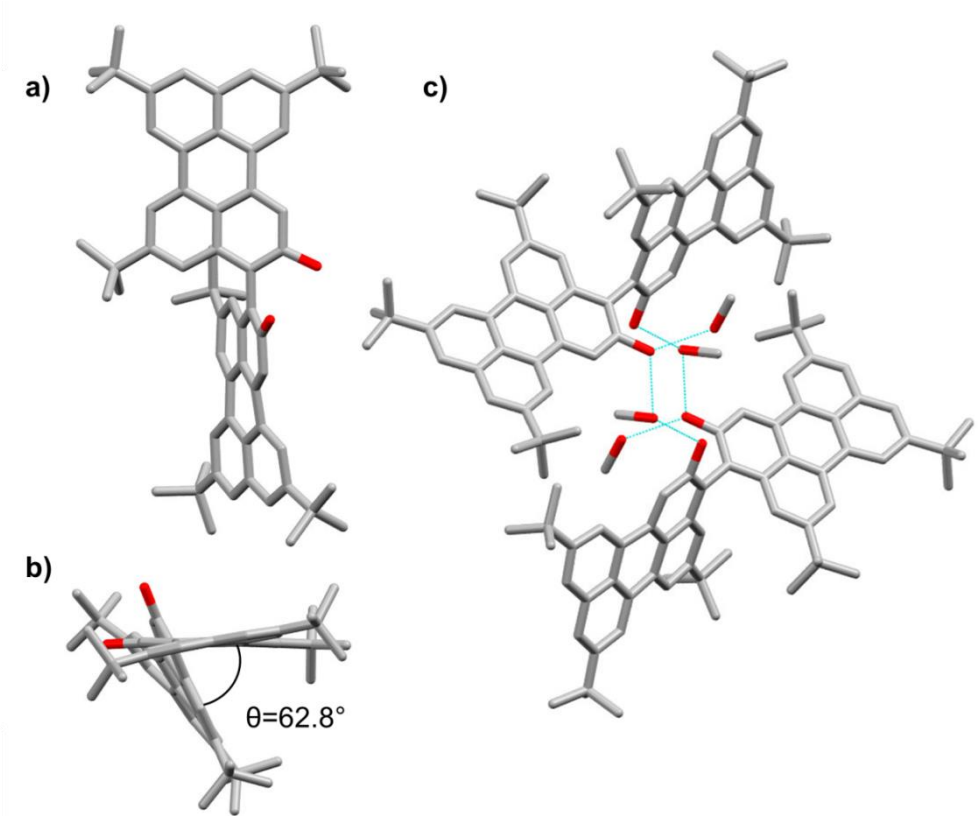

Figure 3.4.4. Top-view (a) and side-view (b) of the crystal structure of **BIPOL** (**3-4**) (50% probability ellipsoids). Solvent for crystallization: CH_2Br_2/MeOH (space group: *P*-1).

In view of synthesizing targeted dinaphtofuran **3-6^{Fur}**, different conditions for the acid-catalyzed intramolecular C-O bond formation were investigated (table 3.4.2). In a first attempt, compound **3-4** was treated with neat methanesulfonic acid (CH_3SO_3H) under reflux leading to the formation of a complex mixture. After a troublesome purification procedure, target compound **3-6^{Fur}** was isolated in a 10% yield (entry 1, table 3.4.2). Slightly better results were obtained refluxing compound **3-4** in presence of a stoichiometric amount of CH_3SO_3H using toluene as solvent for 2 h (entry 2, table 3.4.2).

Table 3.4.2 Conditions tested for the conversion of derivative **3-4** to furanyl derivative **3-6^{Fur}**

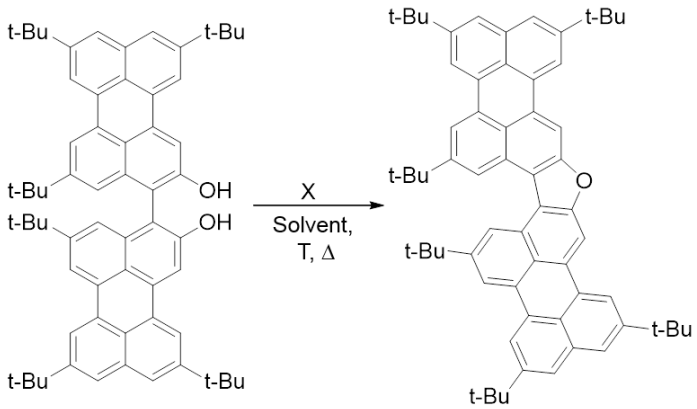

3-4 **3-6^{Fur}**

Entry	X	Solvent	°C/time	Yield (%)
1	CH_3SO_3H	-	140 °C, 2 h	**3-6^{Fur}** (10 %) **3-4** (38 %)
2	CH_3SO_3H	dry toluene	reflux, 24 h	**3-6^{Fur}** (25 %)[a]
3	*p*-TsOH 2 eq.	dry toluene	reflux, 36 h, under Ar	**3-6^{Fur}** (20 %)[a] **3-4** (50 %)
4	*p*-TsOH 2 eq.	dry toluene	reflux, 48 h, under Ar	**3-6^{Fur}** (29 %) **3-4** (49 %) **3-6^{Pp}** (8 %)
5	*p*-TsOH 10 eq.	dry toluene	reflux, 18 h, under Ar	**3-6^{Fur}** (89 %)[a]
6	*p*-TsOH 20 eq.	dry toluene	reflux, 4 h, under Ar	**3-6^{Fur}** (90 %)

[a] formation of traces of compound **3-6^{Pp}** detected by tlc

The reaction conditions reported by *Areephong* et al.[92] using *p*-toluenesulfonic acid as dehydrating agent were applied to our system. Refluxing compound **3-4** in acidic conditions for longer reaction times (more than 12 h) using 2-equivalents of *p*-TsOH gave compound **3-6^{Fur}** in low yields (20-29 %) along with traces of fused derivative **3-6^{Pp}** (entry 2 and 3, table 3.4.2). Nevertheless, optimized reaction conditions were found increasing the equivalents of *p*-TsOH and decreasing the reaction time (entry 6, table 3.4.2). Indeed, compound **3-6^{Fur}** was synthesized in 90 % yield in presence of 20 equivalents of *p*-TsOH in toluene under reflux for 4 h. Furanyl derivative **3-6^{Fur}** was highly fluorescent in solution and in solid state and its structural identity was confirmed by ^{1}H and ^{13}C NMR spectroscopy (*chapter IV*) and HRMS MALDI. High resolution mass spectrum **3-6^{Fur}** is depicted in Figure

3.4.5 and shows the detection of the peak corresponding to the molecular mass at m/z 852.5268 ([M], $C_{64}H_{68}O$, calc.: 852.5270). Moreover, crystal suitable for X-ray diffraction was obtained by slow evaporation of solvent from a benzene-d_6/hexane solution, showing that **3-6^{Fur}** undergoes π-π stacking at the solid state and its organization will be discussed in detail in the next section.

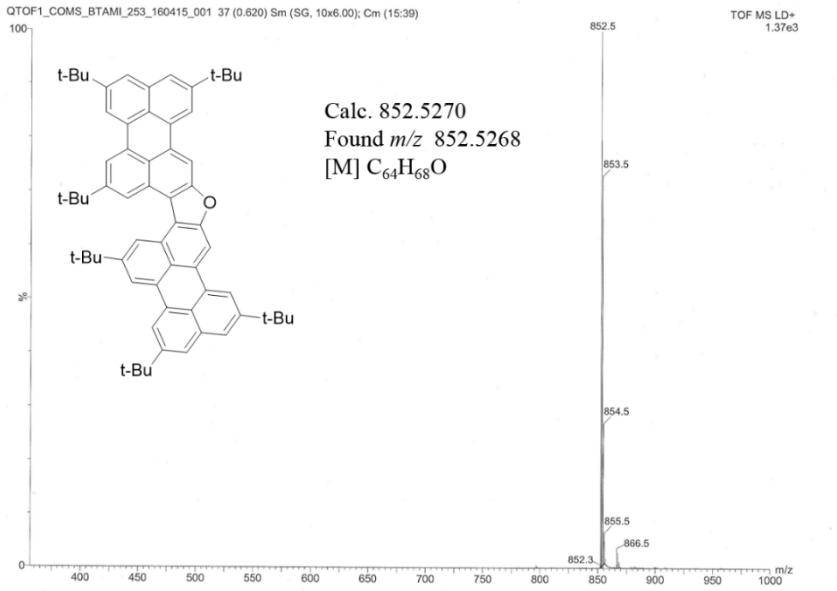

Figure 3.4.5. MALDI-HRMS spectra of **3-6^{Fur}** in positive mode.

Regarding the synthesis of compound **3-6^{Pp}**, the key oxidative metal-mediated formation of C-O bonds in a pyranopyran motif was carried out in the presence of CuI, pivaloic acid in DMSO under open-air conditions. Following the optimized synthetic methodology presented in the work of *Stassen et al*.,[56] target compound **3-6^{Pp}** was prepared in 84 % yield. We found that starting from easily accessible bisperylenol **3-4**, Cu (I) catalysis was working with high yields in an open-air round-bottom flask, with short reaction times. Reagents and reaction conditions are reported in scheme 3.4.5.

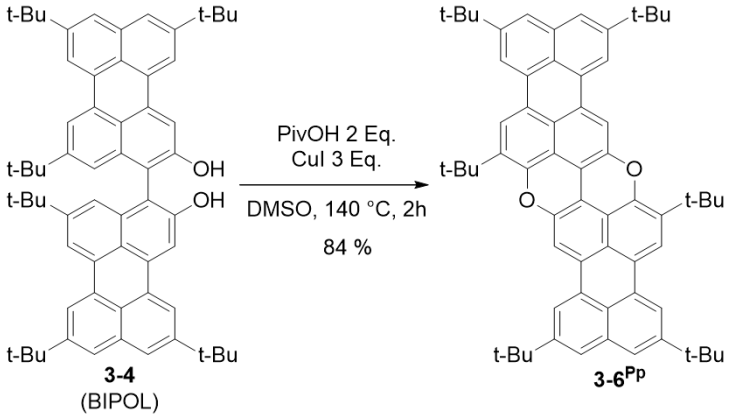

Scheme 3.4.5 Synthesis of **3-6^{Pp}.**

Due to the strong absorption on the silica of compound **3-6^{Pp}**, its purification by classical column chromatography was not possible. Therefore, after laborious re-precipitation cycles from THF/MeOH, we were able to isolate desired pyranopyranyl compound **3-6^{Pp}** as blue solid. We found that the molecule showed a reduced solubility in most of the common organic solvents compared to starting bisperylenol **3-4** due to the planarization of the aromatic scaffold. Different solvents such as CD_2Cl_2, $C_2D_2Cl_4$, C_6D_6, THF-d_8, DMSO-d_6 and TFA-*d* were exploited to characterize **3-6^{Pp}** through ^{1}H-NMR spectroscopy. Surprisingly, even though we found the material partially soluble in some of used solvents (CD_2Cl_2, $C_2D_2Cl_4$, THF-d_8 and TFA-*d*), no NMR signals belonging to the aromatic perylene core were recorded. One example in THF-d_8 is reported in Figure 3.4.6 a. The best result was obtained using C_6D_6 and toluene-d_8 as shown in figure 3.4.6 b and c, respectively. In those solvents very weak peaks in the intensity range of solvent ^{13}C satellites were detected, suggesting that **3-6^{Pp}** undergoes aggregation in solution. The ^{1}H-NMR spectrum shows six signals in the aromatic region that refers to the six perylene hydrogen atoms and three singlet signals around 1.64-1.33 ppm assigned to the *tert*-butyl substituents. Unfortunately, the ^{13}C NMR could not be measured.

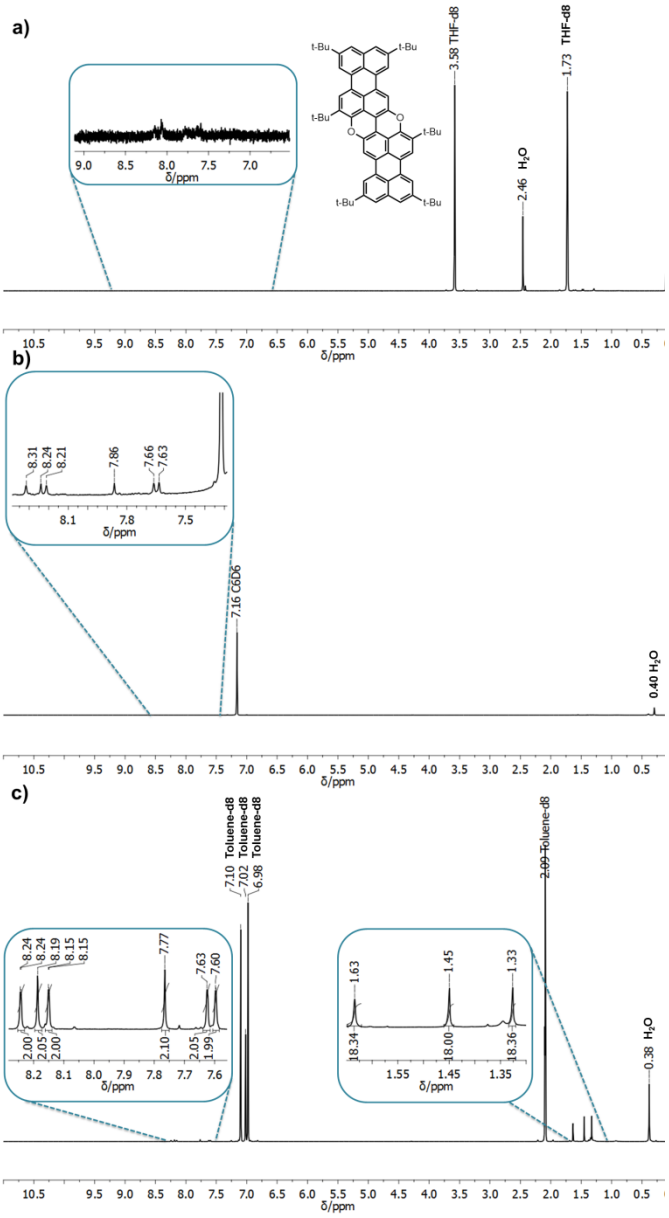

Figure 3.4.6. ^{1}H-NMR (500 MHz) spectra of molecule **3-6^{Pp}** in (a) THF-d_8, (b) benzene-d_6 (recorded overnight) and (c) toluene-d_8 (recorded overnight). Inset: zoom of the aromatic region (left) and aliphatic region (right).

The chemical identification of compound **3-6^{Pp}** was unambiguously accomplished by MALDI-HRMS as displayed in Figure 3.4.7. The analysis revealed the presence of mass peak assigned to the molecular mass of **3-6^{Pp}** at m/z 866.5059 ([M], $C_{64}H_{66}O_2$, calc.: 866.5063). Complete characterization of compound **3-6^{Pp}** is reported in *chapter IV*.

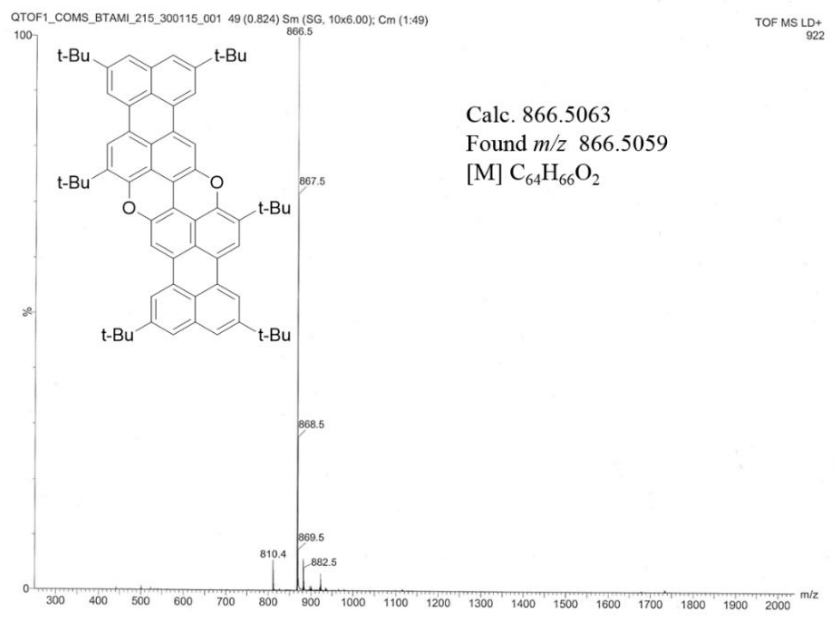

Figure 3.4.7. MALDI-HRMS spectrum of **3-6^{Pp}**in positive mode.

To confirm the aggregation in solution of compound **3-6^{Pp}** we carried out variable temperature ^{1}H-NMR experiment. The measurements were conducted in temperature range from 25 °C to 80°C in toluene-d_8 using a 1.22 × 10^{-5} M solution of **3-6^{Pp}.** An increasing of the intensity of the aromatic peaks was recorded which confirms the mentioned aggregation in solution. (Figure 3.4.8)

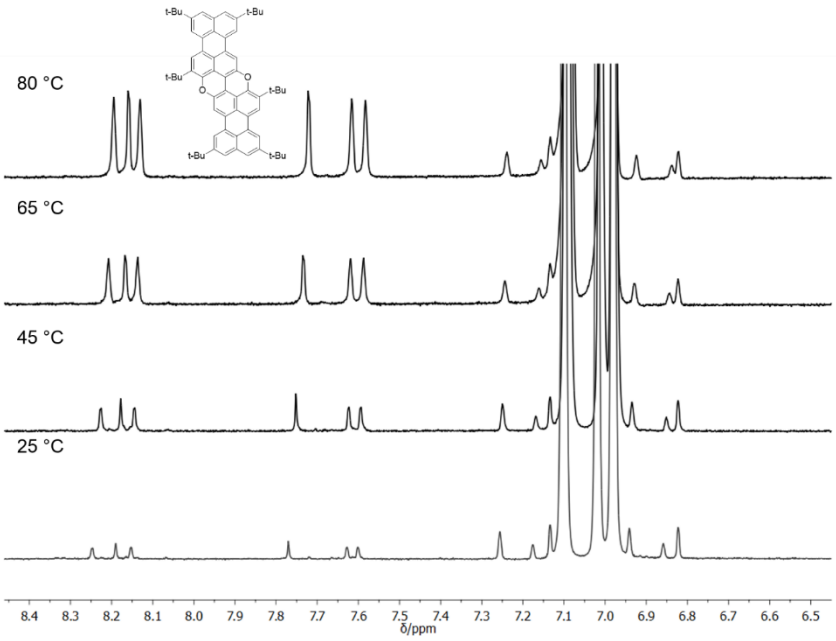

Figure 3.4.8. VT-^{1}H NMR (500 MHz) spectral changes of **3-6^{Pp}** from r.t. to 80 °C in toluene-d_8.

3.4.3 Synthesis of naphthalene-perylene derivatives 3-5^{Fur} and 3-5^{Pp}

Naphthalene-perylene derivatives **3-5^{Fur}** and **3-5^{Pp}** were synthesized according to the retrosynthetic approach reported in scheme 3.4.6. As for parent biperylene derivatives, solubilizing *tert*-butyl groups have been introduced onto the molecular scaffold in order to enhance the solubility of the final molecules.

Analogously to previously synthesized biperylene derivatives **3-6^{Fur}** and **3-6^{Pp}** the synthetic approach involves *(i)* a Friedel-Crafts alkylation of perylene followed by iridium-catalyzed borylation, *(ii)* an oxidative replacement of boron to give the corresponding hydroxyl perylene and *(iii)* a Cu (II)- catalyzed C-C coupling reaction between a perylenol and a naphthol unit. *(iv)* A final Cu (I) mediated C-O intramolecular cyclization reaction for the preparation of pyranyl derivative **3-5^{Pp}** will be adopted while *(v)* an acid-mediated C-O cyclization will be exploited for the formation of furanyl compound **3-5^{Fur}**. The first two steps are in common with the previously reported synthesis of biperylene compounds **3-6^{Fur}** and **3-6^{Pp}** and will be not re-discussed in this section.

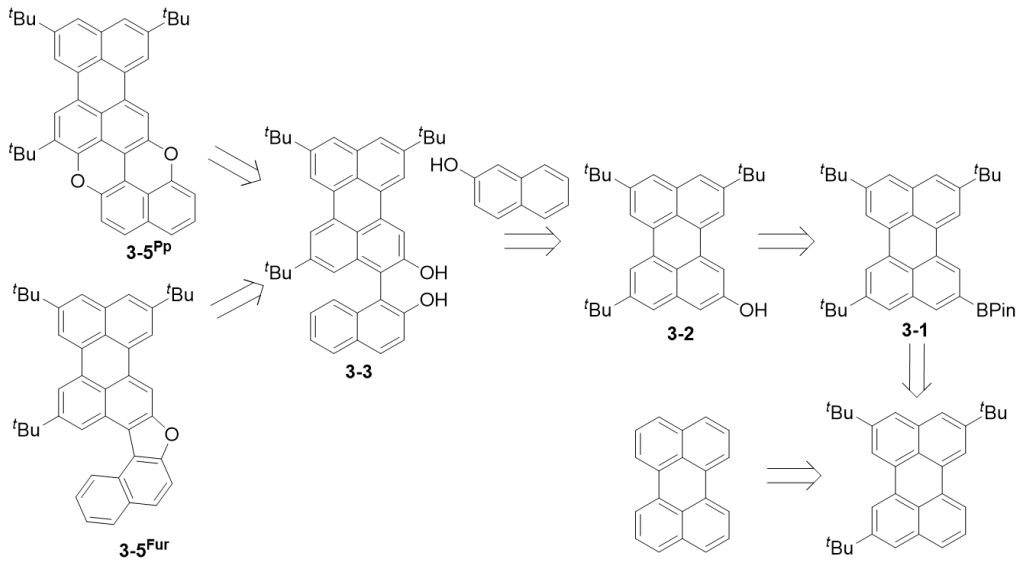

Scheme 3.4.6. Retrosynthetic approach adopted for the preparation of **3-5^{Fur}** and **3-5^{Pp}**.

To commence, preparation of intermediate **3-3** was accomplished by the cross-coupling of hydroxyl perylene **3-2** with a slight excess of 2-naphthol using a Cu(II)-mediated reaction in the presence of Cu-TMEDA catalyst yielding a mixture of three possible coupling products, where desired **3-3** was obtained in 26 % yield (attributed to the lack of reaction chemoselectivity) (scheme 3.4.7). In this case, we found that synthesized compound **3-3** was well soluble in most of the common organic solvents and it was fully characterized by

melting point, IR, ^{1}H- and ^{13}C-NMR spectroscopy and MALDI-HRMS spectrometry (see *Chapter IV*).

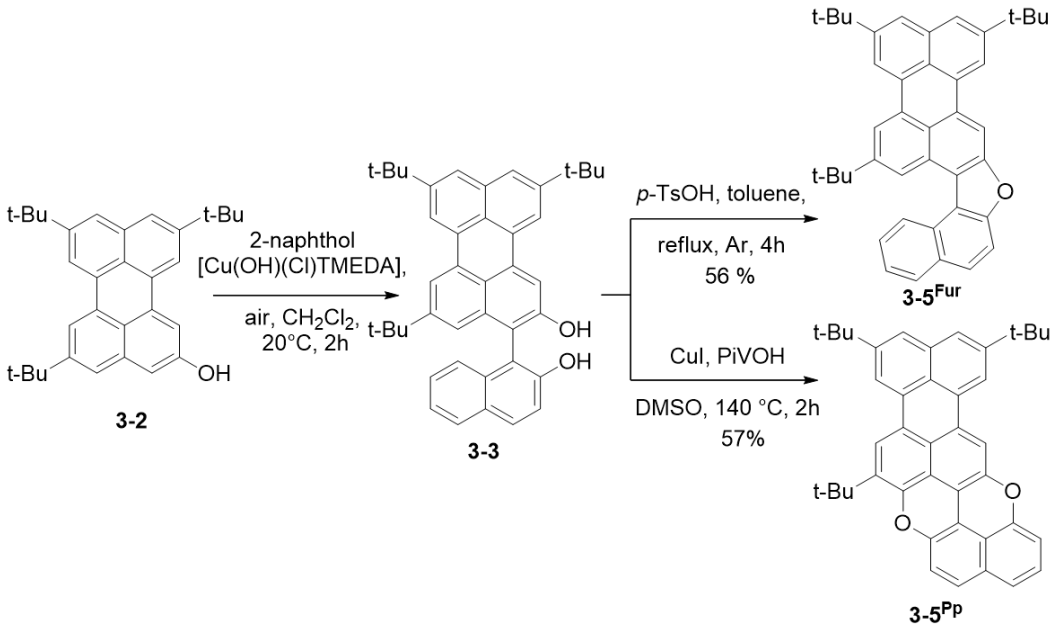

Scheme 3.4.7 Synthesis of **3-5^{Fur}** and **3-5^{Pp}**

Analogously to preparative protocol of **3-6^{Fur},** compound **3-5^{Fur}** was synthesized by refluxing compound **3-3** with 20 eq of *p*-TsOH in toluene for 4 h (scheme 3.4.7) In this case, moderate reaction yield was recorded (56 %) and most of unreacted starting material was recovered. The new synthesized compound was purified by column chromatography and its structural identity was confirmed by melting point, IR ^{1}H-, ^{13}C-NMR spectroscopy (*Chapter IV*) and MALDI-HRMS spectrometry. The high resolution mass spectrum depicted in Figure 3.4.9 shows the detection of the peak corresponding to the molecular mass at m/z 560.3079 ([M], $C_{42}H_{40}O$, calc.: 560.3079). Moreover, crystal suitable for X-ray diffraction was obtained by slow diffusion from a CH_2Br_2/MeOH solution and revealed that furanyl derivative **3-5^{Fur}** undergoes π-π stacking at the solid state and its organization will be discussed in detail in section 3.4.5.

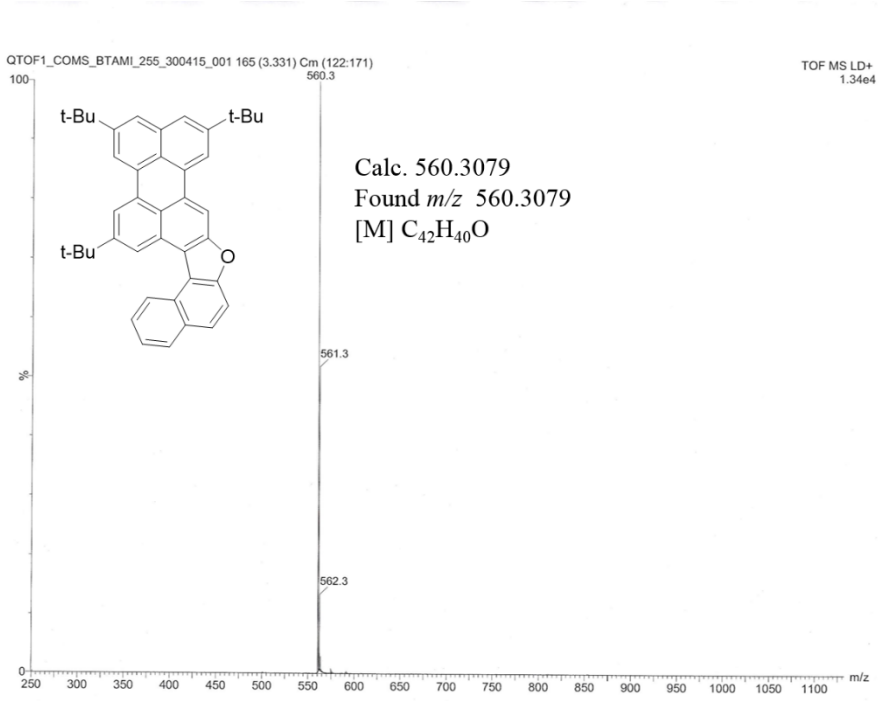

Figure 3.4.9. MALDI-HRMS spectra of **3-5^{Fur}** in positive mode.

Subsequently, molecule **3-3** was transformed into fused derivative **3-5^{Pp}** by the intramolecular oxidative etherification reaction using CuI in the presence of air and PivOH in DMSO at 140 °C forming the planar pyranopyran ring in 57% yield (scheme 3.4.7). Analogously to compound **3-6^{Pp}**, **3-5^{Pp}** was purified by tedious re-precipitation from THF/MeOH and showed decreased solubility compared to the starting **3-3**. The structure of the fused system was confirmed by melting point, ^{1}H-NMR, IR, UV-Vis (*Chapter IV*) and MALDI-HRMS through detection of the peak corresponding to the molecular mass at m/z 574.2889 ([M], $C_{42}H_{38}O_2$, calc.: 574.2872) (Figure 3.4.10). Analogously to compound **3-6^{Pp},** ^{13}C-NMR spectrum could not be recorded probably due to the tendency of the molecule to aggregate in solution.

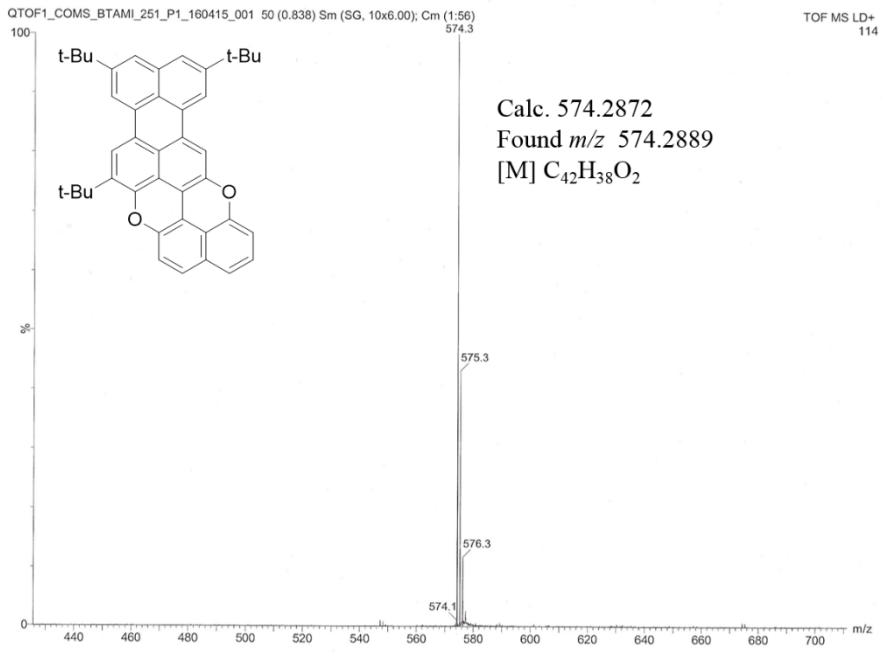

Figure 3.4.10. MALDI-HRMS spectra of **3-5^{Pp}** in positive mode.

3.4.4 Synthesis of naphtalene-phenanthrene derivatives 3-7^{Fur} and 3-7^{Pp} and reference compounds 3-8^{Fur} (DNF) and 3-8^{Pp} (PXX)

In order to study the effect of the extension of the π-conjugated length on our systems we prepared reference compounds **3-8^{Fur}** (DNF) and **3-8^{Pp}** (PXX). The first elongation that will be taken in consideration is the addition of one benzene ring to the aromatic scaffold. To this end, compounds **3-7^{Fur}** and **3-7^{Pp}** were prepared. The retrosynthetic approach adopted for the synthesis of derivatives **3-8^{Fur}** and **3-8^{Pp}** and relative π-extended derivatives **3-7^{Fur}**, **3-7^{Pp}** is reported in scheme 3.4.8. The main reactions involved are the oxidative C-C coupling for the synthesis of the biaryl intermediate following by the planarization of the molecular scaffold through acid- or metal- based cyclization reaction, for the preparation of furanyl and pyranopyranyl derivatives, respectively.

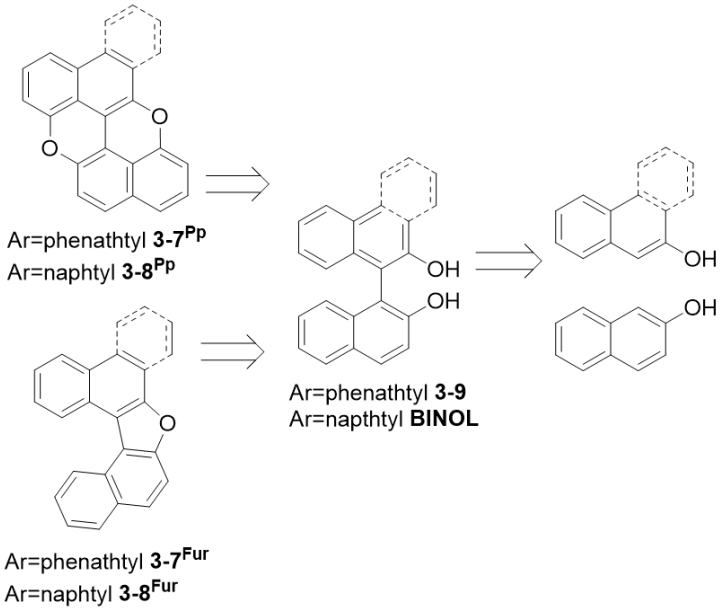

Scheme 3.4.8. Retrosynthesis of furanyl derivatives **3-7**^{Fur} and **3-8**^{Fur} and of pyranopyranyl derivatives **3-7**^{Pp} and **3-8**^{Pp}.

Commercially available BINOL was used as starting material for the synthesis of references **3-8**^{Fur} and **3-8**^{Pp} while for the preparation of compounds **3-7**^{Fur} and **3-7**^{Pp}, derivative **3-9** was synthesized exploiting an oxidative C-C coupling between the 2-naphthol and 9-phenanthrol unit in the presence of copper-TMEDA catalyst under open air conditions. (scheme 3.4.9). A mixture of three possible products was obtained and compound **3-9** was isolated in 31 % yield.

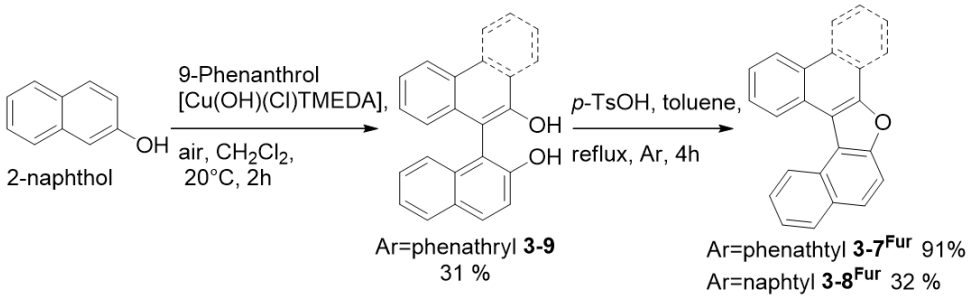

Scheme 3.4.9. Synthesis of furanyl derivatives **3-7**^{Fur} and **3-8**^{Fur}

Subsequently, compound **3-9** was treated with 20 eq. of *p*-toluenesulfonic acid under reflux to afford furanyl derivative **3-7**^{Fur} in a 91% yield. In an analogous way, compound **3-8**^{Fur} was synthesized from commercially available 1,1′-bi-2-naphthol in 32 % yield. Their characterization was in accordance with spectroscopic data reported in literature and are reported in *Chapter IV*.[111,112]

For the preparation of pyranopyranyl references **3-7^{Pp}** and **3-8^{Pp}** the metal-catalyzed C-H activation/C-O cyclization reaction was adopted. (Table 3.4.3.). In table 3.4.3 are listed the different conditions applied. 1,1′-bi-2-naphthol was converted to PXX using CuI in the presence of air and PivOH in DMSO at 140 °C in 86% yield (entry 2, table 3.4.3). Moreover, we extended the protocol reported by *Pummerer* with CuO[59,93] to a microwave-assisted reaction where 2-binaphthol was transformed into PXX in 71% yield (entry 4, table 3.4.3).

Table 3.4.3 Conditions tested for the synthesis of PXX and BPXX via C-H activation/C-O cyclization reaction.

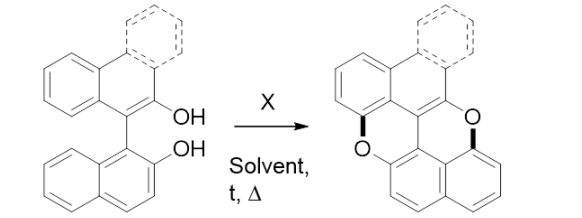

Ar=phenathryl **3-9**
Ar=binaphthyl **BINOL**

Ar=phenathtyl **3-7^{Pp}** (**BPXX**)
Ar=naphtyl **3-8^{Pp}** (**PXX**)

Entry	X	Solvent	°C/time	Compound/Yield (%)
1	CuI 3 eq., PivOH 2 eq. air	DMSO	140 °C, 2 h	**3-7^{Pp}** (13%)
2	CuI 3 eq., PivOH 2 eq. air	DMSO	140 °C, 2 h	**3-8^{Pp}** (86%)[a]
3	CuO, air	$PhNO_2$	180 °C, 2 h, *mw*	**3-7^{Pp}** (37 %)
4	CuO, air	$PhNO_2$	180 °C, 2 h, *mw*	**3-8^{Pp}** (71 %)[b]

[a] 94 % yield reported in literature;[56] [b] 42 % yield reported for classic condition.[56]

Likewise, phenathrol-napthol derivative **3-9** was converted to benzoxanthenonoxanthene **3-7^{Pp}** exploiting Cu (I)-mediated annulation reaction in the presence of CuI and pivaloic acid in 13 % yield (entry 1, table 3.4.3). Low reaction yields can be attributed to the poor solubility of fused derivative **3-7^{Pp}** and to the formation of a complex mixture difficult to purify. In a second attempt, compound **3-9** was converted to derivative **3-7^{Pp}** via CuO-promoted oxidative coupling in nitrobenzene in a microwave-assisted reaction, yielding compound **3-7^{Pp}** in 37 % yield (entry 3, table 3.4.3). The obtained compound exhibited reduced solubility in most of the common organic solvents, preventing the recording of ^{13}C-NMR spectrum. However, the structure of **3-7^{Pp}** was unambiguously confirmed by ^{1}H-NMR at 60 °C, IR and EI-HRMS techniques (Chapter *IV*), thus validating this synthetic approach. From high resolution mass spectrometry (EI) the detection of the peak corresponding to the

molecular radical cation at m/z 332.0824 ($[M+H]^{+\bullet}$, $C_{28}H_{14}O_2^{\bullet+}$, calc.: 332.0837) is visible as depicted in Figure 3.4.11.

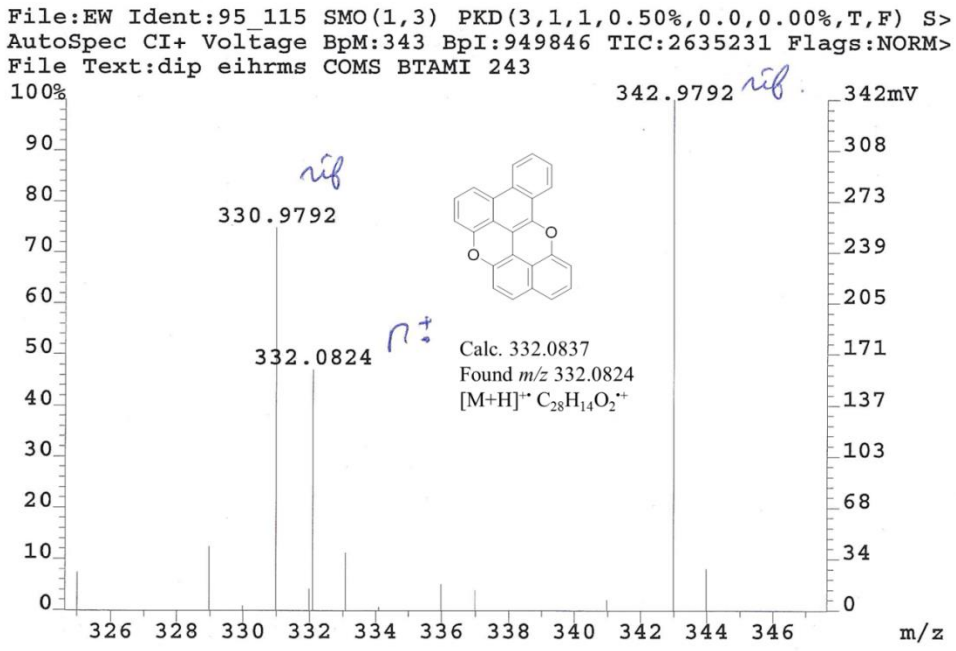

Figure 3.4.11. EI-HRMS spectrum of **3-7^{Pp}**.

3.4.5 Solid-state organization: single-crystal X-ray investigations and scanning electron microscopy (SEM) imaging

To study the solid-state arrangement of π-extended DNF molecules, we succeed to obtain suitable single crystals for X-ray analysis. Transparent (for **3-7^{Fur}**), deep-orange (for **3-5^{Fur}**) and deep-red (for **3-6^{Fur}**) crystals are belonging to the space group *P* $2_12_12_1$, *P* 2_1/c, and *P* 2/c, respectively. Despite many attempts, we did not accomplish to obtain single crystal structures for pyranopyranyl derivatives **3-7^{Pp}**, **3-5^{Pp}** and **3-7^{Pp}**. X-ray single-crystal diffraction confirms that the furanyl derivatives undergo π-π stacking at the solid state.

Analysis of compound **3-5^{Fur}** shows that one crystallographically independent molecule is present in the asymmetric unit. No solvent molecules have been found in the crystal packing. Moreover, weak hydrophobic interactions keep molecules packed and couples of molecules related by crystallographic inversion centers show extensive stacking interactions with mean distance between molecule planes of ~3.7 Å. Measured dihedral angle between perylene and naphthalene moiety which is constrained by planarity of fused furanyl ring, results to be 18.1° (Figure 3.4.12 b).

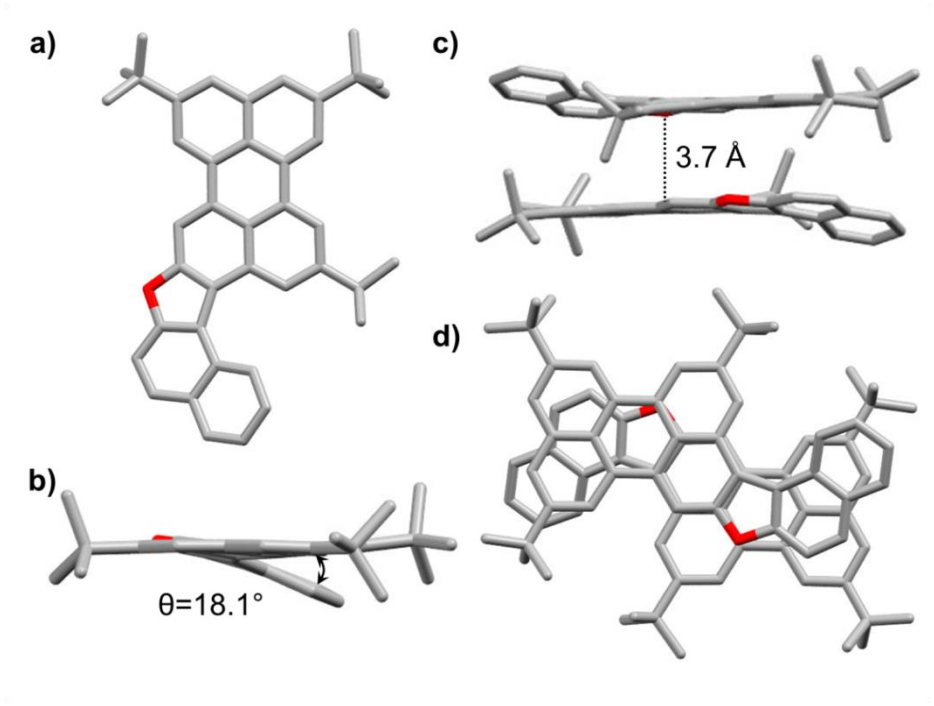

Figure 3.4.12 a,d) Top-view and b,c) side-view of the crystal structure and π-π packing arrangement of **3-5^{Fur}** (top, space group: *P* 2_1/c) (atom colors: blue N, red O, yellow B, gray C; atomic displacement parameters, obtained at 223 K, are drawn at the 50% probability level).

Analyzing the most π-extended derivative of the furanyl family, we found the presence of a crystallographic twofold axis passing through the furan ring that makes half crystallographically **3-6^{Fur}** molecule independent in the asymmetric unit (Figure 3.4.13 c). Disordered hexane molecules have been found in the crystal packing, with a 1:~1.5 **3-6^{Fur}** molecule:solvent ratio. Partial perylene π-π overlaps glue neighbor **3-6^{Fur}** molecules to form layers, parallel to cell *bc* face; these layers are interleaved by hexane channels (aligned with *c* axis), delimited by *tert*-butyl groups. The interplanar angle between furan-fused perylene fragments is 16.7° (Figure 3.4.13 b), which is in agreement with the values found for the other planar furanyl members (**3-5^{Fur}** and **3-7^{Fur}**).

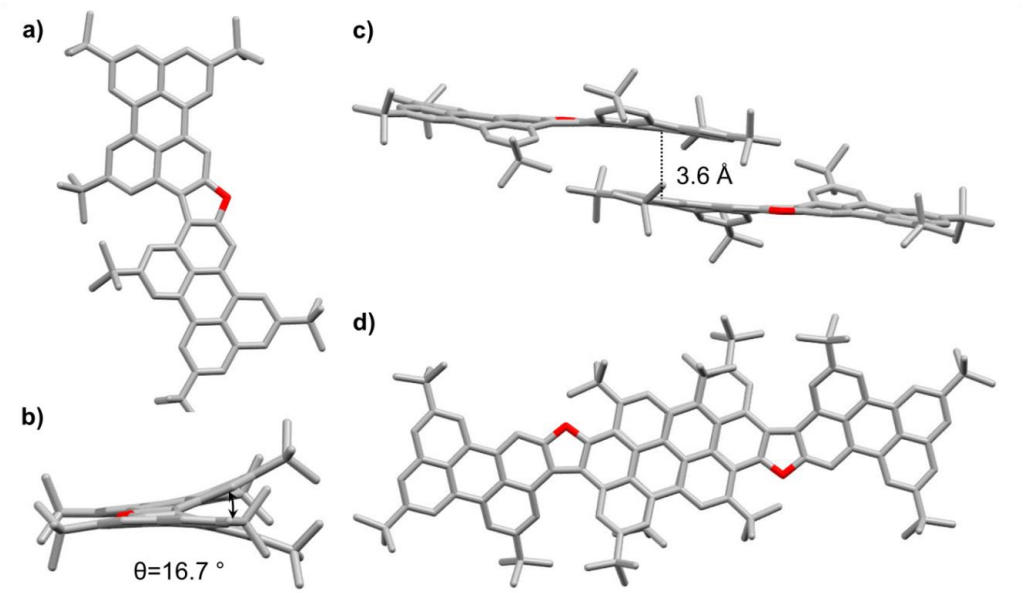

Figure 3.4.13 a,d) Top-view and b,c) side-view of the crystal structure and π-π packing arrangement of **3-6^{Fur}** (center, space group: *P* 2/c) (atom colors: blue N, red O, yellow B, gray C; atomic displacement parameters, obtained at 223 K, are drawn at the 50% probability level).

Crystal of **3-7^{Fur}** suitable for X-ray diffraction was obtained by slow evaporation of solvent from a methylene chloride-d_2 solution. One crystallographically independent molecule is present in the asymmetric unit (Figure 3.4.12 a). In this latter case, no solvent molecules were found in the crystal packing. Pillars, aligned with *a* cell axis, show strong stacking interactions with mean distance between molecule planes of ~3.5 Å, while weak hydrophobic contacts keep neighbour pillars packed through peripheral CH-π bonds. The molecular packing of **3-7^{Fur}** is illustrated in Figure 3.4.15 c/d. The absence of peripheral bulkier *tert*-butyl groups reduces considerably the dihedral angle between the phenanthrene and naphthalene moiety if compared with substituted perylene derivatives **3-5^{Fur}** and **3-6^{Fur}**, which results to be 12.9 ° (Figure 3.4.15 b).

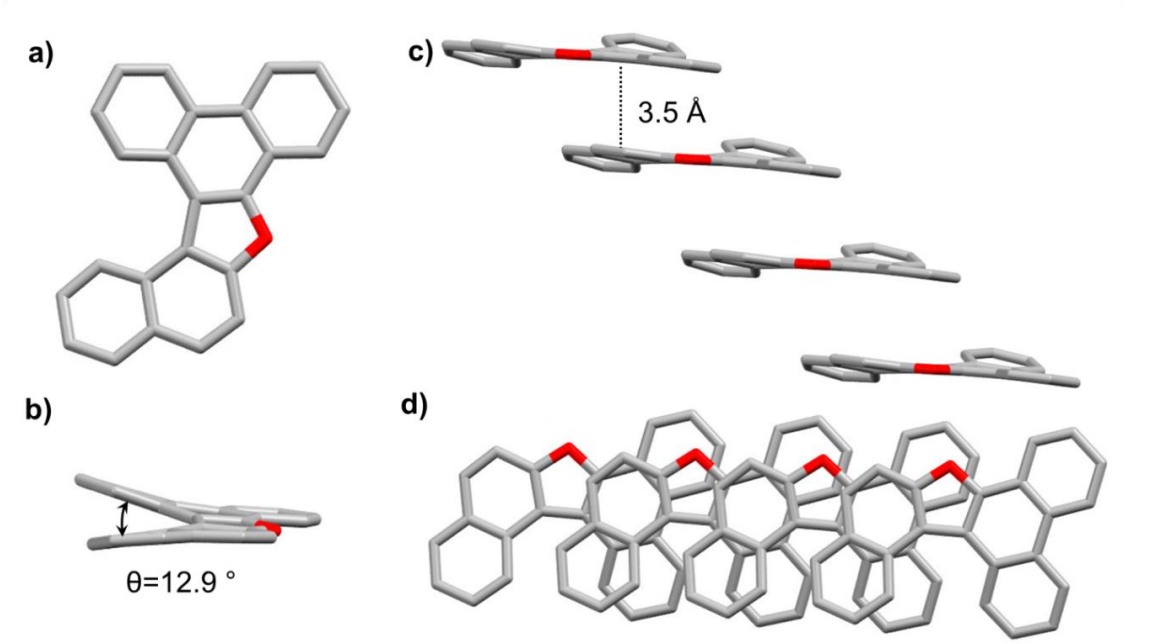

Figure 3.4.15 a,d) Top-view and b,c) side-view of the crystal structure and π-π packing arrangement of **3-7^{Fur}** (bottom, space group: $P\,2_12_12_1$) (atom colors: blue N, red O, yellow B, gray C; atomic displacement parameters, obtained at 223 K, are drawn at the 50% probability level).

Then, we searched for a method to prepare nanostructured materials. Different solvent conditions were screened and the morphology of the formed aggregates was examined by scanning electron microscopy (SEM). Figures 3.4.16 and 3.4.17. display SEM images of the molecular aggregates of compounds **3-5^{Fur}**, **3-5^{Pp}**, **3-6^{Fur}** and **3-6^{Pp}** formed from a THF solution upon addition of MeOH. In these conditions, compound **3-5^{Fur}** leads to the formation of reproducible 3D structures in the shape of elongated hexagonal prism (Figure 3.4.16 a, b). These structures are around 1 µm large and wide with a length in the order of 5-10 µm. It is noteworthy to indicate that some longer needles can also been seen in the sample. Upon drying, **3-6^{Fur}** sample (Figure 3.4.16 c, d) gave disk-like structures with a diameter in the micrometer range. Compound **3-5^{Pp}** bearing a pyranopyranyl motif was found to form stick like structures 3-10 µm long (Figure 3.4.17 a, b). Finally, looking at the morphology of the molecular assembly obtained for compound **3-6^{Pp}**, we can notice that it gave well reproducible stick-like shaped particulate aggregates in the micrometer range.

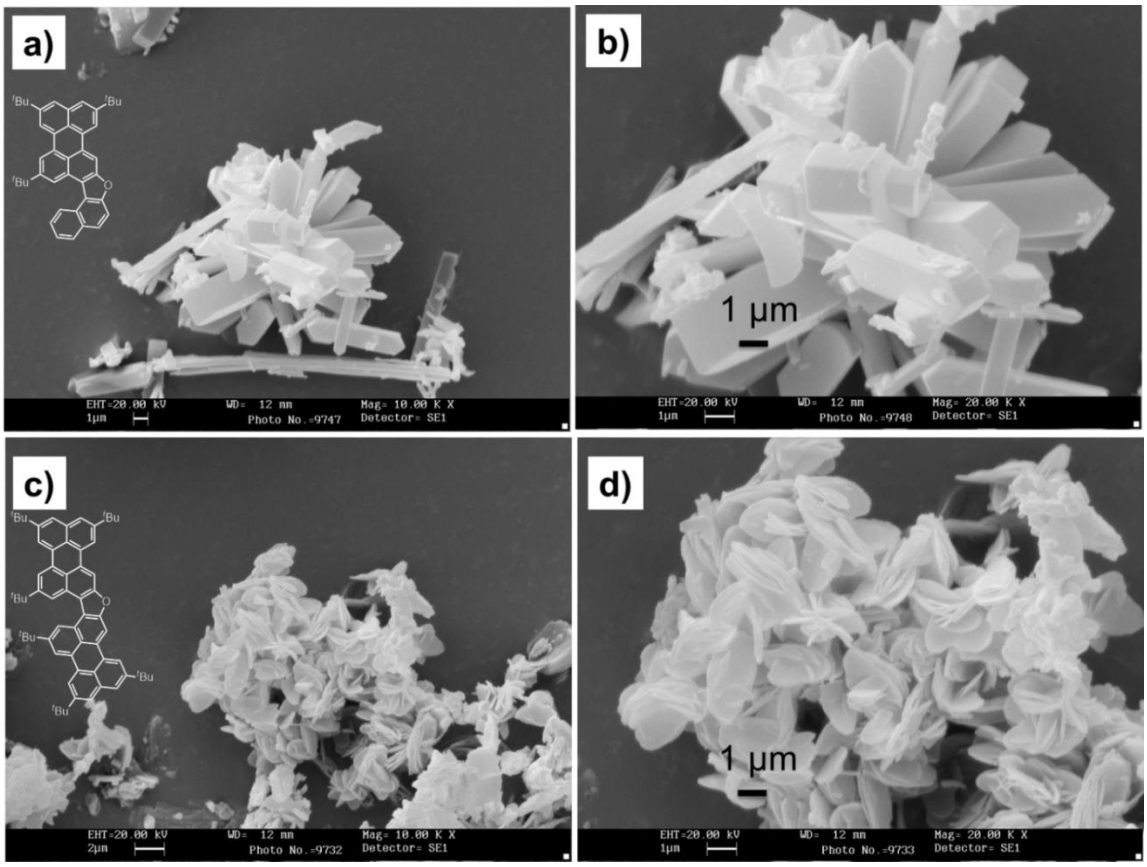

Figure 3.4.16 SEM images of the organic nanostructures obtained from a THF solution upon addition of MeOH for molecules **3-5^{Fur}** (a, b) and **3-6^{Fur}** (c, d).

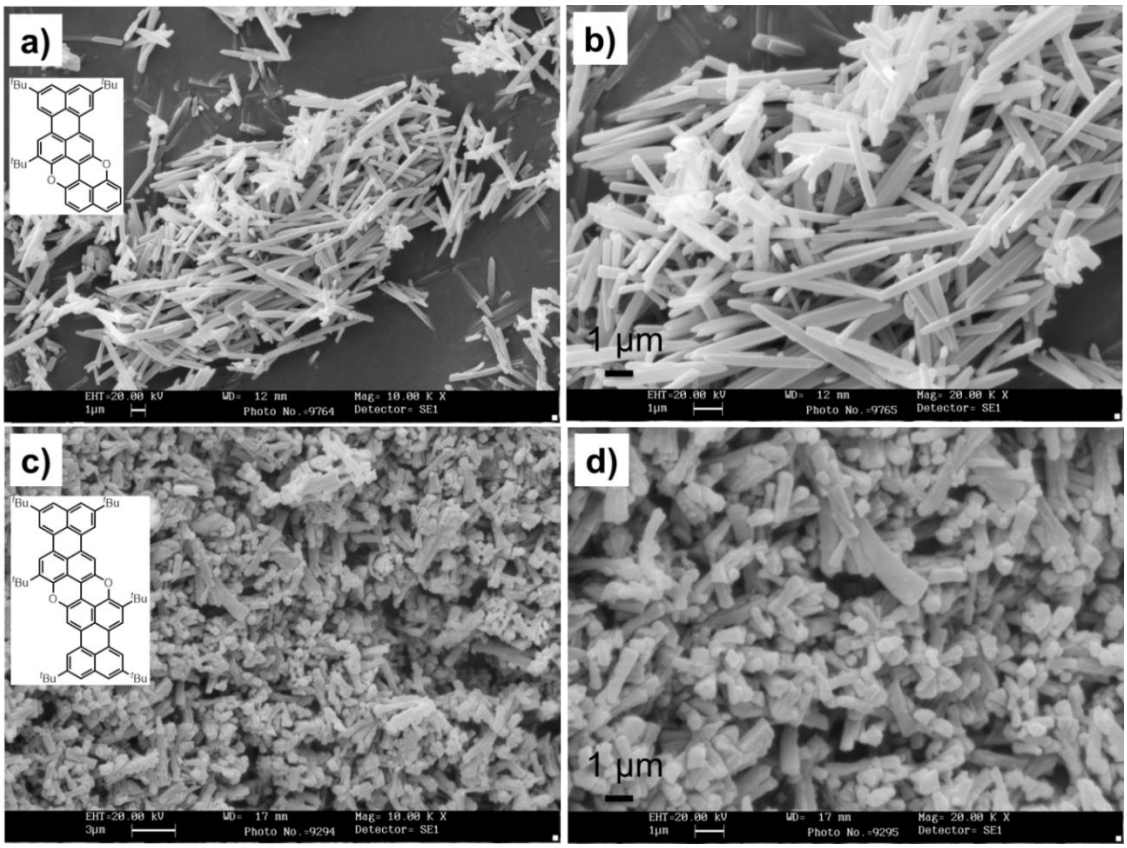

Figure 3.4.16 SEM images of the organic nanostructures obtained from a THF solution upon addition of MeOH for molecules **3-5^{Pp}** (a, b) and **3-6^{Pp}** (c, d).

Upon drop-casting from a 2 mM toluene solution on a silicon wafer, molecule **3-6^{Pp}** forms stick-like structures that appear brittle with size in the micrometer range.

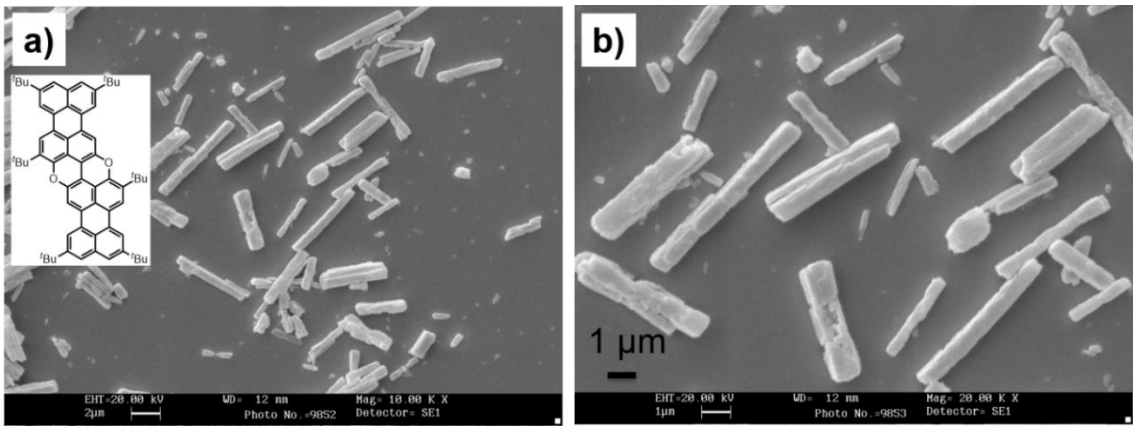

Figure 3.4.17. SEM images of the organic nanostructures obtained from a drop-casted 2 mM toluene solution on a silicon wafer for compound **6^{Pp}**.

3.4.6 Absorption and emission spectroscopy

In this section, the luminescent properties of *naphtalene-phenanthrene* (**3-9**, **3-7^{Fur}** and **3-7^{Pp}**), *napthalene-perylen*e (**3-3**, **3-5^{Fur}** and **3-5^{Pp}**) and *biperylene* (**3-4**, **3-6^{Fur}** and **3-6^{Pp}**) series of compounds are reported and compared with less conjugated reference molecules **3-8^{Fur}** (DNF) and **3-8^{Pp}** (PXX). UV-Vis and emission measurements were carried out in toluene solutions and depicted in figure 3.4.18. In particular, a detailed characterization of the fluorescence lifetimes (τ) and the fluorescence quantum yield (Φ) of the compounds has been performed using Single Photon Counter setup equipped with an integrating sphere. We systematically investigated the *(i)* π-extensions, *(ii)* planarization and *(iii)* oxygen-doping effects on the optical properties of prepared functional chromophores.

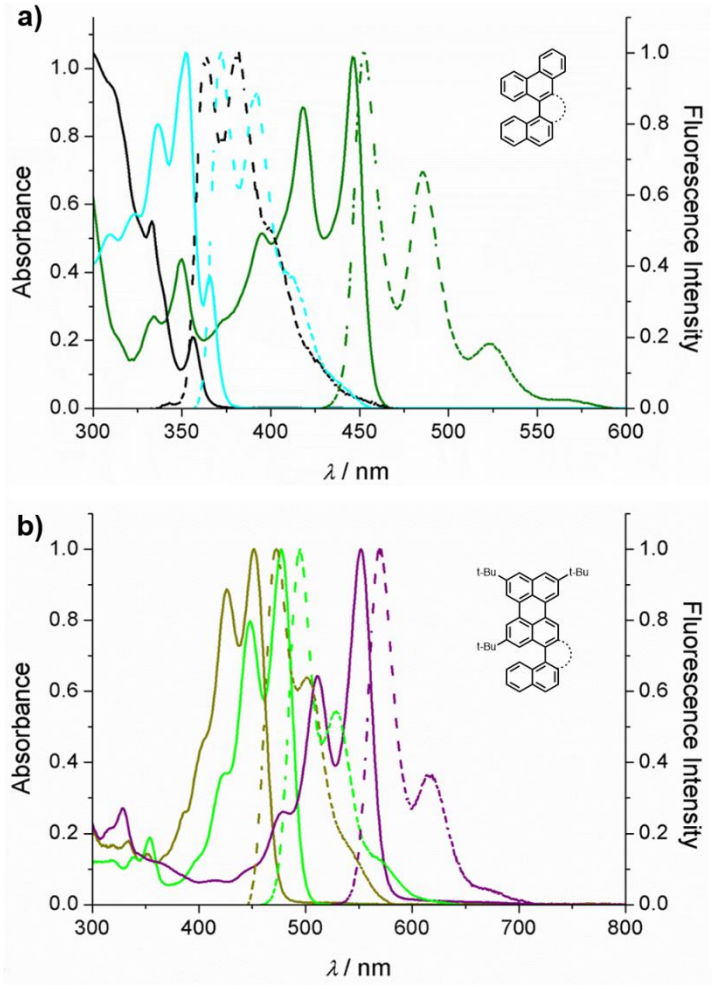

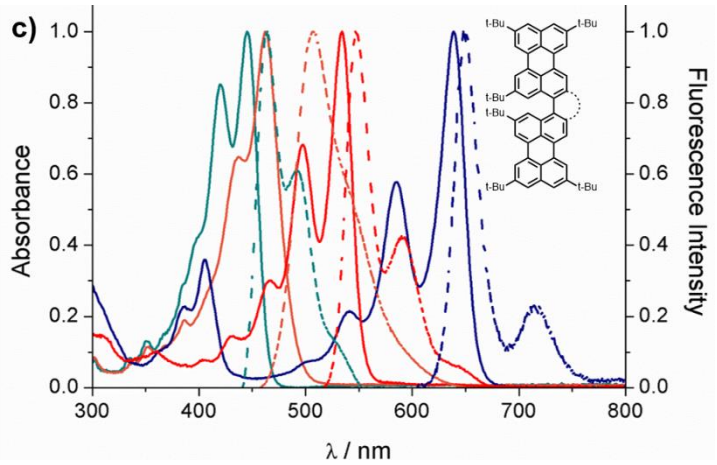

Figure 3.4.18. Normalized absorption (solid line) and emission (dotted line) spectra in toluene at 25 °C of (a) *naphthalene-phenanthrene* series: **3-9** (black), **3-7^{Fur}** (cyan) and **3-7^{Pp}** (olive); (b) *naphtalene-perylene* series: **3-3** (dark yellow), **3-5^{Fur}** (green) and **3-5^{Pp}** (purple) and of (c) *biperylene* series: **3-2** (dark cyan), **3-4** (orange), **3-6^{Fur}** (red) and **3-6^{Pp}** (blue).

UV-Vis absorption profiles show that within each class of compound the change of the dihedral angle leads to a bathochromic shift of the maximum absorption and emission wavelengths. For example, taking in consideration the *biperylene* family, changing the torsion angle from 62.8° for the diol derivative **3-4** to 16.7 ° for furanyl **3-6^{Fur}** a bathochromic shift of the maximum absorption band of 71 nm is observed. A further planarization of the system yields a red-shift of pyranopyranyl **3-6^{Pp}** to a value of 639 nm which is 105 nm shifted in respect to furanyl compound **3-6^{Fur}**.

For a better understanding of the relationship between the different structural features and the optical properties of the compounds, we will report a detailed analysis classifying the compounds in terms of dihedral angles (θ). To this end, three classes of compounds will be considered *diols* (**3-9**, **3-3** and **3-4**), *furanyls* (**3-7^{Fur}**, **3-5^{Fur}** and **3-6^{Fur}**) and *pyranyls* (**3-7^{Pp}**, **3-5^{Pp}** and **3-6^{Pp}**). The concept adopted for achieving higher order *diol*, *furanyl* and *pyranyl* PAHs by extending the aromatic scaffold along the molecular axis is given in Figure 3.4.19 The optical properties of all investigated compounds are summarized in table 3.4.4.

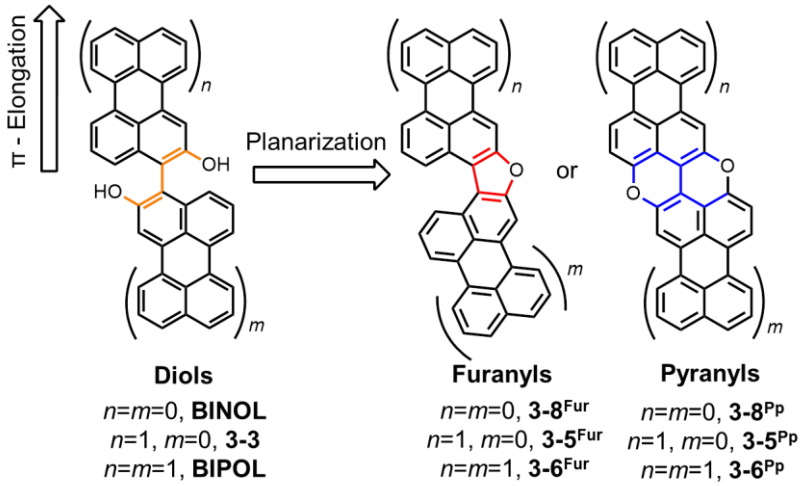

Figure 3.4.19. Schematic representation of the main families synthesized and concept of achieving higher order *diol*, *furanyl* and *pyranyl* PAHs by extending the aromatic scaffold along the molecular axis. Solubilizing *tert*-butyl groups were omitted for clarity.

Table 3.4.4. Optical properties of compounds **3-2** to **3-7**

Comp.	λ [nm][a]	ε [M^{-1} cm^{-1}]	Φ (%)	τ(ns)
3-7^{Fur}	352	26856 ± 195	0.43	5.7
3-7^{Pp}	446	14068 ± 129	0.48	4.8
3-2	445	25580 ± 169	0.55	4.9
3-3	452	33725 ± 232	0.66	3.7
3-4	463	64980 ± 216	0.88	2.7
3-5^{Fur}	477	47306 ± 119	0.84	3.0
3-5^{Pp}	556	36278 ± 360	0.50	3.8
3-6^{Fur}	534	97 449 ± 989	0.80	3.0
3-6^{Pp}	639	66417 ± 327	0.52	2.2

[a] UV-Vis absorption maximum in the visible region in toluene.

Absorption profiles of *diol* class of compounds are reported in Figure 3.4.20. For this family an initial shift towards longer wavelength absorption maximum from 333 nm for BINOL to 452 nm for molecule **3-3** was recorded**.** This strong shift of 119 nm towards the red can be attributed to extension of the aromatic BINOL core with one naphthalene unit (*n*=1, *m*=0) to achieve *naphthalene-perylene* derivative **3-3**. The introduction of a second naphthalene unit

leading to compound **3-4** (BIPOL where *n*=*m*=1) results in a less pronounced additional bathochromic shift of 11 nm. Derivative **3-4** demonstrates an absorption maximum at 463 nm with an absorption coefficient ε = 64980 ± 216 and a distinct bathochromic shift of Δλ ~ 107 nm compared to less conjugated *naphthalene-phenanthrene* **3-9**. It presents a strong fluorescence (Φ_{fl} = 0.88) with a Stokes shift of 44 nm. The emission profiles are reported in figure 3.4.18.

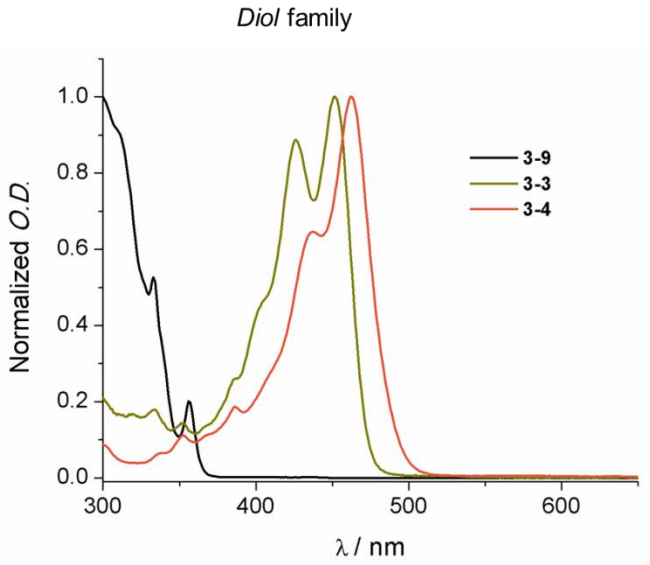

Figure 3.4.20 Normalized UV-Vis absorption spectra of di-hydroxy derivatives **3-9** (black), **3-3** (dark yellow) and **3-4** (orange) in toluene at 25 °C. All spectra were normalized by the maximum absorption peak.

Absorption profiles recorded for *furanyl* compounds are reported in Figure 3.4.21. The absorption spectrum of reference compound **3-8^{Fur}** features the typical electronic transitions at 326, 340 and 356 nm displaying a well-defined narrow profile. The introduction of one benzene unit to the simplest furanyl derivative resulted in a light bathochromic shift of 10 nm. Therefore, compound **3-7^{Fur}** displayed a multipeak band with well-defined structure with an absorption maximum at 352 nm (Figure 3.4.21). Compound **3-5^{Fur}**, exhibits a well-resolved absorption maximum at 477 nm. The enlargement of the conjugated system in **3-5^{Fur}** results in a strong bathochromic shift of 121 nm (ε = 47306 ± 119 M^{-1} cm^{-1}) towards less conjugated **3-8^{Fur}**. Further extension of **3-5^{Fur}** core with one additional naphthalene unit leading to compound **3-6^{Fur}**, results in an additional red shift of 57 nm. The latter absorbs very strongly in the UV−Vis region with an outstanding molar extinction coefficient of 97 450 M^{-1} cm^{-1}at 534 nm. Attributed to the extended π-system, its molar absorption coefficient is twice as high as **3-5^{Fur}**. Moreover, **3-6^{Fur}** has a small Stokes shift of 13 nm and a high quantum yield (Φ_{fl} = 0.80) meaning that a very high portion of the absorbed light is

reemitted. The extension of the π-surface of the DNF core results to be a prominent way of tuning the optical properties modifying the HOMO-LUMO gap of π-conjugates.

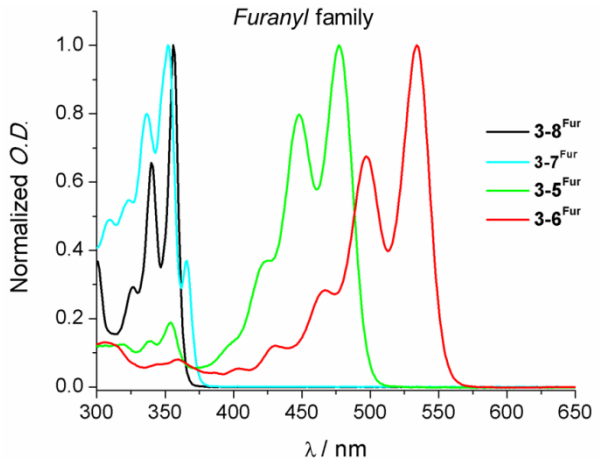

Figure 3.4.21. UV-Vis absorption spectra of **3-5-8^{Fur}** in toluene at 25°C. All spectra were normalized by the maximum absorption peak.

Absorption profiles recorded for *pyranyl* compounds are displayed in Figure 3.4.22. Compound **3-7^{Pp}** in which the PXX core was increased with one benzene unit had a similar absorption and emission profiles to PXX. The simplest PXX derivative prepared has molar extinction coefficient of 14068 ± 129 M^{-1} cm^{-1} at 446 nm. A bathochromic shift of only 1 nm is recorded in comparison to PXX (λ_{max} = 445 in toluene). Whereas, optical properties of **3-5^{Pp}** were strongly bathochromically shifted relative to PXX, thanks to its extended π-systems ($\Delta\lambda$ = 111 nm). In fact, insertion of one naphthalene unit onto the PXX core results in a strong absorption in the UV−Vis region with a molar extinction coefficient of 36278 M^{-1} cm^{-1} at 556 nm. Investigated molecule has a Stokes shift of 19 nm and a quantum yield of 0.50. Interestingly, the absorption spectrum of **3-6^{Pp}** displays a drastic bathochromic shift (195 nm, 175 nm) compared with those of PXX and BIPOL **3-4**, respectively, leading to a great degree of planarity and large delocalization of π-electrons. An absorption maximum in the far red region at 639 nm, a Stokes shift of 9 nm and a quantum yield of 0.52 characterize the most extended PXX derivative synthesized.

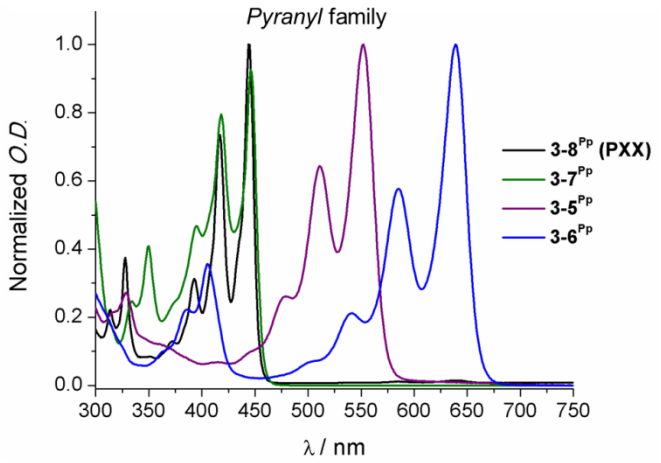

Figure 3.4.22. UV-Vis absorption spectra of **3-8^{Pp}, 3-7^{Pp}, 3-5^{Pp}** and **3-6^{Pp}** in toluene at 25°C. All spectra were normalized by the maximum absorption peak.

In Figure 3.4.23, we report the excitation and emission spectra of 5.46 x10^{-7} M **3-6^{Pp}** solution in toluene. The excitation and fluorescence spectra are well defined structured and mirror image of each other. The excitation spectrum shows bands appeared at 545 nm, 585 nm, with maximum at 639 nm and matches well with absorption spectrum. The optical HOMO-LUMO gap estimated from the absorption spectrum is 1.9 eV. The increased number of aromatic rings among the highly planar derivatives results in a red shift of the maximum absorption band, indicating that the π-conjugated systems are more effectively delocalized over large molecules.

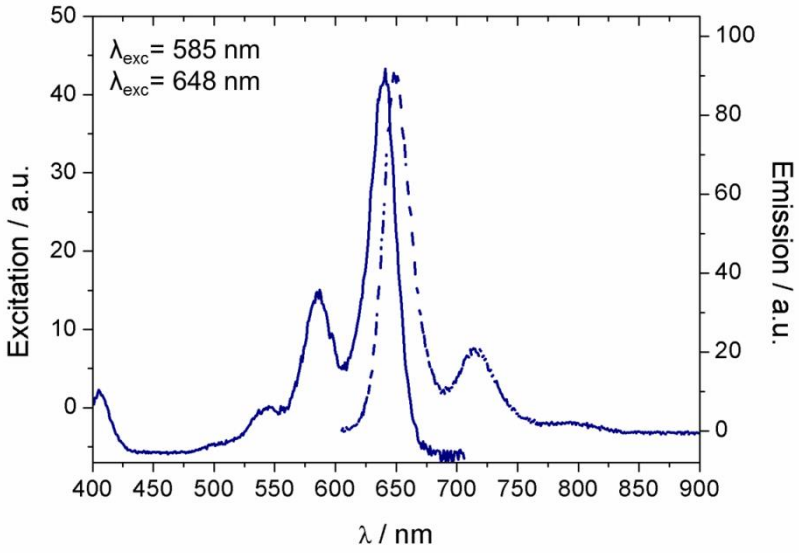

Figure 3.4.23. Excitation (solid line) and emission (dotted line) spectra of perylene derivative **3-6^{Pp}** in toluene at 25 °C.

Recapitulating, for *diol* compounds a significant red shift is observed with the first elongation of the molecular core, followed by a negligible bathochromic shift for the further

aromatic extension. This trend can be attributed to the orthogonal arrangement of the neighbouring aryl rings. In contrary, a strong linear correlation between the maximum absorption wavelength and the π-extension of the aromatic core for *pyranyl* derivatives is observed. Such linearity is not recorded for *furanyl* compounds, indicating that the extension of the π resonance system depends on the shape of the aromatic systems and the conjugation of the π fragments. Such sharp linear relationship is typical for planar systems such as acenes and rylenes, and can be attributed to the effective spread of the π resonance over the entire molecule.[63] The correlation curves for *diols*, *furanyls* and *pyranyls* series are depicted in Figure 3.4.24.

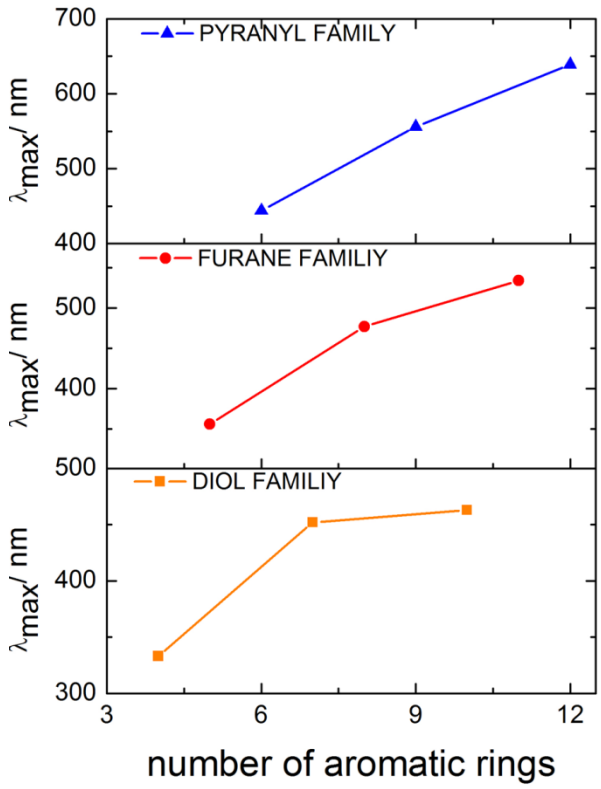

Figure 3.4.24. Study of the π-extension and planarization effect on optical properties of novel perylene-based functional dyes

Moreover, the *furanyl* compounds synthesized (**3-7^{Fur}**, **3-5^{Fur}**and **3-6^{Fur}**) displayed bright fluorescence in the solid state as shown in Figure 3.4.25. While, despite the appreciable fluorescence properties in solution of pyranopyranyl derivatives **3- 5^{Pp}** and **3-6^{Pp}**, no fluorescence is observed for theses dyes in the solid state. The reason might be attributed to the packing arrangement in the dye.

Figure 3.4.25 Photographs of fluorescent powders of compounds **3-7**^{Fur}, **3-5**^{Fur} and **3-6**^{Fur} upon illumination with UV light (365 nm)

In conclusion, higher order *furanyl* derivatives have been characterized by relatively narrow absorption and emission bands, high molar absorption coefficients, and high fluorescence quantum yields, thus making them attractive for a wide range of applications. From the other hand planar *pyranopyranyl* derivatives represent a very intriguing class of compounds where the molecule **3-6**^{Pp} displayed high absorption in the visible range and appreciable emission, reaching the near infrared region. The relatively high fluorescence quantum yield measured for this compound is unusual if compared with higher order rylenes such as *tert*-butyl quatterylene where only poor fluorescence quantum yields are recorded.

The new synthesized dyes exhibit a rainbow of colors as well as tunable spectroscopic properties (Figure 3.4.26). Their absorption and emission maxima can be finely shifted throughout the entire visible region by changing the π-extension of the aromatic scaffold and by planarization of oligonaphthalenes into furane and pyran frameworks. All synthesized compounds are characterized by monoexpontial lifetimes in the range of 2-5 ns. More similarly to oligorylene bisimides, the access to different O-doped π-extended derivatives make them interesting candidates as donor as well as acceptor chromophores for energy- or electron-transfer studies offering probably the opportunity to selectively excite a particular O-doped π-extended homologue (for example, **3-7**^{Pp}, **3-5**^{Pp}, **3-6**^{Pp}).

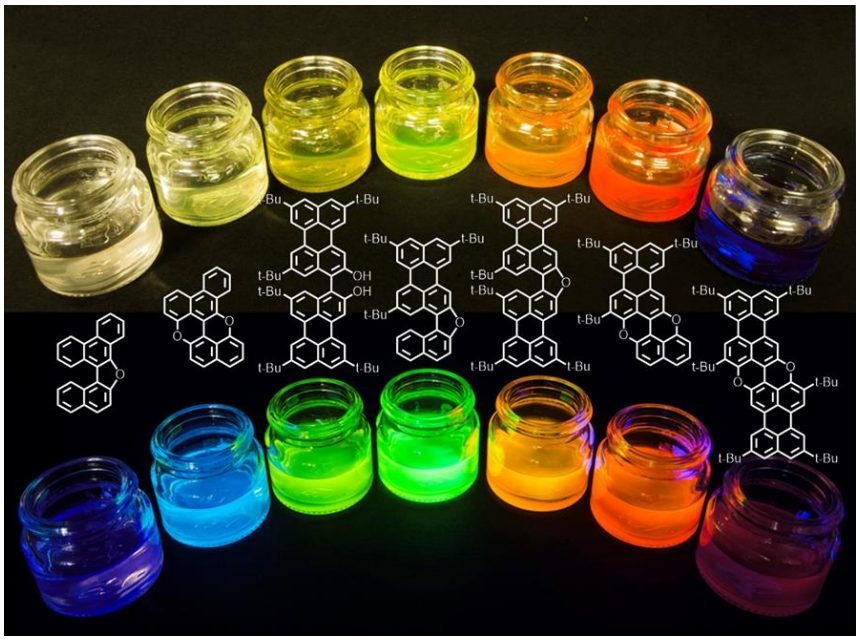

Figure 3.4.26. Image of compounds in toluene solution (from left to right) **3-7^{Fur}**, **3-7^{Pp}**, **3-4**, **3-5^{Fur}**, **3-6^{Fur}**, **3-5^{Pp}** and **3-6^{Pp}** under visible (top) and UV light (bottom).

3.4.7 Thermogravimetric analysis (TGA)

The thermal behavior of biperylene-compounds was evaluated to understand their chemical stabilities against heated conditions, which is an important factor for achieving thermally durable organic materials. Thus**,** TGA analysis of compounds **3-4**, **3-6^{Fur}**, **3-6^{Pp}** and reference compound **3-8^{Pp}** (PXX) was carried out with a heating rate of 10 °C/min under N_2 atmosphere in the temperature range between 100-700 °C and recorded results are portrayed in Figure 3.4.27. The sublimation point of the PXX was determined to be around 265 °C by TGA, while the data recorded for biperylene derivatives reveal that they all have outstanding thermal stability with none of them showing mass loss up to 408, 470 and 505 °C for **3-4**, **3-6^{Fur}**, and **3-6^{Pp}** respectively. The complete evaporation of the solids after the TGA run, suggested that the sharp single step loss recorded for all derivatives can be attributed to their sublimation temperature.

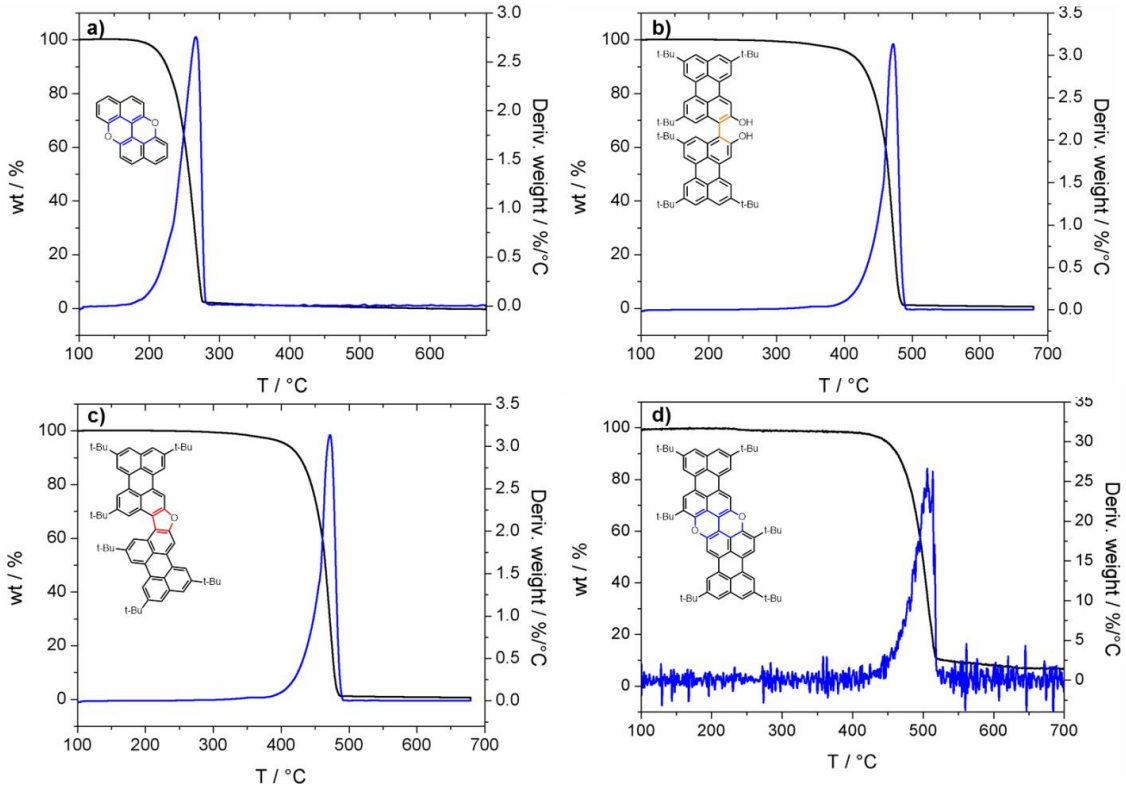

Figure 3.4.27. TG curves (black) and corresponding DTG curves (blue) of (a) **3-8^{Pp}**, (b) **3-4**, (c) **3-6^{Fur}**) and (d) **3-6^{Pp}** with a heating rate of 10°C/min under N_2 atmosphere.

3.5. Toward the functionalization of pyranopyranyl core

One important parameter in the design of novel functional chromophores along with the fine regulation of the energy band-gap, self-organization, charge carrier mobility and chemical inertness and high-thermal stability, is the possibility to attach molecular recognition units to the molecular core. In this regard, the development of reliable, simple and high yielding methodology to attach different functional groups or moieties to a core molecule is extremely important in view of the increasing complexity of molecular systems.[27,113,114] That permits, for instance, the incorporation of photoactive fragments into biomolecules, surfaces,[115] polymers or multicomponent organic materials for fluorescence sensing, light harvesting or solar cells.[116]

Accordingly, this research project started with the aim to extend previous achievements to the development of a second class of precisely substituted π-extended PXX derivatives, with further possibilities of solubility, energy and optical tuning. Therefore, we sought to prepare soluble π-extended PXX derivatives bearing additional functionalization sites. This might be achieved modifying the π-extended PXX core in *peri* positions by introducing a good reactive group which would allow the exploitation of numerous versatile reactions (Figure 3.5.1). In this respect, we propose to introduce triflates substituents onto PXX core that can easily undergo cross-coupling reactions (*i.e. Sonogashir*a or *Suzuki* cross-coupling reaction). Indeed, the chemistry of aryl triflates, has been amply explored and applied to a large array of chemical transformations of aromatic compounds such as carbon-carbon bond formation.[117]

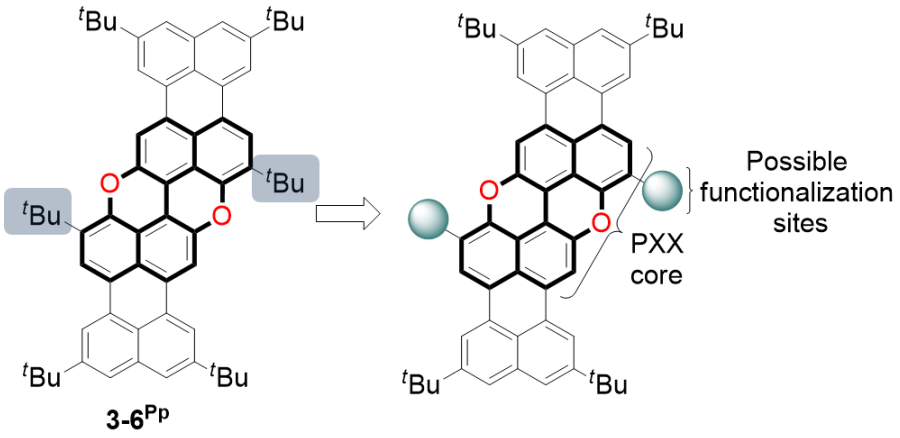

Figure 3.5.1. Molecular structure of a second generation of π-extended PXX derivatives presenting functionalization in positions 5 and 15.

3.5.1 Retrosynthetic strategy

In particular, we wanted to insert acetylene moieties at positions 5 and 15 of desired molecule **3-20** as shown in scheme 3.5.1. The synthetic strategy follows the same pathway described for its *tert*-butyl substituted equivalent $\mathbf{6^{Pp}}$ apart from the use of a new building block, perylene boronic ester **3-11** that replaces perylene **3-1** in the previous pathway.

A straightforward approach exploiting a Cu (II) mediated C-C oxidative coupling by combination of two methoxyperylen-2-ol **3-15** was adopted. Further cyclization of **3-17** using previously developed protocol, followed by demethylation should provide the precursor of desired fully conjugated O-fused derivative $\mathbf{3\text{-}14^{Pp}}$. The latter molecule presents two free hydroxyl groups which can be further functionalized. A triflation reaction followed by a *Sonogashira* cross-coupling protocol for the insertion of an acetylene group as anchor for further derivatization was thought to be a suitable route.

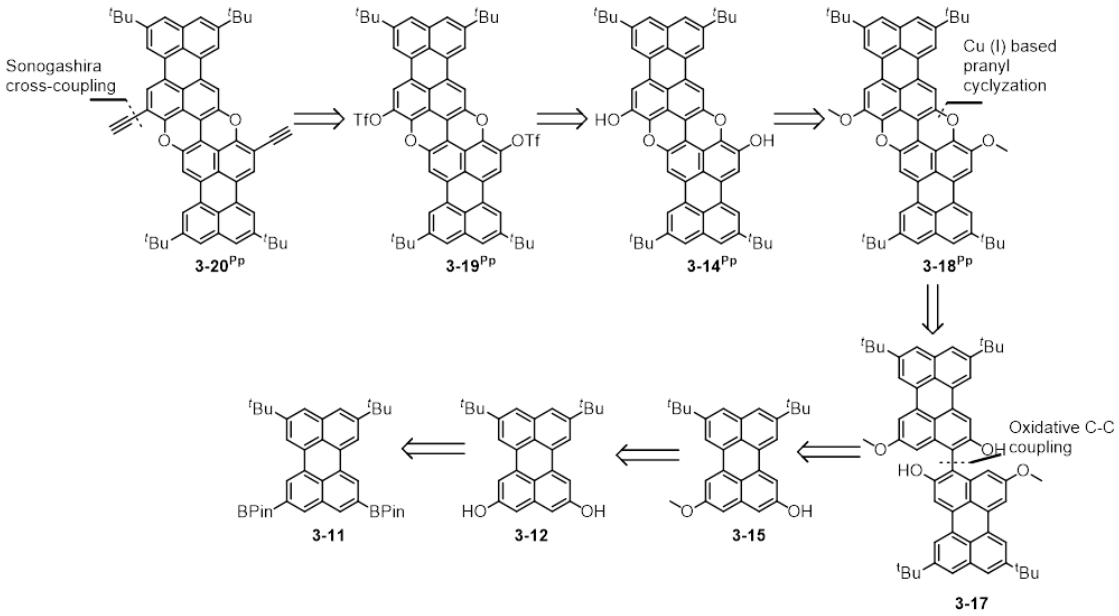

Scheme 3.5.1. Retrosynthesis of compound $\mathbf{3\text{-}20^{Pp}}$

3.5.2 Toward the synthesis of functionalized pyranopyrayl compounds

To commence, perylene derivative **3-11** (prepared starting from commercially available perylene through a two-step reaction protocol reported in the first section of this chapter) was oxidized into dihydroxy perylene **3-12** by treatment with an H_2O_2 aq. solution and NaOH in THF. Using 3 equivalents of NaOH and H_2O_2 per hydroxyl group, desired compound **3-12** was obtained in 36% yield together with coupled tetrahydroxyl biperylene **3-13** in 63% yield (entry 1, table 3.5.1). The chemical structure of **3-13** was confirmed by

^{1}H-, ^{13}C-NMR, UV-Vis, IR, and ESI-HRMS (*Chapter IV, appendix*). ^{1}H-NMR spectrum of compound **3-13** is reported in Figure 3.5.1 We were also able to detect the formation of a third unknown compound (bluish in color) in the reaction mixture.

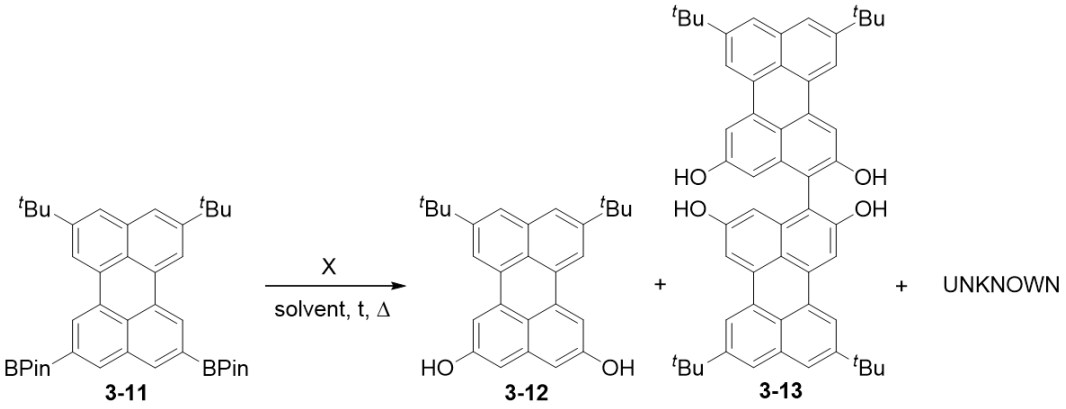

Table 3.5.1 Conditions tested for the oxidation reaction of derivative **3-11**.

Entry	X (equivalents)	Solvent	°C/time	Compound/Yield (%)
1	NaOH **6 Eq.** H_2O_2 **6 Eq.**	THF	r.t., 2 h	**3-12** (36 %) **3-13** (63 %)[a]
2	NaOH **2 Eq.** H_2O_2 **2 Eq.**	THF	r.t., 2 h	**3-12** (77 %) **3-13** (1 %)[a]
3	NaOH **10 Eq**. H_2O_2 **10 Eq.**	THF	r.t., 24 h	**3-12** (19 %) **3-13** (27 %) **unknown** (10 %)
4	NaOH **50 Eq.** H_2O_2 **50 Eq.** THF	THF	r.t., 24 h	**unknown** (49 %)[b]

[a] Unknown compound detected in traces but not quantified;
[b] Reaction performed on 100 mg of starting material. Compounds **3-12** and **3-13** were not separated (47 mg of a mixture of both molecules was recovered after precipitation).

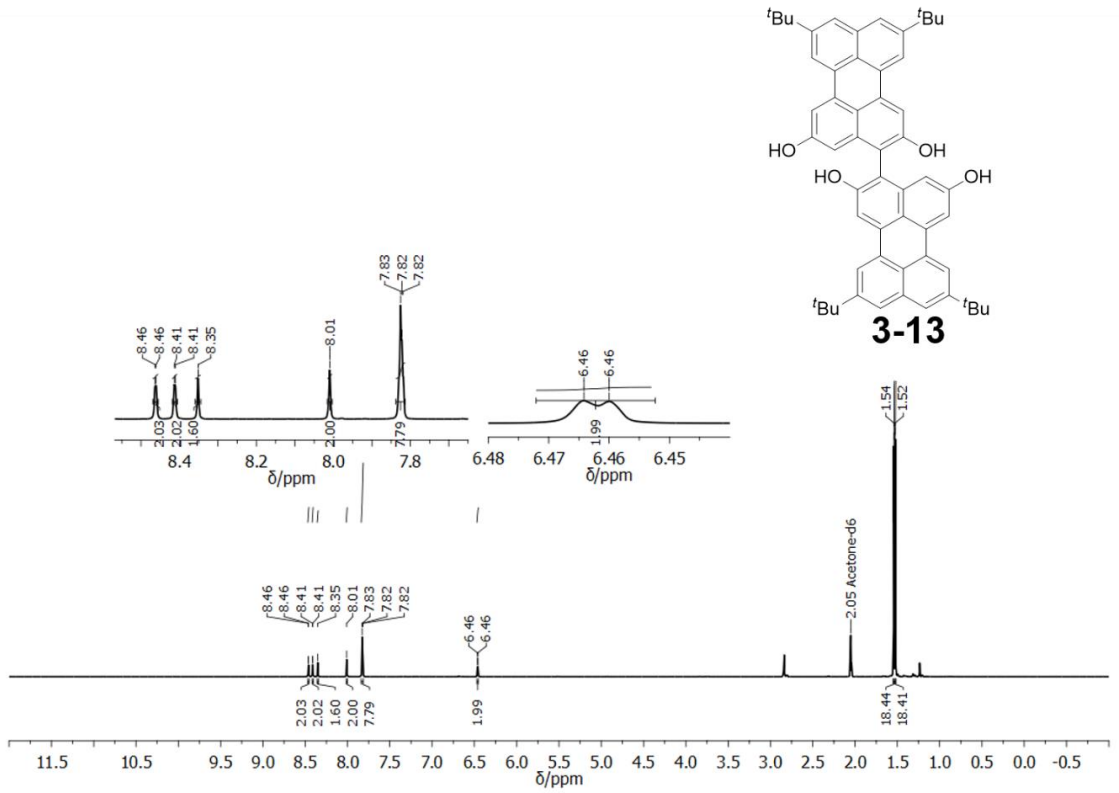

Figure 3.5.1 ^{1}H-NMR (500 MHz) spectrum in acetone-d_6 at 25 °C of **3-13** (inset: zoom of the aromatic region).

Two different strategies were adopted to study the oxidation reaction of compound **3-11**. In the first attempt with the aim to increase the yield of diol **3-12** by decreasing the formation of collateral by-products, we performed the oxidation reaction using a reduced amount of NaOH and H_2O_2. Desired dihydroxyl derivative **3-12** was isolated in 77 % yield as shown in entry 2 of table 3.5.1. Dihydroxyl perylene **3-12** was found to be highly unstable in solution at ambient conditions. In fact, a yellow CH_2Cl_2 solution fleshly prepared of **3-12** turned dark green immediately, resulting in a mixture of by-products.

In the second case, with the aim to investigate the formation of the unknown compound detected before, we decided to perform the oxidation reaction working in a large excess of NaOH and oxidizing agent (entry 3 and 4, table 3.5.1). The reaction was moved toward the formation of the bluish compound treating perylene derivative **3-11** with 50 equivalents of NaOH and H_2O_2 for 24 h under open air conditions. The unknown compound was obtained after several re-precipitation cycles from THF/cold MeOH and analyzed by NMR using DMSO-d_6. ^{1}H-NMR spectrum consists of 6 aromatic peaks and two singlet signals at 1.54 ppm. The low intensities of the peaks account for the poor solubility of the compound in chosen solvent. Moreover, the ^{13}C-NMR spectrum could not be recorded. By MALDI-HRMS analysis it was possible to detect a peak at 786.3732 *m/z*. Both characterization

spectra are reported in Figure 3.5.2. Even if preliminary ^{1}H-NMR and MALDI-HRMS results show us a clean pattern, we were not able to precisely assign a chemical structure.

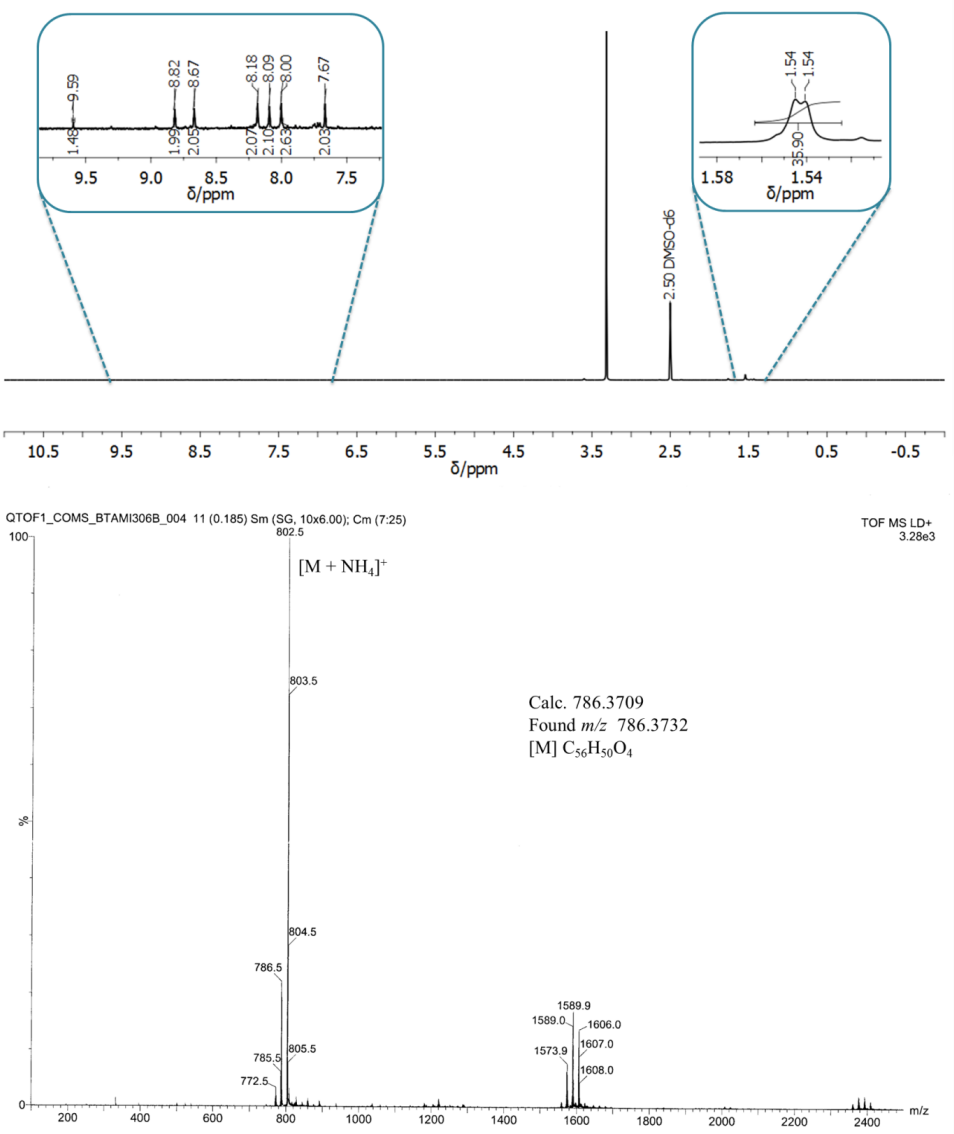

Figure 3.5.2. ^{1}H-NMR (500 MHz) spectrum in DMSO-d_6 at 25 °C (top) (left inset: zoom of the aromatic region; right inset: zoom of the aliphatic region) and MALDI-TOF HRMS (bottom) of unknown derivative obtained from oxidation reaction of **3-11**. .

Driven by the obtained results and with aim to identify the unknown derivative we added to the optimized oxidation conditions (entry 4, table 3.5.1) a step of triflation. In particular, perylene derivative **3-11** was treated with an aq. solution of H_2O_2 (35 % wt) in the presence of a large excess of NaOH in THF for 24 h. (scheme 3.5.2)- Subsequently the reaction crude was directly submitted to triflation reaction in the presence of triflic anhydride and DIPEA in CH_2Cl_2 at r.t. and monitored by t.l.c. After 4 h complete conversion of starting materials

was detected leading to a mixture of three compounds. Their structures are reported in scheme 3.5.2 and correspond to the perylene bistriflate **3-22** and biperylene tetratriflate **3-23**. Moreover, we were able to identify the structure of the third compound which corresponds to quatterylene **3-21**.

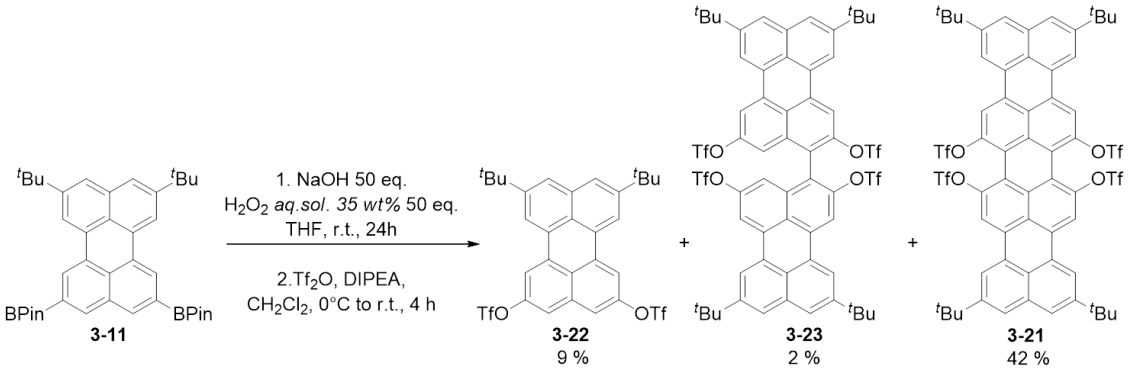

Scheme 3.5.2. Synthesis of quatterylene derivative **3-21**.

Compounds **3-22** and **3-23** were isolated in 9 % and 2 % yield, respectively and fully characterized in terms of melting point, ^{1}H-, ^{13}C-NMR, IR, UV-Vis spectroscopy and HRMS spectrometry (*chapter IV*). Additionally, yellow needle-like crystals suitable for x-ray analysis were grown by slow evaporation of an acetone-d_6 solution of perylene derivative **3-22**. Figure 3.5.3 displays the crystal structure of **3-22** together with the π-π packing arrangement of the crystal (crystallographic data and refinement details are reported in *chapter V*). Module **3-22** arranges at the solid state according to a *P nna* space group. Specifically, the crystal packing of **3-22** shows strong perylene π–π stacking, forming pillars parallel to unit cell axis *b*. Pillars are tightly packed through hydrophobic contacts among peripheral *tert*-butyl and triflate substituents. No solvent molecules have been found in the crystal.

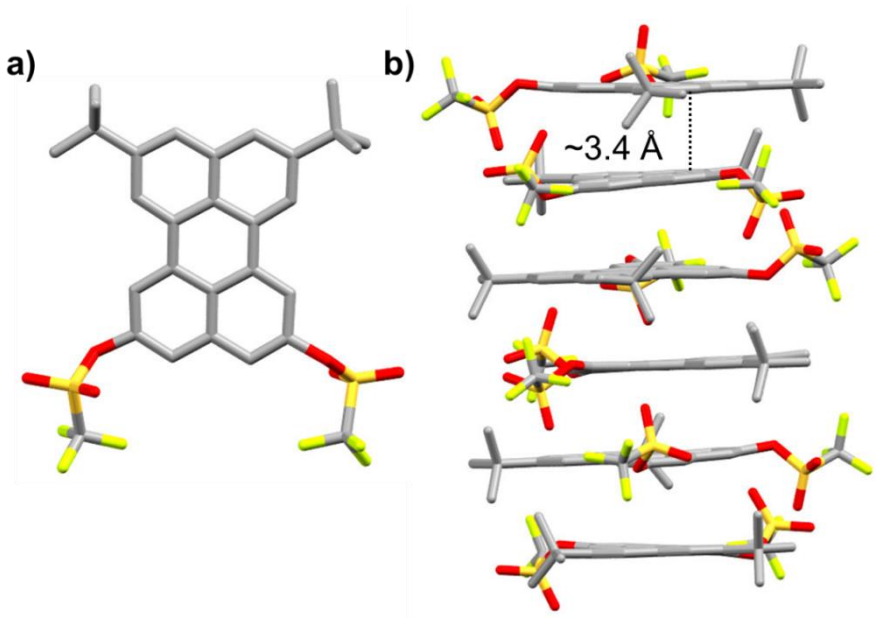

Figure 3.5.3. (a) Top-view of the crystal structure and (b) side-view aof π-π packing arrangement of **3-22** (space group: P_{nna}; $C_{30}H_{26}F_6O_6S_2$; 50% probability ellipsoids). The asymmetric unit contains two crystallographically independent molecules. Hydrogens omitted for clarity.

Such synthetic protocol permits us to isolate for the first time quarrylene **3-21** (42 %) bearing triflates substituent in quatterylene *peri* positions. **3-21** showed a high solubility in all the common organic solvents, *i.e*. hexane, CH_2Cl_2, $CHCl_3$, THF, EtOAc, acetone, and MeOH. This good solubility can be attributed to the twisted bay region due to the presence of bulky triflate groups. NMR spectroscopy in benzene-d_6 of **3-21** showed simple ^{1}H NMR spectrum consisting of two doublet signals (J~1.5) in the region of 8.31-7.71 ppm, one singlet signal at 8.52 ppm and a singlet signal at 1.32 ppm that can be assigned to *tert*-butyl groups (Figure 3.5.4).

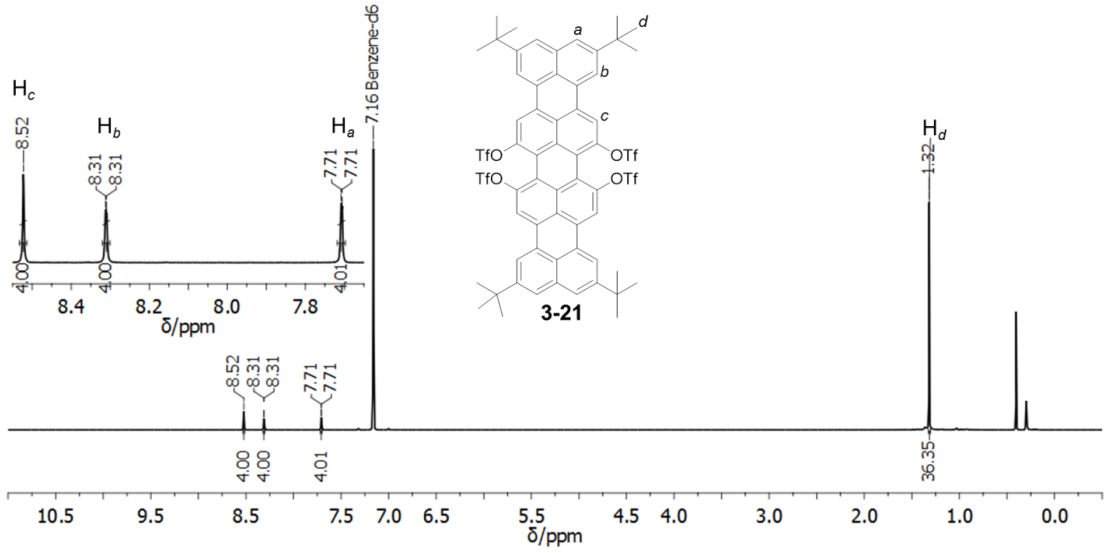

Figure 3.5.4. ^{1}H-NMR (500 MHz) spectrum in C_6D_6 at 25 °C (inset: zoom of the aromatic region) of quaterrylene derivative **3-21**.

In addition, dark-blue needle-like crystals of **3-21** suitable for single-crystal X-ray analysis, obtained by slow evaporation of the solvent from a deuterated benzene solution, were grown. The crystal structure is displayed in Figure 3.5.5 and found to belong to the monoclinic space group *P* $2_1/n$. Compound **3-21** crystallized with one moiety in the unit cell. Hydrophobic CH-π contacts keep the molecules packed and limited π–π stacking among symmetry related molecules can be seen in crystal forms. Perylenes moieties delimit cavities filled by benzene molecules. Higher electronic delocalization improves flatness and the angle between average planes of the two halves of the molecule reduces to 48°. Furthermore, packing and steric hindrance of peripheral *tert*-butyl substituents deform perylene planarity, the angle between naphthyl portions of each perylene unit results to be of ~12.4 °. In fact, bulkier triflate groups increase the perylene distortion inducing a helicoidal shape in the molecule. This considerable twisting of the rylene backbone might inhibit strong π–π interactions. Left and right handed helices are packed in the solid state with equal abundance (related by crystallographic inversion centers). Essential crystal and refinement data are reported in *appendix*.

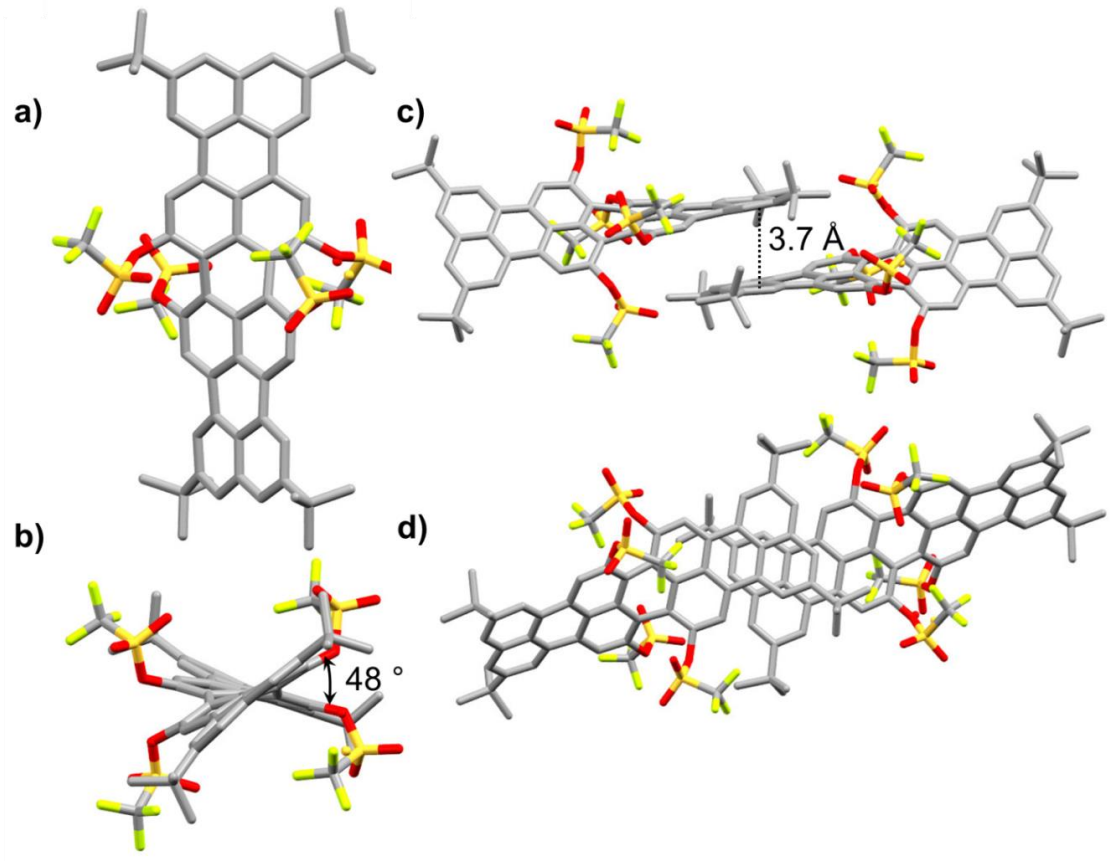

Figure 3.5.5. a, d) Top-view and b, c) side-view of the crystal structure and π-π packing arrangement of **3-21** (space group: *P* $2_1/n$; $C_{60}H_{48}F_{12}O_{12}S_4 \cdot 2C_6H_6$; 50% probability ellipsoids). The asymmetric unit contains one crystallographically independent molecule and two benzene molecules. Hydrogens were omitted for clarity.

3.5.3 Rational for the formation of product 3-21

Calderon and *Thomson* reported in 1988 the formation of the tautomeric dihydroxyperylenequinone (**3-27**) starting from naphthalene-2,7-diol through the formation of its tetrahydoxyl dimer (Figure 3.5.6 a). The autoxidation reaction of the dehydro naphthalene dimer was achieved either by adsorption of the substrate onto silica gel exposed to air or by stirring it in a diluted aq. solution of NaOH under air atmosphere,[118] suggesting that electron-rich substrates undergo dehydrogenation reaction under mild conditions. Analogously, we can assume that the structure of the precursor of quatterylene **3-21** is ascribable to dihydroxyquatterylene-quinone **3-14^{Qq}** as depicted in Figure 3.5.6 b, meaning that dimer **3-13** undergoes dehydrogenation reaction in the presence of NaOH and H_2O_2. This is in accordance with the preliminary ^{1}H-NMR and HRMS spectra obtained for the unknown compound obtained after oxidation of **3-11**.

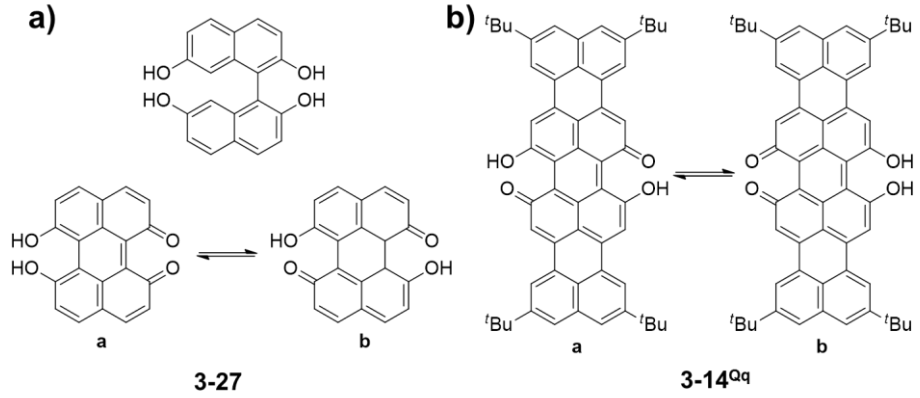

Figure 3.5.6. (a) tautomeric dihydroxyperylenequinone **3-27** (bootom) synthesized from tetrahydroxyl binaphthalene (top) and (b) assumed structure of dihydroxyquatterylene-quinone **3-14^{Qq}**

3.5.4 Toward the synthesis of triflate derivative 3-19^{Pp}

In light of the described results, we proceeded with the synthesis of pyranopyranyl derivative **3-20** as previously discussed. Due to the susceptibility of the dihydroxy diperylenyl moiety under oxidative conditions, we perform a first mono-methylation reaction to protect one hydroxyl group of **3-12**. The synthetic pathway undertaken for the synthesis of intermediate **3-19^{Pp}** is display in scheme 3.5.3.

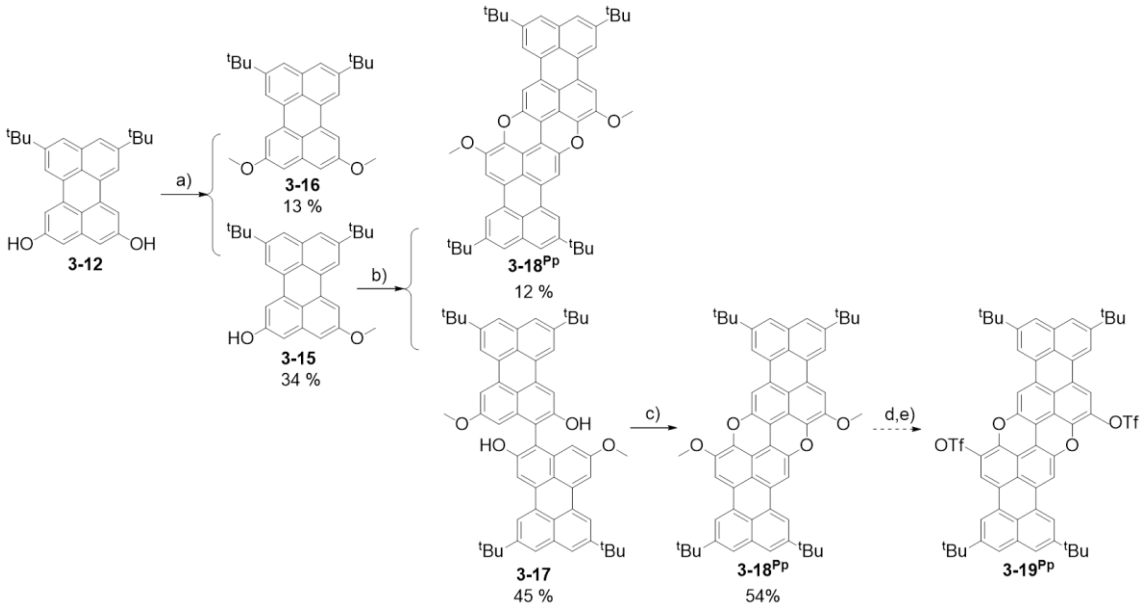

Scheme 3.5.3 Synthetic pathway toward the preparation of **3-19^{Pp}**. Reagents and conditions: a) MeI, K_2CO_3, reflux, 12 h then 3 h r.t., Ar; b) [Cu(OH)(Cl)TMEDA], air, CH_2Cl_2, 20 °C, 1 h; c) CuI, PivOH, DMSO, 140 °C, 2 h; d) BBr_3, CH_2Cl_2, r.t., 12 h, Ar; e) Tf_2O, DIPEA, r.t., 12 h, Ar.

Compound **3-15** (34 %) was obtained by mono-alkylation reaction of dihydroxyl perylene **3-12** by treatment with MeI in the presence of K_2CO_3 in acetone. Alkylation reaction is not preferential and the di-alkylated product **3-16** is obtained (13 %). Molecule **3-15** was then coupled to give BIPOL derivative **3-17** using the analogous protocol to prepare **3-4**. Oxidative coupling of methoxyperylen-2-ol was achieved with the use of stable Cu-TMEDA complex under open air condition. The copper-TMEDA catalyst confirms its effectiveness in catalyzing the oxidation reaction. However, the reaction afforded biaryl product **3-17** in moderate yield (45 %) and further oxidation also occurs to give cyclized derivative **3-18^{Pp}** (12 %) and unidentified by-products. Formation of **3-18^{Pp}** was proved by applying CuI-mediated pyran ring protocol to dimethoxy biperylen-diol **3-17** to obtain derivative **3-18^{Pp}** in appreciable yield as blue powder. Also in this case the purification of pyranopyranyl **3-18^{Pp}** by chromatography was found to be difficult due to adsorption of the compound on SiO_2. Analogously to parent **3-6^{Pp}**, compound **3-18^{Pp}** was purified by repetitive re-precipitation cycles form THF/MeOH. The formed precipitate exhibits reduced solubility in comparison with **3-6^{Pp}** that hampered the record of a relevant ^{1}H-NMR spectrum. In fact, at r.t. ^{1}H-NMR spectrum of compound **3-18^{Pp}** shows very poor solubility in toluene-*d*$_8$ and no signals in the aromatic region were detectable. At higher temperatures barely resolved pattern was recorded as depicted in Figure 3.5.7. The ^{1}H-NMR spectrum reports three areas of peaks; the compound shows six signals in the region between 8.03-7.58 ppm related to 12

aromatic hydrogen atoms, one singlet signal at 3.69 ppm attributed to methoxy substituents and three different *tert*-butyl substituents are visible at 1.59, 1.43 and 1.36 ppm (*appendix*). In particular, the ^{1}H-NMR analysis presented an analogous pattern as described above for pyranopyranyl **3-6^{Pp}**, but in this case the integration was not possible. However, characterization of **3-18^{Pp}** was accomplished by melting point, IR, UV-Vis spectroscopy (*Chapter IV*) and MALDI-HRMS spectrometry (Figure 3.5.8), registering the molecular mass [*M*] at 814.4013 *m/z***.**

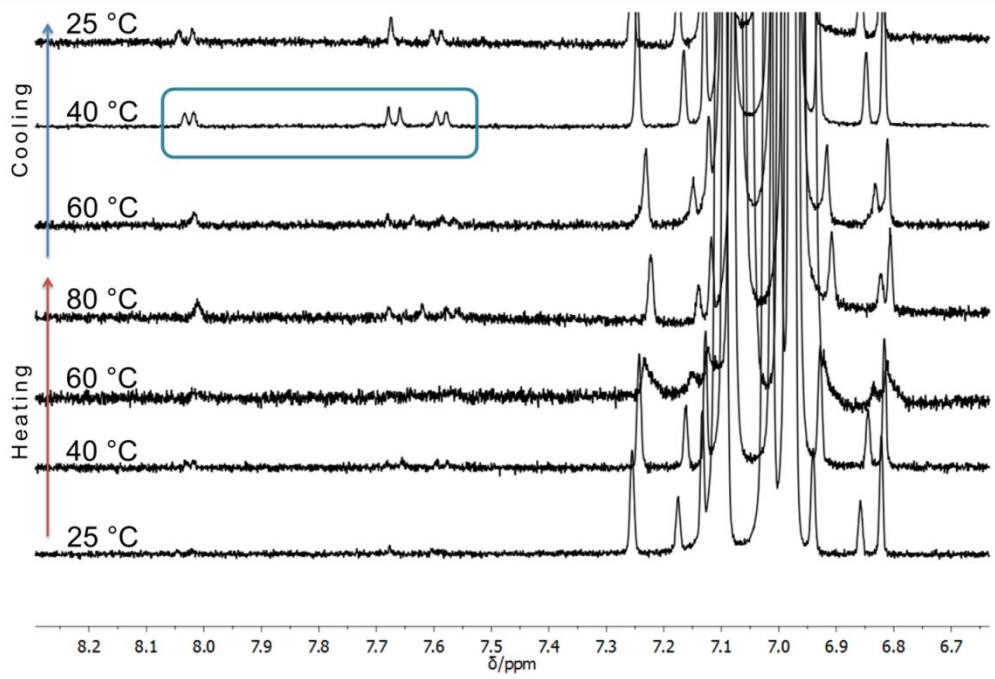

Figure 3.5.7. VT-^{1}H-NMR (500 MHz) spectral changes of **3-18^{Pp}** from r.t. to 80 °C in toluene-d_8.

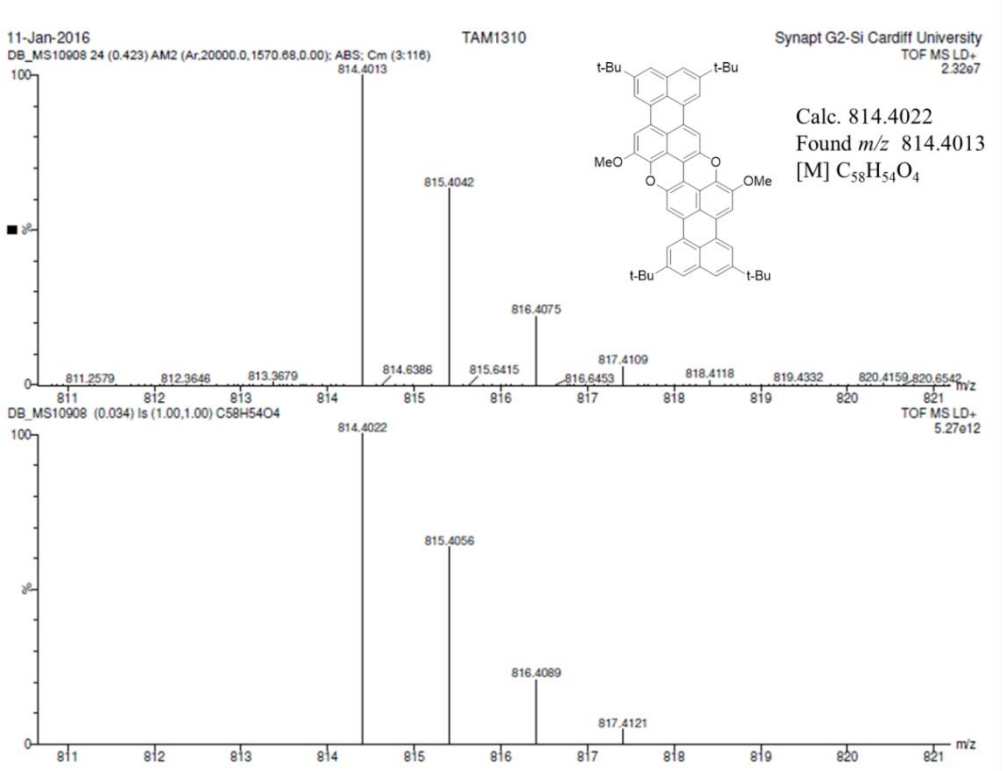

Figure 3.5.8. MALDI-HRMS isotopic pattern of **3-18^{Pp}**: experimental (above) and theoretical (below) peaks. Matrix: SA.

Subsequently, methyl protecting groups of **3-18^{Pp}** were removed by BBr_3 in CH_2Cl_2 and the reaction crude was directly treated with triflic anhydride in presence of a base. The reaction was monitored by t.l.c. and a complete conversion of staring material observed. The crude was purified by tedious re-precipitation cycles from THF/MeOH to give a black solid that shows very poor solubility and no NMR characterization was achieved. The ^{19}F-NMR experiment shows the presence of different peaks indicating that the isolated solid is probably composed by a mixture of compounds. A better understanding and a further optimization of reaction conditions is therefore needed. Moreover, these series of π-extended PXX derivatives bearing only two *tert*-butyl groups on the extremities experiences a severe drop in solubility that makes very difficult their processability.

3.5.5. Absorption and emission spectroscopy

The absorption and emission spectra of compound **3-22** and quatterylene derivative **3-21** have been recorded in toluene at r.t. and compared with the data reported in literature for corresponding *tert*-butyl derivatives without triflate substituents (**3-10** and **3-26**). Chemical structures of the compounds taken in consideration in this study are summarized in Figure 3.5.9

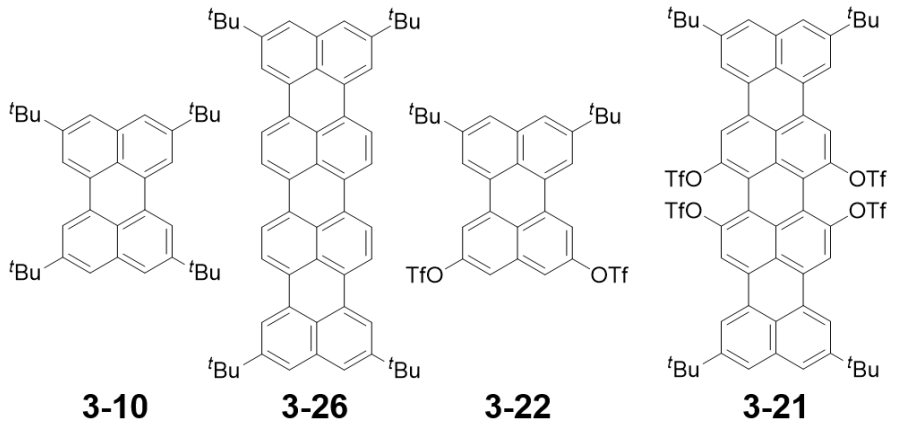

Figure 3.5.9 Chemical structure of tetra *tert*-butyl perylene **3-10** and soluble oligorylene **3-26** reported by Müllen.[32] Molecules **3-10** and **3-26** were used as references for the spectroscopic study.

As shown in figure 3.5.10, triflate compound **3-21** exhibits two distinctive peaks at 609 and 664 nm and a very high molar extinction coefficient of 104 571 M^{-1} cm^{-1}. Compared to *tert*-butyl quaterrylene **3-26**, **3-21** exhibits a bathochromic shifted absorption band (4 nm) and a relative low quantum yield. The introduction of bulky triflate groups caused steric distortion in the molecular backbone that might alter the electronic properties of quaterrylene derivative **3-21.**

In comparison with less conjugated compound **3-22**, **3-21** shows a sever bathochromic shift of the maximum absorption band of 222 nm and four times higher molar extinction coefficient resulting from the π-extension of the system. Optical properties of perylene derivatives **3-10** and **3-22** and quatterylene compounds **3-21** and **3-26** are summarized in table 3.5.2.

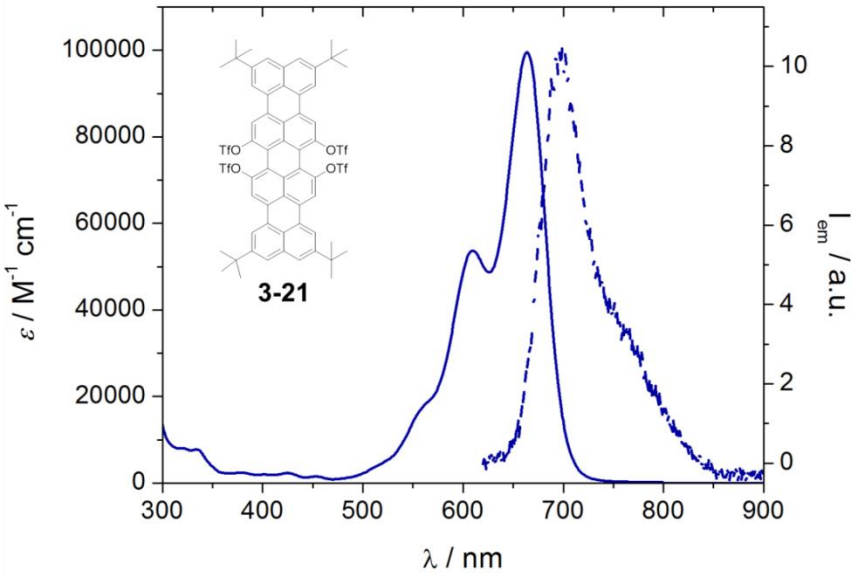

Figure 3.5.10. Absorption (solid line) and emission (dotted line) spectra recorded for compound **3-21** (λ_{exc} = 608 nm, λ_{em} = 699 nm).

Table 3.5.2. Optical properties of perylenes **3-10** and **3-22,** and quatterylenes **3-21** and **3-26**.

Comp.	Colour	λ_{abs} [nm][a]	ε [M^{-1} cm^{-1}]	λ_{em} [nm]	Φ (%)
3-10 [b]	yellow	440	24309±1918	458	0.94 [21]
3-22	yellow	446	24857±17	464	~1[b]
3-21	blue	664	104 571 ± 3950	698	0.015
3-26[29]	blue	660	138 000	678	0.05

[a] UV-Vis absorption maximum in the visible region in toluene. [b] Experimental in toluene at 25 °C; ε = 28 000 M^{-1} cm^{-1} is reported in literature [29] [b] measurement needed to be re-confirmed

Moreover, spectroscopic characterization of so far prepared derivatives **3-15** to **3-18^{Pp}** was carried out in toluene solutions at r.t. Chemical structures of the molecules analyzed in this study are summarized in Figure 3.5.11.

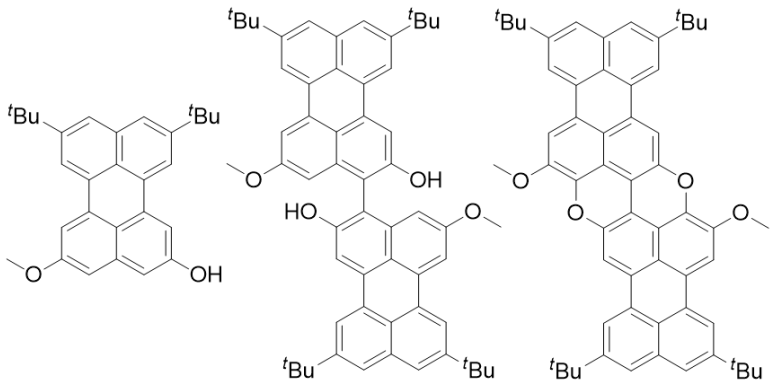

Figure 3.5.11. Chemical structure of perylene derivatives **3-15, 3-17** and **3-18^{Pp}**.

The optical properties of compounds **3-15**, **3-17** and **3-18^{Pp}** are reported in table 3.5.3, and they show a similar trend to the π-extended PXX derivatives synthesized in the previous section. Indeed, the UV−Vis spectrum displayed a bathochromic shift between within each member of the series.

Table 3.5.3 Optical properties of compounds **3-12** to **3-18^{Pp}**.

Comp.	Colour	λ_{abs} [nm][a]	ε [M^{-1} cm^{-1}]	λ_{em} [nm]
3-15	yellow	444	19486±583	472
3-17	yellow	459	56777±1287	502
3-18^{Pp}	blue	638[b]	40887±672	662

[a] UV-vis absorption maximum in the visible region in toluene.
[b] Measurements performed in CH_2Cl_2 due to insolubility in toluene.

Molecule **3-15** exhibits absorption and emission features with maxima at 444 nm (ε = 18 231M^{-1} cm^{-1}) and 467 nm, respectively. Dimer **3-17** demonstrates an absorption maximum at λ_{max}= 458 nm with an absorption coefficient ε = 56 777 and a bathochromic shift of Δ_λ~14 nm compared to monomer **3-15**. The longest wavelength absorption maximum of pyranopyranyl derivative **3-18^{Pp}** is strongly bathochromically shifted of 179 nm with respect to **3-17** suggesting a smaller HOMO-LUMO gap for **3-18^{Pp}**. This behaviour can be explained considering the increased aromatic surface and the planarization effect of the latter compared to non-cyclized compound **3-17**. Absorption and emission spectra of investigated compounds are reported in Figure 3.5.12. Due to the scarce solubility of compound **3-18^{Pp}** in toluene presented measurements were carried out in CH_2Cl_2 in diluted conditions.

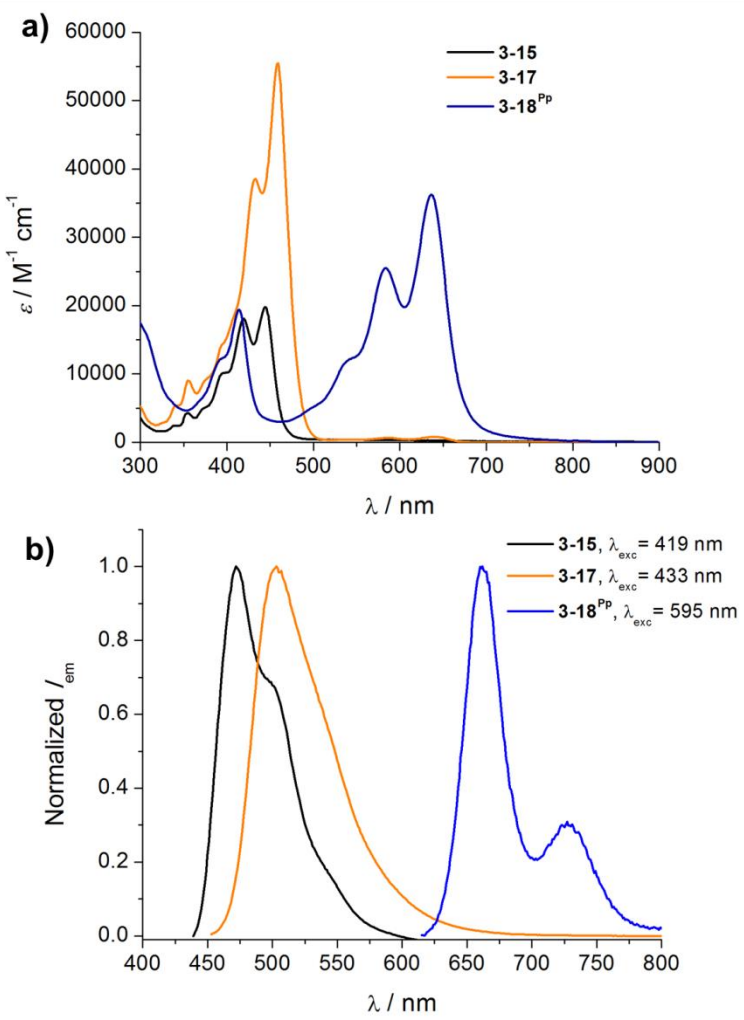

Figure 3.5.12. (a) UV-Vis characterization of compounds **3-15** (black), **3-17** (orange) in toluene at 25 °C and of molecule **3-18^{Pp}** (blue) in CH_2Cl_2 at 25 °C and (b) their normalized emission spectra.

3.6 Synthesis and characterization of biperylene-compounds bearing different dihedral angles

In the previous sections we demonstrated a strong correlation between π-conjugation (aromaticity) and optical properties in O-doped π-extended PAHs. Hereinafter we examined the absorption and emission properties of biperylene-compounds with a particular attention to their dependence upon the dihedral angle between the two perylene moieties. Systematic control of the dihedral angle of the linked perylene moieties can offer a fine-tuning of electronic interactions between the two perylenes.

Previous studies have already focused on the dihedral angle; *Osuka et al*. attempted to control the degree of *π*-conjugation in *meso*-*meso*-linked porphyrin arrays by changing the dihedral angles between the neighboring porphyrin units *via* the variation of strapped chain length, axial ligand coordination, host-guest interactions through hydrogen bonding, and planarization into complete flat structures.[119–121] *Tsubaki et al*. systematically investigated the characteristics of spreading the π-system and controlling the dihedral angles in oligonaphtofuran systems.[63,64]

On that account, we report the synthesis of novel biperylene-compounds in which the dihedral angle between the two aryl motifs is systematically changed by introduction of dioxymethylene strap varying the number of carbon atoms between the two perylenes (figure 3.6.1). Previously prepared furane derivative **3-6^{Fur}** (θ_{exp} = 16.7 °) with a characteristic narrow dihedral angle and compounds **3-4** (θ_{exp} = 62.8 °) and **3-30** (θ_{theor} = 63 °) were used as reference compounds for this study.

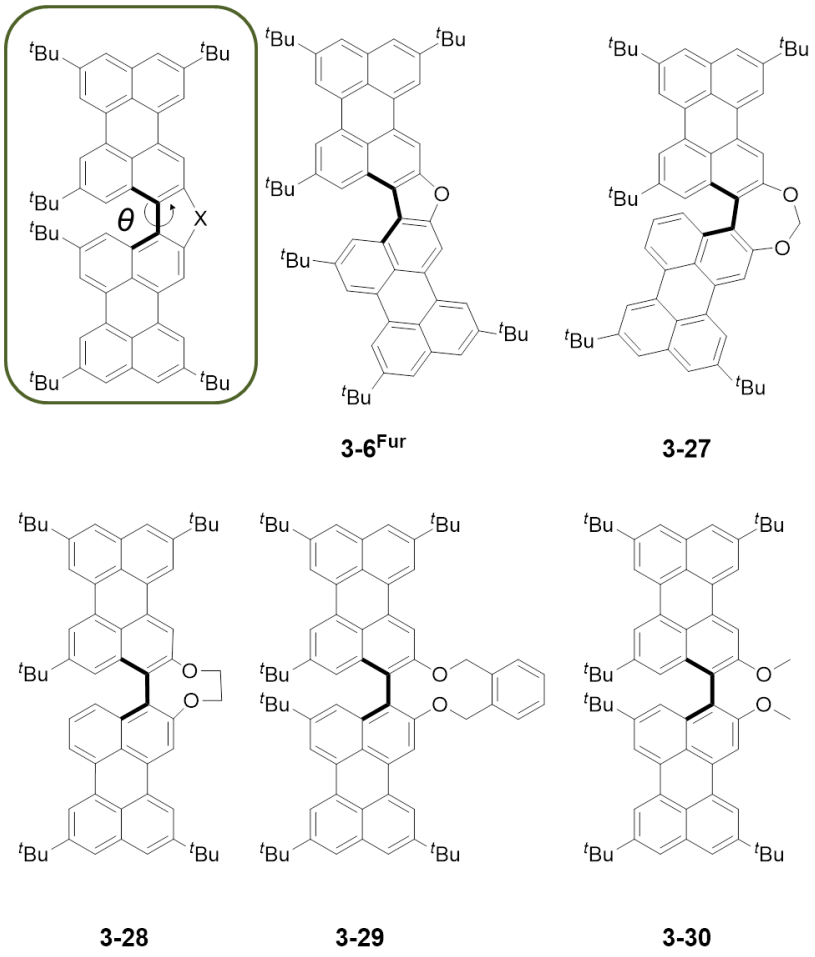

Figure 3.6.1 Novel biperyleno-derivatives bearing different torsion angles.

3.6.1 Synthesis and characterization of novel biperylene compounds

Compound **3-27**, containing a dioxepin system, was synthesized starting from BIPOL **3-4** through a double Williamson ether synthesis in the presence of dibromomethane, in 97 % yield.[122,123] Following the same synthetic protocol, compounds **3-28**, **3-29** and **3-30** were prepared in 24 %, 88 % and 82 %, respectively (scheme 3.6.1). Prepared compounds present good solubility in most of common organic solvents and they were fully characterized by melting point, IR, NMR spectroscopy and HRMS spectrometry (*Chapter IV*).

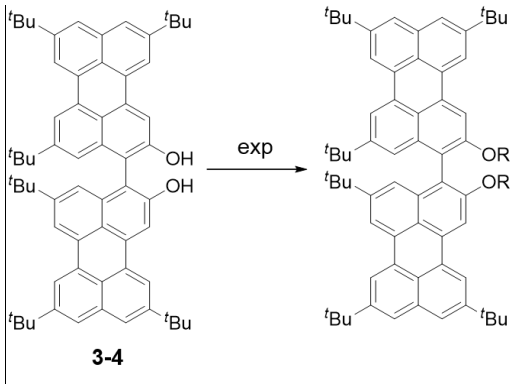

	R	R	exp	Yield (%)
3-27	-CH_2-		CH_2Br_2, K_2CO_3, acetone, 60 °C, 48 h	97
3-28	-$(CH_2)_2$-		$(CH_2)_2Br_2$, K_2CO_3, DMF, 80 °C, 48 h	24
3-29	-CH_2PhCH_2-		α, α'-dibromo-*o*-xylene, DMF, 80°C, 48 h	88
3-30	CH_3	CH_3	MeI, K_2CO_3, acetone, 60 °C, 48 h	82

Scheme 3.6.1. Synthesis of biperyleno-derivatives **3-27** – **3-30**.

Crystals of **3-28** and **3-29** suitable for single-crystal X-ray analysis were grown by slow diffusion from a CH_2Br_2/MeOH solution and by evaporation of a dilute solution, respectively. Figure 3.6.2 displays the crystals structures of compound **3-28** which is arranged according to the spatial group P *n* (crystallographic data and refinement details are reported in *appendix*). **3-28** asymmetric unit contains two crystallographically independent molecules. Only hydrophobic CH-π contacts keep the molecules packed, and perylene's moieties delimit cavities filled by dibromomethane. The crystal packing of **3-29** shows limited perylene π–π stacking among symmetry related molecules. Also in this case perylene motifs delimit cavities filled by solvent (CH_2Cl_2). In both compounds the rotation around the bond 1, 1' is restricted by the alkoxy groups, where the ethylene bridge in **3-28** defines an eight membered ring and a dibenzylene bridge in **3-29** defines a 10 membered ring. As expected the dimension of the ring directly influences the dihedral angle between the two perylene fragments. Figure 3.6.2 e-h display that smaller is the ring connection between the linked perylene moieties more constrained is the angle between the respective planes. Crystallographic data reported for reference compounds **3-4** and **3-6^{Fur}**, shows a nice decrease of the dihedral angle from 62.8 ° for **3-4** to 16.7 ° for **3-6^{Fur}**, where the dihedral angle between the aryl moieties was drastically constrained by planarity of furanyl framework. With the new class of biperylene compounds, we demonstrated the reduction of the dihedral angle from ~71.2 ° in **3-29** to 63 ° in **3-28**. Surprisingly, the interplanar angle of **3-28** did not change significantly compared to non-bridged dihydroxyl **3-4**. Despite that X-Ray structure for dioxepin sysyem **3-27** was not resolved, the dihedral angle expected for this molecule is around 55° as reported in literature for similar systems.[64]

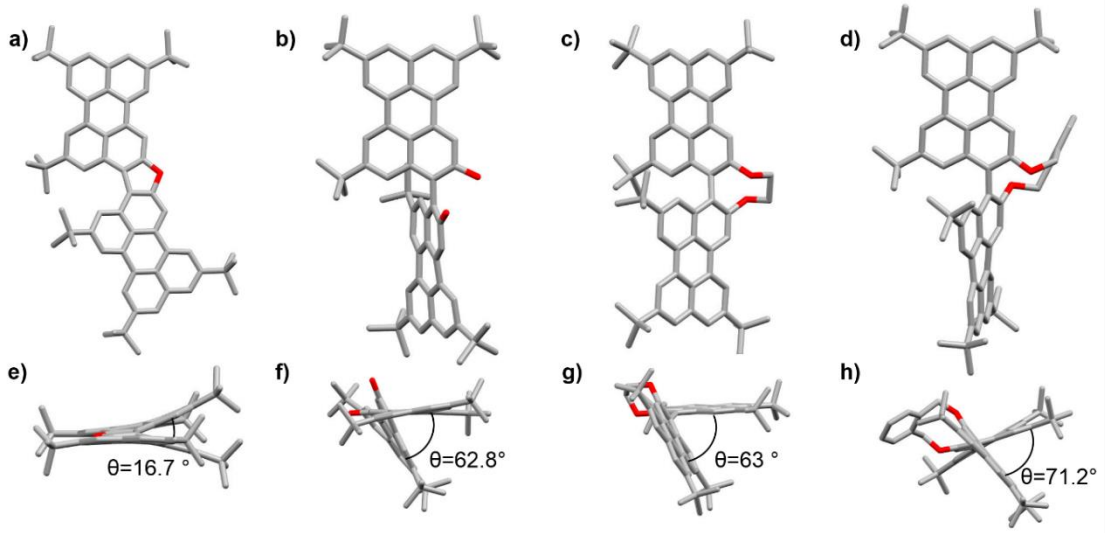

Figure 3.6.2 From the left: a,d) Top-view and e-f) side-view of the crystal structure **3-6^{Fur}** (space group: *P* 2/c)· **3-4** (space group: *P* - 1), **3-28** (space group: *P n*) and **3-29** (right, space group: *P*-1).

3.6.2 Absorption and emission spectroscopy

In this section, the luminescence properties of biperylene-compounds **3-27, 3-28, 3-29** and **3-30** are reported and compared with furan **3-6^{Fur}**. The absorption spectra of the investigated compounds have been recorded at r.t. in toluene (Figure 3.6.3). Upon decrease of the dihedral angle, a progressive bathochromic shift was observed, which, as expected, suggests a shrinking of the HOMO-LUMO gap. Specifically, compound **3-27** containing a dioxepin system exhibits three peaks at 427, 455 and 484 nm, bathochromically shifted and with higher intensities compared to the equivalent compounds bearing larger dihedral angles (**3-28**, **3-29**, **3-30**). When considering furan system **3-6^{Fur}**, the maximum absorption peak at 534 nm is strongly shifted toward the red compared to other biperylenes, which is attributed to the narrow dihedral angle and the effective spread of the π resonance over the entire molecule. The emission spectra observed in toluene solution at r.t. are displayed in Figure 3.6.3b. Similarly, to the absorption, the emission spectra varied in function of the dihedral angle between two adjacent perylenes. All bridged compounds showed relatively small Stokes shift (13-24 nm) compared to non-bridged dimethoxy **3-30** (39 nm), most likely due to the increased rigidity.

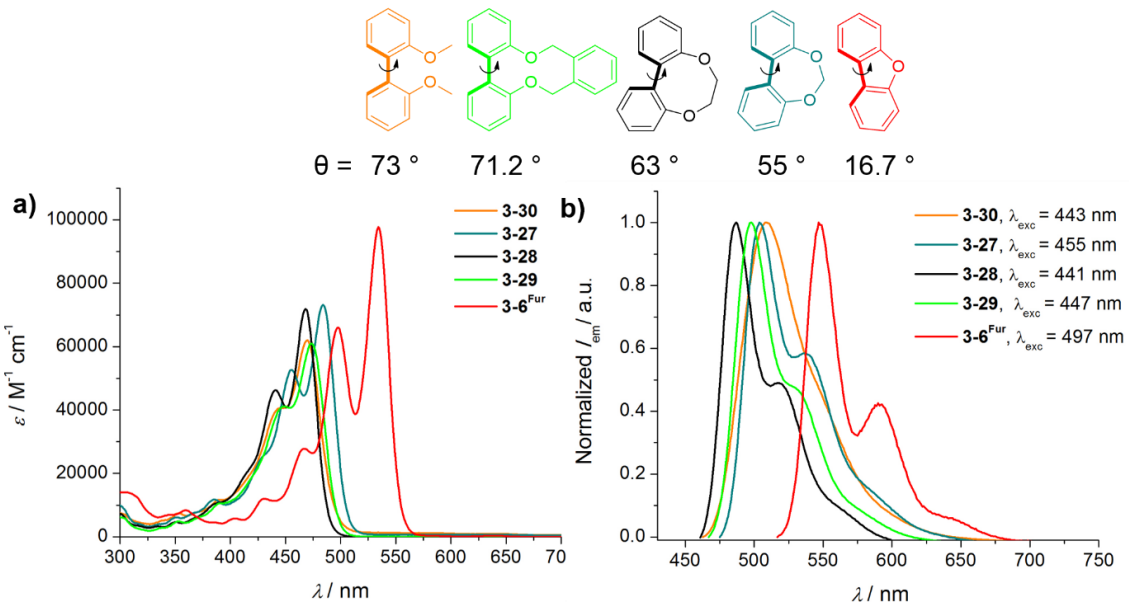

Figure 3.6.3. (a) UV-Vis spectra of compounds **3-27** (cyan), **3-28** (black), **3-29** (green), **3-30** (orange) and **3-6^{Fur}** (red) and (b) respective emission spectra in toluene at r.t.

Optical properties of compounds **3-6^{Fur}**, **3-27**, **3-28**, **3-29** and **3-30** are resumed in table 3.6.1.

Table 3.6.1. Optical properties of compounds **3-6^{Fur}**, **3-27**, **3-28**, **3-29,** and **3-30.**

Comp.	θ [°]	λ_{abs} [nm][c]	ε [M^{-1} cm^{-1}]	λ_{em} [nm]	Stokes shift [nm]
3-6^{Fur}	16.7[a]	534	96000	547	13
3-27	55[b]	484	73400	504	20
3-28	63 [a]	468	72500	487	19
3-29	71.2[a]	474	61 400	498	24
3-30	73[b]	470	59500	509	39

[a] measured from the crystal structure. [b] predicted optimized values by DFT calculations (B3LYP), with basis set 6-31+G(d,p) and Polarizable Continuum Model for the solvent effect of toluene [c] UV-vis absorption maximum in the visible region in toluene.

3.7 Conclusion

This chapter focused on the design of novel O-doped π-extended conjugated systems based on perylene frameworks. The chosen strategy involved an intermolecular C-C bond formation between two PAH subunits followed by the selective formation of an intramolecular diaryl ether bond to produce oxygen-containing five- or six-membered rings, depending on the reaction conditions. In the first section, we described the preparation of unprecedented π-extended benzofuranes and benzopyranes following a planarization strategy. This involves the formation of C-O bonds through an intramolecular acid-catalyzed cyclization originating furan ring or through a Cu(I)-mediated oxidative reaction leading to pyranopyran rings.

Photophysical characterization showed that π-extended DNF and PXX derivatives exhibit tunable spectroscopic properties. Indeed, their absorption and emission maxima could be finely shifted throughout the entire visible region by changing the π-extension of the aromatic scaffold and the dihedral angle. Their strong electronic absorption, moderate to high fluorescence quantum yields, low Stokes shifts and small tendency to aggregate in solution make those materials attractive for a wide range of applications. X-ray diffraction of π-extended furans showed that such derivatives undergo strong π-stacking at the solid state forming well-defined microstructures. The high propensity of this class of molecules to undergo self-aggregation is intriguing in view of the design of new organic functional materials.

In order to further explore this novel route to π-extended system, we planned to prepare a second class of π-extended PXX derivatives in which additional functionalization sites were introduced on the molecular core. The introduction of functional moieties into the molecular core is extremely important in view of tuning opto-electronic properties of the system and permits, for instance, the incorporation of photoactive fragments into multicomponent organic materials for light harvesting or solar cells. In this respect, we successfully addressed the preparation of molecular precursors **3-17** and **3-18^{Pp}**. However, despite the presence of peripheral solubilizing *tert*-butyl groups which were supposed to limit solubility issues related to higher order perylenes, no valuable NMR analyses were observed for intermediate **3-18^{Pp}**. This was ascribed to the formation of strong aggregation between molecules that limited significantly their processability. A suitable synthetic approach for the insertion of additional functional groups onto the PXX core from precursor **3-18^{Pp}** has to be optimized and is currently under investigation.

Simultaneously, we developed a new synthetic protocol for the preparation of highly conjugated quatterylene derivative **3-21** bearing core triflate substituents that are accessible for further functionalization. As a future work the study of the reactivity of molecule **3-21** will be taken in consideration.

The last section of this chapter focused on the design of π-extended conjugated systems based on biperylene-compounds bearing different dihedral angles. Systematic control of the dihedral angle of the linked perylene moieties offered a fine-tuning of electronic interactions between the two perylenes leading to new material with tunable opto-electronic properties.

3.8 Bibliography

[1] A. Facchetti, *Mater. Today* **2007**, *10*, 28–37.

[2] A. Facchetti, *Chem. Mater.* **2011**, *23*, 733–758.

[3] Z. Sun, Q. Ye, C. Chi, J. Wu, *Chem. Soc. Rev.* **2012**, *41*, 7857–7889.

[4] J. Wu, W. Pisula, K. Müllen, *Chem. Rev.* **2007**, *107*, 718–47.

[5] Y. Lin, Y. Li, X. Zhan, *Chem. Soc. Rev.* **2012**, *41*, 4245–72.

[6] L. Chen, Y. Hernandez, X. Feng, K. Müllen, *Angew. Chem. Int. Ed. Engl.* **2012**, *51*, 7640–7654.

[7] L. Zhi, K. Müllen, *J. Mater. Chem.* **2008**, *18*, 1472–1484.

[8] A. Narita, X.-Y. Wang, X. Feng, K. Müllen, *Chem. Soc. Rev.* **2015**, *44*, 6616–6643.

[9] D. Pan, J. Zhang, Z. Li, M. Wu, *Adv. Mater.* **2010**, *22*, 734–738.

[10] Z. Chen, Y. M. Lin, M. J. Rooks, P. Avouris, *Phys. E Low-Dimensional Syst. Nanostructures* **2007**, *40*, 228–232.

[11] K. Müllen, *ACS Nano* **2014**, *8*, 6531–6541.

[12] L. Dössel, L. Gherghel, X. Feng, K. Müllen, *Angew. Chem. - Int. Ed.* **2011**, *50*, 2540–2543.

[13] R. Scholl, C. Seer, *Justus Liebigs Ann. Chem.* **1912**, *394*, 111–177.

[14] Clar E., *Berichte der Dtsch. Chem. Gesellschaft A B Ser.* **1929**, *62*, 1574–1582.

[15] M. M. Haley, R. R. Tykwinski, *Carbon-Rich Compounds: From Molecules to*

Materials, Wiley, **2006**.

[16] R. G. Harvey, *Polycyclic Aromatic Hydrocarbons Ronald G. Harvey*, Wiley-VCH: New York, **1997**.

[17] M. Muller, C. Kubel, K. Mullen, *Chem.--Eur. J.* **1998**, *4*, 2099–2109.

[18] A. C. Grimsdale, K. M??llen, *Angew. Chemie - Int. Ed.* **2005**, *44*, 5592–5629.

[19] D. Adam, P. Schuhmacher, J. Simmerer, L. Häussling, K. Siemensmeyer, K. H. Etzbachi, H. Ringsdorf, D. Haarer, *Nature* **1994**, *371*, 141–143.

[20] E. Clar, *Chem. Ber.* **1948**, *81*, 52–63.

[21] Y. Avlasevich, C. Li, K. Müllen, *J. Mater. Chem.* **2010**, *20*, 3814.

[22] F. Würthner, *Chem. Commun.* **2004**, 1564–1579.

[23] J. A. A. W. Elemans, R. Van Hameren, R. J. M. Nolte, A. E. Rowan, *Adv. Mater.* **2006**, *18*, 1251–1266.

[24] T. Ishi-I, K. I. Murakami, Y. Imai, S. Mataka, *Org. Lett.* **2005**, *7*, 3175–3178.

[25] H. Langhals, S. Christian, A. Hofer, *J. Org. Chem.* **2013**, *78*, 9883–9891.

[26] C. Li, H. Wonneberger, *Adv. Mater.* **2012**, *24*, 613–636.

[27] T. Weil, T. Vosch, J. Hofkens, K. Peneva, K. Müllen, *Angew. Chem. - Int. Ed.* **2010**, *49*, 9068–9093.

[28] W. Scholl, R., Seer, C., R, *Ber. Dtsch. Chem. Ges* **1910**, *43*, 2202–2209.

[29] J. T. Markiewicz, F. Wudl, *ACS Appl. Mater. Interfaces* **2015**, *7*, 28063–28085.

[30] D. e. Jiang, S. Dai, *Chem. Phys. Lett.* **2008**, *466*, 72–75.

[31] C. Former, S. Becker, A. C. Grimsdale, K. Müllen, *Macromolecules* **2002**, *35*, 1576–1582.

[32] K. H. Koch, U. Fahnenstich, M. Baumgarten, K. Müllen, *Synth. Met.* **1991**, *42*, 1619–1622.

[33] S. Karabunarliev, M. Baumgarten, K. Müllen, *J. Phys. Chem. A* **1998**, *102*, 7029–7034.

[34] Q. Peng, Y. Niu, Z. Wang, Y. Jiang, Y. Li, Y. Liu, Z. Shuai, *J. Chem. Phys.* **2011**, *134*, 1–10.

[35] Y. Li, J. Gao, S. Di Motta, F. Negri, Z. Wang, *J. Am. Chem. Soc.* **2010**, *132*, 4208–4213.

[36] Y. Li, Z. Wang, *Org. Lett.* **2009**, *11*, 1385–1387.

[37] W. Jiang, H. Qian, Y. Li, Z. Wang, *J. Org. Chem.* **2008**, *73*, 7369–7372.

[38] Z. Zeng, M. Ishida, J. L. Zafra, X. Zhu, Y. M. Sung, N. Bao, R. D. Webster, B. S. Lee, R. W. Li, W. Zeng, et al., *J. Am. Chem. Soc.* **2013**, *135*, 6363–6371.

[39] A. J. Wise, Y. Zhang, J. Fan, F. Wudl, A. L. Briseno, M. D. Barnes, *Phys. Chem. Chem. Phys.* **2014**, *16*, 15825–30.

[40] S. M. Park, Y. Yoon, C. W. Jeon, H. Kim, M. J. Ko, D.-K. Lee, J. Y. Kim, H. J. Son, S.-K. Kwon, Y.-H. Kim, et al., *J. Polym. Sci. Part A Polym. Chem.* **2014**, *52*, 796–803.

[41] L. Hahn, S. Öz, H. Wadepohl, L. H. Gade, *Chem. Commun.* **2014**, *50*, 4941–3.

[42] M. Kardos, *Patent*, **1913**, 276357.

[43] H. Langhals, *Helv. Chim. Acta* **2005**, *88*, 1309–1343.

[44] L. Zang, Y. Che, J. S. Moore, *Acc. Chem. Res.* **2008**, *41*, 1596–1608.

[45] A. Liscio, G. De Luca, F. Nolde, V. Palermo, K. Müllen, P. Samorì, *J. Am. Chem. Soc.* **2008**, *130*, 780–781.

[46] Z. Chen, M. G. Debije, T. Debaerdemaeker, P. Osswald, F. Würthner, *ChemPhysChem* **2004**, *5*, 137–140.

[47] P. Tinnefeld, K. D. Weston, T. Vosch, M. Cotlet, T. Weil, J. Hofkens, K. Müllen, F. C. De Schryver, M. Sauer, *J. Am. Chem. Soc.* **2002**, *124*, 14310–14311.

[48] S. Schols, S. Verlaak, C. Rolin, D. Cheyns, J. Genoe, P. Heremans, *Adv. Funct. Mater.* **2008**, *18*, 136–144.

[49] N. G. Pschirer, C. Kohl, F. Nolde, J. Qu, K. Müllen, *Angew. Chem.- Int. Ed.* **2006**, 1401–1404.

[50] M. Takase, T. Narita, W. Fujita, M. S. Asano, T. Nishinaga, H. Benten, K. Yoza, K. Müllen, *J. Am. Chem. Soc.* **2013**, *135*, 8031–8040.

[51] T. H. Vo, M. Shekhirev, D. Kunkel, F. Orange, M. J.-F. Guinel, A. Enders, A. Sinitskii, *Chem. Commun.* **2014**, *50*, 4172–4174.

[52] C. Bronner, S. Stremlau, M. Gille, F. Braußе, A. Haase, S. Hecht, P. Tegeder, *Angew. Chem. Int. Ed. Engl.* **2013**, *52*, 4422–4425.

[53] N. Kobayashi, M. Sasaki, T. Ohe, *Semiconductor Device, Method of Manufacturing the Same, and Method of Forming Multilayer Semiconductor Thin Film*, **2013**, 8,399,288 B2.

[54] L. Wang, G. Duan, Y. Ji, H. Zhang, *J. Phys. Chem. C* **2012**, *116*, 22679–22686.

[55] N. Kobayashi, M. Sasaki, K. Nomoto, *Chem. Mater.* **2009**, *21*, 552–556.

[56] D. Stassen, N. Demitri, D. Bonifazi, *Angew. Chem. Int. Ed.* **2016**.

[57] N. C. R. Najer, H.; Armand, J.; Menin, J.; Voronine, *Acad. Sci.* **1965**, 4343.

[58] R. . M. Najer, H.; Giudicelli, *J. Bull SOC. Chim. Fr.* **1966**, 2120.

[59] Daphne Stassen, π − Extension of Hetero-Fused Aromatics : From Synthesis to Self-Assembly, **2015**.

[60] H. Tsuji, C. Mitsui, L. Ilies, Y. Sato, E. Nakamura, *J. Am. Chem. Soc.* **2007**, *129*, 11902–3.

[61] C. Mitsui, J. Soeda, K. Miwa, H. Tsuji, J. Takeya, E. Nakamura, *J. Am. Chem. Soc.* **2012**, *134*, 5448–5451.

[62] C. H. Woo, P. M. Beaujuge, T. W. Holcombe, O. P. Lee, J. M. J. Fr??chet, *J. Am. Chem. Soc.* **2010**, *132*, 15547–15549.

[63] K. Nakanishi, D. Fukatsu, K. Takaishi, T. Tsuji, K. Uenaka, K. Kuramochi, T. Kawabata, K. Tsubaki, *J. Am. Chem. Soc.* **2014**, 7101–7109.

[64] K. Nakanishi, T. Sasamori, K. Kuramochi, N. Tokitoh, T. Kawabata, K. Tsubaki, *J. Org. Chem.* **2014**, 2625–2631.

[65] W. Gu, X. Jing, X. Pan, A. S. . Chan, T.-K. Yang, *Tetrahedron Lett.* **2000**, *41*, 6079–6082.

[66] R. S. Ward, *Nat. Prod. Rep.* **1993**, *10*, 1–28.

[67] M. L. Bolognesi, R. Budriesi, A. Cavalli, A. Chiarini, R. Gotti, A. Leonardi, A. Minarini, E. Poggesi, M. Recanatini, M. Rosini, et al., *J. Med. Chem.* **1999**, *42*, 4214–4224.

[68] Y. Matsumoto, W. Uchida, H. Nakahara, I. Yanagisawa, T. Shibanuma, H. Nohira, *Chem. Pharm. Bull.* **2000**, *48*, 428–432.

[69] C. Torborg, M. Beller, *Adv. Synth. Catal.* **2009**, *351*, 3027–3043.

[70] S. Banerjee, G. Maier, *Chem. Mater.* **1999**, *11*, 2179–2184.

[71] E. Fuhrmann, J. Talbiersky, *Org. Process Res. Dev.* **2005**, *9*, 206–211.

[72] K. W. Anderson, T. Ikawa, R. E. Tundel, S. L. Buchwald, *J. Am. Chem. Soc.* **2006**, *128*, 10694–5.

[73] F. Monnier, M. Taillefer, *Angew. Chem. Int. Ed. Engl.* **2009**, *48*, 6954–71.

[74] E. Buck, Z. J. Song, D. Tschaen, P. G. Dormer, R. P. Volante, P. J. Reider, *Org. Lett.* **2002**, *4*, 1623–1626.

[75] R. Gujadhur, D. Venkataraman, *Synth. Commun.* **2001**, *31*, 2865–2879.

[76] G. Chen, A. S. C. Chan, F. Y. Kwong, *Tetrahedron Lett.* **2007**, *48*, 473–476.

[77] B. Xiao, T.-J. Gong, Z.-J. Liu, J.-H. Liu, D.-F. Luo, J. Xu, L. Liu, *J. Am. Chem. Soc.* **2011**, *133*, 9250–9253.

[78] B. Liu, B. F. Shi, *Tetrahedron Lett.* **2015**, *56*, 15–22.

[79] C. G. Espino, P. M. Wehn, J. Chow, J. Du Bois, *J. Am. Chem. Soc.* **2001**, *123*, 6935–6936.

[80] A. Hinman, J. Du Bois, *J. Am. Chem. Soc.* **2003**, *125*, 11510–11511.

[81] J. a Jordan-Hore, C. C. C. Johansson, E. M. Beck, M. J. Gaunt, *J. Am. Chem. Soc.* **2008**, *130*, 16184–6.

[82] T. Mei, X. Wang, J. Yu, *J. Am. Chem. Soc.* **2009**, 10806–10807.

[83] X. Wang, Y. Lu, H. Dai, J. Yu, *J. Am. Chem. Soc.* **2010**, *132*, 12203–5.

[84] Y. Wei, N. Yoshikai, *Org. Lett.* **2011**, *13*, 5504–7.

[85] J. Zhao, Y. Wang, Y. He, L. Liu, Q. Zhu, *Org. Lett.* **2012**, *14*, 1078–81.

[86] J. Zhao, Q. Zhang, L. Liu, Y. He, J. Li, J. Li, Q. Zhu, *Org. Lett.* **2012**, *14*, 5362–5365.

[87] T. Yamato, pt Chieko Hideshima, G. K. Surya Prakash, G. A. Olah, K. B. Loker Hydrocarbon, *J. Org. Chem* **1991**, *56*, 3192–3194.

[88] T. Takeya, H. Doi, T. Ogata, T. Otsuka, I. Okamoto, E. Kotani, *Tetrahedron* **2004**, 6395–6310.

[89] Y. Cui, H. L. Ngo, W. Lin, *Inorgan. Chem. Commun.* **2002**, *41*, 1033–1035.

[90] X. Xie, T. Y. Zhang, Z. Zhang, *J. Org. Chem* **2006**, *71*, 6522–6529.

[91] A. Arienti, F. Bigi, R. Maggi, P. Moggi, M. Rastelli, G. Sartori, A. Trerè, *J. Chem. Soc. Perkin Trans.* **1997**, *1*, 1391–1393.

[92] J. Areephong, N. Ruangsupapichart, T. Thongpanchang, *Tetrahedron Lett.* **2004**, *45*, 3067–3070.

[93] R. Pummerer, E. Prell, A. Rieche, *Berichte der Dtsch. Chem. Gesellschaft* **1926**, *59*, 2159–2161.

[94] W. G. Prowse, K. I. Arnot, J. A. Recka, R. H. Thomson, J. R. Maxwell, *Tetrahedron* **1991**, *47*, 1095–1108.

[95] T. Asari, N. Kobayashi, T. Naito, T. Inabe, *Bull. Chem. Soc. Jpn.* **2001**, *74*, 53–58.

[96] N. Lv, M. Xie, W. Gu, H. Ruan, S. Qiu, C. Zhou, Z. Cui, *Org. Lett.* **2013**, *15*, 2382–2385.

[97] H. Bünzly, H. Decker, *Berichte der Dtsch. Chem. Gesellschaft* **1905**, *38*, 3268–3273.

[98] R. Pummerer, A. Rieche, *Berichte der Dtsch. Chem. Gesellschaft (A B Ser.* **1926**, *59*, 2161–2175.

[99] P. Stoessel, A. Buesing, H. Heil, *Materials for Organic Electroluminescent Devices*, **2012**.

[100] A. E. Wetherby, S. D. Benson, C. S. Weinert, *Inorganica Chim. Acta* **2007**, *360*, 1977–1986.

[101] C. Song, T. M. Swager, *Macromolecules* **2009**, *42*, 1472–1475.

[102] C. Zimmermann, F. Willig, S. Ramakrishna, B. Burfeindt, B. Pettinger, R. Eichberger, W. Storck, *J. Phys. Chem. B* **2001**, *105*, 9245–9253.

[103] M. Pillow, J.; Kobayashi, S.; Humphries, *patentWO2010013006A2.pdf*, **2010**, WO 2010/013006 A2.

[104] R. O. Al-Kaysi, T. Sang Ahn, A. M. Müller, C. J. Bardeen, *Phys. Chem. Chem. Phys.* **2006**, *8*, 3453–3459.

[105] L. B. Johansson, J. G. Molotkovsky, L. D. Bergelson, *J. Am. Chem. Soc.* **1987**, 7374–7381.

[106] D. N. Coventry, A. S. Batsanov, A. E. Goeta, J. a K. Howard, T. B. Marder, R. N. Perutz, *Chem. Commun.*. **2005**, 2172–2174.

[107] A. G. Crawford, Z. Liu, I. a I. Mkhalid, M.-H. Thibault, N. Schwarz, G. Alcaraz, A. Steffen, J. C. Collings, A. S. Batsanov, J. a K. Howard, et al., *Chem. Eur. J.* **2012**, *18*, 5022–5035.

[108] J. M. Brunel, *Chem. Rev.* **2005**, *105*, 857–897.

[109] M. Nakajima, I. Miyoshi, K. Kanayama, S. I. Hashimoto, M. Noji, K. Koga, *J. Org. Chem.* **1999**, *64*, 2264–2271.

[110] J. Aydin, K. S. Kumar, M. J. Sayah, O. a. Wallner, K. J. Szabó, *J. Org. Chem.* **2007**, *72*, 4689–4697.

[111] I. A. Shuklov, N. V. Dubrovina, H. Jiao, A. Spannenberg, A. Börner, *Eur. J. Org. Chem.* **2010**, *7*, 1669–1680.

[112] S. Wang, B. Lv, Q. Cui, X. Ma, X. Ba, J. Xiao, *Chem. - A Eur. J.* **2015**, *21*, 14791–14796.

[113] J. Guilleme, D. González-Rodríguez, T. Torres, *Angew. Chemie - Int. Ed.* **2011**, *50*, 3506–3509.

[114] A. B. Lowe, C. E. Hoyle, C. N. Bowman, *J. Mater. Chem.* **2010**, *20*, 4745.

[115] G. He, N. Yan, H. Kong, S. Yin, L. Ding, S. Qu, Y. Fang, *Macromolecules* **2011**, *44*, 703–710.

[116] S. Gunes, H. Neugebauer, N. S. Sariciftci, *Chem. Rev.* **2007**, *107*, 1324–1338.

[117] K. Ritter, *Synthesis (Stuttg).* **1993**, 735–762.

[118] J. S. Calderon, R. H. Thomson, *J. Chem. Soc. Perkin trans. I* **1988**, 583–586.

[119] T. K. Ahn, K. S. Kim, D. Y. Kim, S. B. Noh, N. Aratani, C. Ikeda, A. Osuka, D. Kim, *J. Am. Chem. Soc.* **2006**, *128*, 1700–1704.

[120] N. Aratani, A. Osuka, Y. H. Kim, D. H. Jeong, D. Kim, *Angew. Chem. - Int. Ed.* **2000**, *39*, 1458–1462.

[121] N. Aratani, A. Takagi, Y. Yanagawa, T. Matsumoto, T. Kawai, Z. S. Yoon, D. Kim, A. Osuka, *Chem. - A Eur. J.* **2005**, *11*, 3389–3404.

[122] J. J. G. S. van Es, H. A. M. Biemans, E. W. Meijer, *Tetrahedron: Asymmetry* **1997**, *8*, 1825–1831.

[123] M. Yasuda, R. Kojima, H. Tsutsui, D. Utsunomiya, K. Ishii, K. Jinnouchi, T. Shiragami, *J. Org. Chem* **2003**, 7618–7624.

4. Experimental Part

4.1. Instruments, materials and general methods

Compounds were fully characterized (m.p., IR, ^{1}H and ^{13}C NMR and High resolution mass spectrometry (HRMS)).

NMR spectroscopy (^{1}H, ^{13}C, ^{19}F NMR). NMR spectra were obtained on a *Varian* Inova spectrometer (500 MHz ^{1}H and 125 MHz ^{13}C). Chemical shifts are reported in ppm using the solvent residual signal as an internal reference ($CDCl_3$: δ_H = 7.26 ppm, δ_C = 77.23 ppm; CD_2Cl_2: δ_H = 5.32 ppm, δ_C = 53.84 ppm; $(CD_3)_2SO$: δ_H = 2.50 ppm, δ_C = 39.52 ppm; $(CD_3)_2CO$: δ_H = 2.05 ppm, δ_C = 29.84 ppm, 206.26 ppm; toluene-*d8:* δ_H = 7.09, 7.00, 6.98, 2.09 ppm; C_6D_6: δ_H = 7.16 ppm, δ_C = 128.4 ppm). The resonance multiplicity is described as *s* (singlet), *d* (doublet), *t* (triplet), *q* (quartet), *m* (multiplet), *br* (broad signal). Coupling constants are reported in Hertz. All spectra were recorded at 25°C unless specified otherwise.

ESI-High resolution mass spectrometry (HRMS). ESI-HRMS was performed by the "Fédération de Recherche"; ICOA/CBM (FR2708) platform of Orléans in France, on a Bruker maXis Q-TOF in the positive ion mode. The analytes were dissolved in a suitable solvent at a concentration of 1 mg/mL and diluted 200 times in methanol (≈ 5 ng/mL). The diluted solutions (1µL) were delivered to the ESI source by a Dionex Ultimate 3000 RSLC chain used in FIA (Flow Injection Analysis) mode at a flow rate of 200 µL/min with a mixture of CH_3CN/H_2O+0.1% of HCO_2H (65/35). ESI conditions were as follows: capillary voltage was set at 4.5 kV; dry nitrogen was used as nebulizing gas at 0.6 bars and as drying gas set at 200°C and 7.0 L/min. ESI-MS spectra were recorded at 1 Hz in the range of 50-3000 m/z. Calibration was performed with ESI-TOF Tuning mix from Agilent and corrected using lock masses at m/z 299.294457 (methyl stearate) and 1221.990638 (HP-1221). Data were processed using Bruker Data Analysis 4.1 software.

Matrix-Assisted Laser Desorption-Ionisation Time-of-Flight Mass Spectrometry analysis (MALDI-TOF). MALDI-HRMS was performed by the Centre de spectrométrie de masse at the Université de Mons in Belgium, using the following instrumentation: Waters QToF Premier mass spectrometer equipped with a nitrogen laser, operating at 337 nm with a maximum output of 500 mW delivered to the sample in 4 ns pulses at 20 Hz repeating rate. Time-of-flight analyses were performed in the reflectron mode at a resolution of about 10.000. The matrix solution (1 μL) was applied to a stainless steel target and air dried. Analyte samples were dissolved in a suitable solvent to obtain 1 mg/mL solutions. 1 μL aliquots of these solutions were applied onto the target area already bearing the matrix crystals, and air dried. For the recording of the single-stage MS spectra, the quadrupole (rf-only mode) was set to pass ions from 100 to 1000 THz and all ions were transmitted into the pusher region of the time-of-flight analyzer where they were analyzed with 1s integration time.

Infrared absorption spectroscopy (IR). IR spectra (KBr) were recorded on a Perkin Elmer 2000 spectrometer by Mr. Paolo de Baseggio (University of Trieste) or on a Perkin-Elmer Spectrum II FT-IR System UATR, mounted with a diamond crystal (University of Namur). Selected absorption bands are reported by wavenumber (cm^{-1}).

Ultraviolet-Visible absorption spectroscopy (Uv-Vis). UV-Vis absorption spectra were recorded on Varian Cary 5000 UV-Vis-NIR Spectrophotometer. All absorption measurements were performed at 25 °C unless specified otherwise.

Ultraviolet-Visible emission spectroscopy. Emission spectra were recorded on a Varian Cary Eclipse fluorescence spectrophotometer. All fluorimetric measurements were performed at 25 °C unless specified otherwise.

Melting points (m.p.) were measured on a Büchi SMP-20.

Thermogravimetric analysis (TGA) were performed using a TGA Q500 (TA Instruments), treating the samples placed in Pt pans with the following procedure: isotherm at 100°C for 20 min (to remove residual solvent, if any), ramp from 100 to 800°C at 10° C/min, under N_2 (flow rate on the sample of 90 mL/min) for SWCNTs. A ramp from 100 to 700°C at 10° C/min, under N_2 (flow rate on the sample of 90 mL/min) was applied to organic samples **3-4**, **3-6^{Pp}** and **3-6^{Fur}**.

X-ray photoelectron spectroscopy (**XPS**) analyses were performed with a SSX-100 system (Surface Science instrument). The photon source was a monochromatized Al Kα line (hν = 1486.6 eV) applied with a takeoff angle of 35°. In the spectrum analysis, the background signal was subtracted by Shirley's method. The C 1s core level peak position of carbon atoms was taken as the reference at 284.5 eV. The spectrum analysis was carried out by fitting the peak shape obtained in the same analysing conditions and other components with mixed (Gaussian + Lorentzian) line shapes. XPS atomic ratios have been estimated from the experimentally determined area ratios of the relevant core lines, corrected for the corresponding theoretical atomic cross-sections and for a square root dependence of the photoelectrons kinetics energies.

Raman spectroscopy analyses were performed on an inVia Raman microscope (*Renishaw*) at room temperature, equipped with lasers at 532 nm, 633 nm or 785 nm, on solid samples deposited onto a glass coverslip. The laser spot was focused on the sample surface using a long working distance 50x objective. Reported spectra are average of at least 5 measurements performed in different areas of the sample and normalized to the G-Band. The intensity ratio I_D/I_G was obtained by taking peak intensities without baseline corrections. The data were analysed using Origin software.

Scanning electron microscope (SEM): All analysed samples, if not otherwise stated, were gently re-precipitated several times from THF/MeOH, dried under vacuum overnight, and sputter coated with gold in a Edwards S150A apparatus (Edwards High Vacuum, Crawley, West Sussex, United Kingdom), and examined with a Leica Stereoscan 430i scanning electron microscope (Leica Cambridge Ltd.).

X-ray diffraction of compounds 3-4, 3-5^{Fur}, 3-6^{Fur},3-7^{Fur}, 3-11, 3-21, 3-22, 3-28 and 3-29

Data collections were performed at the X-ray diffraction beamline (XRD1) of the Elettra Synchrotron, Trieste (Italy),[1] with a Pilatus 2M image plate detector. Complete datasets were collected at 100 K (nitrogen stream supplied through an Oxford Cryostream 700) with a monochromatic wavelength of 0.700, 0.800 or 0.900 Å through the rotating crystal method. Crystals were dipped in N-paratone and mounted on the goniometer head with a nylon loop.

Complete dataset for the triclinic crystals **3-4**, **3-22** form has been obtained merging two different data collections done on the same crystal, mounted with different orientations. The diffraction data were indexed, integrated and scaled using XDS.[2] The structures were solved by direct methods using SIR2014,[3] and/or the dual space algorithm implemented in the SHELXT code.[4] Several crystals of **3-28** have been tried but all of them diffracted poorly (around 1.5 Å). Furthermore, crystals suffered from serious radiation damage preventing us to collect a full dataset (80 % complete); a model for the molecule has been built from this preliminary X-Ray data, with relatively high - but reasonable - R_1 factor (R_1 = 23%). Fourier analysis and refinement were performed by the full-matrix least-squares based on F^2 implemented in SHELXL-2014.[5] The Coot program was used for modeling.[6]

Diffraction for compound **3-11** crystals was limited to 0.94 Å, due to static disorder on the compound of interest and solvent molecules. Anisotropic thermal motion was applied to all atoms with occupancy greater than 30%. Hydrogen atoms were included at calculated

positions with isotropic $U_{factors}$ = 1.2 U_{eq} or $U_{factors}$ = 1.5 U_{eq} for methyl groups hydroxyl groups. Restrains on bond lengths, angles and thermal motion parameters (DFIX, DANG, SIMU and DELU) have been applied on disordered tert-butyl groups, triflate moieties in **3-22** and **3-21** and disordered dichloromethane in **3-29**. **3-28** model has been refined fully isotropically, due to the poor data/parameters ratio; a full set of restrains for the **3-28** and dibromomethane molecules has been used, forcing planarity of perylene but refining the angle between linked polyaromatic moieties. A contribution of an extended region of heavily disordered solvent have been removed with the SQUEEZE routine of PLATON software[7] (1210 e^-/cell in 1530 $Å^3$). Pictures were prepared using ORTEP-3[8] and Pymol[9] software.

Adsorption silica chromatography columns (SCC): Merck silica gel 60 (40-63 μm) was used.

Chemicals were purchased from Sigma Aldrich, TCI, Acros, Fluorochem and Alfa Aesar and used as received, unless otherwise stated. Sodium sulphide, anhydrous (65122, CAS: 1313-82-2, Lot: H02Z007) was purchased from Alfa Aesar. High purity single-walled CoMoCAT® carbon nanotubes enriched in (7,6) chirality, ≥77% (carbon as SWNT), 0.7-1.1 nm diameter manufactured by SouthWest NanoTechnologies (SWeNT®), Inc (SWeNT product: SG 76) were purchased by Sigma Aldrich and used as received. Cu-TMEDA catalyst (CAS: 30698-64-7; Lot: A0290621) and *p*-toluenesulfonic acid monohydrate, ACS reagent ≥ 98.5 % (CAS: 6192-52-5, Lot.: MKBC8188) were purchased from Sigma Aldrich. 9-Phenanthrol, technical grade (CAS: 484-17-3; Lot: BGBB3193V) was purchased from Sigma Aldrich and purified by SiO_2 column chromatography (eluent: PET/ETOAc, 9:1) prior to use.

Solvents were purchased from VWR, Sigma Aldrich and Acros, and deuterated solvents from Sigma Aldrich, Fluorochem and Cambridge Isotope Laboratories and used as received. All solvents used in reactions were anhydrous and purchased from Sigma Aldrich, TCI, Acros and Alfa Aesar and used as received.

Omnipore Hydrophilic PTFE membrane filter with a 0.45 μm pore size were purchased from Merck Millipore**.**

Device fabrication and characterization: FTO/glass substrates (Pilkington, TEC15, 15 Ohm/sq) were etched with metallic Zn and 2M HCl. They were cleaned in an ultrasonic bath in water, acetone and isopropanol for 15 min each. Finally, they were immersed into a TL1 washing solution ($H_2O_2/NH_3/H_2O$ 5:1:1, v/v) and heated to 80°C for 10 min to remove organic contamination, then rinsed 10 times in water. To make a compact TiO_2 blocking layer of 80 nm, 300 μL of 0.15 M titanium diisopropoxidebis(acetylacetonate) (75% Aldrich) in 1-butanol (Aldrich) solution was twice spin-coated (3000 rpm) on the cleaned FTO glasses and, after each deposition, heated at 125°C for 5 min on a hot plate. After coating, the films were cooled down to the room temperature; final, a third layer of thicker TiO_2 was deposited, following the same procedure, by a 0.3 M titanium diisopropoxidebis(acetylacetonate) solution in 1-butanol. The coated FTO glasses were finally heated at 520°C for 2 hours in oven in order to obtain a pinhole-free compact-TiO_2 film. CH_3NH_3I was first synthesized following the conventional procedure reported in literature.[33] The prepared CH_3NH_3I and PbI_2 (Aldrich) powders, for 1M $CH_3NH_3PbI_3$ solution, were stirred in a mixture of dimethyl sulfoxide and γ-butyrolactone (7:3 v/v) at 60°C for 30 minutes. When it is back to room temperature, 200 μL of the 0.20 μm filtered solution was spin-coated onto the compact-TiO_2/FTO substrate at 1000 and 4000 rpm for, respectively, 20 and 60 seconds. During the second spin-coating step, 200 μL of dichloromethane were dropped on the 2 cm x 2 cm substrate. Therefore, the coated films

were then annealed on a hot-plate set at 100°C for 10 minutes. Ox-SWNTs and functionalized SWNTs have been dispersed in CB in a concentration of 0.8 mg/ml, by sonication processes for 60 minutes at 50°C, and then centrifuged at 6000 rpm for 20 minutes. The clear solution has been used for preparing the Spiro-OMeTAD solutions and the following dilutions. The standard doped Spiro-OMeTAD solution was prepared solving 63 mg of Spiro-OMeTAD in 1 ml of chlorobenzene, 27.8 μL of tert-butylpyridine and 30.7 μL of 510 mg/mL LiTFSI in acetonitrile solution were added as doping agents; all the HTM solutions were cast onto the perovskite coated substrate and spun at a rate of 2500 rpm for 45 seconds. Finally, solar cell devices were completed by thermal evaporation of 80 nm Au electrodes. All the device areas (0.09 cm^2) were measured by an optical microscope equipped with a ruler. The devices were characterized under AirMass 1.5Global (AM 1.5G) solar simulator with an irradiation intensity of 100 mW/cm^2. Current–Voltage characteristics devices were studied using a Keithley 2400 Source Measure Unit and a solar simulator Spectra Physics Oriel 150 W, with AM1.5G filter set. The integrated intensity was set on 100 mW/cm^2, using a thermopile radiant power meter with fused-silica window (Spectra Physics Oriel, model 70260). The current-voltage characterizations reported were performed through a black metal mask (area 0.09 cm^2), the step voltage and the delay time ware fixed, respectively, at 10 mV and at 100 ms, in order to reach the quasi-steady-state measurement conditions and, therefore, minimize the hysteresis effect.[10]

4.2 Synthesis and detailed experimental procedures

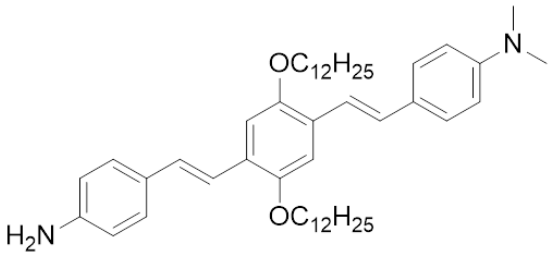

4-((E)-4-((E)-4-aminostyryl)-2,5-bis(dodecyloxy)styryl)-N,N-dimethylaniline 2-1

A mixture of nitro compound **2-8** (210 mg, 0.28 mmol) and $SnCl_2$ (323 mg, 1.70 mmol) in EtOAc (20 mL) was refluxed overnight. A saturated sodium bicarbonate aq. solution was then added to the reaction mixture to achieve alkalinity. The mixture was filtered, and the filtrate extracted with EtOAc to obtain the crude product, which was purified by silica gel column chromatography (SiO_2, eluent: EtOAc-CHX, 0.5:10) to afford target compound **2-1** (117 mg, **59%**) as a yellow solid. **M.p.**: 46-47°C. **^{1}H-NMR** (500 MHz, CD_2Cl_2): δ = 7.41 (*d*, ^3J = 8.5 Hz, 2H), 7.34 (*d*, ^3J = 8 Hz, 2H), 7.26 (*d*, *J* =16.5 Hz, 2H, C*H*), 7.10 (*s*, 1H), 7.09 (*s*, 1H), 7.07-7.04 (*d*, *J* = 16.5 Hz, 1H, C*H*), 7.05 – 7.02 (*d*, ^3J = 16.5 Hz, 1H, C*H*), 6.72 (*d*, ^3J = 8.5 Hz, 2H), 6.67 (*d*, ^3J = 8.0 Hz, 2H), 4.03 (*t*, ^3J = 6.5 Hz, 4H, $OCH_2(CH_2)_{11}$), 3.80 (*s*, 2H, NH_2), 2.98 (*s*, 6H, $N(CH_3)_2$), 1.89-1.82 (*m*, 4H; $OCH_2CH_2(CH_2)_9CH_3$), 1.44-1.38 (*m*, 4H, $O(CH_2)_2CH_2(CH_2)_7CH_3$), 1.35-1.27 (*m*, 32H, $O(CH_2)_3(CH_2)_8CH_3$), 0.88 (*t*, 6H; $O(CH_2)_{11}CH_3$).**^{13}C-NMR** (125 MHz, CD_2Cl_2): δ = 151.41, 151.31, 150.72, 146.99, 129.09, 128.98, 128.85, 128.84, 128.17, 127.99, 127.50, 127.02, 126.80, 120.10, 119, 33, 115.54, 112.90, 110.69, 110.50, 70.17, 70.12, 40.78, 32.52, 30.32, 30.29, 30.26, 30.18, 30.08, 29.97, 26.93, 26.91, 26.88, 23.28, 14.47; some peaks are missing probably due to overlap. **IR** (KBr) ν (cm^{-1}) = 3436.84, 3035.26, 2918.85, 2850.87, 2347.76, 1609.96, 1517.04, 1494.36, 1470.85, 1444.80, 141972, 1392.58, 1359.22, 1287.53, 1256.21, 1203.21, 1189.16, 1177.19, 1127.99, 1061.91, 1035.09, 1007.38, 961.98, 840.66, 807.92, 719.51, 519.14. **HRMS** (ESI, m/z): $[M+2H]^{2+}$ calc. for $C_{48}H_{74}N_2O_2$, 355.2869, found: 355.2875.

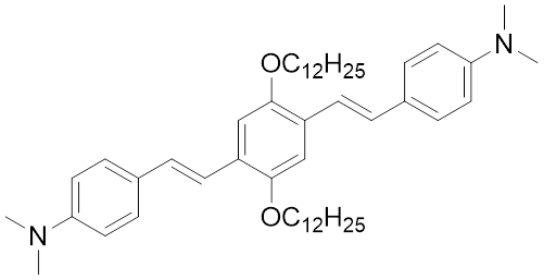

4,4'-((1E,1'E)-(2,5-bis(dodecyloxy)-1,4-phenylene)bis(ethene-2,1-diyl))bis(N,N-dimethylaniline) 2-6a

Bisphosphonate derivative **2-5** (100 mg, 0.133 mmol) and *p*-dimethylaminobenzaldehyde (49.93 mg, 0.33 mmol) were dissolved in anhydrous DMF (7 mL). Sodium *tert*-butoxide (90.0 mg, 0.93 mmol) was added to the solution at 0 °C and the reaction mixture allowed to warm up at r.t and stirred overnight under Ar. The reaction was quenched with H_2O and the aqueous phase extracted with $CHCl_3$ (3 × 20 mL) and combined organic layers were washed with brine and dried over anhydrous Na_2SO_4. Solvent was removed in *vacuo* and the residue was purified by column chromatography (SiO_2, eluent: CH_2Cl_2-PET, 2:8) to yield compound **2-6a** (85 mg, **87%**) as yellow solid. **M.p.**: 98 °C. **^{1}H-NMR** (500 MHz, CD_2Cl_2/TFA-*d*): δ = 7.71 (*d*, ^3J = 8.5 Hz, 4H), 7.56 (*d*, *J* = 16.5 Hz, 2H; C*H*), 7.52 (*d*, ^3J = 8.5 Hz, 4H), 7.21 (*d*, *J* = 16.5 Hz, 2H; C*H*), 7.18 (*s*, 2H), 4.09 (*t*, ^3J = 6.5 Hz, 4H; OCH_2(CH$_2$)$_{10}$CH$_3$'), 3.33 (*s*, 12H, N(CH_3)$_2$), 1.98-1.75 (*m*, 4H; OCH$_2$CH_2(CH$_2$)$_9$CH$_3$), 1.60-1.48 (*m*, 4H, O(CH$_2$)$_2$CH_2(CH$_2$)$_8$CH$_3$), 1.40 (*m*, 4H, O(CH$_2$)$_3$CH_2(CH$_2$)$_7$CH$_3$), 1.31-1.26 (*m*, 28H, O(CH$_2$)$_4$(CH_2)$_7$CH$_3$), 0.87 (*t*, ^3J = 7.0 Hz, 6H; O(CH$_2$)$_{11}$CH_3); **^{13}C-NMR** (67.5 MHz, CD_2Cl_2/TFA-*d*): δ = 152.09, 141.47, 141.14, 129.13, 127.55, 127.44, 127.11, 121.12, 111.85, 70.56, 47.91, 32.46, 30.21, 30.18, 30.16, 29.91, 29.88, 26.69, 23.20, 14.34; some peaks are missing probably due to overlap**. IR** (KBr) ν (cm^{-1}) = 3436.55, 3039.25, 2918.31, 2950.78, 2800.55, 1607.63, 1556.00, 1525.08, 1494.42, 1472.92, 1444.19, 1420.36,

1394.16, 1384.15, 1358.76, 1257.64, 1219.52, 1204.83, 1188.55, 1168.76, 1128.63, 1062.02, 1036.87, 960.88, 839.49, 807.20, 719.90, 522.86; **HRMS** (ESI, m/z): $[M+2H]^{2+}$, calc. for $C_{50}H_{78}N_2O_2$, 369.3026, found: 369.3032. Crystal suitable for X-ray diffraction was obtained by slow diffusion from a CH_2Cl_2/MeOH solution.

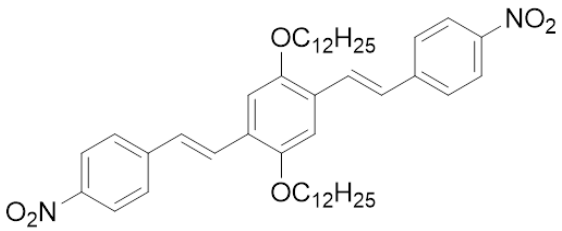

4,4'-((1E,1'E)-(2,5-bis(dodecyloxy)-1,4-phenylene)bis(ethene-2,1-diyl))bis(nitrobenzene) 2-6b

Bisphosphonate compound **2-5** (1.0 g, 1.33 mmol) and *p*-nitrobenzaldehyde (0.505 g, 3.34 mmol) were dissolved in anhydrous DMF (20 mL) and sodium *tert*-butoxide (0.895 g, 9.31 mmol) was added at 0 °C. The reaction mixture was allowed to warm up at r.t and stirred overnight under Ar. Water was added to quench the reaction, and the aqueous phase extracted with $CHCl_3$ (3 × 100 mL). Combined organic layers were washed with brine and dried over anhydrous Na_2SO_4. The solvent was removed in *vacuo* and the crude purified by column chromatography (SiO_2, eluent: CH_2Cl_2-PET, 1:9 →1:1) to afford compound **2-6b** (0.626 g, **63%**) as orange powder. **M.p.**: 83-85 °C. **^{1}H-NMR** (500 MHz, CD_2Cl_2): δ = 8.21 (*d*, ^3J = 8.5 Hz, 4H), 7.72 – 7.64 (*m*, 6H), 7.27 (*d*, ^3J = 16.5 Hz, 2H; C*H*),7.18 (*s*, 2H), 4.10 (*t*, *J* = 6.5 Hz, 4H; OCH_2(CH$_2$)$_{10}$CH$_3$),1.95-1.82 (*m*, 4H; OCH$_2$CH_2(CH$_2$)$_9$CH$_3$), 1.56 (*m*, 4H, O(CH$_2$)$_2$CH_2(CH$_2$)$_8$CH$_3$), 1.47-1.39 (*m*, 4H, O(CH$_2$)$_3$CH_2(CH$_2$)$_7$CH$_3$), 1.38-1.24 (*m*, 28H, O(CH$_2$)$_4$ (CH_2)$_7$CH$_3$), 0.87 (*t*, ^3J = 7 Hz, 6H; O(CH$_2$)$_{11}$CH_3). **^{13}C-NMR** (125 MHz, CD_2Cl_2): δ = 152.09, 147.26, 145.02, 128.45, 127.56, 127.43, 127.37, 124.64, 111.37, 70.08, 32.49, 30.28, 30.24, 30.21, 30.00, 29.98, 29.94, 26.86, 23.26, 14.44; some peaks are missing

probably due to overlap. **IR** (KBr) ν (cm^{-1}) = 3436.97, 3057.40, 2917.08, 2852.08, 1625.49, 1591.00, 1513.23, 1488.90, 1471.50, 1424.83, 1392.93, 1384.25, 1316.91, 1258.54, 1231.07, 1205.07, 1184.08, 1150.12, 1108.11, 1073.58, 1057.83, 1034.55, 1019.26, 998.23, 968.58, 952.92, 868.54, 854.38, 825.97, 774.25, 750.96, 719.01, 694.64, 544.95, 502.44, 460.33; **HRMS** (ESI, m/z): [M+HCO_2H-H] calc. for $C_{47}H_{65}N_2O_8$, 785.4746, found: 785.4735.

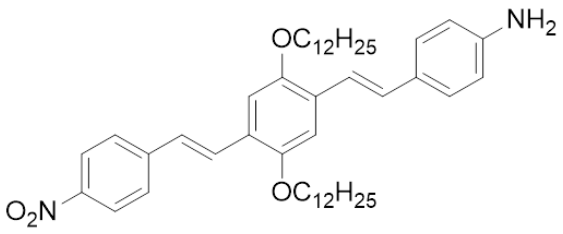

(4-((E)-2,5-bis(dodecyloxy)-4-((E)-4-nitrostyryl)styryl)aniline 2-7

The mono-reduction reaction of **2-6** was performed following a procedure reported in literature.[11] Compound **2-6** (0.5 g, 0.67 mmol) was dissolved in pyridine (13 mL) and heated at 90 °C. A sodium sulphide aqueous solution (1.45 mL), previously prepared by dissolving sodium sulphide (1.0 g) in 2.33 mL of water and 0.35 mL of concentrated hydrochloric acid (37%), was added drop-wise.Water (0.5 mL) was added immediately after sodium sulphide addition and 5 mL more were added over a period of 30 min. The reaction mixture was cooled down at °C until a dark red solid was formed. The precipitate was separated by centrifugation and washed several times with water. Further purification by column chromatography (SiO_2, eluent: CH_2Cl-CHX, 3:7 → 1:1) gave compound **2-7** as a dark red solid (0.331 g, **69%**). **M.p.**: 62°C. **^{1}H-NMR** (500 MHz, $CDCl_3$): δ = 8.21 (*d*, ^3J = 8.5 Hz, 2H), 7.65 - 7.61 (*m,* 3H),7.38 (*d*, ^3J = 8.5 Hz, 2H), 7.32 – 7.28 (*d*, *J* = 16.5 Hz, 1H; C*H*), 7.18 – 7.15 (*d*, *J* = 16.5 Hz, 1H; C*H*), 7.11 – 7.07 (*m*, 3H), 6.76 (*d*, ^3J = 8.5 Hz, 2H), 4.07 (*t*, ^3J = 6.5 Hz, 2H; $OCH_2(CH_2)_{10}CH_3$), 4.03 (*t*, ^3J = 6.5 Hz, 2H; $OCH_2(CH_2)_{10}CH_3$), 1.91 - 1.84 (*m*, 4H; $OCH_2CH_2(CH_2)_9CH_3$), 1.57 - 1.51 (*m*, 4H, $O(CH_2)_2CH_2(CH_2)_8CH_3$), 1.44 - 1.40

(*m*, 4H, $O(CH_2)_3CH_2(CH_2)_7CH_3$), 1.26 (*m*, 28H, $O(CH_2)_4$ $(CH_2)_7CH_3$), 0.88 (*m*, 6H; $O(CH_2)_{11}CH_3$). **^{13}C-NMR** (125 MHz, $CDCl_3$): δ = 151.84, 150.90, 146.55, 144.92, 144.73, 129.71, 129.56, 129.24, 128.55, 128.06, 126.79, 125.97, 124.84, 124.28, 120.22, 116.11, 111.19, 110.24, 69.80, 69.56, 32.08, 32.06, 29.86, 29.83, 29.81, 29.79, 29.65, 29.62, 29.60, 29.52, 29.51, 26.46, 26.43, 22.85, 22.84, 14.28, 14.26; some peaks are missing probably due to overlap. **IR** (KBr) ν (cm^{-1}) = 3446.98, 3378.68, 3051.83, 2920.81, 2850.73, 2442.62, 1619.56, 1584.11, 1515.57, 1467.33, 1423.08, 1384.88, 1336.92, 1318.94, 1292.98, 1281.09, 1253.53, 1206.04, 1177.82, 1108.86, 1034.43, 967.60, 853.00, 833.25, 819.74, 750.62, 722.11, 691.84, 596.00, 519.02, 504.86. **HRMS** (ESI, m/z): $[M+H]^+$ calc. for $C_{46}H_{67}N_2O_4$, 711.5095, found: 711.5092.

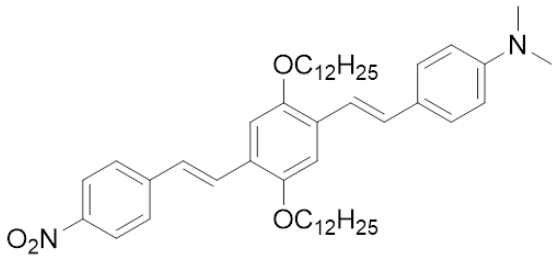

4-((E)-2,5-bis(dodecyloxy)-4-((E)-4-nitrostyryl)styryl)-N,N-dimethylaniline 2-8

To a mixture of **2-7** (55 mg, 0.077 mmol), paraformaldehyde (23.3 mg, 0.77 mmol), and sodium cyanoborohydride (14.5 mg, 0.231 mmol), acetic acid (5 mL) was added. The whole mixture was stirred at room temperature overnight and then poured into 100 mL of water. pH was adjusted to 8-9 using a sat. aq. solution of Na_2CO_3. Aqueous phase was extracted with $CHCl_3$ (3 × 10 mL) and the combined organic layers were dried over Na_2SO_4. Evaporation of the solvent in *vacuo* and further purification of the residue by column chromatography (SiO_2, eluent: EtOAC-CHX, 0.5:10) yielded compound **2-8** (55 mg, **97%**) as a dark red solid. **M.p.**: 118 °C. **^{1}H-NMR** (500 MHz, CD_2Cl_2): δ = 8.20 (*d*, ^3J = 9.0 Hz,

2H), 7.69 – 7.65 (*m*, 3H;), 7.43 (*d*, ^3J = 9.0 Hz, 2H), 7.29 – 7.26 (*d*, *J* = 16.5 Hz, 1H; C*H*), 7.23 – 7.20 (*d*, *J* = 16.5 Hz, 1H; C*H*), 7.15 – 7.11 (*m*, 3H), 6.72 (*d*, ^3J = 9.0 Hz, 2H), 4.09 (*t*, ^3J = 6.5 Hz, 2H; OCH_2(CH$_2$)$_{10}$CH$_3$), 4.05 (*t*, ^3J = 6.5 Hz, 2H, OCH_2(CH$_2$)$_{10}$CH$_3$), 2.99 (*s*, 6H, N(CH_3)$_2$), 1.95 - 1.83 (*m*, 4H; OCH$_2$CH_2(CH$_2$)$_9$CH$_3$), 1.59 – 1.53 (*m*, 4H, O(CH$_2$)$_2$CH_2(CH$_2$)$_8$CH$_3$), 1.48 – 1.39 (*m*, 4H, O(CH$_2$)$_3$CH_2(CH$_2$)$_7$CH$_3$), 1.36 – 1.24 (*m*, 28H, O(CH$_2$)$_4$(CH_2)$_7$CH$_3$), 0.88 (*t*, ^3J = 7.5 Hz, 6H, O(CH$_2$)$_{11}$CH_3). **^{13}C-NMR** (125 MHz, CD_2Cl_2): δ = 152.34, 151.17, 150.90, 146.97, 145.45, 130.39, 129.92, 128.86, 128.20, 127.20, 126.34, 126.14, 124.87, 124.61, 118.88, 112.85, 111.46, 110.25, 70.18, 69.99, 40.74, 32.52, 32.50, 30.32, 30.29, 30.27, 30.26, 30.25, 30.22, 30.11, 30.07, 30.04, 30.3, 29.97, 29.94, 26.90, 26.89, 23.28, 23.27, 14.46; some peaks are missing probably due to overlap. **IR** (KBr) *v* (cm^{-1}) = 3436.18, 3072.49, 3044.88, 2918.13, 2851.39, 2434.32, 1608.81, 1584.46, 1560.38, 1521.33, 1509.06, 1471.08, 1443.97, 1424.35, 1393.92, 1333.01, 1317.46, 1256.39, 1242.74, 1207.08, 1188.50, 1167.63, 1127.71, 1106.88, 1060.81, 1036.96, 1007.33, 962.00, 865.12, 853.30, 836.55, 808.61, 750.97, 718.64, 692.01, 592.41, 527.14, 504.62; **HRMS** (ESI, m/z): $[M+H]^+$ calc. for $C_{48}H_{71}N_2O_4$, 739.5408, found: 739.5410.

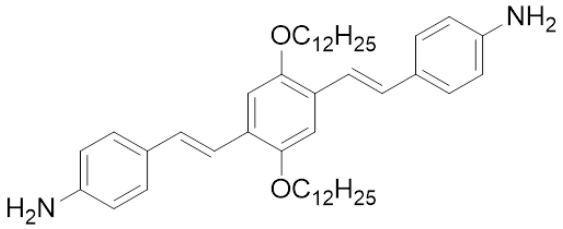

4,4'-((1E,1'E)-(2,5-bis(dodecyloxy)-1,4-phenylene)bis(ethene-2,1-diyl))dianiline 2-9

The reduction reaction of **2-6b** was obtained following a similar procedure reported for compound **2-7** (mono-reduction). Compound **2-6b** (1.5 g, 2.02 mmol) was dissolved in pyridine (39 mL) and heated at 90 °C. A sodium sulphide aqueous solution (4.37 mL), prepared by dissolving anhydrous sodium sulphide (2.0 g, new batch) in 4.66 mL of water

and 0.69 mL of concentrated hydrochloric acid (37%), was added dropwise. Water (1.5 mL) was added immediately after the end of the addition of sodium sulphide solution and 15 mL more, over a period of 45 min. Then the reaction mixture was cooled down at O°C and the formedprecipitate filtered and washed several times with water. Further purification of the product by column chromatography (neutral Al_2O_3; CH_2Cl_2- PET, 1:1) gave compound **2-9** as a light brown solid (976 mg, **71%** yield). **M.p.**: 39-41 °C. **^{1}H-NMR** (500 MHz, CD_2Cl_2): δ = 7.34 (*d*, ^3J = 8.5 Hz, 4H), 7.27 (*d*, *J* = 16.5 Hz, 2H, C*H*), 7.10 (*s*, 2H), 7.04 (*d*, *J* = 16.5 Hz, 2H, C*H*), 6.67 (*d*, ^3J= 8.5 Hz, 4H), 4.03 (*t*, ^3J = 6.5 Hz, 4H; OCH_2(CH_2)$_{10}CH_3$), 3.85 (*bs*, 4H, NH_2), 1.91-1.81 (*m*, 4H, $OCH_2CH_2(CH_2)_9CH_3$), 1.60-1.47 (*m*, 4H, $O(CH_2)_2CH_2(CH_2)_8CH_3$), 1.46-1.38 (*m*, 4H, $O(CH_2)_3CH_2(CH_2)_7CH_3$), 1.37-1.22 (*m*, 28H, $O(CH_2)_4(CH_2)_7CH_3$), 0.88 (*t*, ^3J= 7.0 Hz, 6H, $O(CH_2)_{11}CH_3$).**^{13}C-NMR** (125 MHz, CD_2Cl_2): δ = 151.38, 147.01, 128.97, 128.18, 127.25, 120.06, 115.52, 110.65, 70.13, 32.52, 30.29, 30.26, 30.24, 30.23, 30.14, 30.06, 29.96, 26.88, 23.28, 14.46**;** some peaks are missing probably due to overlap. **IR** (KBr) *v* (cm^{-1}) = 3436.40, 3038.76, 2920.67, 2850.58, 1604.80, 1604.80, 1561.04, 1516.40, 1495.05, 1467.01, 1419.93, 1396.91, 1384.86, 1345.07, 1281.41, 1255.07, 1205.83, 1176.71, 1127.79, 1035.94, 967.38, 845.06, 813.93, 723.29,635.98, 544.05, 516.65. **HRMS** (ESI, m/z): $[M+2H]^{2+}$ calc. for $C_{46}H_{70}N_2O_2$, 341.2713, found: 341.2720.

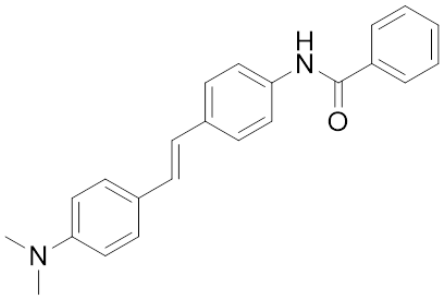

(E)-N-(4-(4-(dimethylamino)styryl)phenyl)benzamide 2-10

To a solution dimethylaniline **2-2** (50 mg, 0.209 mmol) and Et_3N (58 µL, 0.418 mmol) in acetone (5 mL, previously dried over 4 Å molecular sieves), benzoyl chloride (48 µL, 0.418 mmol) was added at 0 °C. The reaction mixture was stirred at r.t. for 2 h under Argon atmosphere. The reaction was quenched by slow addition of a $NaHCO_3$ aq. solution to neutralize formed acid. Precipitated amide was separated by centrifugation, washed several times with MeOH and dried under *vacuo* to give compound **2-10** as a pale brownish solid (67 mg, **98%**). **M.p**.: 242 – 243 °C.**^{1}H-NMR** (500 MHz, DMSO-d_6): δ = 10.27 (*s*, 1H, N*H*CO), 7.96 (*d*, ^3J = 8.5 Hz, 2H), 7.78 (*d*, *J* = 8.5 Hz, 2H), 7.59 (*m*, 1H, Ar*H*), 7.55 – 7.51 ((*m*, 4H), 7.42 (*d*, ^3J = 8.5 Hz, 2H), 7.09 – 7.05 (*d*, *J* = 16.0 Hz, 1H; C*H*), 6.96 – 6.93 (*d*, *J* = 16.0 Hz, 1H; C*H*), 6.72 (*d*, ^3J= 8.5 Hz, 2H), 2.93 (*s*, 6H, N*(*CH_3)$_2$); **^{13}C-NMR** (125 MHz, DMSO-d_6): δ = 165.35, 149.83, 137.81, 134.98, 133.33, 131.50, 128.36, 127.61, 127.58, 127.31, 126.04, 125.14, 123.23, 120.39, 112.27, 39.98; some peaks are missing probably due to overlap. **IR** (KBr) ν (cm^{-1}) = 3437.12, 2920.20, 1661.17, 1613.59, 150.12, 1520.02, 1489.99, 1445.91, 1410.89, 1384.34, 1361.66, 1323.79, 1277.18, 1257.50, 1220.36, 1184.59, 1166.87, 1116.98, 1073.95, 1026.25, 959.60, 897.87, 824.01, 711.78, 689.21, 678.99, 628.32, 537.60; **HRMS** (ESI, m/z): $[M+H]^+$ calc. for $C_{23}H_{23}N_2O$, 343.1805, found: 343.1804.

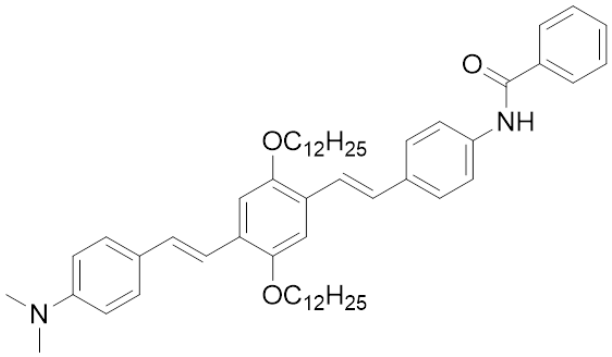

N-(4-((E)-4-((E)-4-(dimethylamino)styryl)-2,5-bis(dodecyloxy)styryl)phenyl)benzamide 2-11

To a solution of derivative **2-1** (50 mg, 0.0705 mmol) and Et_3N (19 µl, 0.141 mmol) in acetone (5 mL, previously dried over 4Å molecular sieves), benzoyl chloride (16 µl, 0.141 mmol) was added at 0 °C. The reaction mixture was stirred at r.t. for 2 h under Argon atmosphere. The reaction was quenched by slow addition of an aq. sol. of $NaHCO_3$ to neutralize formed acid. Precipitated amide was separated by centrifugation, washed several times with MeOH and dried under *vacuo* to give compound **2-11** as a yellow solid (50 mg, **87%**). **M.p.**: 168 °C. **^{1}H-NMR** (500 MHz, CD_2Cl_2): δ = 7.92 (*s*, 1H; N*H*CO), 7.88 (*m*, 2H), 7.67 (*d*, ^3J = 8.5, 2H, Ar*H*), 7.61 – 7.50 (*m*, 5H), 7.47-7.44 (*d*, ^3J = 16.5, 2H, C*H*), 7.43 (*d*, ^3J = 9, 2H), 7.29 – 7.26 (*d*, *J* = 16.5, 2H: C*H*), 7.17 – 7.13 (*m*, 3H), 7.11 – 7.09 (*d*, *J* = 16.5, 2H; C*H*), 6.72 (*d*, ^3J = 9, 2H), 4.06 (*m*, 4H, OCH_2(CH$_2$)$_{10}$CH$_3$), 2.99 (*s*, 6H, N(CH_3)$_2$), 1.93 – 1.83 (*m*, 4H, OCH$_2$CH_2(CH$_2$)$_9$CH$_3$), 1.59 – 1.53 (*m*, 4H; O(CH$_2$)$_2$CH_2(CH$_2$)$_8$CH$_3$), 1.45 – 1.40 (*m*, 4H; O(CH$_2$)$_3$CH_2(CH$_2$)$_7$CH$_3$), 1.28 (*m*, 28H; O(CH$_2$)$_4$ (CH_2)$_7$CH$_3$), 0.87 (*m*, 6H; O(CH$_2$)$_{11}$CH_3). **^{13}C-NMR** (125 MHz, CD_2Cl_2): δ = 165.83, 151.73, 151.26, 150.78, 137.92, 135.64, 134.97, 132.38, 129.52, 129.34, 128.32, 128.06, 127.96, 127.55, 127.52, 123.38, 120.73, 119.21, 112.89, 111.02, 110.43, 70.18, 70.08, 40.77, 32.52, 30.33, 30.30, 30.28, 30.27, 30.25, 30.15, 30.12, 30.08, 30.06, 29.97, 29.96, 26.91, 26.88, 23.28, 14.46. **IR** (KBr) ν (cm^{-1}) = 3437.17, 2921.28, 2850.33, 1647.95, 1521.06, 1489.94, 1466.20, 1425.91,

1411.07, 1325.86, 1269.60, 1200.85, 1071.33, 962.14, 872.81, 721.98, 484.09; **HRMS** (ESI, m/z): $[M+H]^+$ calc. for $C_{55}H_{77}N_2O_3$, 813.5929, found: 813.5922.

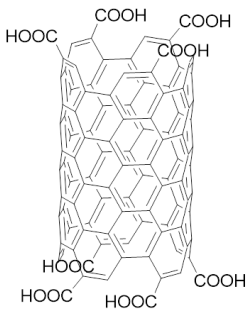

Ox-SWCNTs

Pristine SWCNTs (7, 6) (***p*-SWNCNTs**, 100 mg, Carbon nanotube, single-walled; 704121-1G, lot#MKBK1791V, Sigma Aldrich) were sonicated for 5 min in 100 ml of a 3:1 3M H_2SO_4 : 3M HNO_3 aq. solution and refluxed for 2 h. The resulting suspension was then poured into 200 mL of H_2O and filtered through 0.45 μm membrane. The black precipitate was re-dispersed through 5 min sonication in H_2O (200 mL) and filtered through 0.45 μm membrane. The dispersion/precipitation in H_2O was repeated until the filtrate reached neutral pH. Finally, the black solid was re-dispersed in MeOH (200 mL) to ease the drying and filtered. The product was dried under reduced pressure overnight. 95 mg of oxidized material was collected (yield = **95%** w/w). Characterization: TEM, XPS, TGA, Raman spectroscopy (λ_{exc}= 532nm).

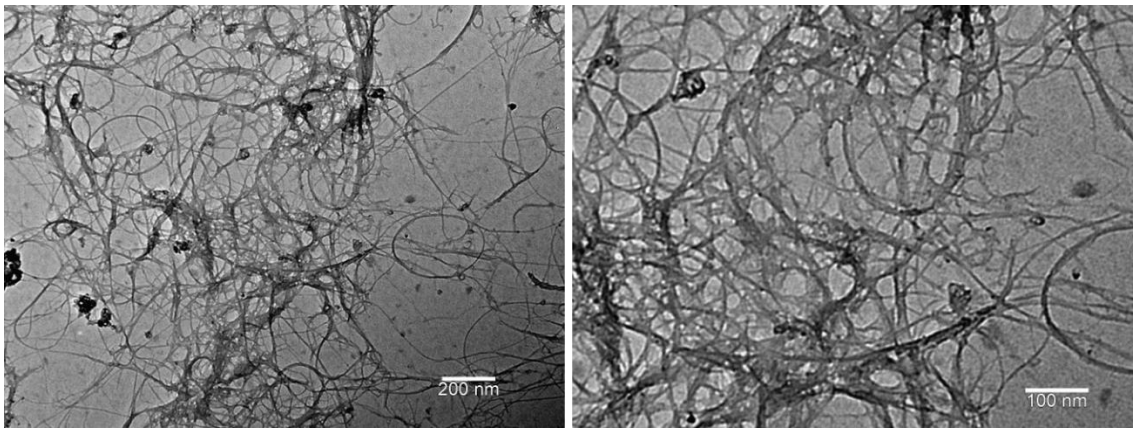

Figure 4.1 TEM images of a carbon-coated copper grid after the deposition of few drops Ox-SWCNTs DMF dispersion. (c ~ 0.1 mg/mL).

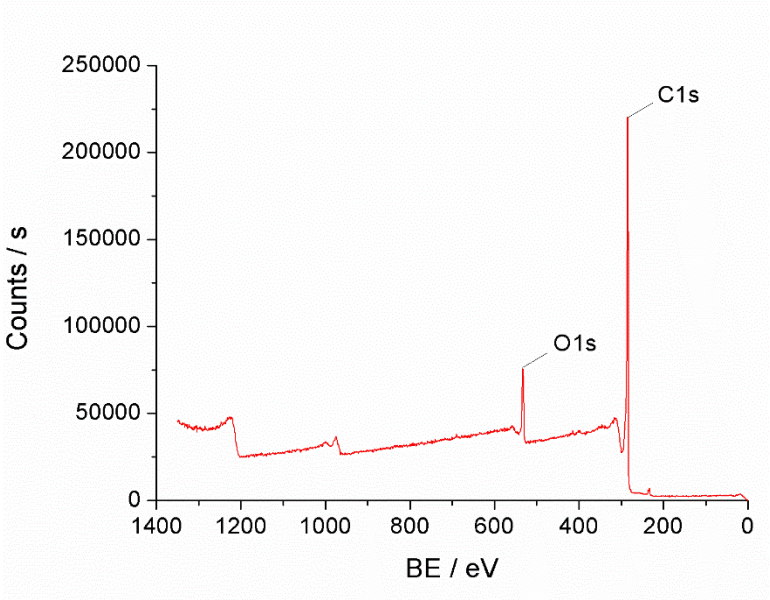

Figure 4.2. XPS Survey spectrum of **ox-SWNTs (7, 6)**

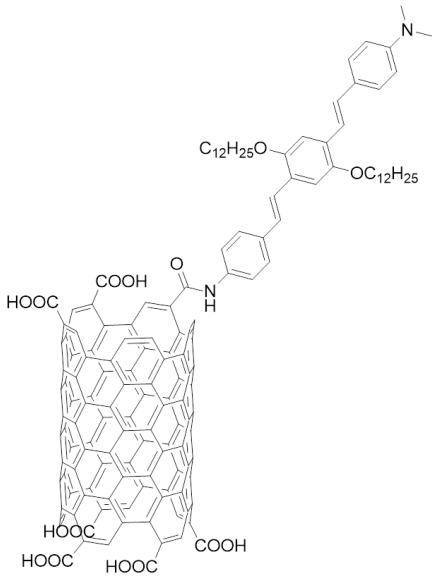

OPV 2-1 functionalized SWCNT (7,6) f-SWCNT-1

30 mg of **ox–SWCNTs** were dispersed in 5 mL of DMF through sonication for 10 min. $SOCl_2$ (15 mL) was added and the mixture heated at 70°C for 24 h. The dispersion was centrifuged and the acidic supernatant decanted and the black precipitate washed with dry THF (5 × 10 mL) and dried under reduced pressure.[12] The obtained SWNTs acyl chloride were re-dispersed into 15 mL of DMF(10 min sonication) and. compound **2-1** (10 mg, 14.10 μmol) added. The reaction mixture was cooled down at 0 °C and Et_3N (1 mL) added drop-wise. The reaction mixture was allowed to warm up r.t. and stirred for 24 h under Ar atmosphere. The dispersion was washed with water (100 mL), re-dispersed into 200 mL of CH_2Cl_2 through 5 min sonication and filtered through a PTFE filter (0.45 μm pore size). The re-dispersion/filtration cycles were repeated using DMF (200 mL × 4), CH_2Cl_2 (200 mL) until the filtered solution was completely colorless, MeOH (200 mL × 2), H_2O (200 mL), MeOH (200 mL × 2), EtOAc (200 mL × 2) and added of few mL of Et_2O to ease the drying under reduced pressure. The collected black precipitate was dried under *vacuo* overnight, yielding 24.9 mg of functionalized **f-SWNTs-1**(yield = **83%** w/w). Characterization: TEM, XPS, TGA, Raman spectroscopy (λ_{exc} = 532).

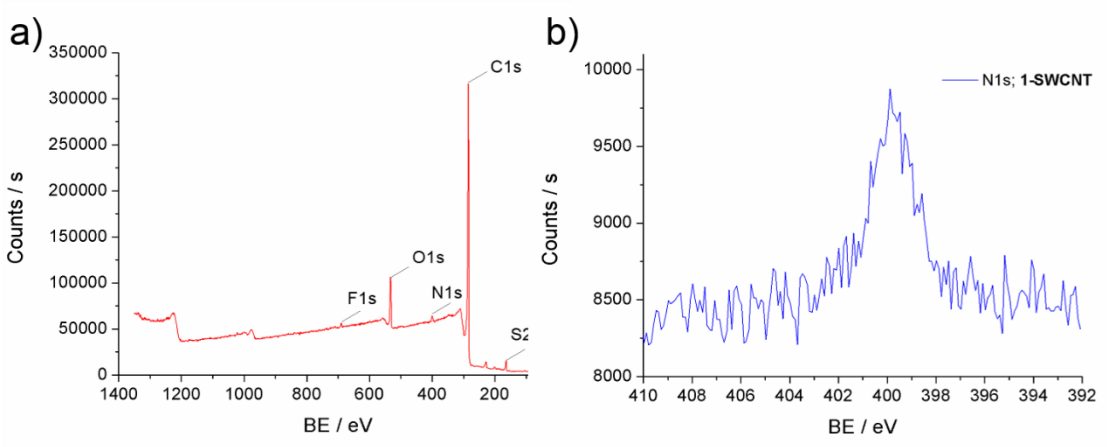

Figure 4.3. (a) XPS Survey spectrum of **ox-SWNTs (7, 6),** (b) XPS high-resolution N 1s spectrum of **f-SWCNT-1**.

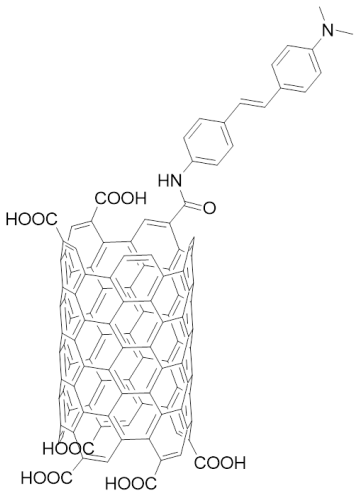

OPV 2-2 functionalized SWCNT (7,6) f-SWCNT-2

20 mg of **ox–SWCNTs** were dispersed in anhydrous DMF (5 mL) through sonication for 10 min. $SOCl_2$ (10 mL) was added, and the mixture heated at 70 °C for 24 h. The dispersion was centrifuged and the acidic supernatant decanted. The black precipitate was washed with anhydrous THF (5 × 10 mL) and dried under reduced pressure.[12] The SWNTs-acyl chloride were re-dispersed into 10 mL of DMF (10 min sonication) and compound **2-2** (10 mg, 42 µmol) added. The reaction mixture was cooled to 0 °C, Et_3N (1 mL) added drop-wise and the mixture allowed to warm up at r.t. and stirred for 24 h under Ar atmosphere. The dispersion was washed with water (100 mL), dispersed into 200 mL of CH_2Cl_2 (5 min

sonication), and filtered through a polytetrafluoroethylene filter (0.45 μm pore size). The re-dispersion/filtration cycles were repeated using DMF (4 × 200 mL), CH_2Cl_2 (200 mL) until the filtered solution was completely colourless, MeOH (2 × 200 mL), H_2O (200 mL), MeOH (2 × 200 mL), EtOAc (2 × 200 mL) and Et_2O (10 mL). The collected black precipitate was dried under vacuum overnight, yielding 16.8 mg of f-SWCNTs-**2** (yield = **84%** w/w). Characterization: TEM, XPS, TGA, Raman spectroscopy (λ_{exc}= 532 nm).

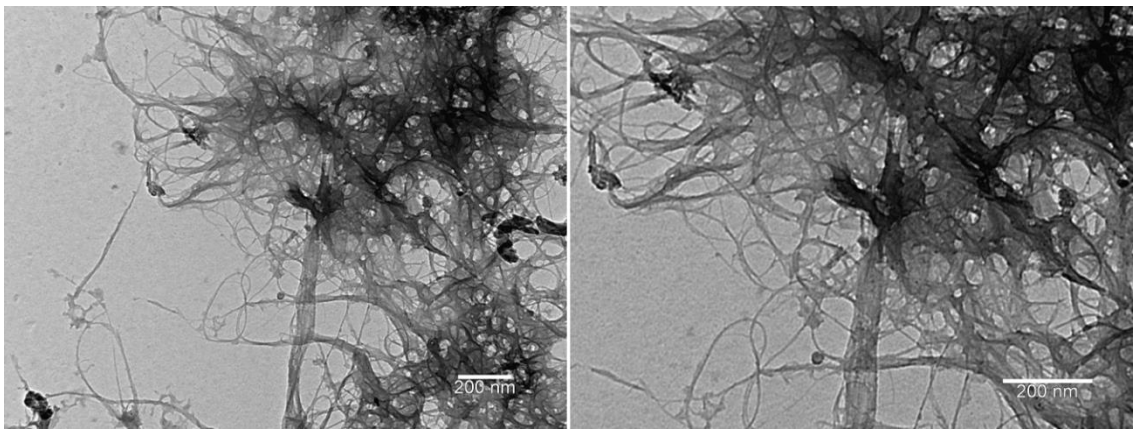

Figure 4.4 TEM images of a carbon-coated copper grid after the deposition of few drops **f-SWCNTs-2** DMF dispersion. (c ~ 0.1 mg/mL).

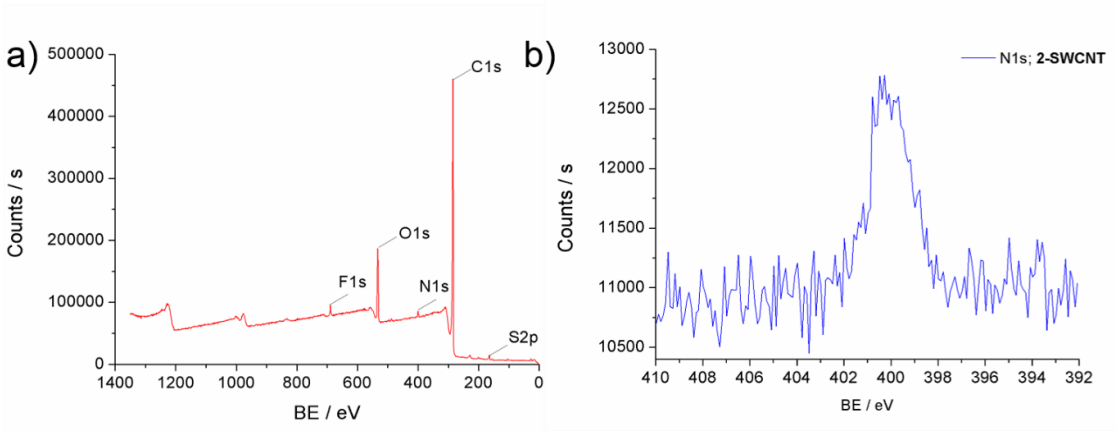

Figure 4.5. (a) XPS Survey spectrum of **ox-SWNTs (7, 6),** (b) XPS high-resolution N 1s spectrum of **f-SWCNT-1**

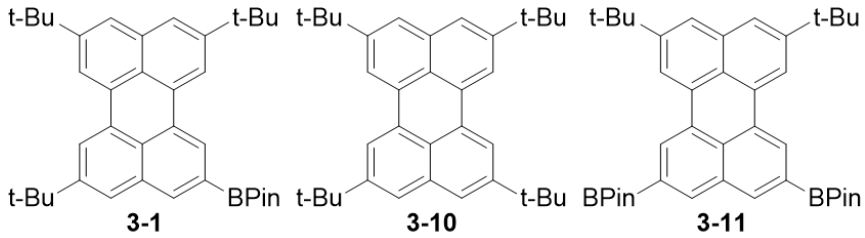

4,4,5,5-tetramethyl-2-(5,8,11-tri-tert-butylperylen-2-yl)-1,3,2-dioxaborolane 1a[13]

2,5,8,11-tetra-*tert*-butylperylene 1b

2,2'-(8,11-di-tert-butylperylene-2,5-diyl)bis(4,4,5,5-tetramethyl-1,3,2-dioxaborolane) 1c

In a flame-dried two-neck round-bottom flask, perylene (1.0 g, 3.96 mmol) was dissolved in ODCB (100 mL, previously dried over 4 Å molecular sieves) and the solution cooled to 0°C (i). Anhydrous $AlCl_3$ (528 mg, 3.96 mmol) was added in portions followed by the drop-wise addition of *t*BuCl (32.52 ml, 297.2 mmol) and the green suspension allowed to warm up at r.t. and stirred for 24 h under Ar. The reaction was quenched by pouring the mixture into ice water and the organic layer separated and solvent removed in *vacuo*. The green residue was re-dispersed in CH_2Cl_2 (250 mL), washed with water (3 × 200 mL) and dried over Na_2SO_4. The crude was subjected to flash column chromatography (Al_2O_3, eluent: CHX) to afford 2,5,8,11-tetra-*tert*-butylperylene **3-10** (173 mg) and a mixture of 2, 5, 8, 11-tetra-; 2, 5, 8-tri-; and 2, 5-di-*tert*-butylperylene (1.4 g as orange solid). The obtained mixture (1.4 g, 5.54 mmol, calc. in respect to perylene), di-*tert*-butyl-2,2-bipyridine (dtbpy) (297 mg, 1.18 mmol), B_2Pin_2 (5.63 g, 22.16 mmol) and anhydrous *n*-hexane (7 mL) were added to a flame-dried Schlenk flask under Ar. The reaction mixture was degassed following freeze-pump-thaw procedure (3 ×). $[Ir(COD)(OMe)]_2$ (367 mg, 0.554 mmol) was added as last, and the reaction mixture degassed one last time and stirred at 80 °C for 24h. The reaction mixture was concentrated under reduced pressure and purified by column chromatography (SiO_2,

CHX (Et_3N, 5 % v/v), toluene-CHX, 1:9 (Et_3N, 5% v/v) and toluene (Et_3N, 5% v/v) to afford compound **3-10** (405 mg, 33 % (total yield obtained)) as bright yellow solid, compound **3-1** (426 mg, **20 %**) as yellow solid evaporated from MeOH, and finally compound **3-11,** which was re-precipitated from cold MeOH to yield **3-11** as a yellow solid (684 mg, **30 %**).

For 4,4,5,5-tetramethyl-2-(5,8,11-tri-tert-butylperylen-2-yl)-1,3,2-dioxaborolane (**3-1**): **M.p**.: 126 °C; **^{1}H NMR** (500 MHz, CD_2Cl_2): δ = 8.46 (*s*, 1H, Ar*H*), 8.35 (*d*, ^4J = 1.5 Hz, 1H, Ar*H*), 8.30 (*d*, ^4J =1.5 Hz, 1H, Ar*H*), 8.26 (*d*, ^4J = 1.5 Hz, 1H, Ar*H*), 8.14 (*s*, 1H, Ar*H*), 7.72 (*d*, ^4J = 1.5 Hz, 1H, Ar*H*), 7.65 (*m*, 2H, Ar*H*), 1.50 (*s*, 9H, C(CH_3)$_3$), 1.49 (*s*, 18H, C(CH_3)$_3$), 1.42 (*s*, 12H, C(CH_3)$_2$). **^{13}C-NMR** (125 MHz, CD_2Cl_2): δ = 149.64, 149.52, 149.45, 136.43, 135.49, 134.79, 131.46, 130.97, 130.93, 130.74, 129.32, 126.04, 124.58, 124.28, 124.12, 123.97, 120.05, 118.86, 118.42, 84.60, 35.42, 35.36, 31.62, 31.60, 31.54, 25.33; some peaks are missing probably due to overlap. **IR** (KBr) ν (cm^{-1}) = 3436.85, 2963.14, 2868.24, 1629.09, 1604.05, 1509.14, 1439.32, 1421.76, 1385.43, 1367.34, 1336.27, 1320.34, 1258.57, 1209.12, 1165.02, 1142.97, 1104.98, 972.49, 99.01, 893.95, 879.61, 854.30, 786.82, 694.62, 670.54, 645.26. **HRMS** (ESI, m/z): $[M+H]^+$ calc. for $C_{38}H_{48}BO_2$, 547.3748, found: 547.3736.

For 2,5,8,11-tetra-*tert*-butylperylene (**3-10**): **M.p**.: > 300 °C; **^{1}H-NMR** (500 MHz, $CDCl_3$): δ = 8.24 (*d*, ^4J = 1.5 Hz, 4H, Ar*H*), 7.62 (*d*, ^4J = 1.5 Hz, 4H, Ar*H*), 1.50 (s, 36H, C*(CH$_3$)$_3$*). In accordance with spectroscopic data reported in literature.[14] **^{13}C-NMR** (125 MHz, $CDCl_3$) δ= 148.85, 135.01, 130.90, 125.90, 123.40, 117.81, 35.04, 31.50.

For 2,2'-(8,11-di-tert-butylperylene-2,5-diyl)bis(4,4,5,5-tetramethyl-1,3,2-dioxaborolane) (**3-11**): **M.p.**:>300 °C. **^{1}H-NMR** (500 MHz, CD_2Cl_2,): δ = 8.56 (*s*, 2H, Ar*H*), 8.31(*d*, ^4J = 1.5 Hz, 2H, Ar*H*), 8.20 (*s*, 2H, Ar*H*), 7.67 (*d*, ^4J = 1.5 Hz, 2H, Ar*H*), 1.51(*s*, 18H, C(CH_3)$_3$), 1.42 (*s*, 24H, C(CH_3)$_2$). **^{13}C-NMR** (125 MHz, CD_2Cl_2,): δ = 149.71, 136.95, 135.44, 134.05,

132.48, 131.08, 130.85, 125.98, 124.12, 118.92, 84.68, 35.44, 31.64, 25.32; some peaks are missing probably due to overlap**. IR** (KBr) ν (cm^{-1}) = 3436.26, 3055.69, 2973.88, 2869.49, 1626.50, 1596.43, 1513.14, 1462.98, 1416.13, 1390.03, 1369.19, 1341.38, 1300.04, 1270.05, 1204.85, 1142.60, 1105.03, 1004.50, 974.72, 964.16, 907.40, 897.01, 880.02, 855.07, 829.37, 817.09, 788.45, 710.82, 691.60, 659.02, 617.96, 578.34, 543.43, 517.23. **HRMS** (ESI, m/z): $[M+H]^+$ calc. for $C_{40}H_{51}B_2O_4$, 617.3981, found: 617.3973. Crystal suitable for X-ray diffraction was obtained by slow diffusion from a CH_2Cl_2/MeOH solution.

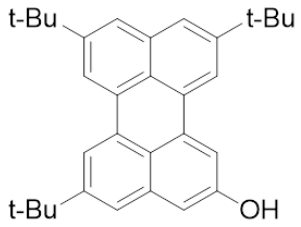

5,8,11-tri-*tert*-butylperylen-2-ol 3-2

Compound **3-1** (200 mg, 0.36 mmol) and NaOH (43 mg, 1.08 mmol) were dissolved in THF (14 ml). An aq. sol. of H_2O_2 (92 µL, 1.08 mmol, 35 wt%) was added drop-wise and the reaction mixture stirred at r.t. for 2 h. The solution was acidified to pH 1-2 by addition of 1 M HCl solution. The reaction mixture was extracted with CH_2Cl_2 (3 × 20 mL) and combined organic layers dried over Na_2SO_4 and the solvent removed in *vacuo*. The crude was purified by column chromatography (SiO_2, eluent: toluene-CHX, 9:1) to afford hydroxyl perylene **3-2** as a yellow solid (130 mg, **83%**). **M.p.**: 224-226 °C. **^{1}H-NMR** (500 MHz, $(CD_3)_2CO$): δ = 8.60 (s, 1H, O*H*), 8.44 (*d*, ^4J =1.5 Hz, 1H, Ar*H*), 8.34 (*d*, ^4J =2.0 Hz, 1H, Ar*H*), 8.31 (*d*, ^4J =2.0 Hz, 1H, Ar*H*), 7.94 (*d*, ^4J = 2.0 Hz, 1H, Ar*H*), 7.76 (*d*, ^4J =1.5 Hz, 1H, Ar*H*), 7.75 (*d*, ^4J =1.5 Hz, 1H, Ar*H*), 7.55 (*d*, ^4J =1.5 Hz, 1H, Ar*H*), 7.11 (*d*, ^4J = 2.0 Hz, 1H, Ar*H*), 1.50 (*s*, 9H, C(C*H*$_3$)$_3$), 1.49 (*s*, 9H, C(C*H*$_3$)$_3$), 1.47 (*s*, 9H, C(C*H*$_3$)$_3$). **^{13}C-NMR** (125MHz, $(CD_3)_2CO$): δ = 156.77, 150.16, 149.79, 149.77, 137.80, 135.95, 133.55, 131.67, 131.50,

131.00, 126.37, 124.70, 124.35, 123.32, 122.83, 119.23, 119.02, 116.93, 111.90, 110.74, 35.54, 35.53, 35.48, 31.55, 31.52. **IR** (KBr) ν (cm^{-1}) = 3509.34, 2962.54, 2905.73, 2868.25, 1612.40, 1600.94, 1478.15, 1460.05, 1430.39, 1382.61, 1366.78, 1336.94, 125.69, 1200.35, 1178.91, 1150.36, 1009.51, 957.77, 920.28, 890.82, 872.76, 859.65, 820.22. 780.48, 736.92, 642.94, 619.89, 535.85, 432.07; **HRMS (**ESI, m/z): [M] calc. for $C_{32}H_{36}O$, 436.2760, found: 436.2758; **UV-Vis** (toluene): λ_{max} = 445 nm (25580±169 M^{-1} cm^{-1}).

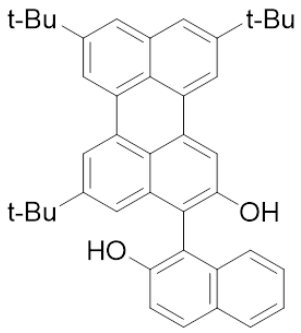

5,8,11-tri-tert-butyl-3-(2-hydroxynaphthalen-1-yl)perylen-2-ol 3-3

In an open single-neck round-bottom flask (50 mL), naphthalen-2-ol (70 mg, 0.48 mmol) and tri-*tert*-butylperylen-2-ol **3-2** (140 mg, 0.32 mmol) were dissolved in CH_2Cl_2 (6 mL). To this solution copper-TMEDA catalyst, $[Cu(OH)(Cl)TMEDA]_2$ (2.5 mg, 5.4 μmol), was added and the reaction mixture stirred at 20 °C, for 1.5 h. The reaction mixture was filtered over a thin pad of silica and washed with CH_2Cl_2. The solvent was removed in *vacuo* and the reaction crude purified by column chromatography (SiO_2, eluents: PET-CH_2Cl_2,9:1→7:3) to afford first compound **3-4** as a dark yellow solid (26 mg, **9%**), then with PET/CH_2Cl_2 [6:4] to afford compound **3-3** as dark yellow solid once evaporated from MeOH (46 mg, **25 %**) and an un-purified fraction (68 mg) containing a mixture of compound **3-3** and starting 2-naphthol. **M.p.**: 173-175 °C. **^{1}H-NMR (**500 MHz, $(CD_3)_2CO$): δ = 8.48 (*d*, ^4J = 1.5 Hz, 1H, ArH_{peryl}), 8.43 (*d*, ^4J =1.5 Hz, 1H, ArH_{peryl}), 8.33 (*d*, ^4J =1.5 Hz, 1H, ArH_{peryl}), 8.14 (*s*,

1H, ArH_{peryl}), 7.98 (*s*, 1H, O*H*), 7.93 (*d*, ^3J = 9 Hz, 1H, ArH_{napht}), 7.89 (*d*, ^3J = 8 Hz, 1H, ArH_{napht}), 7.81(*d*, ^4J =1.5 Hz, 1H, ArH_{peryl}), 7.79 (*d*, ^4J =1.5 Hz, 1H, ArH_{peryl}), 7.37 (*d*, ^3J = 9 Hz, 1H, ArH_{naph}), 7.31 – 7.21 (*m*, 3H$_{napht}$), 7.03 (7.03 (*d*, ^4J =1.5 Hz, 1H), 1.53 (*s*, 9H, C(CH_3)$_3$), 1.51 (*s*, 9H, C(CH_3)$_3$), 1.17 (*s*, 9H, C(CH_3)$_3$). One O*H* peak is not visible due to signal overlap (at 7.81 ppm). **^{13}C-NMR** (125 MHz, $(CD_3)_2CO$): δ = 154.37, 153.63, 149.05, 149.00, 136.07, 135.03, 134.42, 132.58, 130.94, 130.71, 130.10, 129.79, 129.08, 128.00, 126.10, 125.30, 124.71, 123.80, 123.47, 122.90, 122.76, 120.54, 118.58, 118.34, 118.26, 115.95, 114.65, 113.98, 111.34, 34.70, 34.67, 34.45, 30.66, 30.39. **IR** (ATR) ν (cm^{-1}) = 3534.78, 2960.8, 2869.11, 1602.11, 1515.05, 1464.38, 1433.22, 1393.61, 1363.35, 1345.95, 1254.86, 1211.55, 1141.78, 948.09, 922.97, 871.3, 817.52, 786.65, 748.66, 636.11; **HRMS** (ESI, m/z): $[M+1]^+$ calc. for $C_{42}H_{43}O_2$, 579.3258, found: 579.3248; **UV-Vis** (toluene): λ_{max} = 452 nm (33725±232 M^{-1} cm^{-1}).

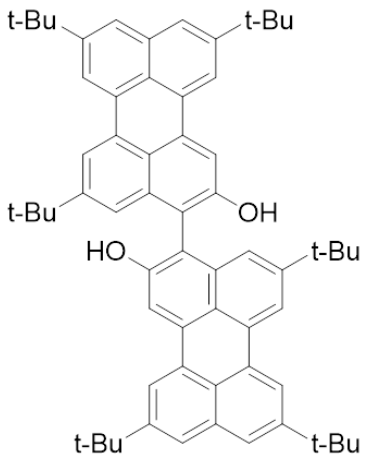

5,5',8,8',11,11'-hexa-tert-butyl-[3,3'-biperylene]-2,2'-diol 3-4

In a 50 mL single-neck round-bottom flask mounted with a reflux condenser, 5, 8, 11-tri-*tert*-butylperylen-2-ol (**3-2**) (150 mg, 0.34 mmol) was dissolved in CH_2Cl_2 (10 mL). To this solution copper-TMEDA catalyst, $[Cu(OH)(Cl)TMEDA]_2$ (2.0 mg, 4.3 μmol), was added and the reaction mixture stirred at 20 °C, for 1h. The mixture was filtered over a thin pad of

silica and washed abundantly with CH_2Cl_2. The solvent was evaporated in *vacuo* and the reaction crude purified by column chromatography (SiO_2, eluent: toluene-CHX, 7:3) to afford compound **3-4.** Evaporation from MeOH gave a dark yellow solid (106 mg, **71%**). **M.p.**: >300 °C. **^{1}H-NMR** (500 MHz, $(CD_3)_2CO$): δ = 8.50 (*d*, ^4J = 1.0 Hz, 2H, Ar*H*), 8.46 (*d*, ^4J=1.0 Hz, 2H, Ar*H*), 8.36 (*d*, ^4J=1.0 Hz, 2H, Ar*H*), 8.17 (*s,* 2H, Ar*H*), 7.94 (s, 2H, O*H*), 7.82 (*d*, ^4J=1.0 Hz, 2H, Ar*H*), 7.80 (*d*, ^4J=1.0 Hz, 2H, Ar*H*), 7.18 (*d*, ^4J=1.0 Hz, 2H, Ar*H*), 1.54 (*s*, 18H, C(C*H*$_3$)$_3$), 1.52 (*s*, 18H, C(C*H*$_3$)$_3$), 1.19 (*s*, 18H, C(C*H*$_3$)$_3$). **^{13}C-NMR** (125 MHz, $(CD_3)_2CO$): δ = 155.20, 149.95, 136.89, 135.98, 133.56, 131.84, 131.65, 131.03, 126.22, 124.76, 124.41, 123.80, 121.93, 119.34, 119.21, 116.83, 115.49, 112.37, 35.63, 35.60, 35.45, 31.59, 31.41; some peaks are missing probably due to overlap. **IR** (KBr) ν (cm^{-1}) = 3535.60, 2962.02, 2907.26, 2869.05, 1603.47, 1477.84, 1463.88, 1434.19, 1393.92, 1363.28, 1254.96, 1212.99, 1183.55, 1151.60, 1031.23, 958.03, 922.15, 871.54, 822.53, 787.90, 726.02, 636.50; **HRMS** (ESI, m/z): [M] calc. for $C_{64}H_{70}O_2$, 870.5370, found: 870.5360. **UV/Vis** (toluene): λ_{max}= 463 nm (64980±216 M^{-1} cm^{-1}); Crystal suitable for X-ray diffraction was obtained by slow diffusion from a CH_2Br_2/MeOH solution.

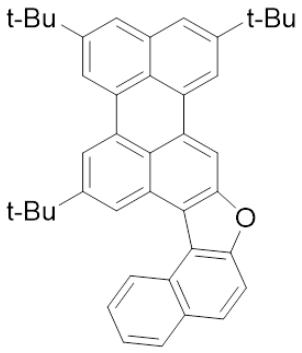

10,13,16-tri-tert-butylnaphtho[2,1-b]peryleno[3,2-d]furan 3-5^{Fur}

Compound **3-3** (11 mg, 19 μmol) was dissolved in toluene (1.5 mL) and refluxed in the presence of *p*-TsOH (72 mg, 380 μmol) for 4 h under Ar atmosphere. The reaction was

quenched with aq.sat. K_2CO_3 solution (5 mL) and extracted with CH_2Cl_2 (3 × 10 mL). Combined organic layers were washed with brine and dried over Na_2SO_4. The solvent was removed in *vacuo* and the crude purified by short silica gel column chromatography with CHX-toluene, 8:2 as eluent to afford compound **3-5^{Fur}** as orange solid (6 mg, **56%**). **M.p.**: 288-290°C. **^{1}H-NMR** (500 MHz, C_6D_6): δ = 9.30 (*d*, ^3J = 8.5 Hz, 1H, Ar-H_{naph}), 9.18 (*s*, 1H, Ar-H_{peryl}), 8.68 (*d*, ^4J =1.5 Hz, 1H, Ar-H_{peryl}), 8.64 (*d*, ^4J =1.5 Hz, 1H, Ar-H_{peryl}), 8.57 (s, 1H, Ar-H_{peryl}), 8.37 (*d*, ^4J =1.0 Hz, 1H, Ar-H_{peryl}), 7.84 (*d*, ^3J = 8.0 Hz, 1H, Ar-H_{naph}), 7.74 (*m*, 2H, Ar-H_{peryl}), 7.65 – 7.60 (*m*, 2H, Ar-H_{naph}), 7.57 (*t*, ^3J =8.5 Hz, 1H, Ar-H_{naph}), 7.38 (t, ^3J =7.5 Hz, 1H, Ar-H_{naph}), 1.54 (s, 9H, C(CH_3)$_3$), 1.48 (s, 9H, C(CH_3)$_3$), 1.40 (s, 9H, C(CH_3)$_3$). **^{13}C-NMR** (125 MHz, C_6D_6,): δ = 156.18, 155.46 , 135.60, 132.88, 132.24, 131.98, 131.75, 131.23, 130.98, 129.91, 129.10, 128.62, 126.39, 126.16, 126.08, 125.87, 124.74, 124.46, 124.26, 122.47, 120.23, 120.19, 119.22, 118.82, 118.01, 112.91, 105.88, 35.57, 35.06, 35.04, 31.65, 31.51, 31.45; some peaks are missing probably due to overlap**.** **IR** (ATR) ν (cm^{-1}) = 2959.89, 2906.07, 2868.3, 1608.6, 1478.23, 1463.31, 1393.02, 1367.21, 1332.81, 1260.69, 1204.09, 1066.73, 1028.96, 1009.32, 954.26, 922.33, 895.36, 873.55, 846.54, 800.9, 742.25, 722.03, 636.14, 524.21. **HRMS** (MALDI, m/z): [M] calc. for $C_{42}H_{40}O$, 560.3079, found: 560.3079. **UV-Vis** (toluene): λ_{max} = 477 nm (47306±119 M^{-1} cm^{-1}). Crystal suitable for X-ray diffraction was obtained by slow diffusion from a C_6D_6/MeOH solution.

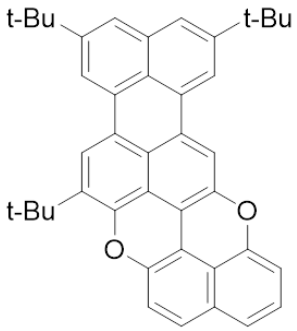

9,12,15-tri-tert-butylbenzo[1,8]isochromeno[5,4,3-cde]benzo[5,10]anthra[9,1,2-hij]isochromene 3-5^{Pp}

To compound **3-3** (20 mg, 34 µmol), CuI (20 mg, 103 µmol) and pivaloic acid (6.9 mg, 68 µmol), anhydrous DMSO (1.5 mL) was added and the resulting mixture stirred under open air conditions at 140 °C for 2 h. CH_2Cl_2 (5 mL) was added and the solution washed with NH_4OH_{sat} (3 ×10 mL), water (10 mL) and brine (10 mL). The aqueous phase was subsequently washed with CH_2Cl_2 (2 × 20 mL) and combined organic layers dried over Na_2SO_4.The solvent was evaporated under reduced pressure and the material purified by re-precipitation from THF/MeOH to afford compound **3-5^{Pp}** as purple solid (11 mg, **57%**). **M.p.**: > 300 °C. **^{1}H-NMR** (500 MHz, C_6D_6): δ = 8.22 (*s*, 1H, ArH_{peryl}), 8.13 (*s*, 1H, ArH_{peryl}), 8.01 (*s*, 1H, ArH_{peryl}), 7.65 (*s*, 1H, ArH_{peryl}), 7.59 (*s*, 1H, ArH_{peryl}), 7.58 (*s*, 1H, ArH_{peryl}), 6.91 (*d*, ^3J = 8.5 Hz, 1H, ArH_{napht}), 6.87 – 6.86 (*m*, 2H, ArH_{napht}), 6.66 – 6.64 (*m*, 1H, ArH_{napht}), 6.61 (*d*, ^3J = 9 Hz, 1H, ArH_{napht}), 1.53 (*s*, 9H, C(CH_3)$_3$), 1.41 (*s*, 9H, C(CH_3)$_3$), 1.32 (*s*, 9H, C(CH_3)$_3$). **IR** (ATR) ν (cm^{-1}) = 2 954.07, 1596.38, 1479.35, 1459.17, 1424.09, 1390.48, 1363.9, 1247.83, 1128.29, 1069.12, 886.4, 865.55, 855.19, 810.55, 792.32, 777.09, 738.83, 714.15, 696.03, 632.63; **HRMS** (MALDI, m/z): [M] calc. for $C_{42}H_{38}O_2$, 574.2872, found: 574.2889; **UV-Vis** (toluene): λ_{max} = 556 nm (36278±360 M^{-1} cm^{-1}).

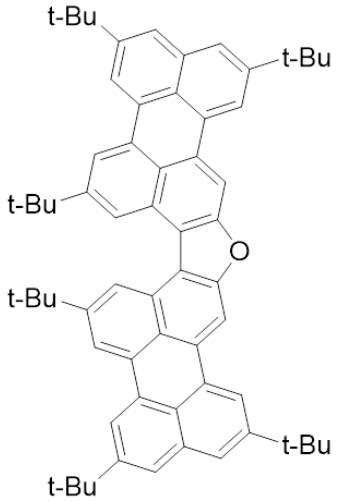

2,5,8,14,17,20-hexa-tert-butyldiperyleno[2,3-b:3',2'-d]furan 3-6^{Fur}

The acid catalysed cyclization of -biperylene-diol **3-4** has been achieved following a slightly modified procedure reported in literature for the synthesis of 7-oxa-[5] helicene derivatives.[15] Compound **3-4** (20 mg, 23 µmol) was dissolved in toluene (1.5 mL) and refluxed in the presence of *p*-TsOH (87.5 mg, 460 µmol) for 4 h under Ar atmosphere. The reaction was quenched with aq. sat. K_2CO_3 solution (5 mL) and extracted with CH_2Cl_2 (3 × 10 mL). Combined organic layers were washed with brine and dried over Na_2SO_4. The solvent was removed in *vacuo* and the crude purified by short column chromatography (SiO_2, eluent: PET/toluene, to afford compound **3-6^{Fur}** as red powder (17.8 mg, **90%**). **M.p.**: > 300 °C. **^{1}H-NMR** (500 MHz, C_6D_6): δ = 9.02 (*d*, ^4J= 1.0 Hz, 2H, Ar*H*), 8.68 (*s*, 4H, Ar*H*), 8.63 (*d*, ^4J = 1.0 Hz, 2H, Ar*H*), 8.41 (*d*, ^4J = 1.0 Hz, 2H, Ar*H*), 7.75 (*d*, ^4J = 1.0 Hz, 2H, Ar*H*), 7.74 (*d*, ^4J = 1.0 Hz, 2H, Ar*H*), 1.57 (*s*, 18H, C(C*H*$_3$)$_3$), 1.49 (*s*, 18H, C(C*H*$_3$)$_3$), 1.39 (*s*, 18H, C(C*H*$_3$)$_3$). **^{13}C-NMR** (125 MHz, C_6D_6): δ = 156.94, 149.46, 149.22, 149.15, 135.60, 133.17, 132.35, 131.78, 131.28, 126.17, 126.14, 124.54, 124.29, 121.16, 120.50, 119.31, 119.17, 118.99, 105.59, 35.58, 35.08, 35.04, 31.67, 31.52, 31.46; one peak is missing probably due to overlap. **IR** (ATR) ν (cm^{-1}) = 2955.52, 1692.39, 1599.03, 1463.09, 1393.57, 1366.27, 1330.62, 1259.48, 1034.77, 864.17, 844.52, 805.47, 781.08, 636.36. **HRMS** (MALDI, m/z):

[M] calc. for $C_{64}H_{68}O$, 852.5270, found 852.5268. **UV/Vis** (toluene): λ_{max} = 534 nm (97 449 ± 989 M^{-1} cm^{-1}). Crystal suitable for X-ray diffraction was obtained by slow evaporation of solvent from a C_6D_6/hexane solution.

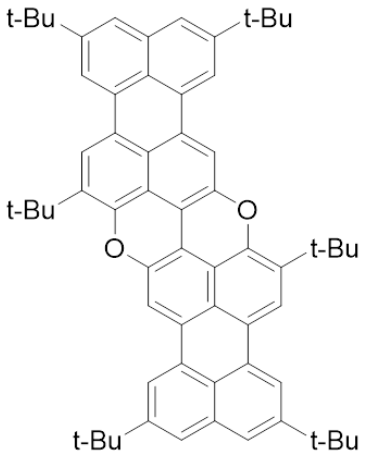

2,5,9,12,15,19-hexa-tert-butylbenzo[5',10']anthra[9',1',2':7,8,1]isochromeno[5,4,3-cde]benzo[5,10]anthra[9,1,2-hij]isochromene 3-6^{Pp}

To a 5 mL round bottom flask was added biperylene'-diol **3-4** (25 mg, 29 µmol), CuI (16.4 mg, 86 µmol), PivOH (6.0 mg, 58 µmol) and anhydrous DMSO (2.5 mL). The resulting mixture was stirred under open air conditions at 140 °C for 2 h. CH_2Cl_2 (5 mL) was added and the solution washed with NH_4OH_{sat} (3 × 10 mL), water (10 mL) and brine (10 mL). The aqueous phase was extracted with CH_2Cl_2 (2 × 15 mL). The combined organic layers were dried over Na_2SO_4 and evaporated in *vacuo*. The residue was purified by re-precipitation in THF/MeOH affording compound **3-6^{Pp}** as dark blue powder (21 mg, **84%**). **M.p.**: > 300 °C; **^{1}H-NMR** (500 MHz, $C_6D_5CD_3$): δ = 8.24 (*d*, ^4J = 1.0 Hz, 2H, Ar*H*), 8.19 (*s*, 2H, Ar*H*), 8.15 (*d*, ^4J = 1.0 Hz, 2H, Ar*H*), 7.77 (*s*, 2H, Ar*H*), 7.63 (*s*, 2H, Ar*H*), 7.60 (*s*, 2H, Ar*H*), 1.64 (*s*, 18H, C(C*H*$_3$)$_3$), 1.45 (*s*, 18H, C(C*H*$_3$)$_3$), 1.33 (*s*, 18H, C(C*H*$_3$)$_3$). ^{13}C-NMR spectrum was not possible to record. **IR** (KBr) ν (cm^{-1}) = 3511.40, 3430.26, 2955.24, 2909.03, 2870.14,

1619.30, 1590.20, 1478.70, 1463.90, 1434.57, 1417.94, 1392.82, 1325.38, 1286.92, 1259.82, 1228.30, 1202.09, 1188.35, 1125.25, 1109.12, 1036.21, 962.23, 946.42, 870.32, 854.07, 815.46, 788.20, 765.43, 706.87, 650.98, 628.07, 505.68; **HRMS** (MALDI, m/z): [M] calc. for $C_{64}H_{66}O_2$, 866.5063, found 866.5059. **UV-Vis** (toluene): λ_{max}= 639 nm (66417±327 M^{-1} cm^{-1}).

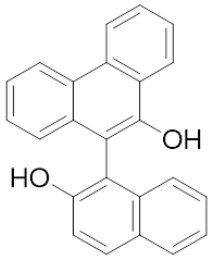

10-(2-hydroxynaphthalen-1-yl)phenanthren-9-ol 3-9

In an open single-neck round-bottom flask (100 mL), naphthalen-2-ol (300 mg, 2.08 mmol) and freshly purified 9-phenanthrol (367 mg, 1.89 mmol) were dissolved in CH_2Cl_2 (23 mL). To this solution copper-TMEDA catalyst, $[Cu(OH)(Cl)TMEDA]_2$ (13 mg, 28.4 μmol), was added and the reaction mixture stirred at 20 °C, for 2 h. The reaction mixture was filtered over a thin pad of silica and washed with CH_2Cl_2. The solvent was removed in *vacuo* and the reaction crude purified by column chromatography (SiO_2, CHX-EtOAc, 10:0.5) to afford first [9,9'-biphenanthrene]-10,10'-diol as white solid (152 mg, **21 %**), compound **3-9** as a light yellow solid (195 mg, **31%**), an un-purified mixture of compound **3-9** and unreacted starting materials (160 mg) and as last, a fraction containing [1,1'-binaphthalene]-2,2', which yield was not quantifiable probably due to the presence of other oxidized by-products. **M.p.**: 85-87 °C. **^{1}H-NMR** (500 MHz, (CD_2Cl_2): δ = 8.82 (*d*, ^3J = 8.5, 1H), 8.76 (*d*, ^3J = 8.5, 1H), 8.43 (*d*, ^3J = 8.0, 1H), 8.04 (*d*, ^3J = 9.0, 1H), 7.94 (*d*, ^3J = 8.0, 1H), 7.84 – 7.81 (*m*, 1H), 7.75-7.72 (*m*, 1H), 7.57-7.53 (*m*, 1H), 7.46 – 7.35 (*m*, 3H), 7.33 – 7.27 (*m*, 1H), 7.21 (d, *J* = 8.5

Hz, 1H), 7.14 (d, *J* = 8.5 Hz, 1H), 5.53 (s, 1H, Ar-O*H*), 5.23 (bs, 1H, Ar-O*H*). **^{13}C-NMR** (125 MHz, CD_2Cl_2): δ = 153.69, 149.68, 134.21, 132.48, 132.35, 132.10, 130.21, 129.01, 128.65, 128.11, 127.99, 127.63, 127.43, 125.48, 125.37, 125.30, 124.71, 124.61, 123.83, 123.50, 123.27, 118.33, 111.60, 107.84; **IR** (ATR) ν (cm^{-1}) = 3503.69, 3060.51, 1619.45, 1593.99, 1515.22, 1494.09, 1466.24, 1449.91, 1407.44, 1388.12, 1326.75, 1301.1, 1266.4, 1211.86, 1149, 1134.9, 1109.1, 1094.82, 1029.71, 961.27, 819.41, 758.08, 725.65, 670.83, 575.73. **HRMS** (ESI, m/z): $[M+H]^+$ calc. for $C_{24}H_{17}O_2$, 337.1223, found: 337.1223.

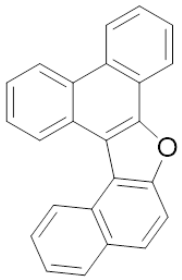

Naphtho[2,1-b]phenanthro[9,10-d]furan 3-7^{Fur}

Compound **3-9** (28 mg, 83 μmol) was dissolved in toluene (4 mL) and refluxed in presence of *p*-TsOH (317 mg, 1.66 mmol) for 4 h under Ar atmosphere. The reaction was quenched with aq. sat. K_2CO_3 solution and extracted three times with CH_2Cl_2 Combined organic layers were washed with brine and dried over Na_2SO_4. The solvent was removed in *vacuo* and the crude purified by short silica gel column chromatography with CHX/EtOAc [9.5:0.5] as eluent to afford compound **3-7^{Fur}** as white solid (24 mg, **91%**). Characterization in accordance with spectroscopic data reported in literature.[16] **M.p.**: 205-207 °C. **^{1}H-NMR** (500 MHz, (CD_2Cl_2): δ = 9.17 (*d*, ^3J = 8.5, 1H), 9.14 (*d*, ^3J = 8.5, 1H), 8.88 (*d*, ^3J = 8.5, 1H), 8.81 (*d*, ^3J = 7.5, 1H), 8.57 (*m*, 1H), 8.11 (*d*, ^3J =8.5, 1H), 8.0 (*d*, ^3J =9.0, 1H), 7.95 (*d*, ^3J = 9.0, 1H), 7.87 – 7.71 (*m*, 5H), 7.61 (*t,* ^3J = 7.5 Hz, 1H); **^{13}C-NMR** (125 MHz, CD_2Cl_2): δ = 154.72, 151.63, 132.02, 130.89, 130.00, 129.26, 129.03, 128.63, 128.45, 127.91, 127.59,

127.16, 126.80, 126.65, 126.13, 125.84, 125.08, 124.59, 123.83, 122.74, 121.87, 120.44, 117.20, 113.21; **IR** (ATR) ν (cm^{-1}) = 2922.27, 2851.36, 1608.46, 1583.81, 1505.38, 1442.67, 1390.79, 1365.55, 1311.42, 1256.77, 1234.66, 1085.44, 1031.39, 996.98, 949.59, 860.11, 806.26, 755.18, 748.02, 723.05, 698.95, 623.06, 528.41, 514.15. **HRMS** (MALDI, m/z): $[M+H]^{+\bullet}$: calc. for $C_{24}H_{14}O$, 318.1045 , found: 318.1044. **UV-Vis** (toluene): λ_{max} = 352 nm (26856±195 M^{-1} cm^{-1}). Crystal suitable for X-ray diffraction was obtained by slow evaporation of solvent from a methylene chloride-d_2 solution.

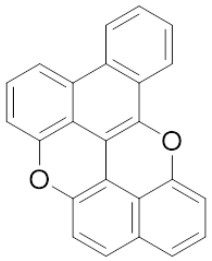

Benzo[c]xantheno[2,1,9,8-klmna]xanthene 3-7^{Pp}

Method A: To a 5 mL round-bottom flask, compound **3-9** (45 mg, 0.13 mmol), CuI (76.2 mg, 0.4 mmol) and pivaloic acid (26.5 mg, 0.26 mmol) and DMSO (1.5 mL) were added. The resulting mixture was stirred under open air conditions at 140 °C for 2h. CH_2Cl_2 (20 mL) was then added and the solution was washed with NH_4OH_{sat}, water and brine. The aqueous phase was then washed with CH_2Cl_2. Combined organic layers were dried over Na_2SO_4 and the solvent evaporated *in vacuo*. The solid crude was purified by flash column chromatography (SiO_2, eluent: CHX-EtOAC,10:0.5) to afford compound **3-7^{Pp}** as bright yellow solid (5.6 mg, **13%**).

Method B: In a 10 mL microwave-reactor tube containing a stirring bar, compound**3-9** (20 mg, 59 μmol) and CuO (57 mg, 0.71 mmol) were dissolved into 0.2 mL of nitrobenzene. The reaction vessel was sealed and placed into the microwave reactor. The temperature

heating profile for the reaction mixture was as follows: rt → 240 °Cover a 4-min period (200-W maximum power), the reaction mixture was held at 240 °C (200-W maximum power) for 120 min. The crude was filtered over celite and washed abundantly with CH_2Cl_2. The solvent was removed in *vacuo* and the residue re-precipitated several times from hot THF and MeOH to yield compound **3-7^{Pp}** as yellow solid (7.4 mg, **37%**). **M.p.**: >300 °C. **^{1}H-NMR** (500 MHz, C_6D_6, 65 °C): δ = 8.18 (*dd*, *J* = 8.5, 1.0 Hz, 1H), 8.15 (d, ^3J = 8.5 Hz, 1H), 7.66 (*d*, ^3J = 8.0 Hz, 1H),), 7.38 – 7.33 (m, 1H), 7.30 – 7.25 (m, 1H), 7.04 (*t*, ^3J = 8.0 Hz, 1H), 6.97 (*d*, ^3J = 9.0 Hz, 1H), 6.91 – 6.84 (*m*, 2H), 6.80 (*d*, ^3J = 8.0 Hz, 1H), 6.75 (*d*, ^3J =9.0 Hz, 1H), 6.67 (*dd*, *J* = 7.0, 1.5 Hz, 1H); **IR** (ATR) ν (cm^{-1}) = 2922.31, 2852.72, 1623.2, 1493.66, 1457, 1431.6, 1318.83, 1273.94, 1238.01, 1090.14, 822.3, 768.35, 747.82. **HRMS** (EI, m/z): $[M+H]^{+\bullet}$: calc. for $C_{28}H_{14}O_2^{\bullet+}$, 332.0837, found: 332.0824; **UV-Vis** (toluene): λ_{max} = 446 nm (14068±129 M^{-1} cm^{-1}).

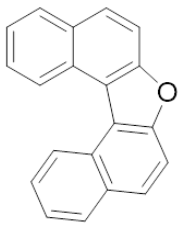

Dinaphtho[2,1-b:1',2'-d]furan 3-8^{Fur}[17]

[1,1'-binaphthalene]-2,2'-diol (200 mg, 0.69 mmol) was dissolved in toluene (35 mL) and refluxed in presence of *p*-TsOH (1.3 g, 6.9 mmol) overnight under Ar atmosphere. The reaction was quenched with aq. sat. K_2CO_3 solution and extracted three times with CH_2Cl_2 Combined organic layers were washed with brine and dried over Na_2SO_4. The solvent was removed in *vacuo* and the crude purified by short column chromatography (SiO_2, eluent:CHX/EtOAc,10:0.5)to afford compound **3-8^{Fur}** as crystalline white solid (60 mg, **32%**). 130 mg of unreacted starting material was collected. Characterization in accordance

with spectroscopic data reported in literature.[17] **^{1}H-NMR** (500 MHz, $CDCl_3$): δ = 9.17 (*d*, ^3J = 8.0 Hz, 2H), 8.08 (*d*, ^3J = 8.0 Hz, 2H), 7.97 (*d*, ^3J = 9.0 Hz, 2H), 7.85 (*d*, ^3J = 9.0 Hz, 2H), 7.76 (*t*, ^3J = 8.0 Hz, 2H), 7.60 (*t*, ^3J =8.0 Hz, 1H); **^{13}C-NMR** (125 MHz, C_6D_6): δ = 154.51, 131.38, 129.65, 128.78, 128.49, 126.35, 125.78, 124.56, 119.58, 112.90.

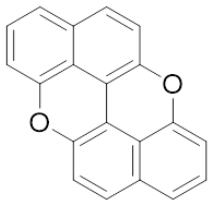

Xantheno[2,1,9,8-klmna]xanthene 3-8^{Pp}[18]

Commercialy available [1,1'-binaphthalene]-2,2'-diol (100 mg, 0.35 mmol), CuI (200 mg, 1.05 mmol), PivOH (71.5 mg, 0.7 mmol) and DMSO (4 mL) were stirred open to air at 140 °C for 2h. CH_2Cl_2 (15 mL) was added and the solution washed with NH_4OH_{sat} (20 mL × 3) and brine. The aqueous phase was washed with CH_2Cl_2 (3 × 20 mL). The organic layers were collected, dried over Na_2SO_4 and evaporated *in vacuo*. The residue was purified by column chromatography (SiO_2, eluents: PET:CH_2Cl_2, 9:1) affording PXX as a yellow fluorescent solid (83 mg, **86 %**). Characterization in accordance with spectroscopic data reported in literature.[19] **^{1}H-NMR** (500 MHz, C_6D_6): δ = 6.89 (*d*, ^3J = 9.0 Hz, 2H), 6.81 (*m*, 4H), 6.69 (*d*, ^3J = 9.0 Hz, 2H), 6.56 (*m*, 2H); **^{13}C-NMR** (125 MHz, C_6D_6): δ = 153.18, 144.70, 131.76, 127.36, 126.56, 122.13, 120.37, 117.50, 112.01, 108.95.

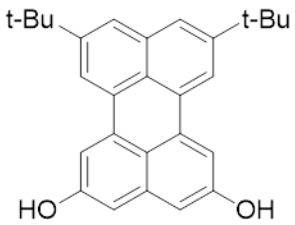

8,11-di-tert-butylperylene-2,5-diol 3-12

Compound **3-11** (530 mg, 0.86 mmol) and NaOH (69 mg, 1.72 mmol) were dissolved in THF (40 mL). An aqueous solution of H_2O_2 (140 µL, 1.72 mmol, 35 wt%) was added drop-wise and the reaction mixture stirred at r.t. for 3 h. The solution was acidified to pH 1-2 by addition of 1 M HCl solution andextracted with CH_2Cl_2 (3 × 25 mL). Combined organic layers were dried over Na_2SO_4 and the solvent removed in *vacuo*. The crude was purified by column chromatography (SiO_2, eluents: toluene-EtOAc,9:1) affording 8,11-di-tert-butylperylene-2,5-diol (**3-12**) as a greenish solid (263 mg, 77%). **M.p.**: 204-205 °C. **^{1}H-NMR** (500 MHz, $(CD_3)_2CO$, 25 °C): δ = 8.52 (s, 2H, O*H*), 8.32 (*d*, ^4J =1.5 Hz, 2H, Ar*H*), 7.80 (*d*, ^4J =2.0 Hz, 2H, Ar*H*), 7.76 (*d*, ^4J =1.5 Hz, 2H, Ar*H*), 6.93 (*d*, ^4J = 2.0 Hz, 2H, Ar*H*), 1.49 (*s*, 18H, C(C*H*$_3$)$_3$). **^{13}C-NMR** (125 MHz, $(CD_3)_2CO$): δ = 157.13, 149.79, 139.53, 135.81, 133.73, 131.01, 126.17, 124.63, 120.16, 119.40, 109.95, 109.27, 35.54, 31.54. **IR** (KBr) ν (cm^{-1}) = 3288.63, 2953.02, 2906.73, 2868.15, 1604.77, 1463.97, 1417.68, 1392.61, 1377.17, 1363.67, 1340.53, 1255.66, 1215.15, 1172.72, 1141.86, 1114.86, 1070.49, 1028.06, 989.48, 941.26, 898.83, 875.68, 856.39, 817.82, 777.31, 748.38, 650.01, 621.08, 569.00, 549.71, 534.28, 472.56, 420.48, 412.77, 406.98; **HRMS (**ESI, m/z): $[M+H]^+$ calc. for $C_{28}H_{29}O_2$, 397.2162, found: 397.2158; **UV-Vis** (toluene): λ_{max}= 449 nm (18231±474 M^{-1} cm^{-1}). Compound **3-12** undergoes oxidation under ambient conditions.

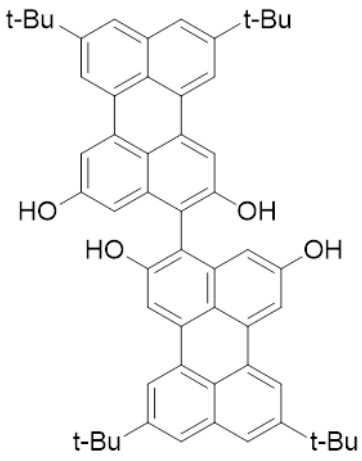

8,8',11,11'-tetra-tert-butyl-[3,3'-biperylene]-2,2',5,5'-tetraol 3-13

Compound **3-11** (1.0 g, 1.62 mmol) and NaOH (390 mg, 9.73 mmol) were dissolved in THF (80 mL). An aqueous solution of H_2O_2 (0.836 mL, 9.73 mmol, 35 wt%) was added drop-wise and the reaction mixture stirred at r.t. for 2 h. The solution was acidified to pH 1-2 by addition of 1 M HCl solution and extracted with CH_2Cl_2 (3 × 50 mL). Combined organic layers were dried over Na_2SO_4 and the solvent removed in *vacuo*. The crude was purified by column chromatography (SiO_2, eluents: toluene/EtOAc, 10:0.5) affording 8,11-di-tert-butylperylene-2,5-diol (**3-13**) as orange solid (402 mg, **63 %**) and compound **3-12** as greenish powder (232 mg, **36%**). **M.p.**: >300 °C. **^{1}H-NMR** (500 MHz, $(CD_3)_2CO$): δ = 8.46 (*d*, ^4J = 1.0 Hz, 2H, Ar*H*), 8.41 (*d*, ^4J = 1.5 Hz, 2H, Ar*H*), 8.35 (s, 2H, O*H*), 8.01 (s, 2H, Ar*H*), 7.84-7.80 (*m*, 8H), 6.46 (*d*, ^4J = 2.0 Hz, 2H, Ar*H*), 1.54 (*s*, 18H, C(CH_3)$_3$), 1.52 (*s*, 18H, C(CH_3)$_3$). **^{13}C-NMR** (125 MHz, $(CD_3)_2CO$): δ =157.44, 155.68, 150.00, 149.97, 138.93, 135.82, 134.07, 133.75, 131.11, 130.98, 126.01, 124.71, 124.69, 120.61, 119.67, 119.50, 114.08, 110.25, 109.93, 108.13, 35.63, 31.57; some peaks are missing probably due to overlap. **IR** (ATR) ν (cm^{-1}) = 3527.80, 3358.07, 2954.95, 2906.73, 2868.15, 1600.92, 1521.84, 1463.97, 1436.97, 1392.61, 1361.74, 1340.53, 1290.38, 1255.66, 1209.37, 1176.58, 1138.00, 1068.56, 993.34, 945.12, 877.61, 856.39, 819.75, 777.31, 765.74, 732.95, 644.22, 621.08, 590.22, 503.42, 416.62, 405.05; **HRMS (**ESI, m/z): $[M+H]^+$ calc. for

$C_{56}H_{55}O_4$, 791.4095, found: 791.4088; **UV-Vis** (toluene): λ_{max}=463 nm (99577 ±1370 M^{-1} cm^{-1}).

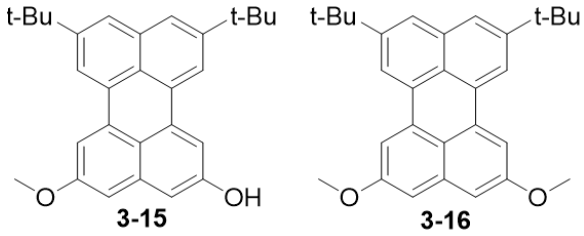

8,11-di-tert-butyl-5-methoxyperylen-2-ol 3-15

For 2,5-di-tert-butyl-8,11-dimethoxyperylene 3-16

In a flame-dried Schlenk flask compound **3-11** (520 mg, 1.31 mmol), K_2CO_3 (197 mg, 1.44 mmol) and acetone (10 mL) were added. The resulting mixture was degassed three times by freeze-pump-thaw procedureMeI (87 μL, 1.44 mmol) was added under argon at room temperature and the reaction mixture refluxed for 12 h and further stirred for 3 h at room temperature. A 1 M aqueous solution of HCl (10 mL) and CH_2Cl_2 (10 mL) were added to the solution. The mixture was washed with H_2O (2 × 20 mL) and the aqueous layer extracted with CH_2Cl_2 (2 × 20 mL). The combined organic layers were dried over Na_2SO_4 and evaporated in *vacuo*. The residue was purified by column chromatography (SiO_2, eluent: toluene) affording **3-15** as a yellow solid (182 mg, **34%**), **3-16** as yellow powder (65 mg, 13 %) and unreacted starting material (221 mg, 43%).

For **8,11-di-tert-butyl-5-methoxyperylen-2-ol (3-15)**: **M.p.**: 249-250 °C. **^{1}H-NMR** (500 MHz, $(CD_3)_2SO$): δ = 8.59 (s, 1H, O*H*), 8.39 (*d*, ^4J = 1.5 Hz, 1H, Ar*H*), 8.33 (*d*, ^4J = 1.5 Hz, 1H, Ar*H*), 7.84 (*d*, ^4J = 2.5 Hz, 1H, Ar*H*), 7.78 (*d*, ^4J = 2.0 Hz, 1H, Ar*H*), 7.77 (*d*, ^4J = 1.5 Hz, 2H, Ar*H*), 7.05 (*d*, ^4J = 2.0 Hz, 1H, Ar*H*), 7.02 (*d*, ^4J = 2.5 Hz, 1H, Ar*H*), 3.93 (s, 3H, OCH_3), 1.49 (*m*, 18H, C(CH_3)$_3$). **^{13}C-NMR** (125MHz, $(CD_3)_2CO$): δ = 159.66, 157.27,

149.91, 149.80, 139.35, 135.78, 133.71, 133.61, 130.89, 130.81, 126.15, 124.73, 124.71, 120.53, 119.74, 119.46, 110.31, 110.23, 110.05, 105.95, 55.55, 35.58, 35.55, 31.54, 31.53; **IR** (ATR) ν (cm^{-1}) = 3259.70, 2945.30, 2868.15, 1606.70, 1585.49, 1519.91, 1462.04, 1444.68, 1431.18, 1381.03, 1369.46, 1319.31, 1292.31, 1257.59, 1226.73, 1199.72, 1166.93, 1155.36, 1147.65, 1116.78, 1076.28, 1051.20, 1002.98, 956.69, 904.61, 875.68, 852.54, 817.82, 802.39, 777.31, 750.31, 719.45, 667.37, 655.80, 621.08, 555.50, 536.21, 462.92, 420.48, 412.77. **HRMS (**ESI, m/z): $[M+H]^+$ calc. for $C_{29}H_{31}O_2$, 411.2319, found: 411.2316; **UV-Vis** (toluene): λ_{max}= 444 nm (19486±583 M^{-1} cm^{-1}).

For 2,5-di-tert-butyl-8,11-dimethoxyperylene (**3-16**): **M.p.**: 254-255 °C. **^{1}H-NMR** (500 MHz, $(CD_3)_2SO$): δ = 8.40 (*d*, ^4J =1.5 Hz, 2H, Ar*H*), 7.83 (*d*, ^4J = 2.0 Hz, 1H, Ar*H*), 7.78 (*d*, ^4J = 1.5 Hz, 2H, Ar*H*), 7.14 (*d*, ^4J =2.0 Hz, 1H, Ar*H*), 3.95 (s, 6H, OCH_3), 1.50 (*s*, 18H, C(CH_3)$_3$). **^{13}C-NMR** (125 MHz, $(CD_3)_2CO$): δ= 159.76, 149.94, 139.18, 135.77, 133.61, 130.69, 126.13, 12,4.83, 120.96, 119.82, 110.58, 106.74, 55.60, 35.60, 31.52. **IR** (ATR) ν (cm^{-1}) = 3007.02, 2951.09, 2852.72, 1602.85, 1517.98, 1454.33, 1429.25, 1382.96, 2904.80, 1334.74, 1290.38, 1257.59, 1230.58, 1209.37, 1192.01, 1161.15, 1116.78, 1080.14, 1060.85, 1033.85, 985.62, 954.76, 920.05, 904.61, 875.68, 856.39, 848.68, 829.39, 817.82, 777.31, 746.45, 669.30, 655.80, 623.01, 536.21, 520.78, 466.77, 416.62, 403.12. **HRMS (**ESI, m/z): $[M+H]^+$ calc. for $C_{30}H_{33}O_2$, 425.2475, found: 425.2469.

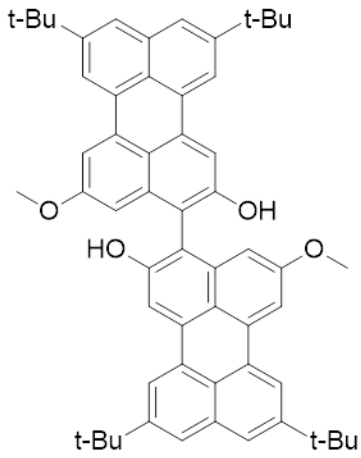

8,8',11,11'-tetra-tert-butyl-5,5'-dimethoxy-[3,3'-biperylene]-2,2'-diol 3-17

In a 50 mL single-neck round-bottom flask mounted with a reflux condenser, compound **3-15** (182 mg, 0.44 mmol) was dissolved in CH_2Cl_2 (13 mL). To this solution $[Cu(OH)(Cl)TMEDA]_2$ (6.1 mg, 13.2 µmol) was added and the reaction mixture stirred at 20 °C for 1 h. The mixture was filtered over a thin pad of silica and washed abundantly with CH_2Cl_2. The solvent was evaporated in *vacuo* and the reaction crude purified by column chromatography (SiO_2, eluent: toluene) to afford desired compound **3-17** as a dark yellow solid (81 mg, **45 %**) and compound **3-18^{Pp}** as blue solid (21 mg, 12 %). **M.p.**: 268-269 °C. **^{1}H-NMR** (500 MHz, $(CD_3)_2CO$): δ = 8.46 (*m*, 4H, Ar*H*), 8.07 (*s,* 2H, Ar*H*), 7.95 (bs, 2H, O*H*), 7.86 (*d*, ^4J = 2.5 Hz, 2H, Ar*H*), 7.83 (*d*, ^4J = 2.0 Hz, 2H, Ar*H*), 7.82 (*d*, ^4J = 1.5 Hz, 2H, Ar*H*), 6.59 (*d*, ^4J = 2.5 Hz, 2H, Ar*H*), 3.58 (s, 6H, OCH_3), 1.54 (*s*, 18H, C(CH_3)$_3$), 1.52 (*s*, 18H, C(CH_3)$_3$). **^{13}C-NMR** (125 MHz, $(CD_3)_2CO$): δ = 159.86, 155.79, 150.07, 149.98, 138.58, 138.02, 135.79, 133.99, 133.80, 130.96, 130.91, 126.02, 124.80, 121.16, 119.98, 119.60, 114.75, 110.71, 109.87, 105.20, 55.35, 35.66, 35.64, 31.58, 31.56. **IR** (ATR) ν (cm^{-1}) = 3529.73, 2953.02, 2906.73, 2866.22, 1600.92, 1517.98, 1460.11, 1429.25, 1379.10, 1361.74, 1290.38, 1257.59, 1209.37, 1176.58, 1163.08, 1141.86, 1114.86, 1068.56, 1043.49, 993.34, 956.69, 929.69, 898.83, 877.61, 858.32, 819.75, 804.32, 775.38, 729.09, 646.15, 624.94, 505.35, 466.77, 432.05, 418.55. **HRMS** (ESI, m/z): $[M+H]^+$ calc. for

$C_{58}H_{59}O_4$, 819.4408, found: 819.4385. **UV-Vis** (toluene): λ_{max} = 459 nm (56777±1287 M^{-1} cm^{-1}).

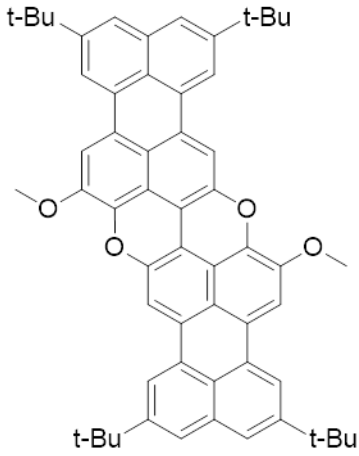

2,9,12,19-tetra-tert-butyl-5,15-dimethoxybenzo[5',10']anthra[9',1',2':7,8,1]isochromeno[5,4,3-cde]benzo[5,10]anthra[9,1,2-hij]isochromene 3-18^{Pp}

To a 5 mL round-bottom flask, compound **3-17** (8 mg, 9.7 µmol), CuI (5.6 mg, 29 µmol) and pivaloic acid (2.0 mg, 19.4 µmol) and DMSO (1 mL) were added. The resulting mixture was stirred under open air conditions at 140 °C for 2h. CH_2Cl_2 (5 mL) was added and the solution washed with NH_4OH_{sat} (3 × 10 mL), water (10 mL) and brine (10 mL). The aqueous phase was extracted with CH_2Cl_2. Combined organic layers were dried over Na_2SO_4 and the solvent evaporated in *vacuo*. The solid crude was dissolved in THF and repeatedly precipitated from MeOH and finally washed with cold MeOH to afford compound **3-18^{Pp}** as dark blue powder (4.3 mg, **54 %**). **M.p.:** > 300 °C. **IR** (ATR) ν (cm^{-1}) = 2951.09, 2904.80, 2866.22, 1618.28, 1598.99, 1589.34, 1508.33, 1462.04, 1417.68, 1390.68, 1367.53, 1348.24, 1328.95, 1280.73, 1257.59, 1234.44, 2904.80, 1199.72, 1170.79, 1130.29, 1091.71, 1035.77, 989.48, 960.55, 947.05, 889.18, 867.97, 850.61, 806.25, 781.17, 769.60, 719.45, 704.02, 686.66, 665.44, 653.87, 646.15, 626.87, 619.15, 597.93, 569.00, 543.93,

495.71, 462.92, 428.20, 408.91, 401.19. **HRMS** (MALDI, m/z): [M] calc. for $C_{58}H_{54}O_4$, 814.4022, found: 814.4013. **UV-Vis** (CH_2Cl_2): λ_{max} = 638 nm (40887±672 M^{-1} cm^{-1}). ^{1}H-NMR and ^{13}C-NMR were not recorded due to insolubility issue.

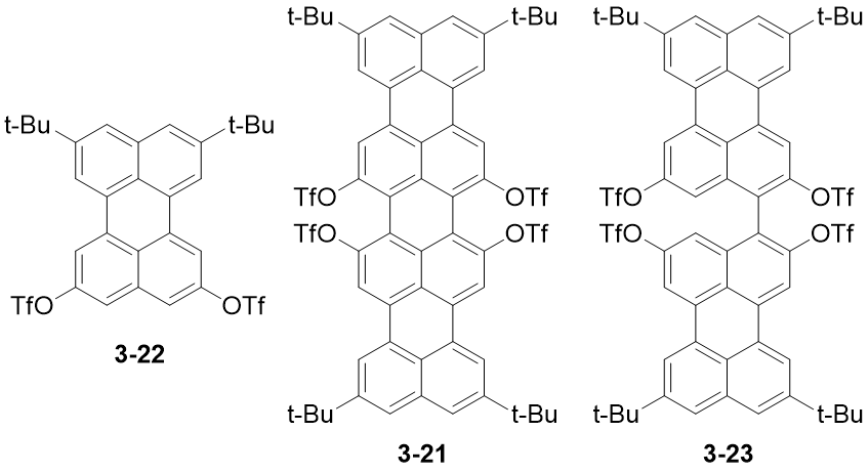

Compound 3-21

8,11-di-tert-butylperylene-2,5-diyl bis(trifluoromethanesulfonate) 3-22

8,8',11,11'-tetra-tert-butyl-[3,3'-biperylene]-2,2',5,5'-tetrayl tetrakis(trifluoromethanesulfonate) 3-23

Compound **3-11** (100 mg, 0.162 mmol) and NaOH (324 mg, 8.11 mmol) were dissolved in THF (10 mL). An aqueous solution of H_2O_2 (0.7 mL, 8.11 mmol, 35 wt%) was added drop-wise and the reaction mixture stirred at r.t. for 24 h. The solution was acidified to pH 1-2 by addition of 1 M HCl solution and extracted with CH_2Cl_2 (3 × 15 mL). Combined organic layers were dried over Na_2SO_4 and the solvent removed in *vacuo*. The crude was dissolved in anhydrous CH_2Cl_2 (5 mL), and DIPEA (50 µL) was added. The mixture was cooled to 0°C and Tf_2O (50 µL) was added dropwise leading to the formation of an intense blue colored solution. The reaction mixture was allowed to warm up at r.t. and stirred overnight under Ar. The organic phase was washed with H_2O (10 mL), aq. 1 M HCl (10 mL), brine (10

mL) and dried over Na_2SO_4. The solvent was removed in *vacuo* and the crude purified by preparative t.l.c. (eluents: PET-toluene; 7:3) to afford compounds **3-22** as yellow solid (10 mg, 9%), **3-22** as yellow solid (2 mg, 2 %) and **3-21** as intense blue solid (45 mg, **42 %**).

For **8,11-di-tert-butylperylene-2,5-diyl bis(trifluoromethanesulfonate) 3-22: M.p.**: 281 °C. **^{1}H-NMR** (500 MHz, $(CD_3)_2CO$): δ = 8.59 (*d*, ^4J = 1.5 Hz, 2H, Ar*H*), 8.55 (*d*, ^4J = 2.5 Hz, 2H, Ar*H*), 7.96 (*m*, 4H, Ar*H*), 1.50 (*s*, 18H, C(CH_3)$_3$). **^{13}C-NMR** (125 MHz, $(CD_3)_2CO$): δ = 150.70, 150.48, 137.26, 136.55, 135.64, 128.90, 128.10, 126.88, 125.46, 121.94, 119.07, 115.48, 35.76, 31.42, 29.84. **IR** (ATR) ν (cm^{-1}) = 2956.87, 1608.63, 1398.39, 1247.94, 1205.51, 1136.07, 997.20, 937.40, 869.90, 815.89, 613.36, 597.93, 584.43, 570.93, 511.14, 499.56. **HRMS** (EI, m/z): [M] calc. for $C_{30}H_{26}F_6O_6S_2$, 660.1075, found: 660.1067. **UV-Vis** (toluene): λ_{max}= 446 nm (24857 ± 17 M^{-1} cm^{-1}). Crystal suitable for X-ray diffraction was obtained by slow evaporation of solvent from an acetone-d_6 solution.

For **8,8',11,11'-tetra-tert-butyl-[3,3'-biperylene]-2,2',5,5'-tetrayl tetrakis(trifluoromethanesulfonate) 3-23**: **M.p.**: > 300 °C. **^{1}H-NMR** (300 MHz, $(CD_3)_2CO$): δ = 8.75 (*m*, 6H, Ar*H*), 8.72 (*d*, ^4J = 1.8 Hz, 2H, Ar*H*), 8.09 (*d*, ^4J = 1.5 Hz, 2H, Ar*H*), 8.06 (*d*, ^4J = 1.5 Hz, 2H, Ar*H*), 7.32 (*d*, ^4J = 2.4 Hz, 2H, Ar*H*), 1.55 (*s*, 18H, C(CH_3)$_3$), 1.53 (*s*, 18H, C(CH_3)$_3$). **^{13}C-NMR** (75 MHz, $(CD_3)_2CO$): δ = 151.25, 151.04, 150.90, 149.06, 138.13, 137.11, 136.83, 135.59, 128.82, 128.52, 128.43, 127.77, 127.22, 125.23, 122.78, 122.57, 121.89, 117.64, 115.94, 115.16, 35.84, 35.82, 31.42, 31.39; one peak is missing probably due to overlap. **^{19}F-NMR** (376 MHz, $(CD_3)_2CO$): -74.18, -75.18. **IR** (ATR) ν (cm^{-1}) = 2964.59, 2872.01, 1604.77, 1427.32, 1247.94, 1215.15, 1139.93, 1006.84, 943.19, 881.47, 817.82, 607.58. **HRMS** (ESI, m/z): $[M+H]^+$ calc. for $C_{60}H_{51}F_{12}O_{12}S_4$, 1319.2072, found: 1319.2100.

For **Compound 3-21**: **M.p.**: > 300 °C.**^{1}H-NMR** (500 MHz, C_6D_6): δ = 8.52 (*s*, 4H, Ar*H*), 8.31 (*d*, ^4J = 1.5 Hz, 4H, Ar*H*), 7.71 (*d*, ^4J = 1.5 Hz, 4H, Ar*H*), 1.32 (*s*, 36H, C(CH_3)$_3$); **^{13}C-**

NMR (125 MHz, C_6D_6): δ = 150.22, 147.14, 135.52, 135.28, 134.95, 127.03, 126.55, 125.09, 121.52, 117.81, 115.32, 34.98, 31.22; one peak is missing probably due to overlap. **^{19}F-NMR** (470 MHz, C_6D_6, 25 °C): δ = -73.56. **IR** (ATR) ν (cm^{-1}) = 2954.95, 2908.65, 2870.08, 1600.92, 1583.56, 1568.13, 1479.40, 1425.40, 1409.96, 1396.46, 1365.60, 2904.80, 1246.02, 1199.72, 1172.72, 1132.21, 1080.14, 1055.06, 1029.99, 1008.77, 987.55, 941.26, 879.54, 860.25, 815.89, 785.03, 769.60, 758.02, 725.23, 707.88, 677.01, 648.08, 628.79, 603.72, 570.93, 557.43, 514.99, 493.78, 433.98, 424.34, 418.55, 410.84. **HRMS** (ESI, m/z): [M] calc. for $C_{60}H_{48}F_{12}O_{12}S_4$, 1316.1837, found: 1316.1796. **UV/Vis** (toluene): λ_{max}= 664 nm (104 571 ± 3950 M^{-1} cm^{-1}). Crystal suitable for X-ray diffraction was obtained by slow evaporation of solvent from a C_6D_6 solution.

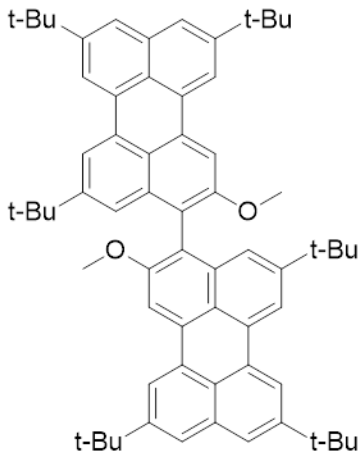

5,5',8,8',11,11'-hexa-tert-butyl-2,2'-dimethoxy-3,3'-biperylene 3-30

To a stirred mixture of compound **3-4** (30 mg, 34 µmol) and K_2CO_3 (30 mg, 220 µmol) in acetone (2 mL) at 60 °C under Ar, MeI (16.5 µL, 272 µmol) was added, and the mixture stirred at 60 °C for 48 h under Ar. After cooling to r.t. the solvent was removed in *vacuo* and the residue taken in CH_2Cl_2 (10 mL) and washed with H_2O (3 × 15 mL) and brine (15 mL). The organic layer was dried over Na_2SO_4, and evaporated. The reaction crude was purified by column chromatography (SiO_2, eluents: PET-toluene, 8:2) to afford compound **3-30** (29

mg, **82 %**) as yellow solid. **M.p.**: >300 °C. **^{1}H-NMR** (500 MHz, C_6D_6,): δ = 8.55 (*d*, ^4J = 1.5 Hz, 2H, Ar*H*), 8.50 (*d*, ^4J = 1.5 Hz, 2H, Ar*H*), 8.44 (*d*, ^4J = 1.5 Hz, 2H, Ar*H*), 8.23 (*s,* 2H, Ar*H*), 7.75 (*d*, ^4J = 1.5 Hz, 2H, Ar*H*), 7.73 (*d*, ^4J = 1.5 Hz, 2H, Ar*H*), 7.71 (*d*, ^4J = 1.5 Hz, 2H, Ar*H*), 3.53 (s, 6H, OCH_3), 1.47 (*s*, 18H, C(CH_3)$_3$), 1.44 (*s*, 18H, C(CH_3)$_3$), 1.20 (*s*, 18H, C(CH_3)$_3$). **^{13}C-NMR** (125 MHz, C_6D_6): δ = 156.72, 149.44, 149.06, 148.86, 136.50, 135.73, 133.10, 131.88, 131.84, 131.40, 126.52, 124.34, 123.95, 122.20, 121.25, 118.54, 118.34, 117.06, 107.88, 56.29, 35.04, 35.02, 35.00, 31.52, 31.49, 31.29; **IR** (ATR) ν (cm^{-1}) = 2951.09, 2904.80, 2868.15, 1597.06, 1583.56, 1508.33, 1477.47, 1460.11, 2904.80, 1392.61, 1367.53, 1340.53, 1325.10, 1253.73, 1211.30, 1205.51, 1180.44, 1141.86, 1093.64, 1043.49, 1028.06, 999.13, 972.12, 918.12, 896.90, 875.68, 867.97, 848.68, 823.60, 788.89, 742.59, 727.16, 636.51, 609.51, 557.43, 459.06, 437.84, 416.62, 405.05; **HRMS** (MALDI, m/z): [M] calc. for $C_{66}H_{74}O_2$, 898.5689 found: 898.5671. **UV-Vis** (toluene): λ_{max} = 470 nm (59557±1025 M^{-1} cm^{-1})**.**

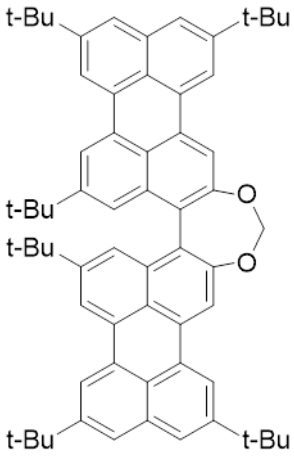

2,10,13,16,19,22-hexa-tert-butyldiperyleno[2,3-d:3',2'-f][1,3]dioxepine 3-27

To a stirred mixture of compound **3-4** (30.0 mg, 34 µmol), NaI (catalytic amount) and K_2CO_3 (30 mg, 220 µmol) in acetone (2 mL) at 60 °C under Ar, CH_2Br_2 (10 µL, 136 µmol) was added, and the mixture refluxed for 48 h. After cooling to r.t. the solvent was removed in

vacuo and the residue taken in CH_2Cl_2 (10 mL) and washed with H_2O (3×15 mL) and brine (15 mL). The organic layer was dried over Na_2SO_4, and evaporated. The reaction crude was purified by column chromatography (SiO_2, eluents: CHX-toluene, 9.5:0.5) to afford compound **3-27** (29 mg, **97 %**) as yellow solid. **M.p.**: >300 °C; **^{1}H-NMR** (500 MHz, CD_2Cl_2): δ = 8.37 (*d*, ^4J =1.5 Hz, 2H, Ar*H*), 8.35 (*d*, ^4J =1.5 Hz, 2H, Ar*H*), 8.33 (*d*, ^4J =1.0 Hz, 2H, Ar*H*), 8.20 (*s,* 2H, Ar*H*), 7.74 (*d*, ^4J =1.0 Hz, 2H, Ar*H*), 7.73 (*d*, ^4J =1.5 Hz, 2H, Ar*H*), 7.42 (*d*, ^4J =1.5 Hz, 2H, Ar*H*), 5.82 (s, 2H, OCH_2O), 1.53 (*s*, 18H, C(CH_3)$_3$), 1.52 (*s*, 18H, C(CH_3)$_3$), 1.21 (*s*, 18H, C(CH_3)$_3$); **^{13}C-NMR** (125 MHz, CD_2Cl_2, 25 °C): δ = 152.81, 149.80, 149.76, 149.52, 135.37, 134.21, 134.10, 131.85, 131.00, 130.36, 126.31, 125.62, 124.75, 124.29, 122.93, 119.53, 118.99, 118.61, 114.39, 103.40, 35.48, 35.46, 35.39, 31.65, 31.63, 31.32; **IR** (ATR) ν (cm^{-1}) = 3061.03, 2953.02, 2904.80, 2868.15, 1598.99, 1477.47, 1462.04, 1436.97, 1392.61, 1361.74, 1338.60, 1327.03, 1255.66, 1207.44, 1176.58, 1141.86, 1105.21, 1083.99, 1024.20, 1010.70, 991.41, 954.76, 918.12, 896.90, 873.75, 823.60, 808.17, 798.53, 786.96, 756.10, 715.59, 634.58, 594.08.; **HRMS** (MALDI, m/z): [M] calc. for $C_{65}H_{70}O_2$, 882.5376 found: 882.5356. **UV/Vis** (toluene): λ_{max}= 484 nm (73469 ± 1839 M^{-1} cm^{-1}).

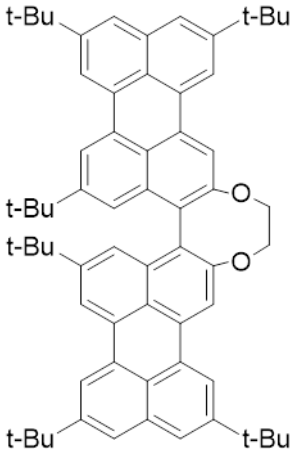

2,11,14,17,20,23-hexa-tert-butyl-6,7-dihydrodiperyleno[2,3-e:3',2'-g][1,4]dioxocine 3-28

To a stirred mixture of compound **3-4** (40.0 mg, 46 µmol) and K_2CO_3 (14 mg, 102.2 µmol) in anhydrous DMF (2 mL), $(CH_2)_2Br_2$ (7 µL, 55.2 µmol) was added dropwise, and the mixture degassed following freeze-pump-thaw protocol. The reaction mixture was stirred at 80 °C for 48 h under Ar atmosphere and after cooled to r.t. The solvent was removed in *vacuo* and the residue taken in CH_2Cl_2 (10 mL) and washed with H_2O (3×15 mL) and brine (15 mL). The organic layer was dried over Na_2SO_4, and evaporated. The reaction crude was purified by column chromatography (SiO_2, eluent: CHX-/toluene, 8:2) to afford compound **3-28** (10 mg, **24 %**) as yellow solid. **M.p.**: >300 °C. **^{1}H-NMR** (500 MHz, CD_2Cl_2): δ = 8.35 (*d*, ^4J = 1.5 Hz, 2H, Ar*H*), 8.34 (*d*, ^4J = 1.0 Hz, 2H, Ar*H*), 8.28 (*d*, ^4J = 1.0 Hz, 2H, Ar*H*), 8.18 (*s,* 2H, Ar*H*), 7.74 (*d*, ^4J = 1.5 Hz, 2H, Ar*H*), 7.72 (*d*, ^4J = 1.0 Hz, 2H, Ar*H*), 7.20 (*d*, ^4J = 1.0 Hz, 2H, Ar*H*), 4.56 (*d*, *J* = 9.0 Hz, 2H, OCH_2), 4.33 (*d*, *J* = 9.0 Hz, 2H, OCH_2), 1.53 (*s*, 18H, C(CH_3)$_3$), 1.52 (*s*, 18H, C(CH_3)$_3$), 1.14 (*s*, 18H, C(CH_3)$_3$). **^{13}C-NMR** (125 MHz, CD_2Cl_2): δ = 158.09, 149.71, 149.70, 149.63, 135.39, 134.98, 134.40, 131.48, 131.10, 130.40, 125.69, 125.42, 124.63, 124.61, 124.15, 123.58, 119.27, 118.85, 118.13, 116.02, 74.14, 35.49, 35.44, 35.29, 31.65, 31.30. **IR** (ATR) ν (cm^{-1}) = 2951.09, 2906.73, 2866.22, 2904.80, 1585.49, 1477.47, 1460.11, 1431.18, 1392.61, 1361.74, 1338.60, 1325.10,

1255.66, 1222.87, 1207.44, 1178.51, 1145.72, 1103.28, 1082.07, 981.77, 956.69, 927.76, 896.90, 875.68, 823.60, 808.17, 754.17, 721.38, 640.37, 619.15, 592.15, 428.20, 420.48, 401.19; **HRMS** (MALDI, m/z): [M] calc. for $C_{66}H_{72}O_2$, 896.5532 found: 896.5521. **UV/Vis** (toluene): λ_{max}= 468 nm (72562 ± 1442 M^{-1} cm^{-1}). Crystal suitable for X-ray diffraction was obtained by slow diffusion from a CH_2Br_2/MeOH solution.

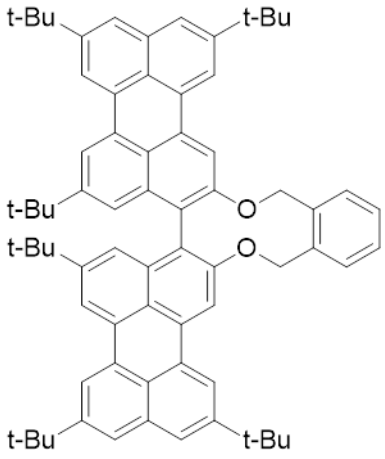

2,15,18,21,24,27-hexa-tert-butyl-6,11-dihydrobenzo[h]diperyleno[2,3-b:3',2'-d][1,6]dioxecine 3-29

To a stirred mixture of compound **3-4** (30.0 mg, 34 µmol) and K_2CO_3 (10,4 mg, 75 µmol) in anhydrous DMF (2 mL), 1,2-bis(bromomethyl)benzene (10 mg, 34 µmol) was added dropwise, and the mixture degassed following the freeze-pump-thaw protocol. The reaction mixture was stirred at 80 °C for 48 h under Ar atmosphere. After cooling to r.t. the mixture was poured into water (10 ml) and extracted with CH_2Cl_2 (3 × 15 mL). The organic layer was subsequently washed with water (2 × 20 mL) and brine (20 mL) and dried over Na_2SO_4. The solvent was removed in *vacuo* and the reaction crude purified by column chromatography (SiO_2, eluent: CHX-toluene, 9:1) to afford compound **3-29** (29 mg, **88 %**) as yellow solid. **M.p**.: > 300 °C. **^{1}H-NMR** (500 MHz, CD_2Cl_2): δ = 8.31 (*m,* 4H, Ar*H*), 8.21 (*s*, 4H, Ar*H*), 7.72 (*s*, 2H, Ar*H*), 7.70 (*s,* 2H, Ar*H*), 7.56 (*t*, ^3J = 4.5 Hz, 2H, Ar*H*), 7.34 (*dd*,

J = 4.5, 3.5 Hz, 2H, Ar*H*), 7.21 (*s*, 2H, Ar*H*), 5.58 (*d*, *J* = 11.5 Hz, 2H, OCH_2), 5.46 (*d*, *J* = 11.5 Hz, 2H, OCH_2), 1.57 (*s*, 18H, C(CH_3)$_3$), 1.51 (*s*, 18H, C(CH_3)$_3$), 1.16 (*s*, 18H, C(CH_3)$_3$). **^{13}C-NMR** (125 MHz, CD_2Cl_2): δ = 149.65, 149.62, 149.56, 136.93, 135.39, 135.25, 132.72, 132.02, 131.51, 131.18, 130.69, 129.55, 125.77, 124.33, 124.28, 124.01, 122.54, 122.41, 118.84, 118.73, 117.55, 110.80, 72.66, 35.46, 35.42, 35.30, 31.69, 31.64, 31.33. **IR** (KBr) ν (cm^{-1}) = 2951.09, 2904.80, 2875.86, 1598.99, 1587.42, 1473.62, 1460.11, 1431.18, 1392.61, 1363.67, 1340.53, 1323.17, 1255.66, 1232.51, 1211.30, 1176.58, 1157.29, 2904.80, 1103.28, 1085.92, 1070.49, 1026.13, 999.13, 970.19, 958.62, 937.40, 920.05, 894.97, 877.61, 867.97, 854.47, 846.75, 823.60, 792.74, 752.24, 734.88, 723.31, 671.23, 640.37, 624.94, 586.36, 565.14, 547.78, 511.14, 457.13, 418.55, 412.77, 405.05; **HRMS** (ESI, m/z): $[M+H]^+$ calc. for $C_{72}H_{77}O_2$, 973.5918 found: 973.5888. **UV-Vis** (toluene): λ_{max}= 474 nm (61 474 M^{-1} cm^{-1}). Crystal suitable for X-ray diffraction was obtained by slow evaporation of solvent from a methylene chloride-d_2 solution.

4.3 Bibliography

[1] A. Lausi, M. Polentarutti, S. Onesti, J. R. Plaisier, E. Busetto, G. Bais, L. Barba, A. Cassetta, G. Campi, D. Lamba, et al., *Eur. Phys. J. Plus* **2015**, *130*, DOI 10.1140/epjp/i2015-15043-3.

[2] W. Kabsch, *Acta Cryst. D* **2010**, *66*, 125–132.

[3] G. P. M. C. Burla, R. Caliandro, B. Carrozzini, G. L. Cascarano, C. Cuocci, C. Giacovazzo, M. Mallamo, A. Mazzone, *J. Appl. Cryst.* **2015**, 306–309.

[4] G. M. Sheldrick, *Acta Cryst.* **2015**, *A71*, 3–8.

[5] G. M. Sheldrick, *Acta Cryst.* **2008**, *A64*, 112–122.

[6] K. C. P. Emsley, *Acta Cryst. D* **2004**, *60,* 2126–2132.

[7] A. L. Spek, *Acta Cryst. D* **2009**, 148–155.

[8] L. J. Farrugia, *J. Appl. Cryst.* **2012**, *45*, 849–854.

[9] Schrodinger, LLC, **2015**, "The PyMOL Molecular Graphics System." Schrodinger.

[10] E. L. Unger, E. T. Hoke, C. D. Bailie, W. H. Nguyen, A. R. Bowring, T. Heumüller, M. G. Christoforo, M. D. McGehee, *Energy Environ. Sci.* **2014**, *7*, 3690–3698.

[11] U. Caruso, M. Casalboni, a. Fort, M. Fusco, B. Panunzi, a. Quatela, a. Roviello, F. Sarcinelli, *Opt. Mater.* **2005**, *27*, 1800–1810.

[12] C.-H. Andersson, H. Grennberg, *Eur. J. Org. Chem.* **2009**, 4421–4428.

[13] M. Pillow, J.; Kobayashi, S.; Humphries, *patent*, **2010**, WO 2010/013006 A2.

[14] R. O. Al-Kaysi, T. Sang Ahn, A. M. Müller, C. J. Bardeen, *Phys. Chem. Chem. Phys.* **2006**, *8*, 3453–9.

[15] J. Areephong, N. Ruangsupapichart, T. Thongpanchang, *Tetrahedron Lett.* **2004**, *45*, 3067–3070.

[16] S. Wang, B. Lv, Q. Cui, X. Ma, X. Ba, J. Xiao, *Chem. - A Eur. J.* **2015**, *21*, 14791–14796.

[17] I. A. Shuklov, N. V. Dubrovina, H. Jiao, A. Spannenberg, A. Börner, *Eur. J. Org. Chem.* **2010**, *7*, 1669–1680.

[18] Daphne Stassen, π − Extension of Hetero-Fused Aromatics : From Synthesis to Self-Assembly, **2015**.

[19] D. Stassen, N. Demitri, D. Bonifazi, *Angew. Chem. Int. Ed.* **2016**.

Appendix

A.1 Selected ^{1}H-NMR, ^{13}C-NMR and HRMS spectra

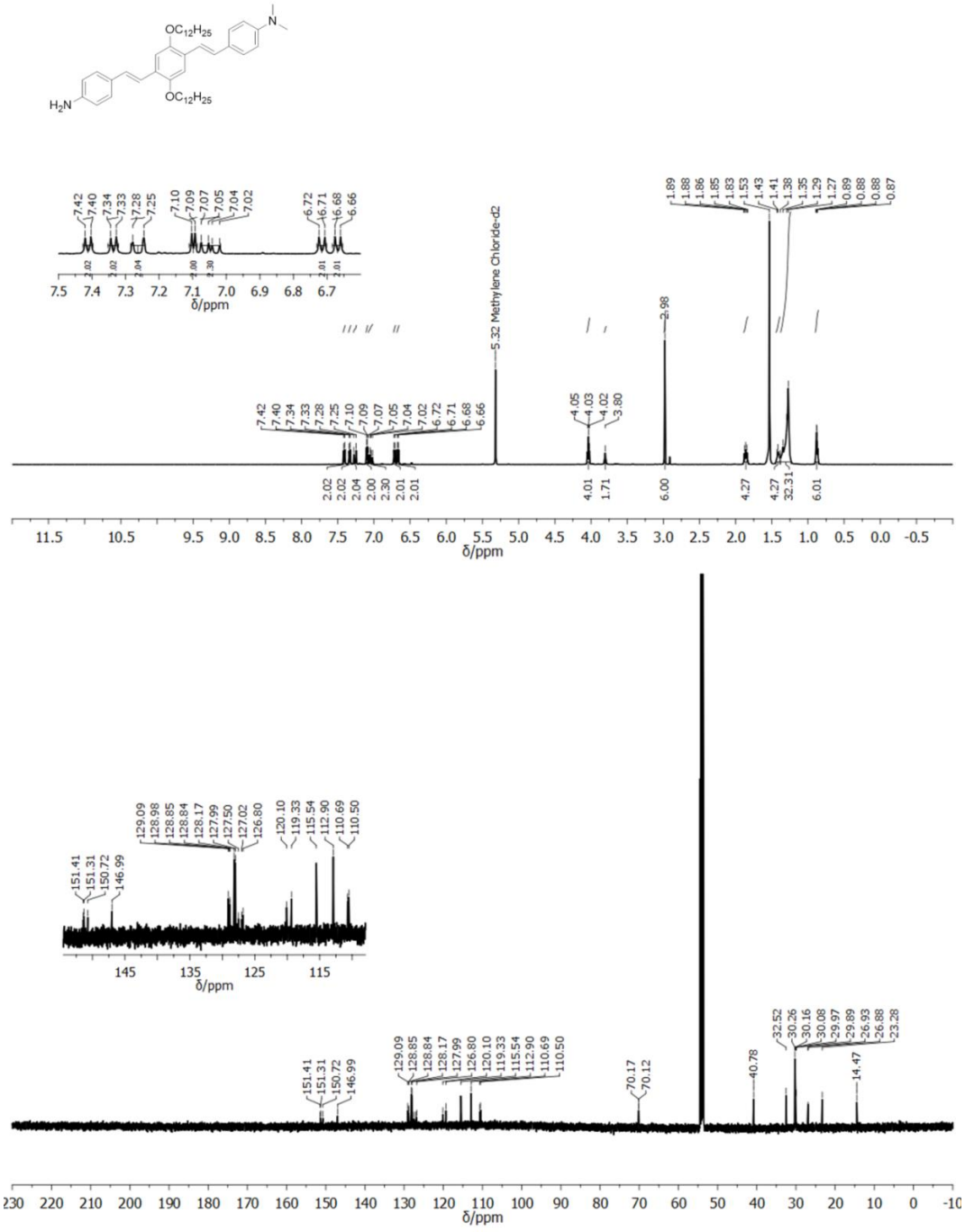

Figure A1. 500 MHz ^{1}H-NMR (top) and 125 MHz ^{13}C-NMR (bottom) spectra of **2-1** in CD_2Cl_2.

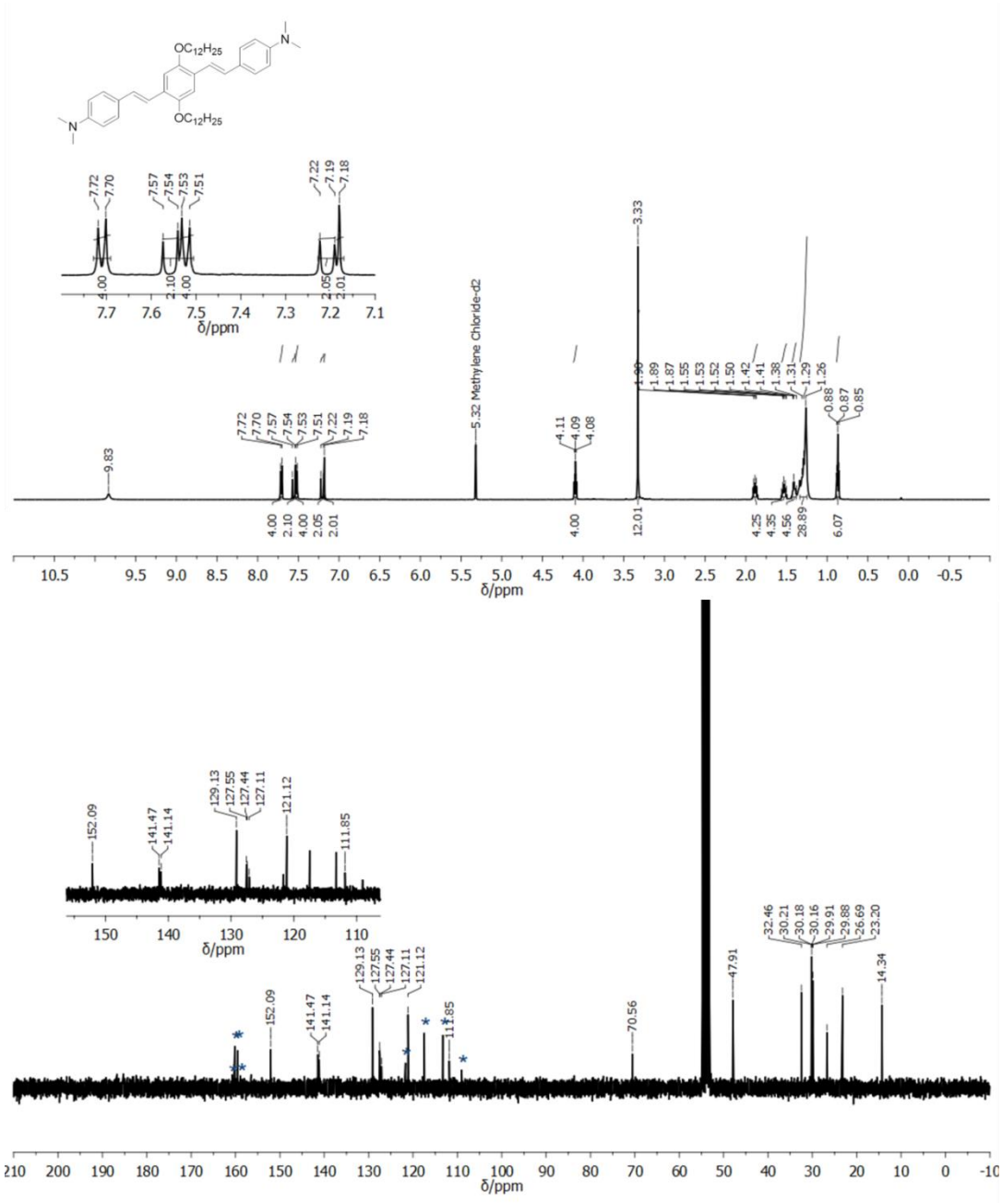

Figure A2. 500 MHz ^{1}H-NMR (top) and 67.5 MHz ^{13}C-NMR (bottom) spectra of **2-6a** in CD_2Cl_2-d2/TFA-d (TFA signals marked).

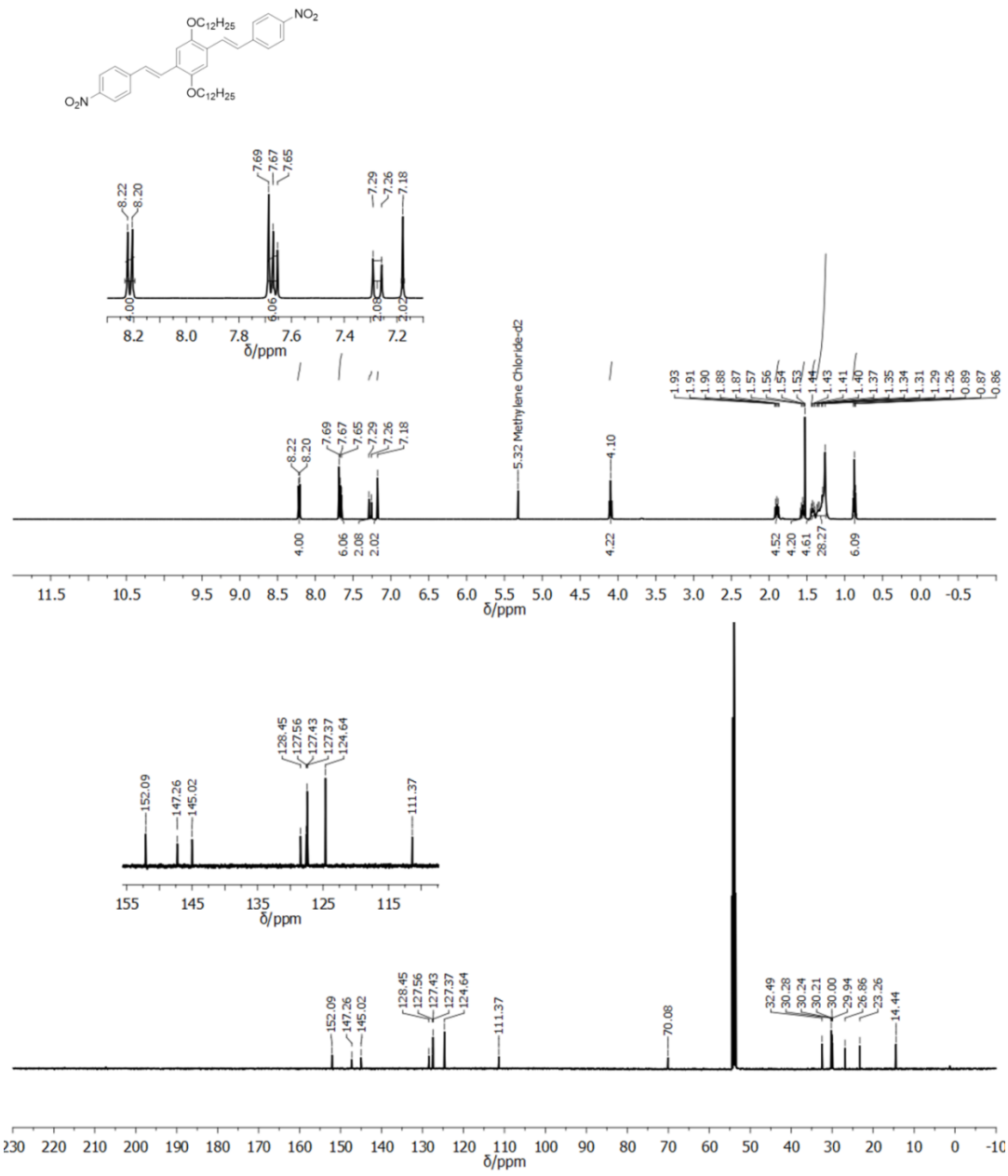

Figure A3. 500 MHz ^{1}H-NMR (top) and 125 MHz ^{13}C-NMR (bottom) spectra of **2-6b** in CD_2Cl_2

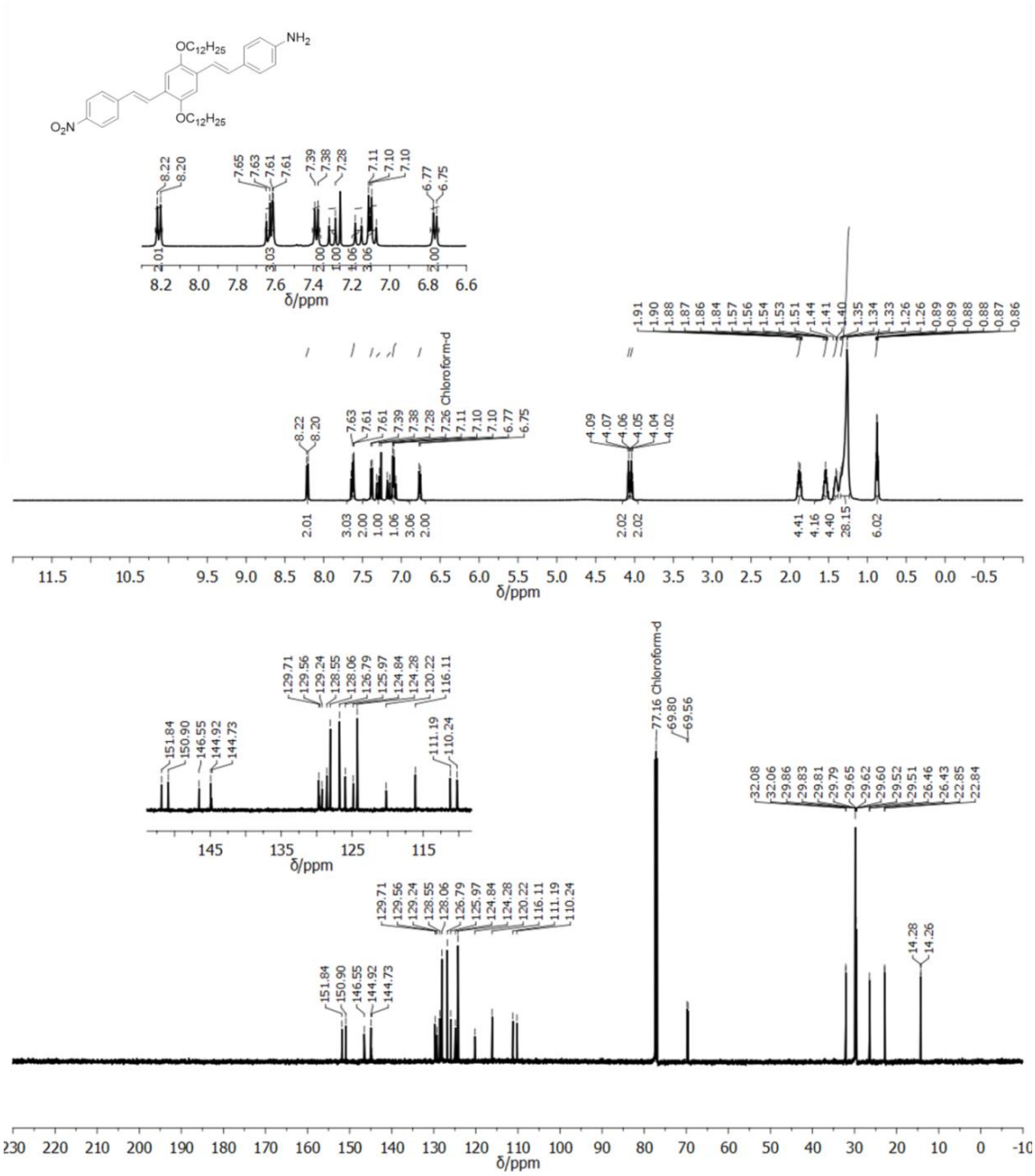

Figure A4. 500 MHz 1H-NMR (top) and 125 MHz ^{13}C-NMR (bottom) spectra of **2-7** in $CDCl_3$.

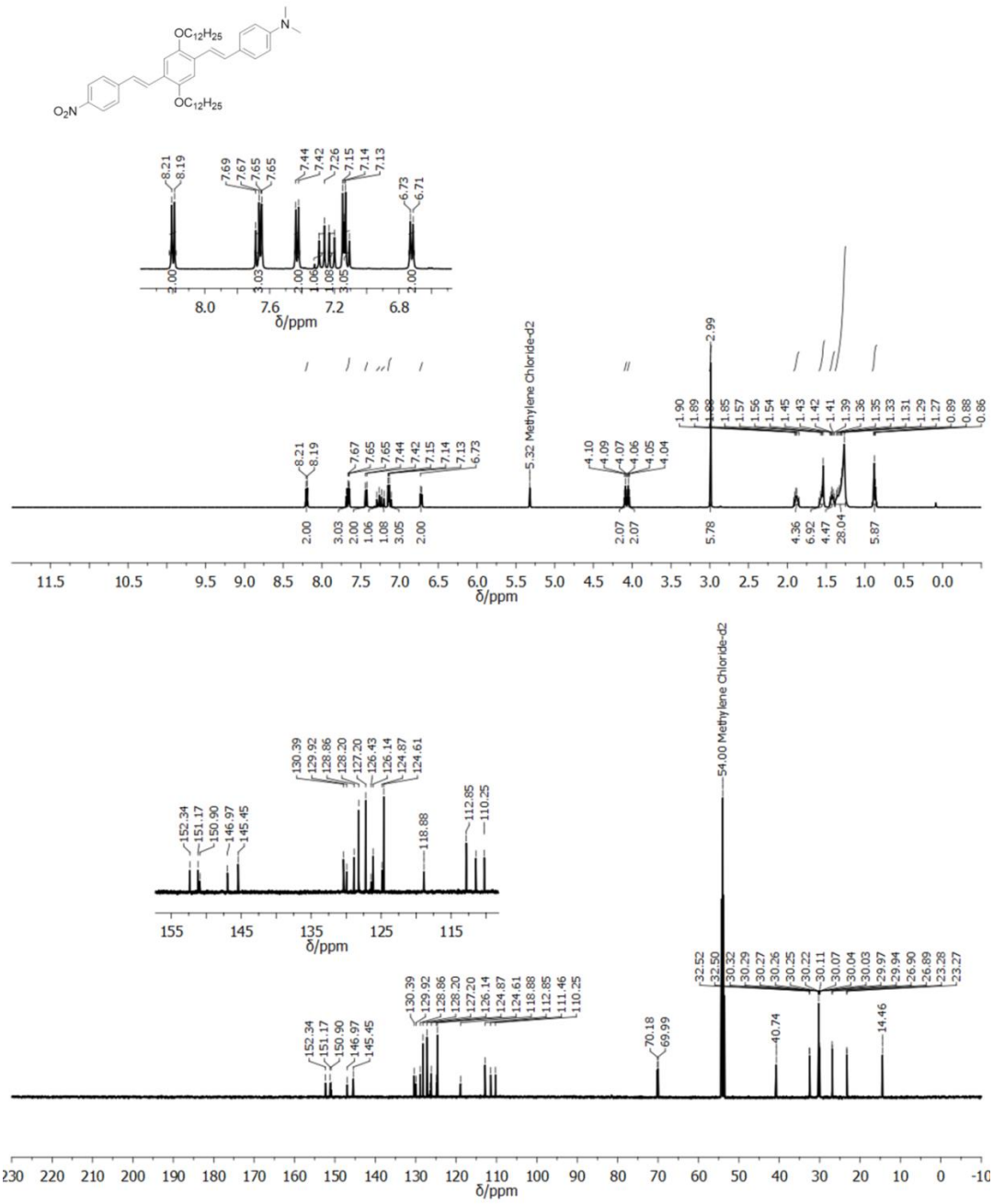

Figure A5. 500 MHz ^{1}H-NMR (top) and 125 MHz ^{13}C-NMR (bottom) spectra of **2-8** in CD_2Cl_2

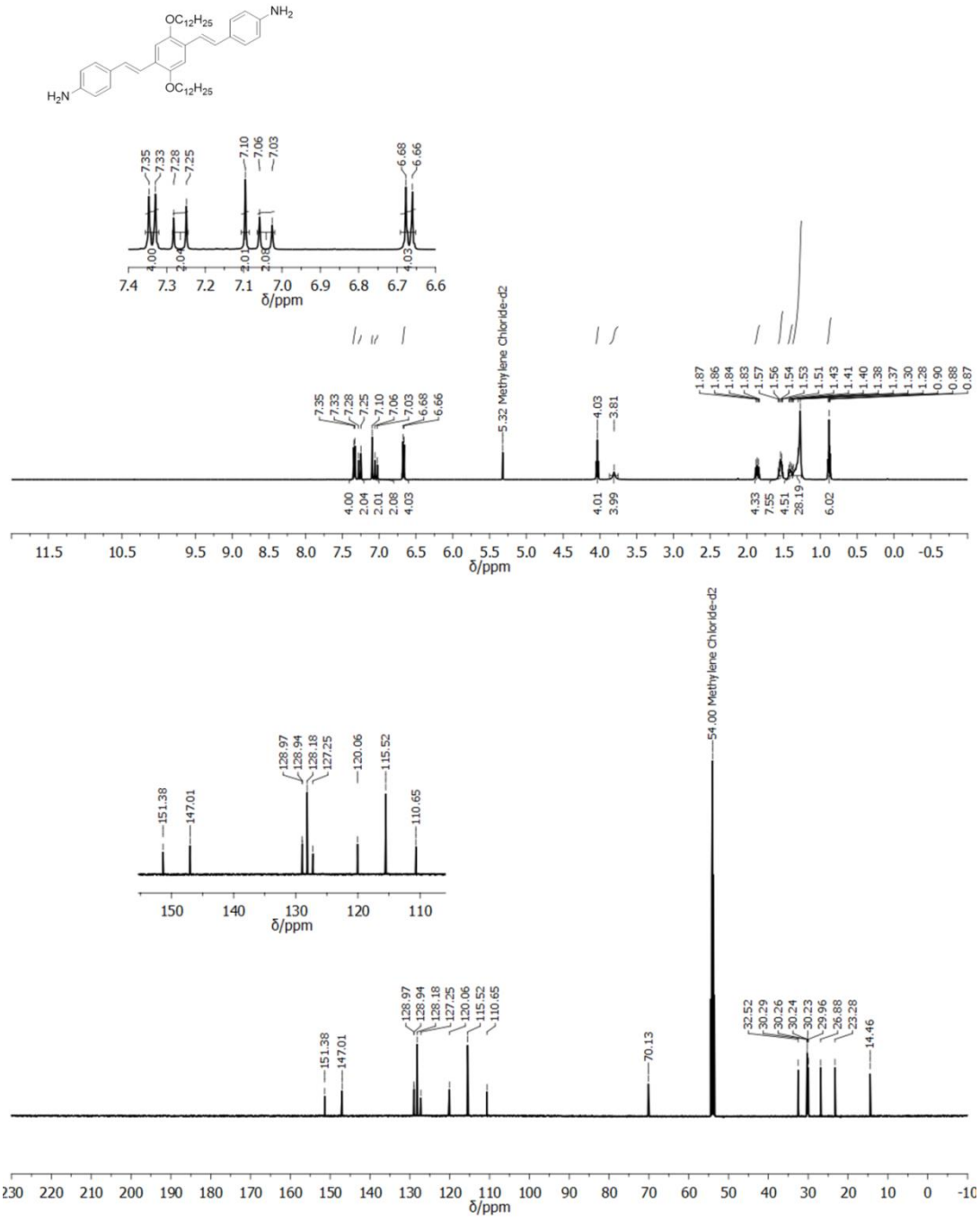

Figure A6. 500 MHz ^{1}H-NMR (top) and 125 MHz ^{13}C-NMR (bottom) spectra of **2-9** in CD_2Cl_2.

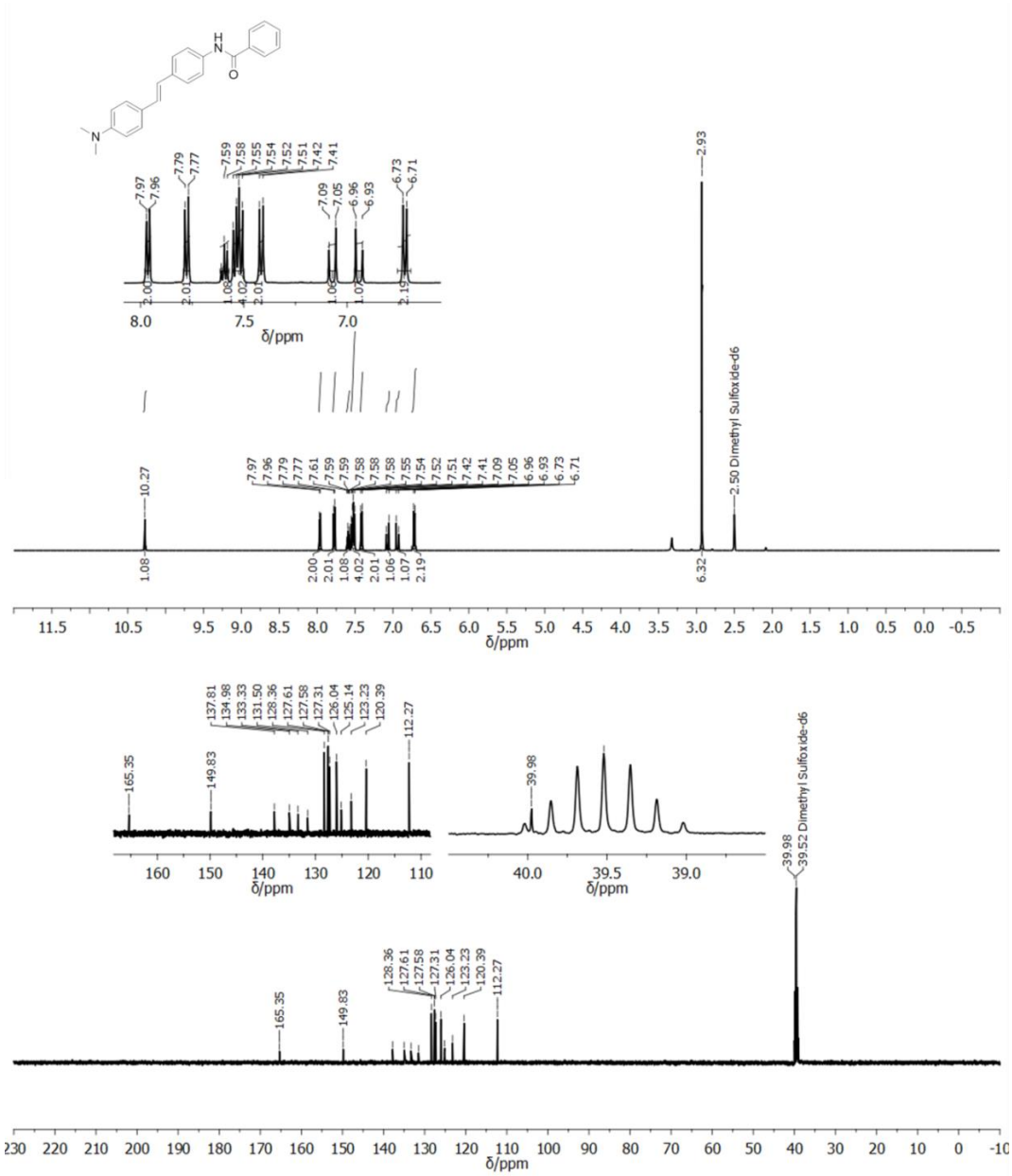

Figure A7. 500 MHz ^{1}H-NMR (top) and 125 MHz ^{13}C-NMR (bottom) spectra of **2-10** in DMSO-d_6.

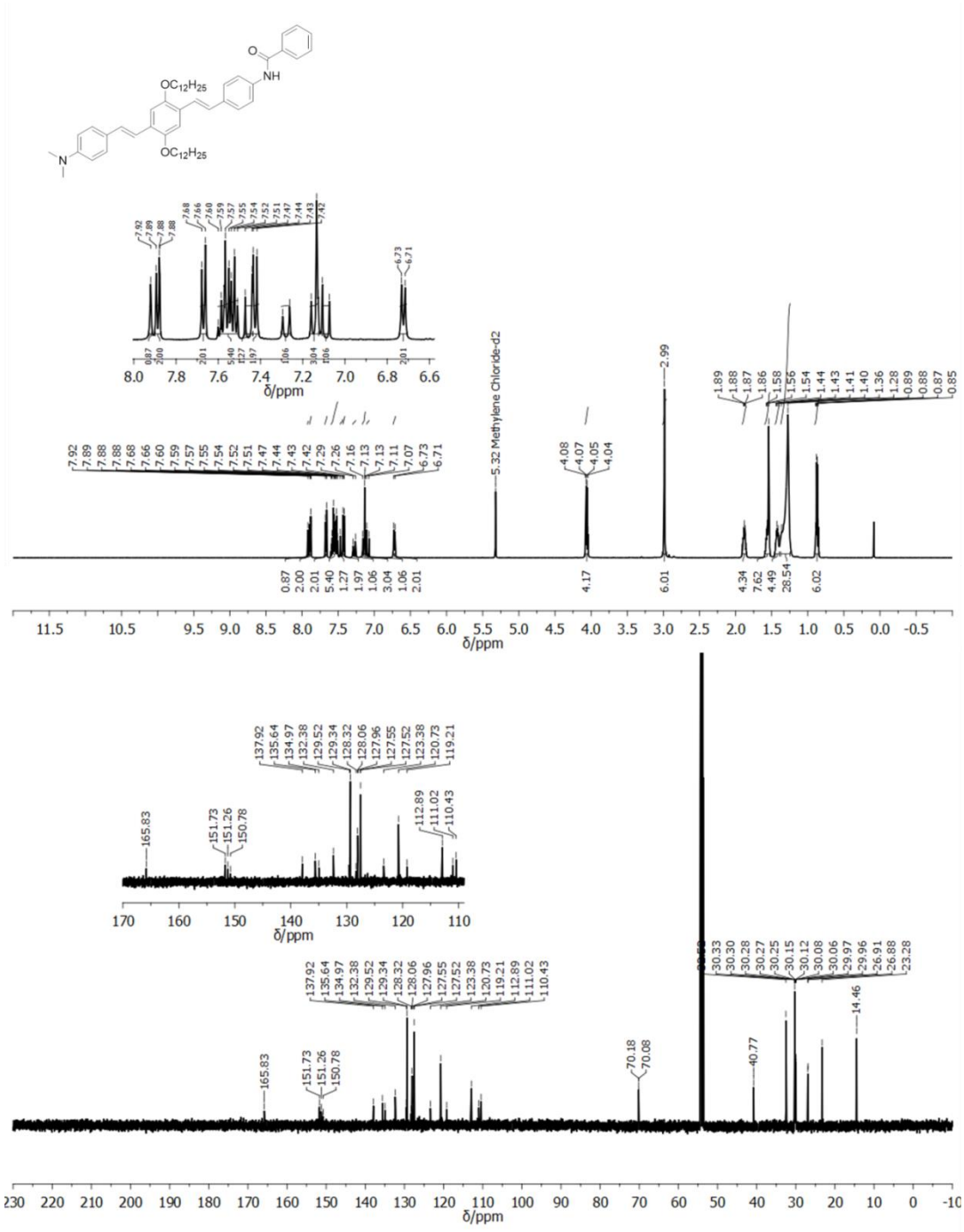

Figure A8. 500 MHz ^{1}H-NMR (top) and 125 MHz ^{13}C-NMR (bottom) spectra of **2-11** in CD_2Cl_2.

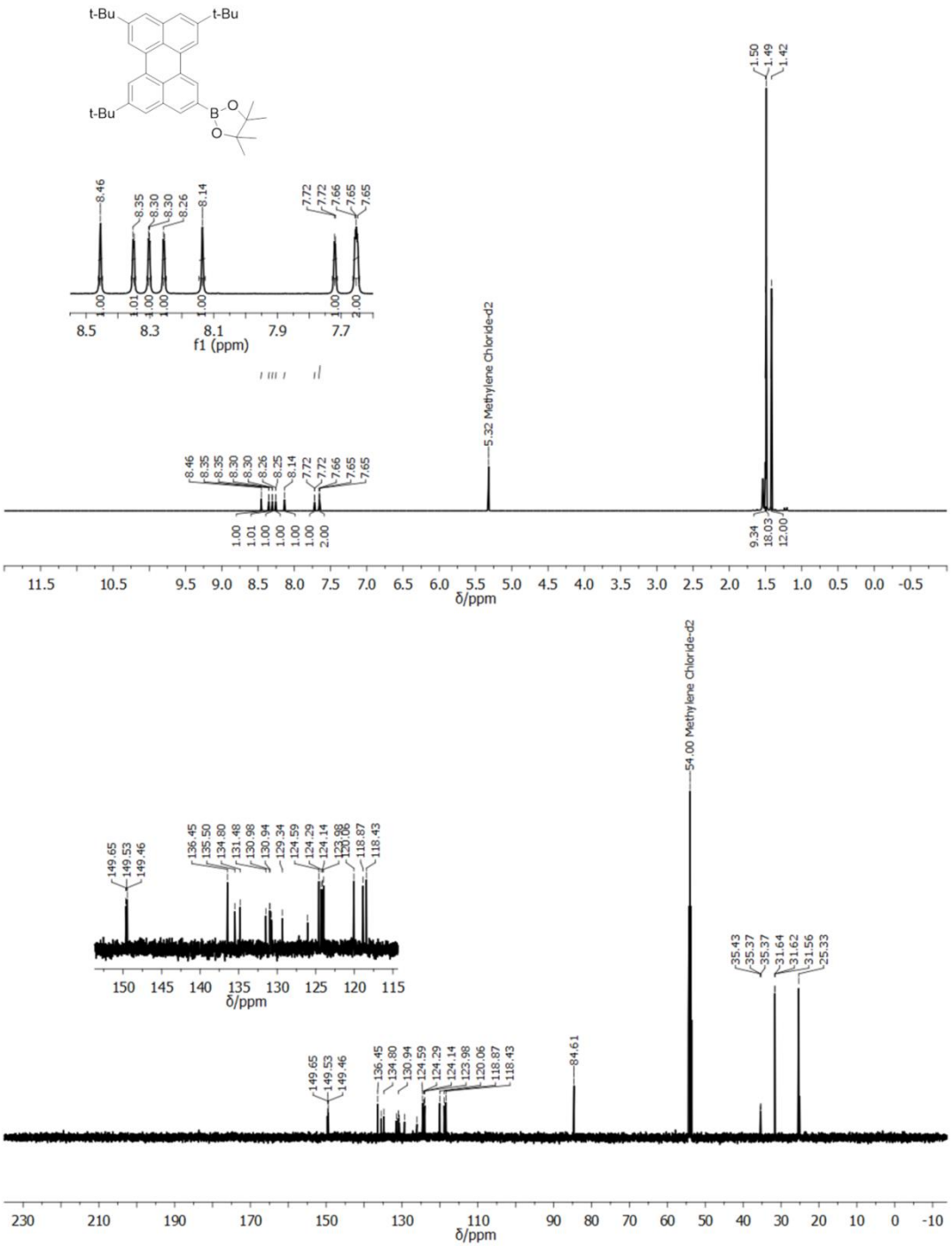

Figure A9. 500 MHz ^{1}H-NMR (top) and 125 MHz ^{13}C-NMR (bottom) spectra of **3-1** in CD_2Cl_2.

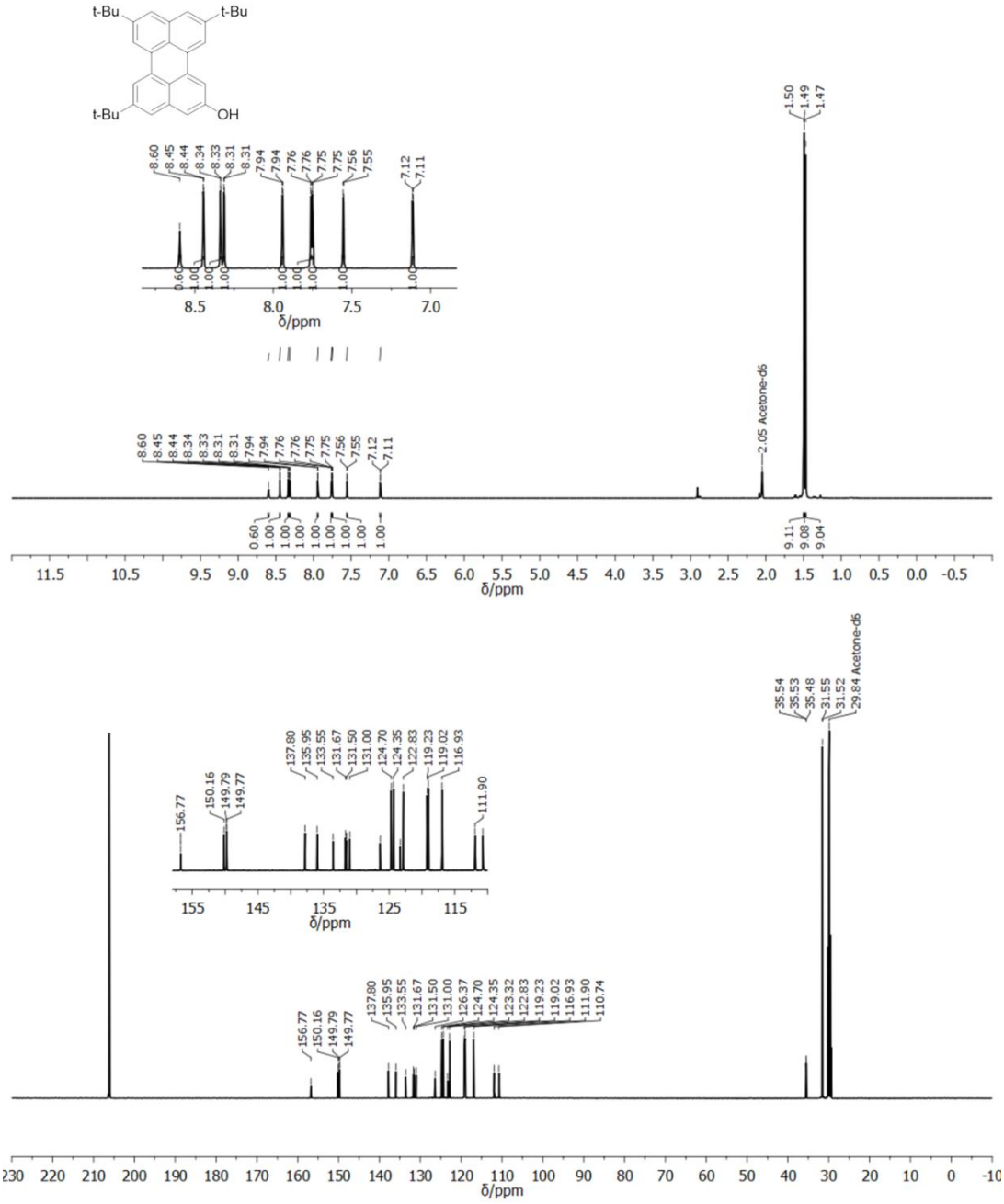

Figure A10. 500 MHz ^{1}H-NMR (top) and 125 MHz ^{13}C-NMR (bottom) spectra of **3-2** in acetone-d_6.

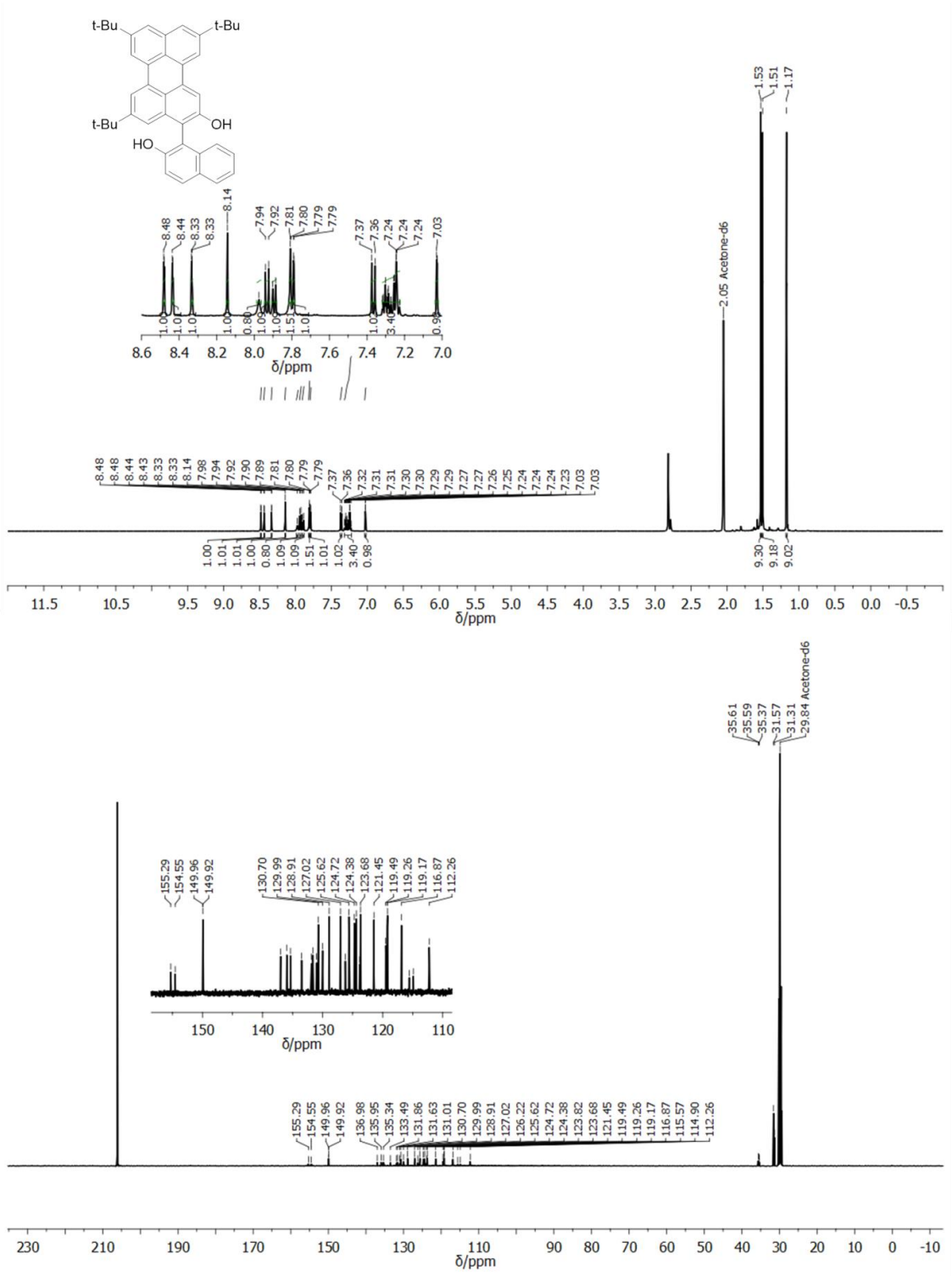

Figure A11. 500 MHz ^{1}H-NMR (top) and 125 MHz ^{13}C-NMR (bottom) spectra of **3-3** in acetone-d_6.

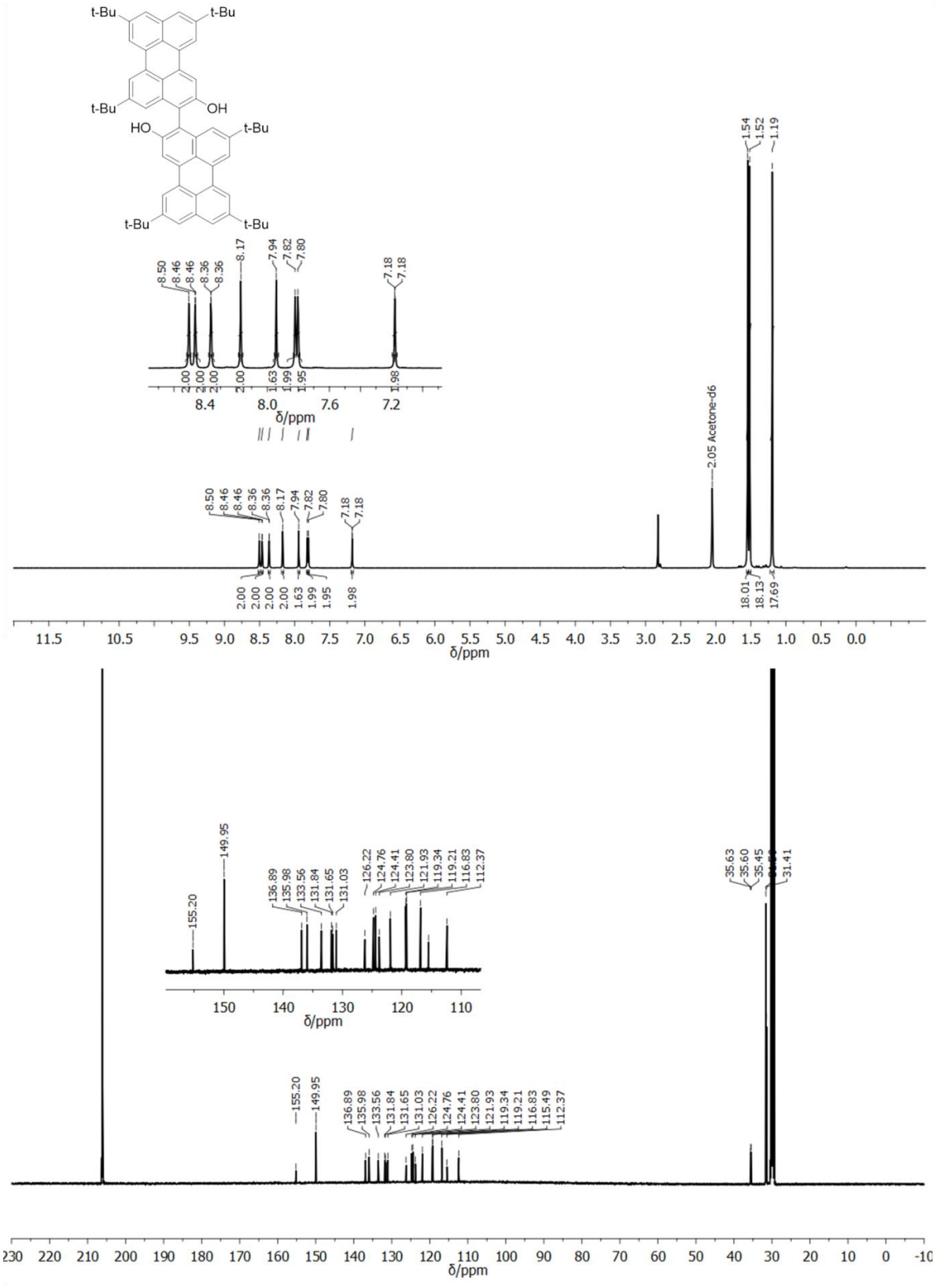

Figure A12. 500 MHz ^{1}H-NMR (top) and 125 MHz ^{13}C-NMR (bottom) spectra of **3-4** in acetone-d_6.

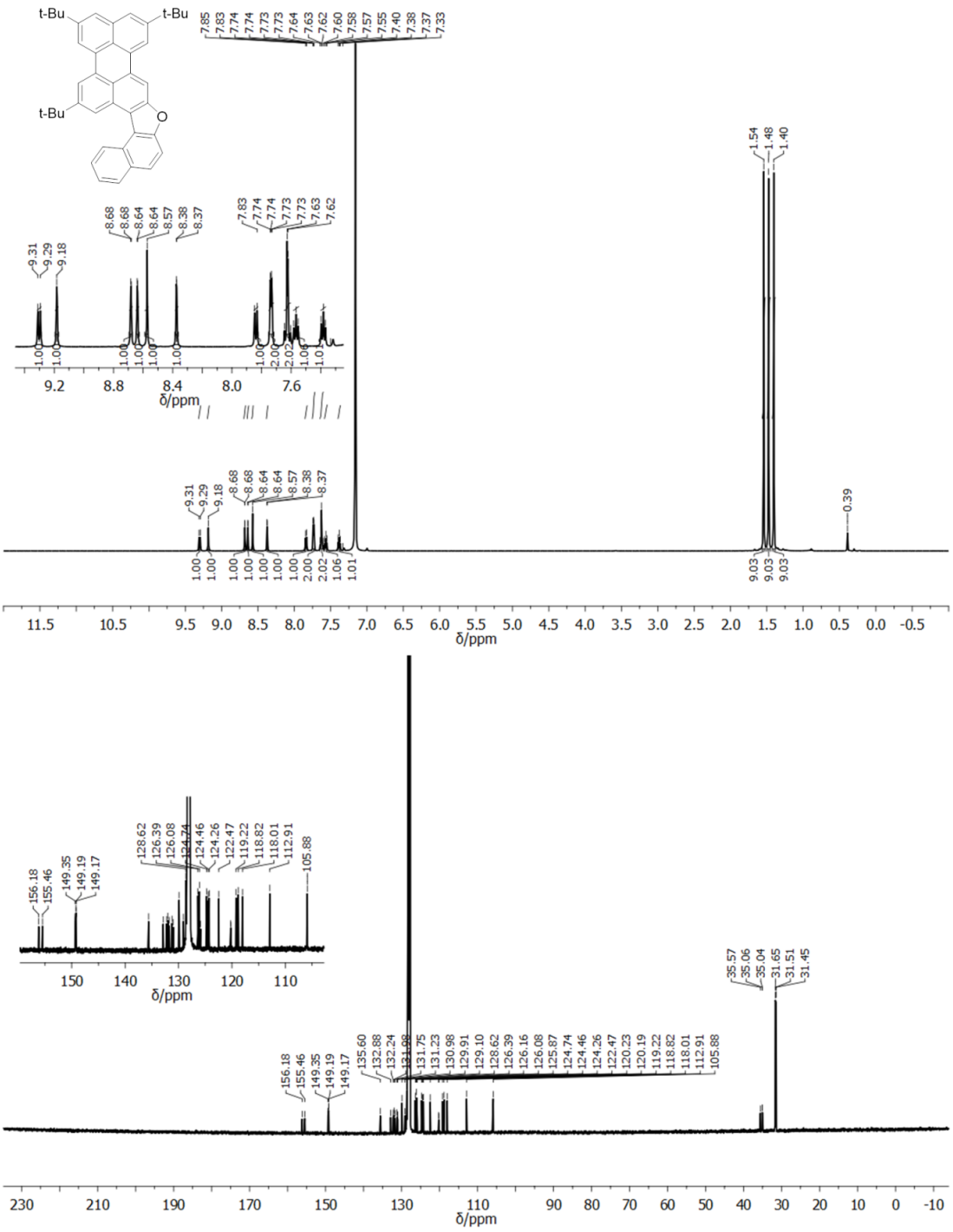

Figure A13. 500 MHz ^{1}H-NMR (top) and 125 MHz ^{13}C-NMR (bottom) spectra of **3-5^{Fur}** in C_6D_6.

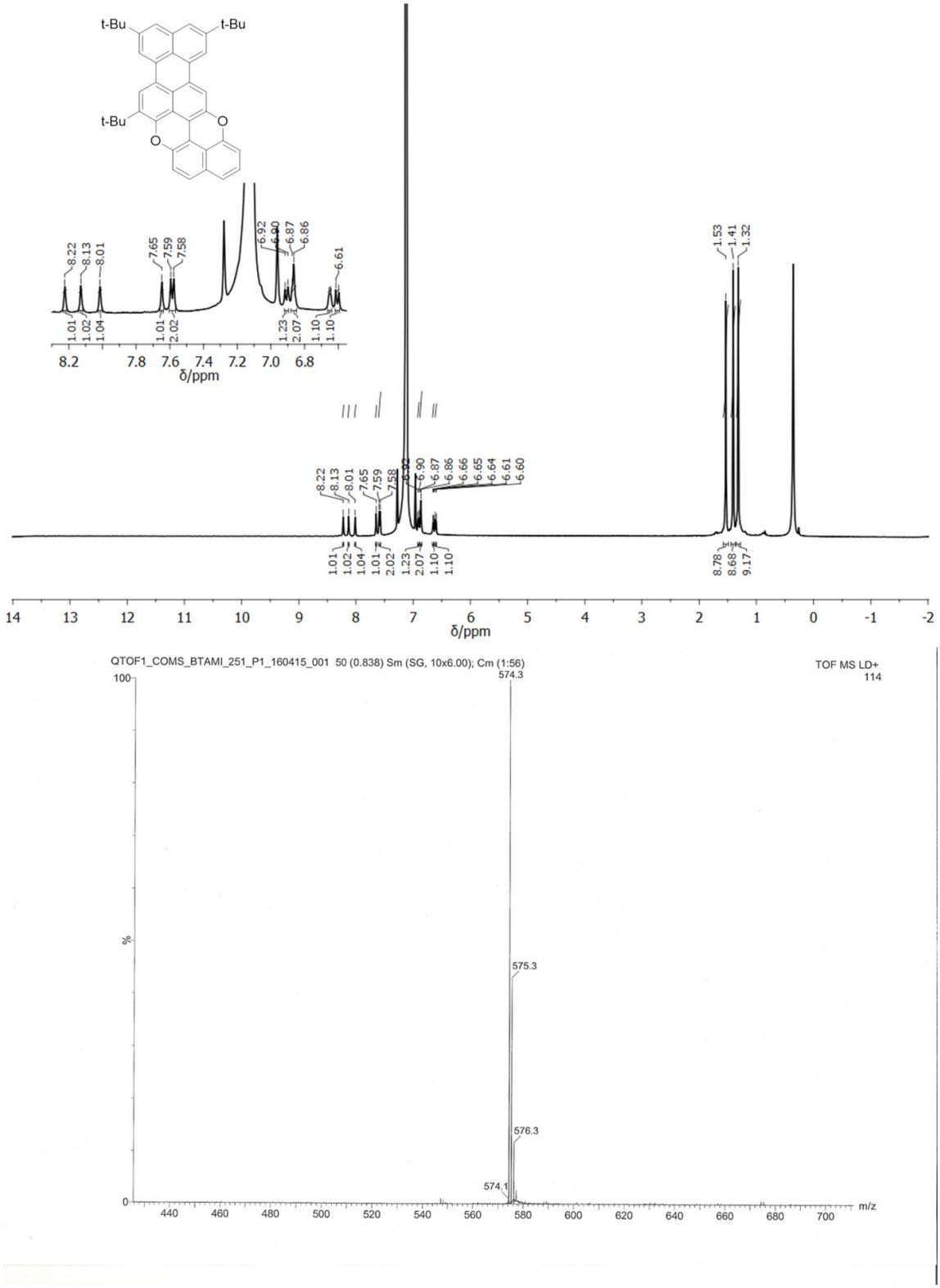

Figure A14. 500 MHz ^{1}H-NMR (top) spectrum of **3-5^{Pp}** in C_6D_6 and MALDI-HRMS spectrum (bottom)

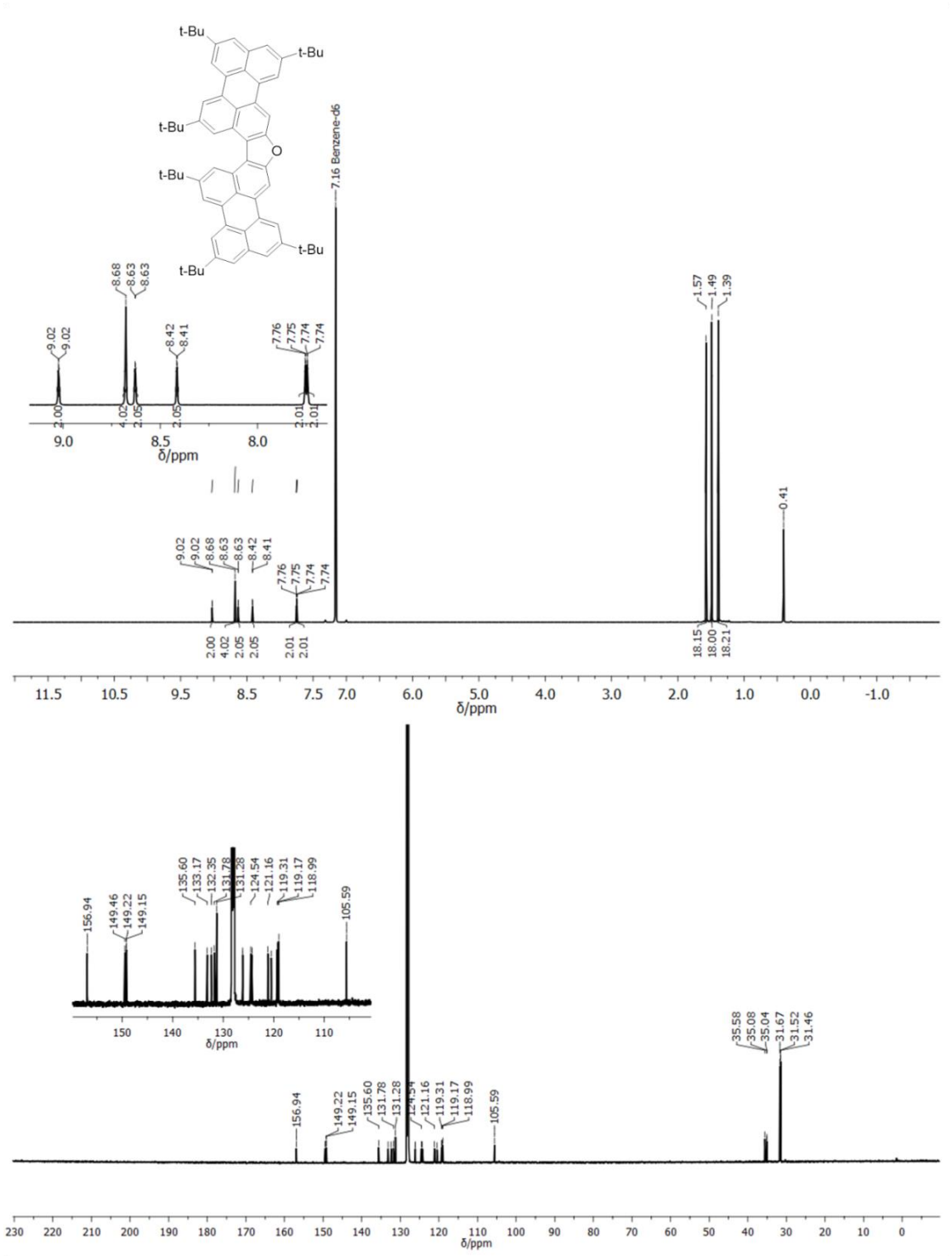

Figure A15. 500 MHz ^{1}H-NMR (top) and 125 MHz ^{13}C-NMR (bottom) spectra of **3-6^{Fur}** in C_6D_6.

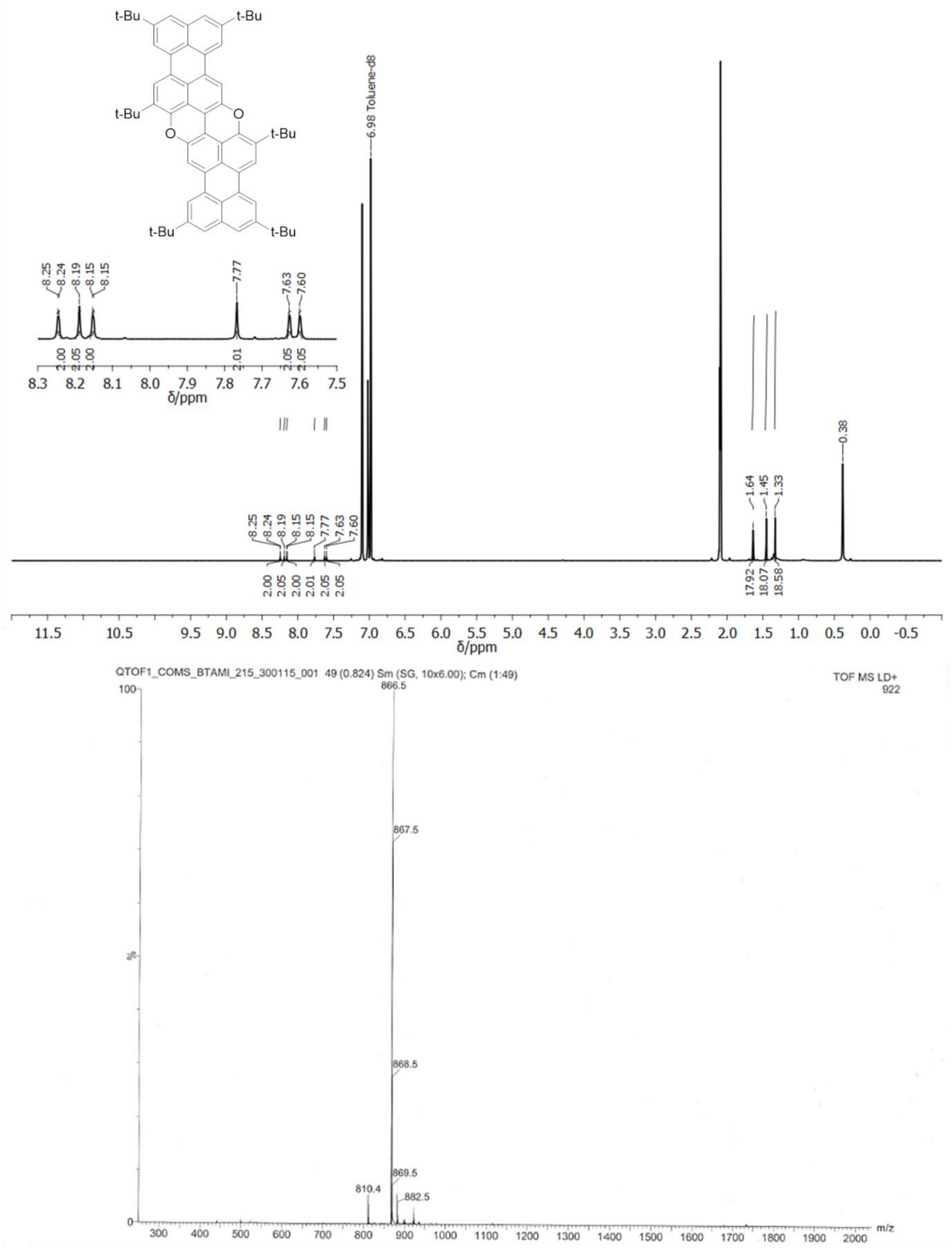

Figure A16. 500 MHz ^{1}H-NMR (top) spectrum of **3-6^{Pp}** in toluene-d_8 and MALDI-HRMS spectrum (bottom).

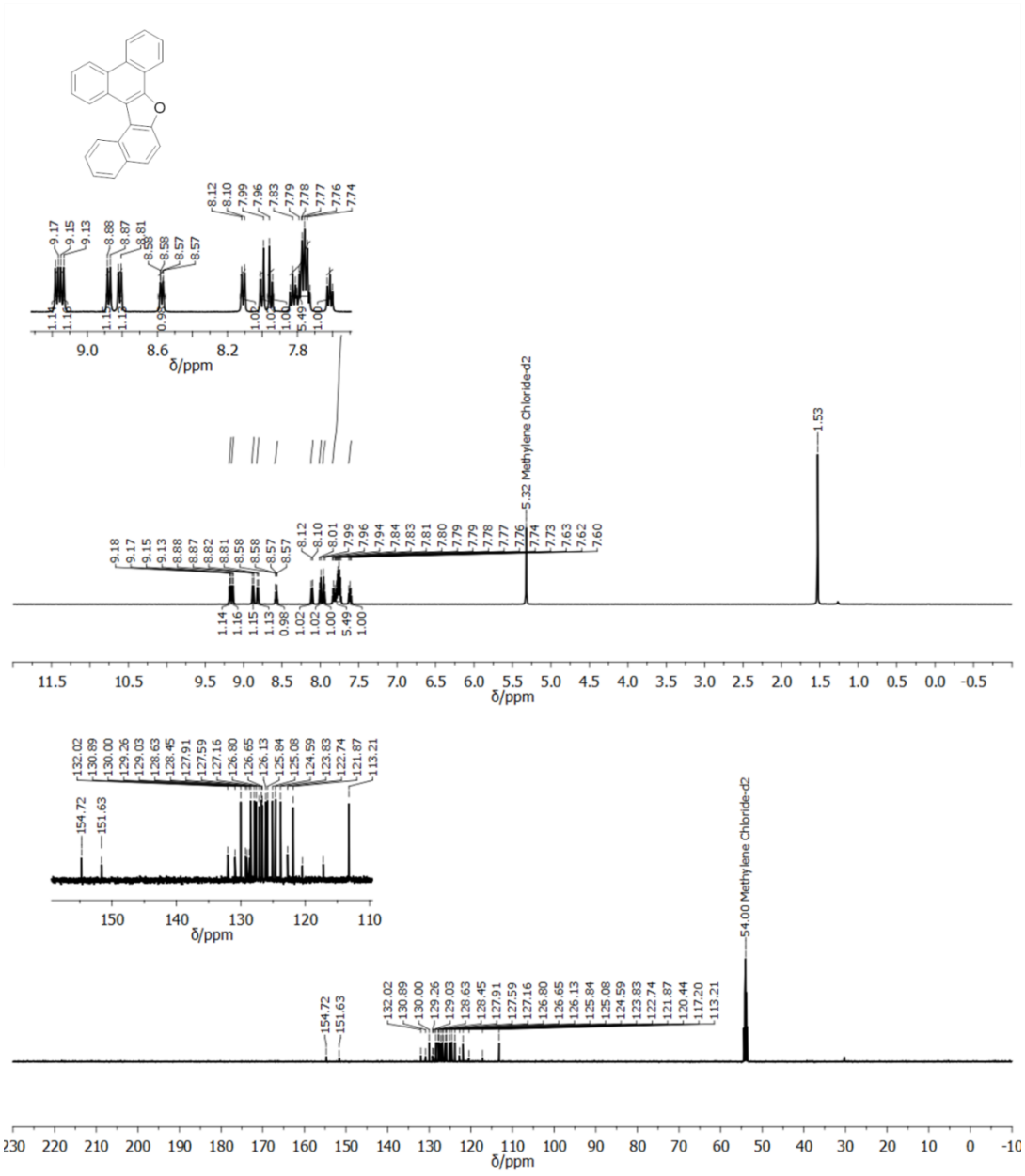

Figure A17. 500 MHz ^{1}H-NMR (top) and 125 MHz ^{13}C-NMR (bottom) spectra of **3-7^{Fur}** in CD_2Cl_2.

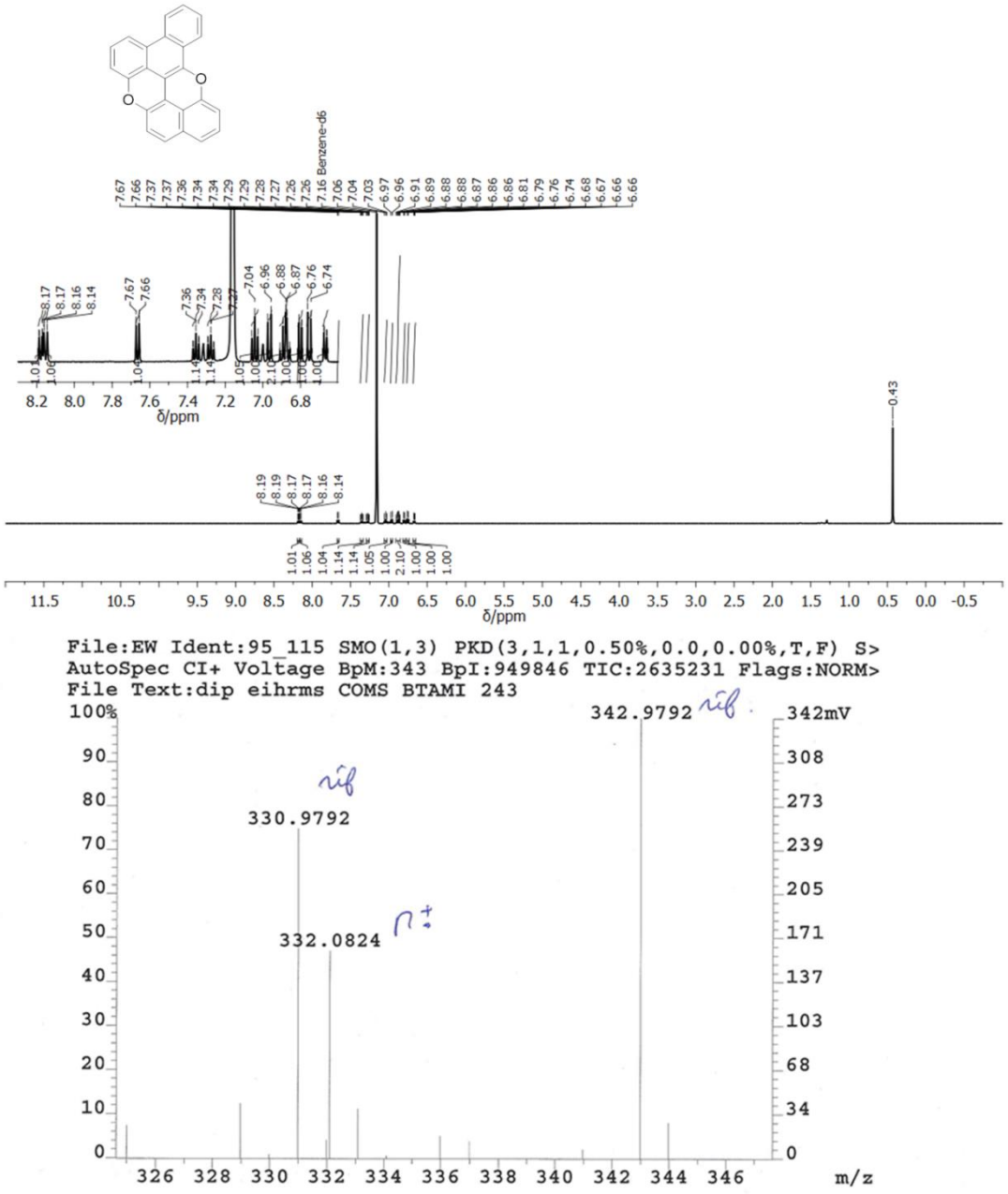

Figure A18. 500 MHz ^{1}H-NMR (top) spectrum of **3-7^{Pp}** in C_6D_6 at 65°C and MALDI-HRMS spectrum (bottom).

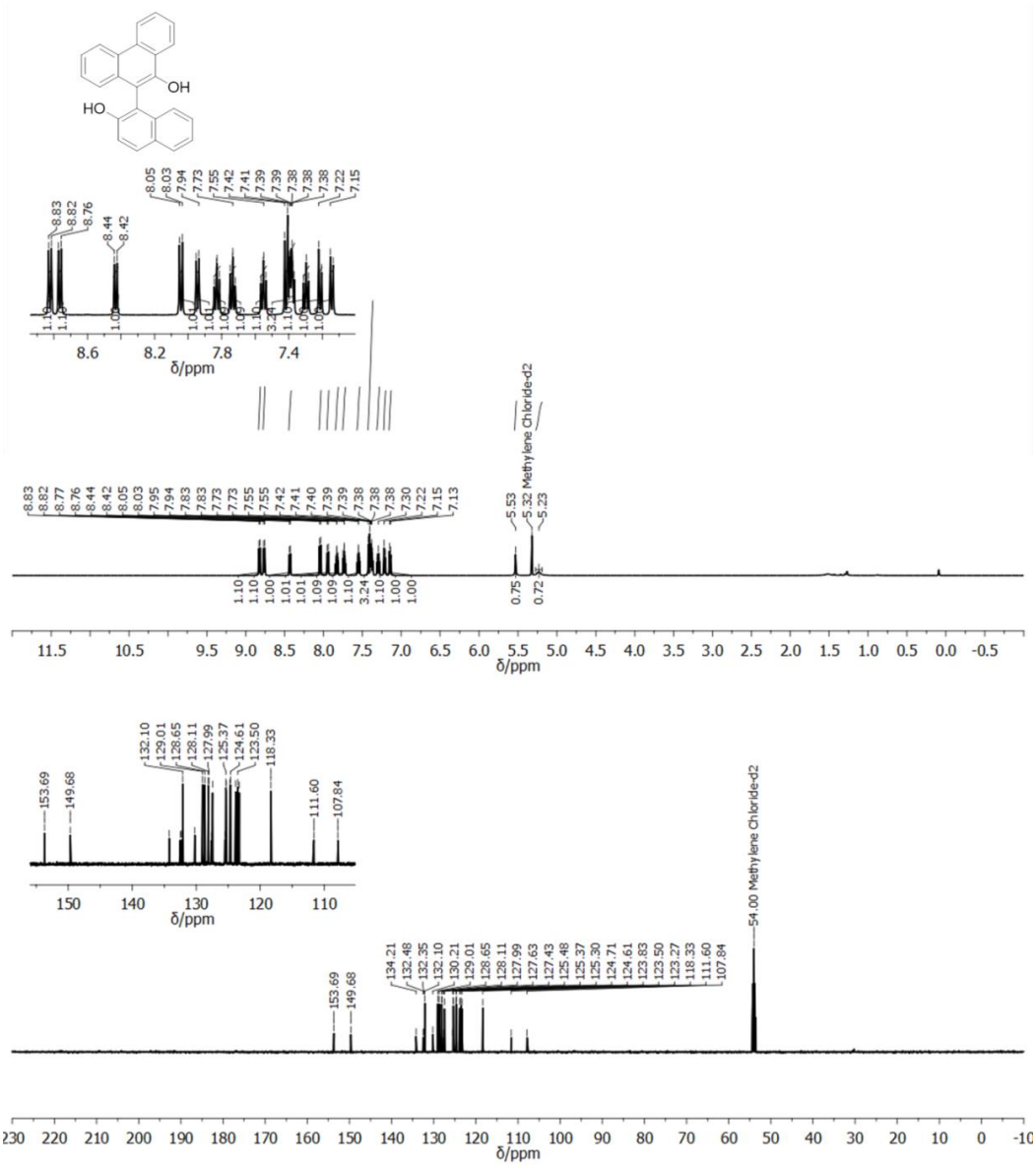

Figure A19. 500 MHz ^{1}H-NMR (top) and 125 MHz ^{13}C-NMR (bottom) spectra of **3-9** in CD_2Cl_2.

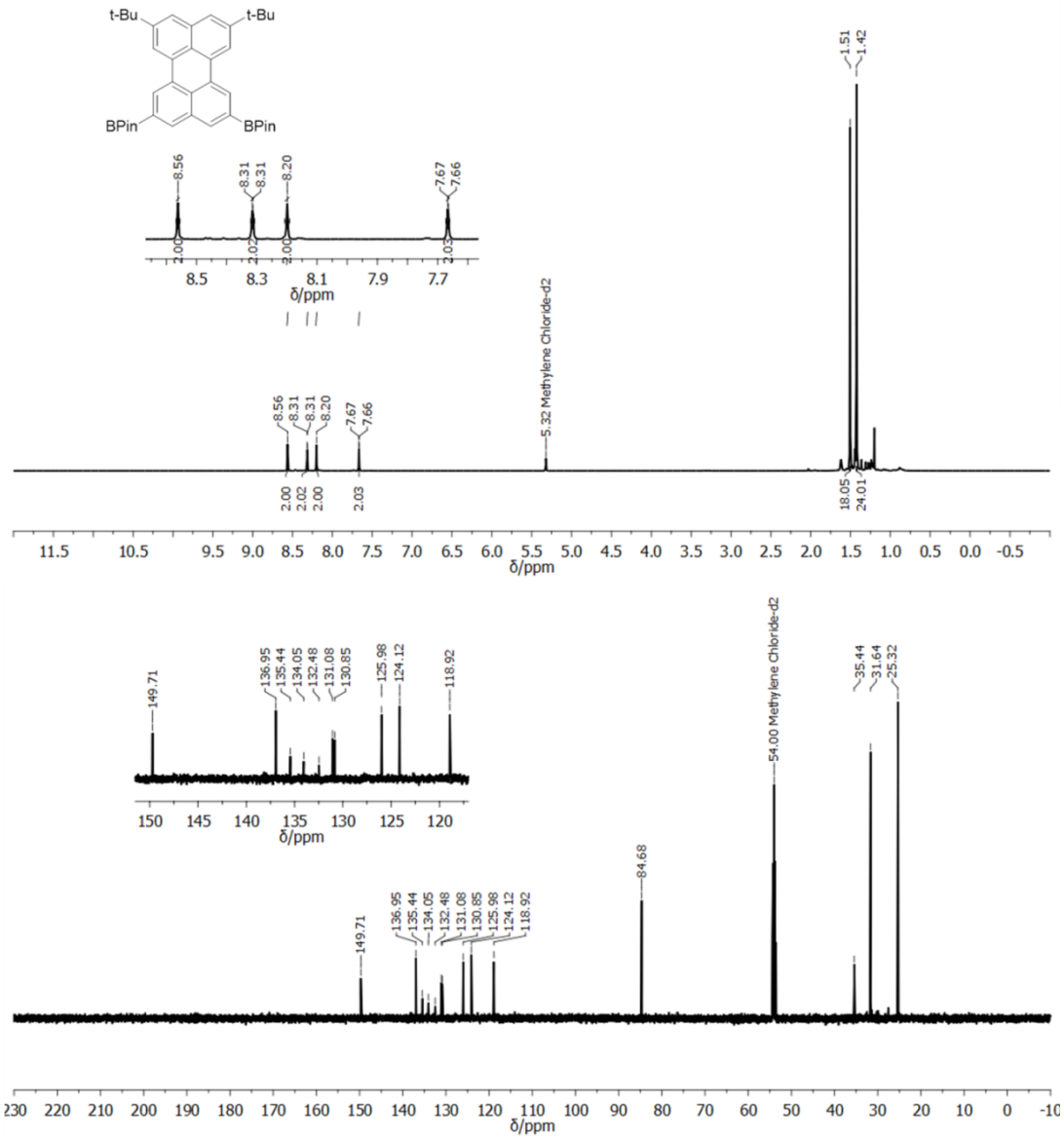

Figure A20. 500 MHz ^{1}H-NMR (top) and 125 MHz ^{13}C-NMR (bottom) spectra of **3-10** in CD_2Cl_2.

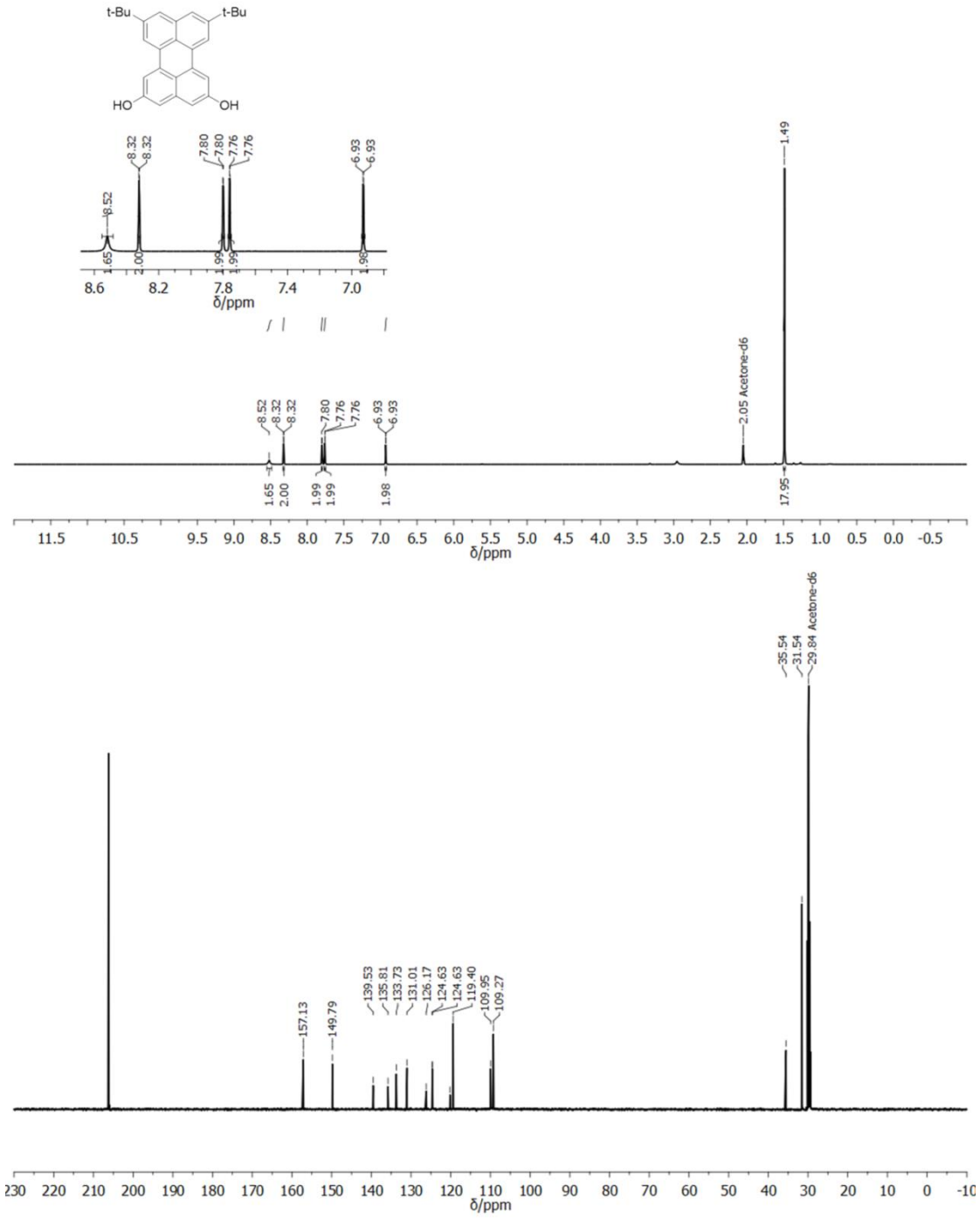

Figure A21. 500 MHz ^{1}H-NMR (top) and 125 MHz ^{13}C-NMR (bottom) spectra of **3-12** in acetone-d_6.

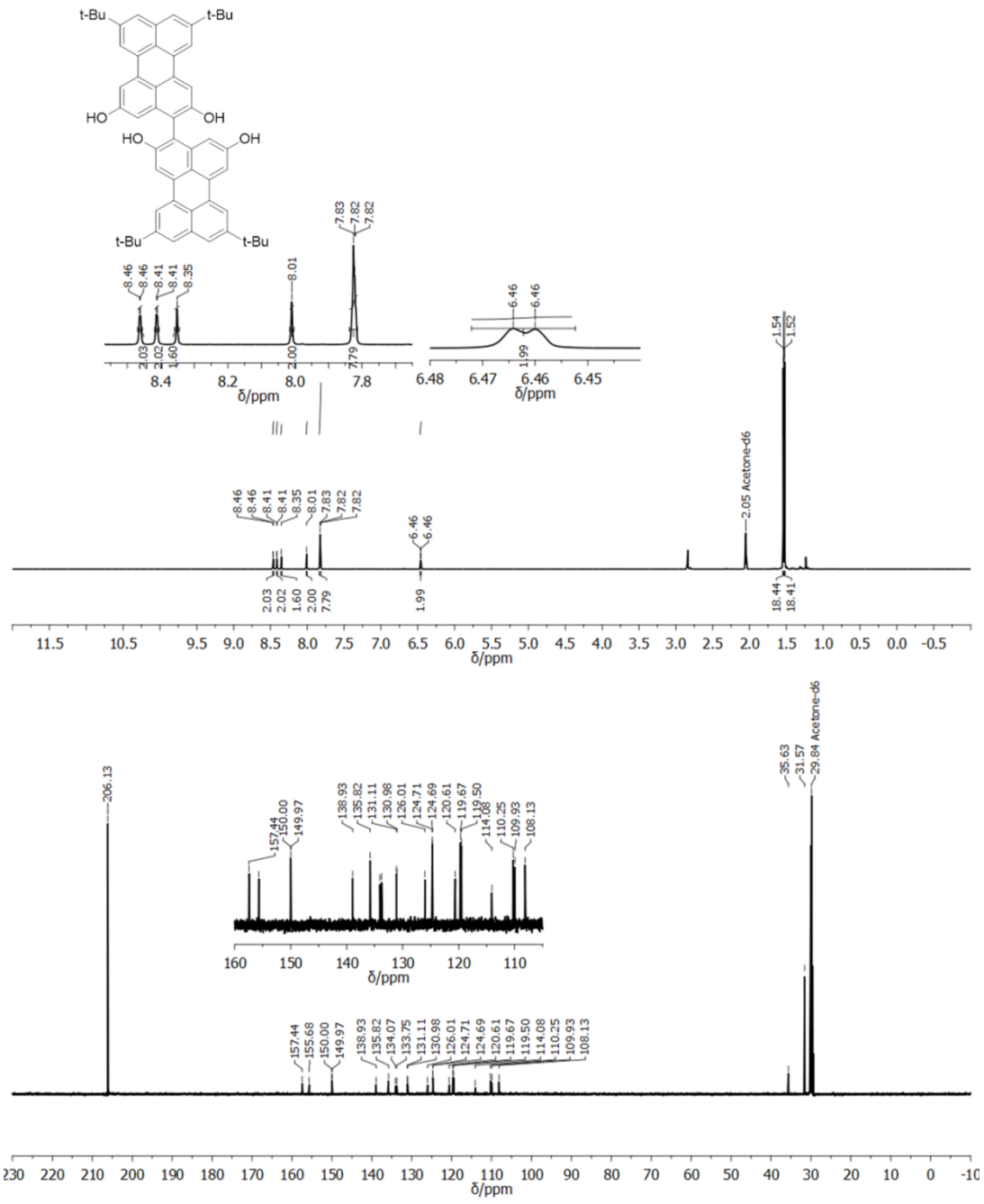

Figure A22. 500 MHz ^{1}H-NMR (top) and 125 MHz ^{13}C-NMR (bottom) spectra of **3-13** in acetone-d_6.

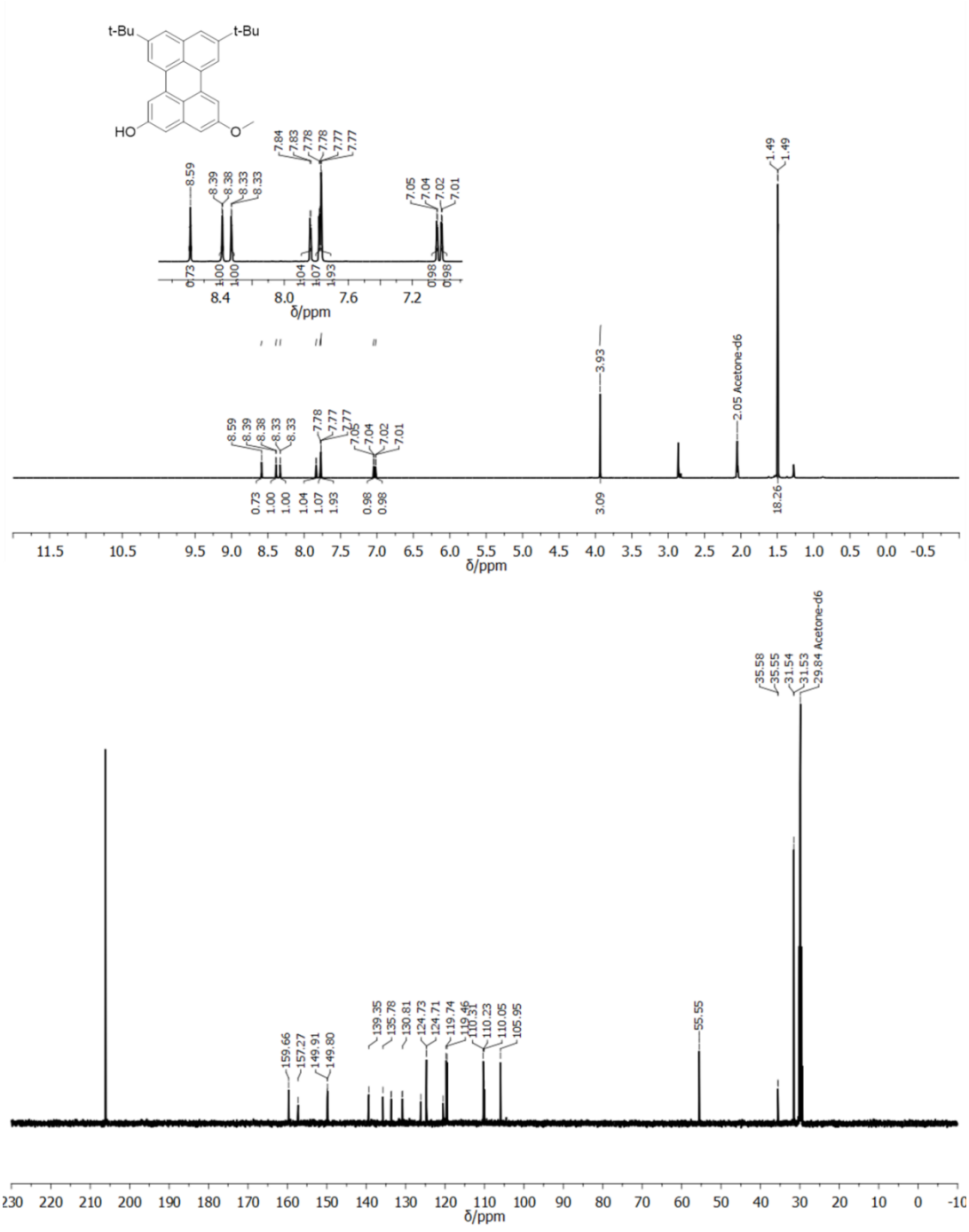

Figure A23. 500 MHz ^{1}H-NMR (top) and 125 MHz ^{13}C-NMR (bottom) spectra of **3-15** in acetone-d_6.

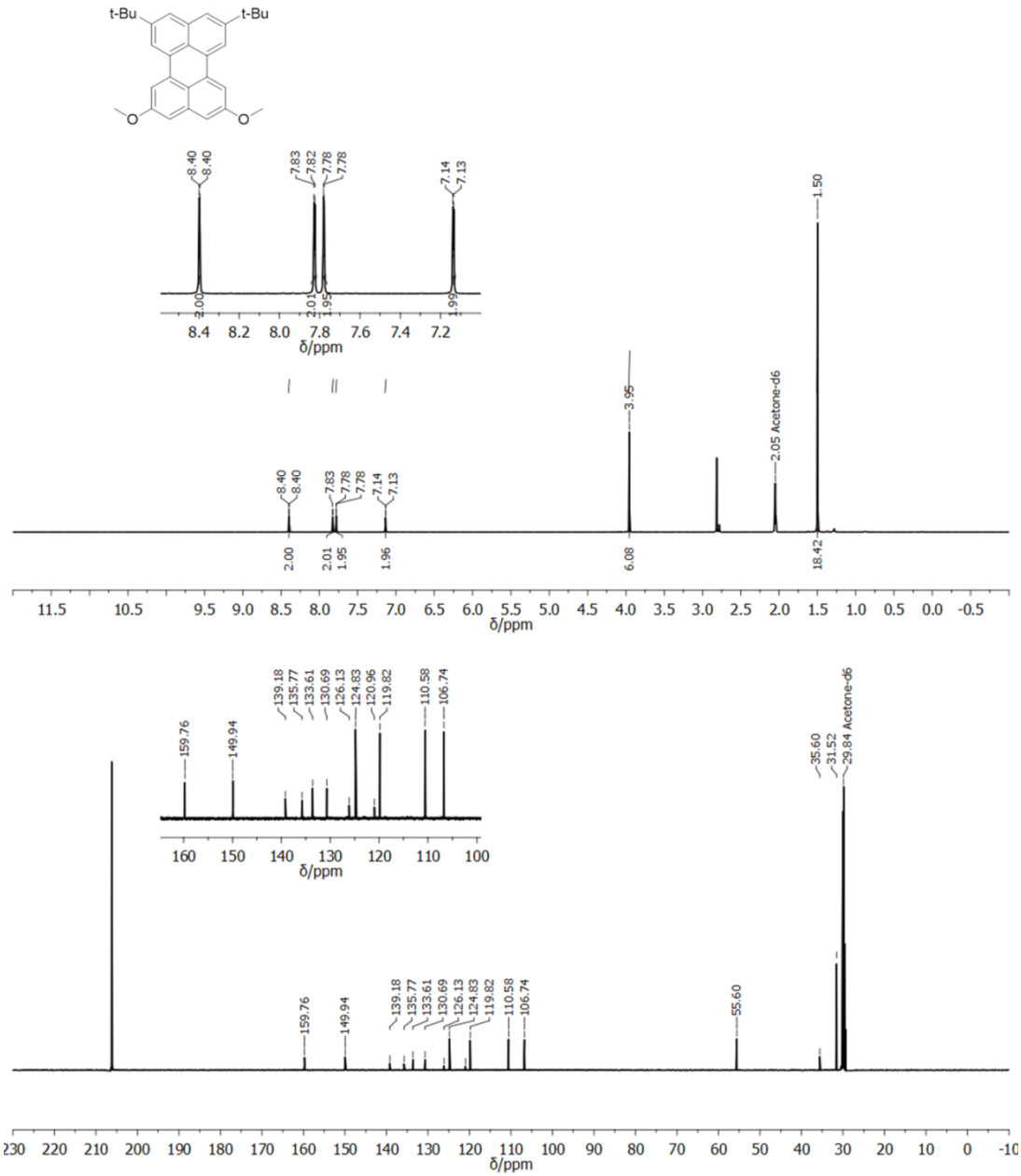

Figure A24. 500 MHz ^{1}H-NMR (top) and 125 MHz ^{13}C-NMR (bottom) spectra of **3-16** in acetone-d_6.

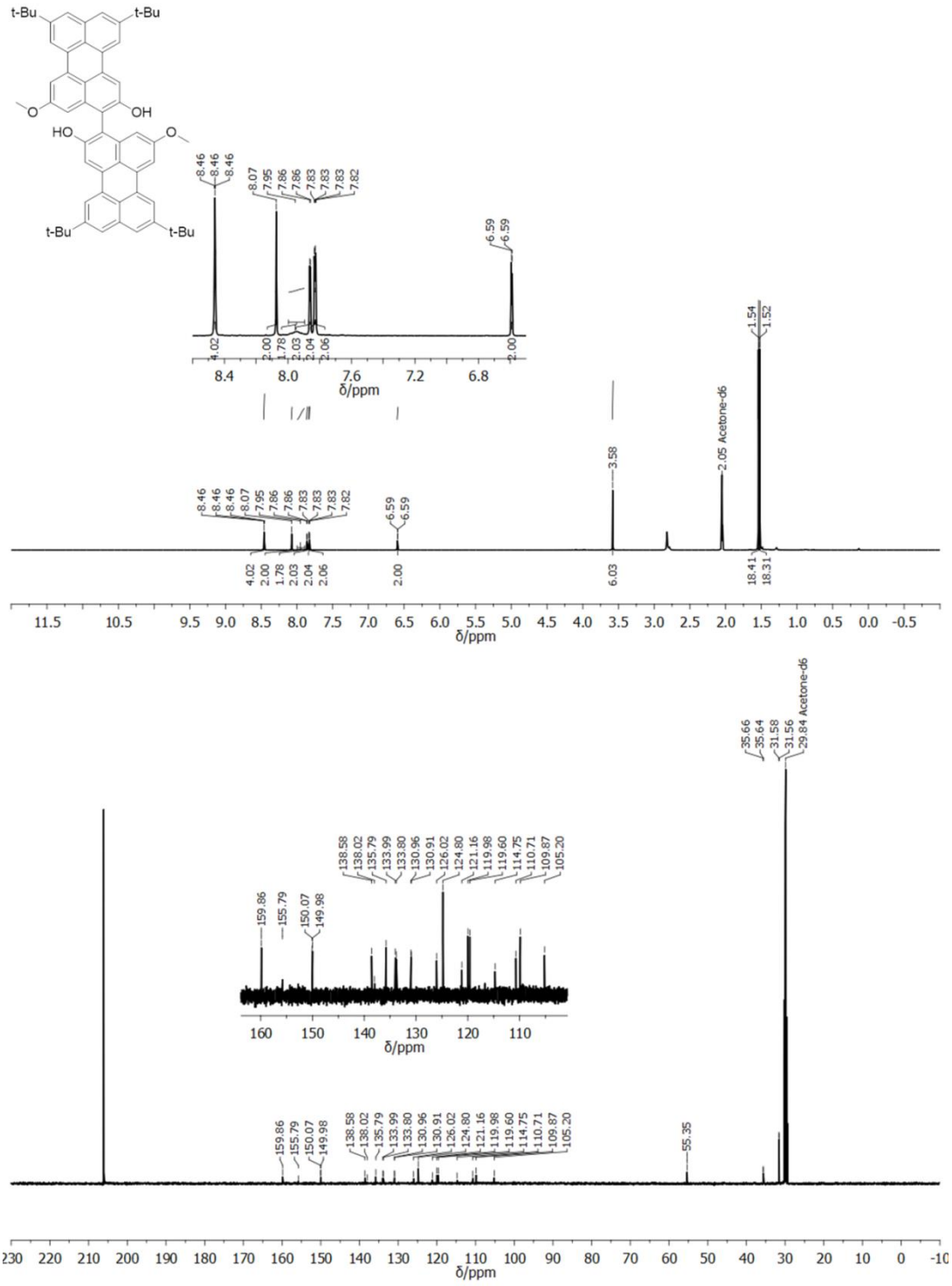

Figure A25. 500 MHz ^{1}H-NMR (top) and 125 MHz ^{13}C-NMR (bottom) spectra of **3-17** in acetone-d_6.

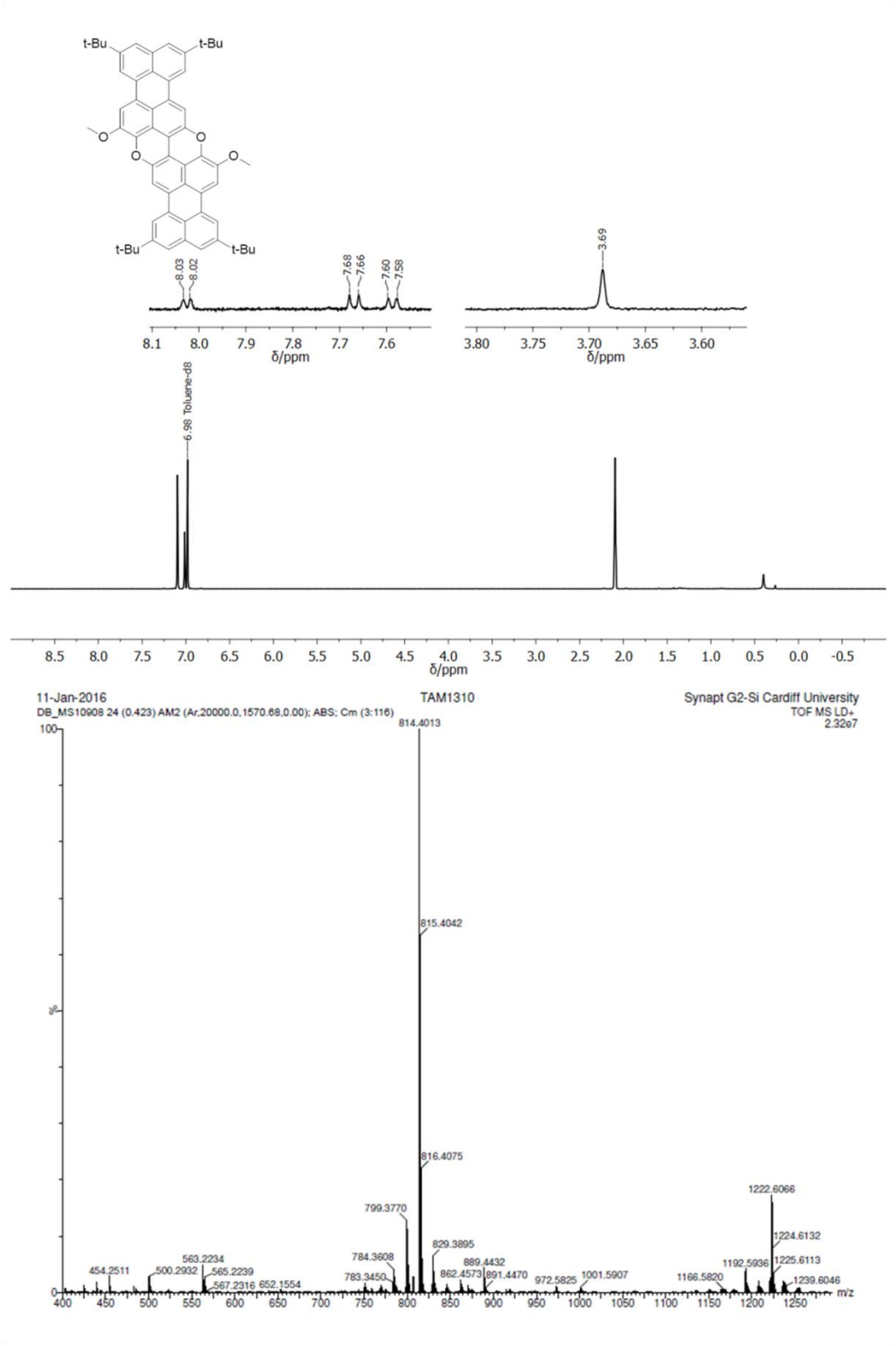

Figure A26. 500 MHz ^{1}H-NMR (top) spectrum of **3-18^{Pp}** in toluene-d_8 at 40 °C and MALDI-HRMS spectrum (bottom).

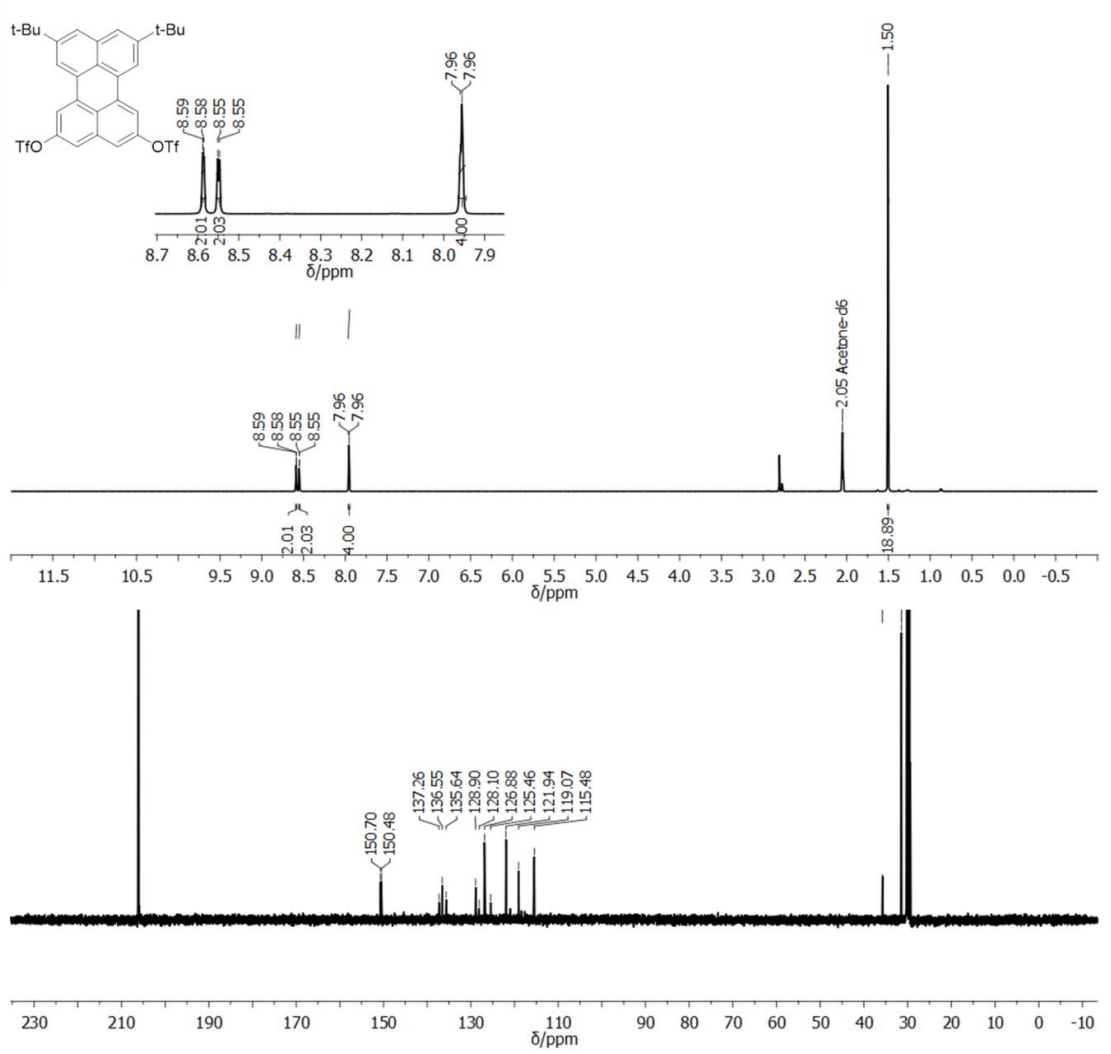

Figure A27. 500 MHz ^{1}H-NMR (top) and 125 MHz ^{13}C-NMR (bottom) spectra of **3-22** in acetone-d_6.

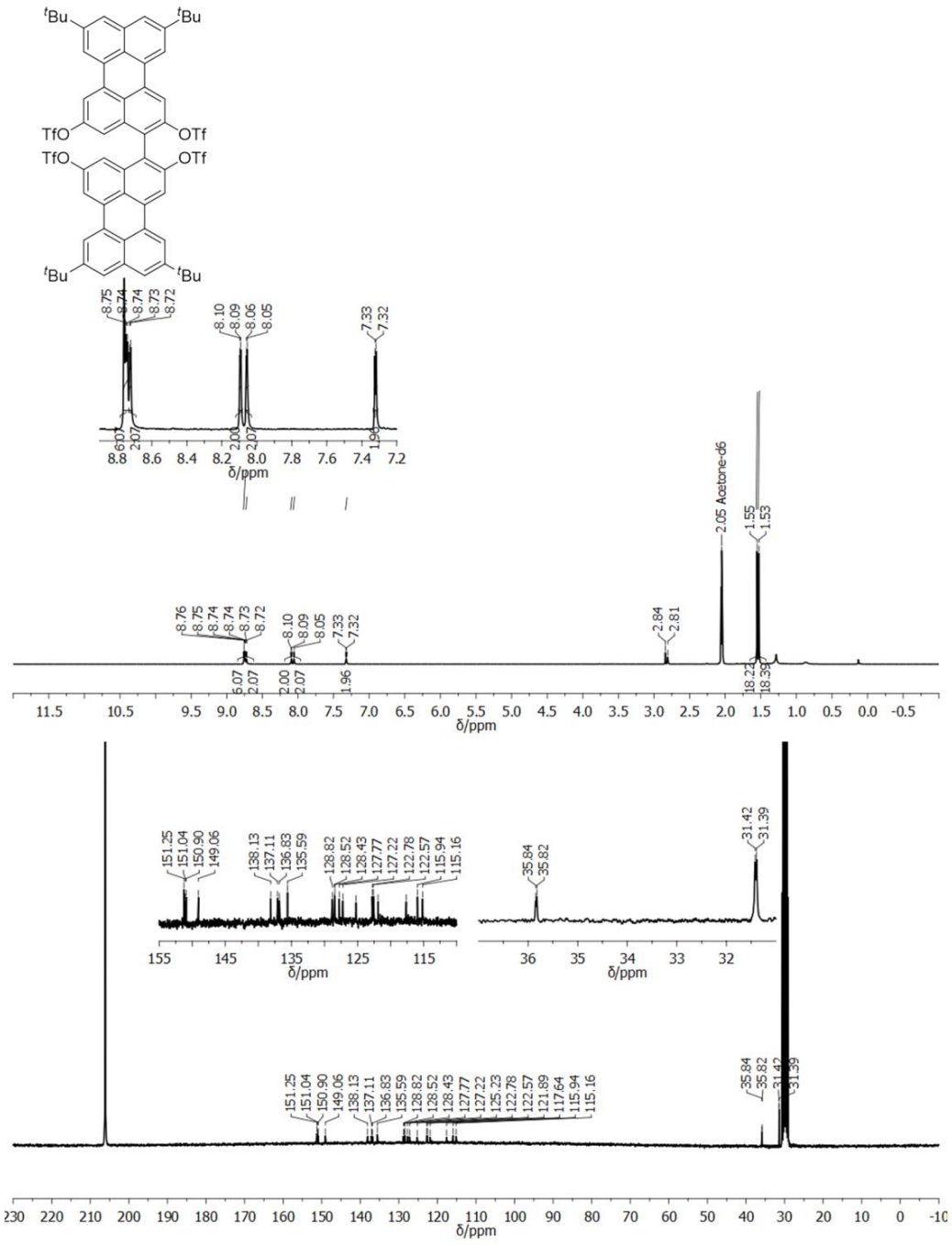

Figure A28. 300 MHz ^{1}H-NMR (top) and 75 MHz ^{13}C-NMR (bottom) spectra of **3-23** in acetone-d_6.

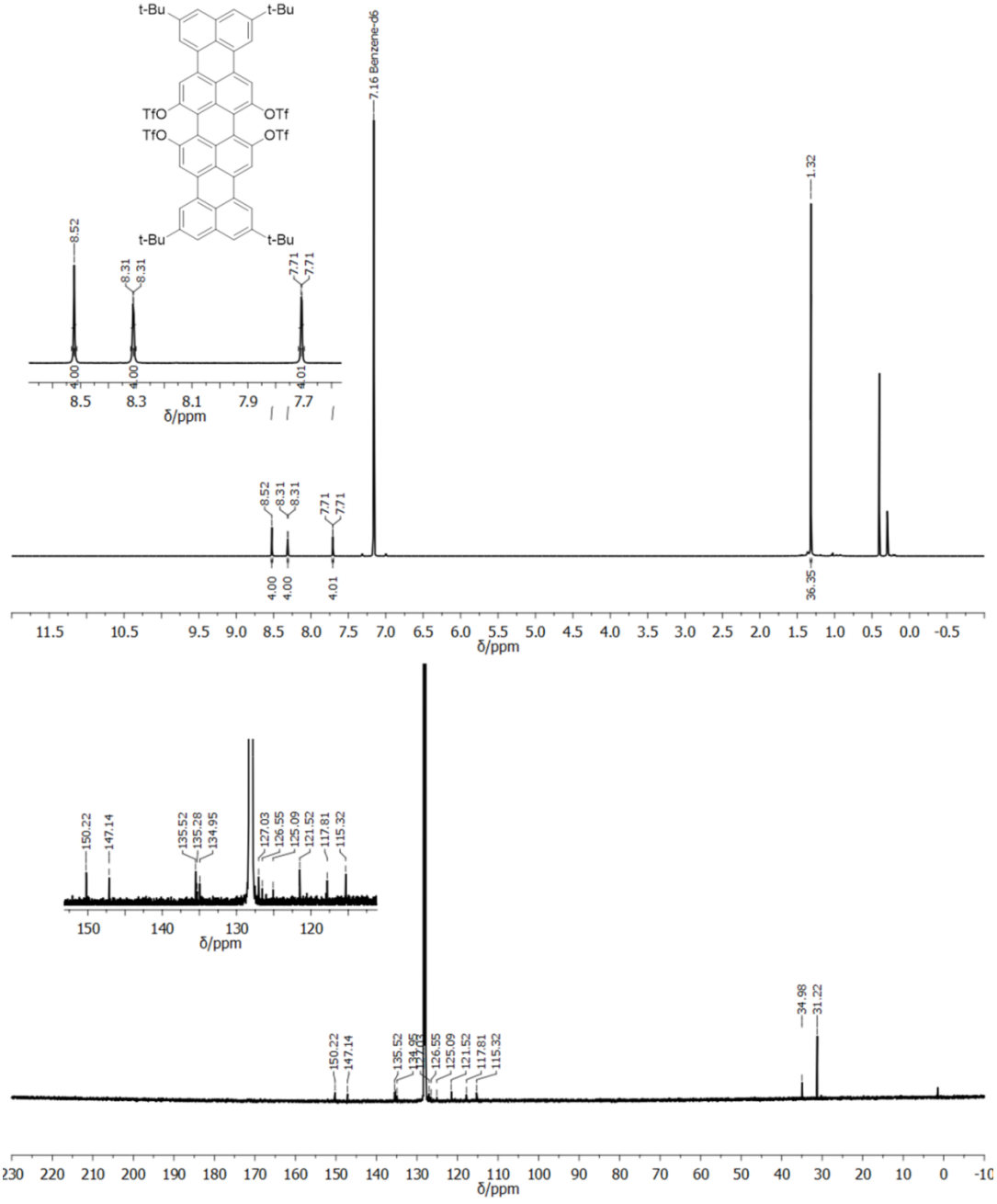

Figure A29. 500 MHz ^{1}H-NMR (top) and 125 MHz ^{13}C-NMR (bottom) spectra of **3-21** in C_6D_6.

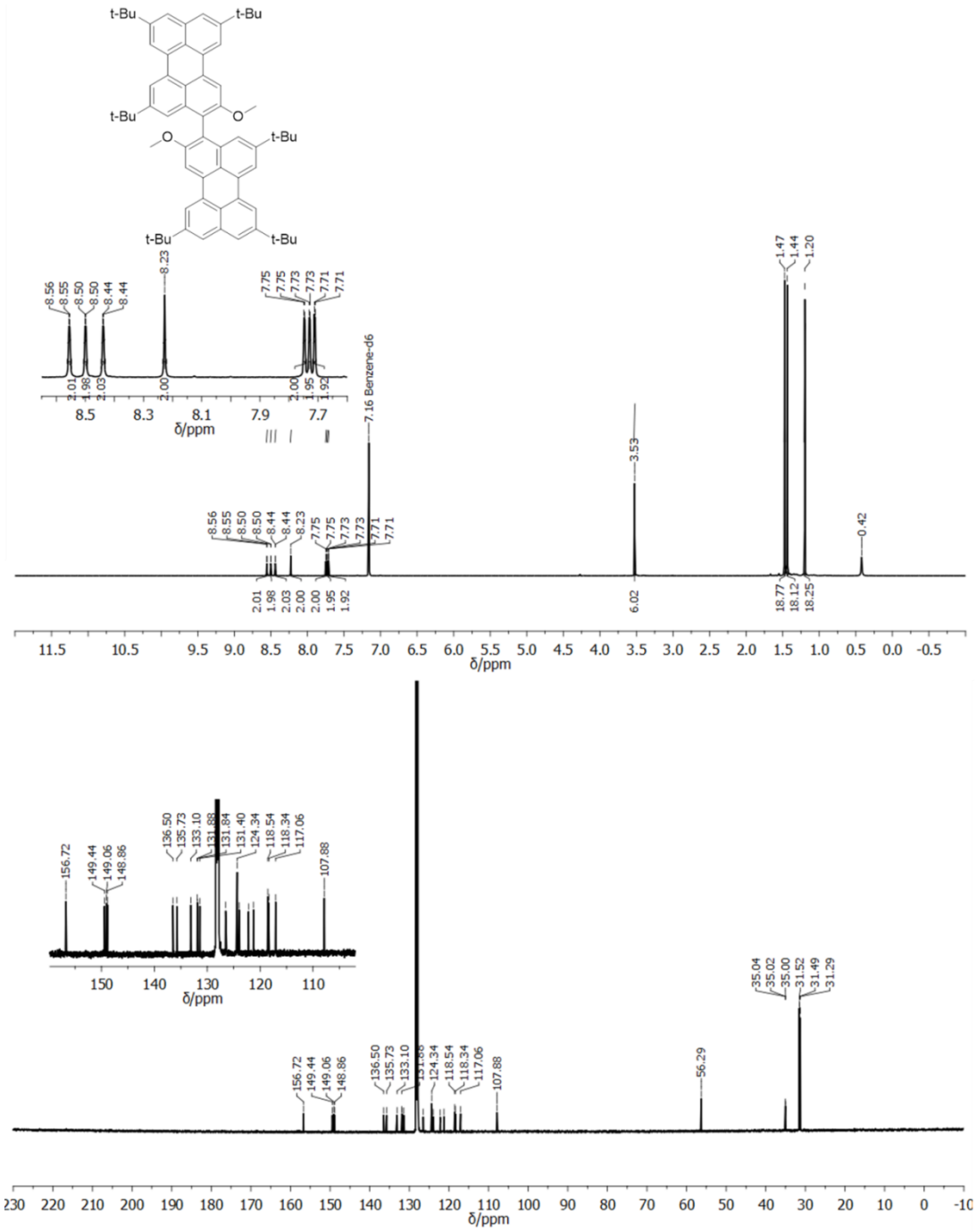

Figure A30. 500 MHz ^{1}H-NMR (top) and 125 MHz ^{13}C-NMR (bottom) spectra of **3-30** in C_6D_6.

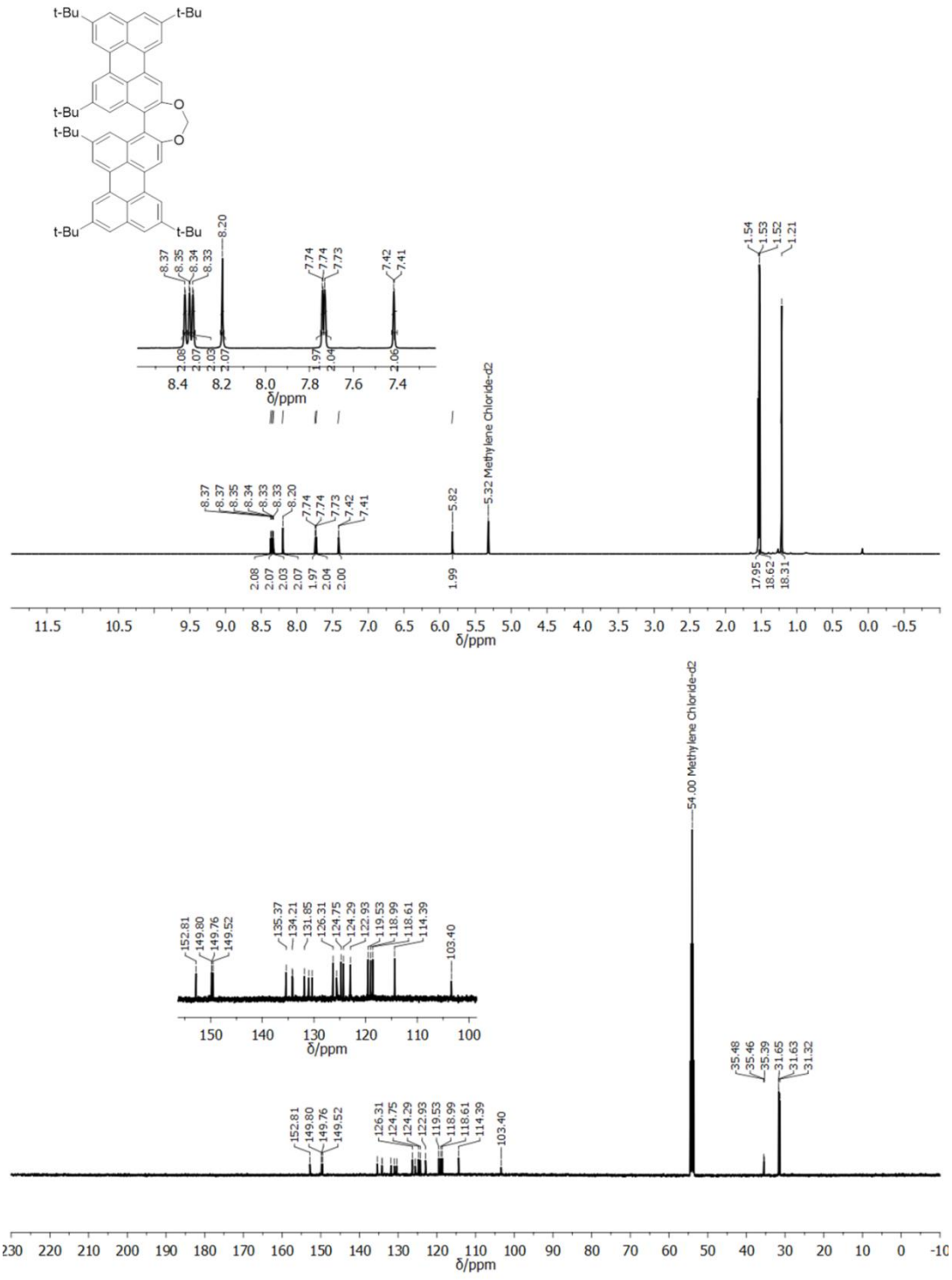

Figure A31. 500 MHz ^{1}H-NMR (top) and 125 MHz ^{13}C-NMR (bottom) spectra of **3-27** in CD_2Cl_2.

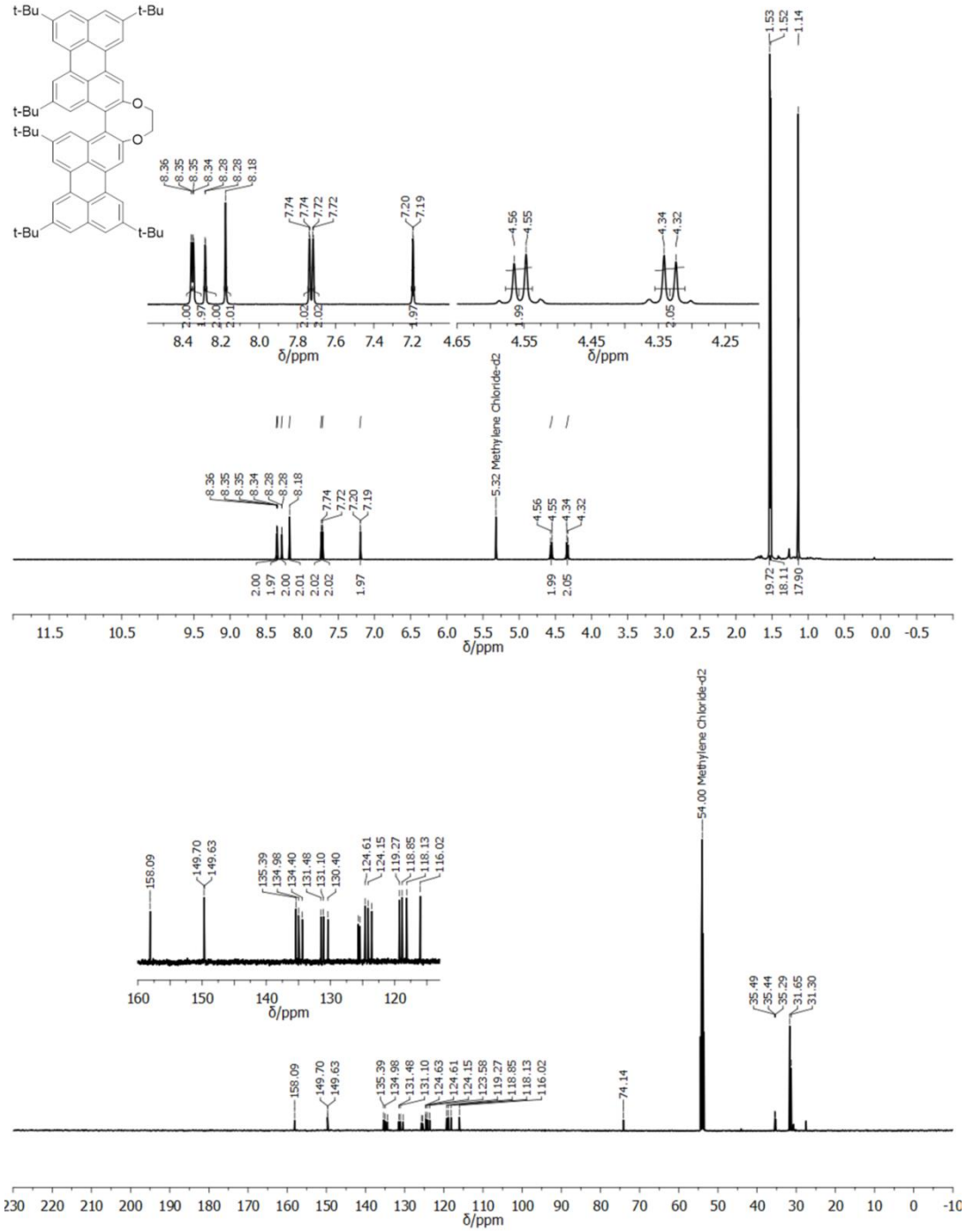

Figure A32. 500 MHz ^{1}H-NMR (top) and 125 MHz ^{13}C-NMR (bottom) spectra of **3-28** in CD_2Cl_2.

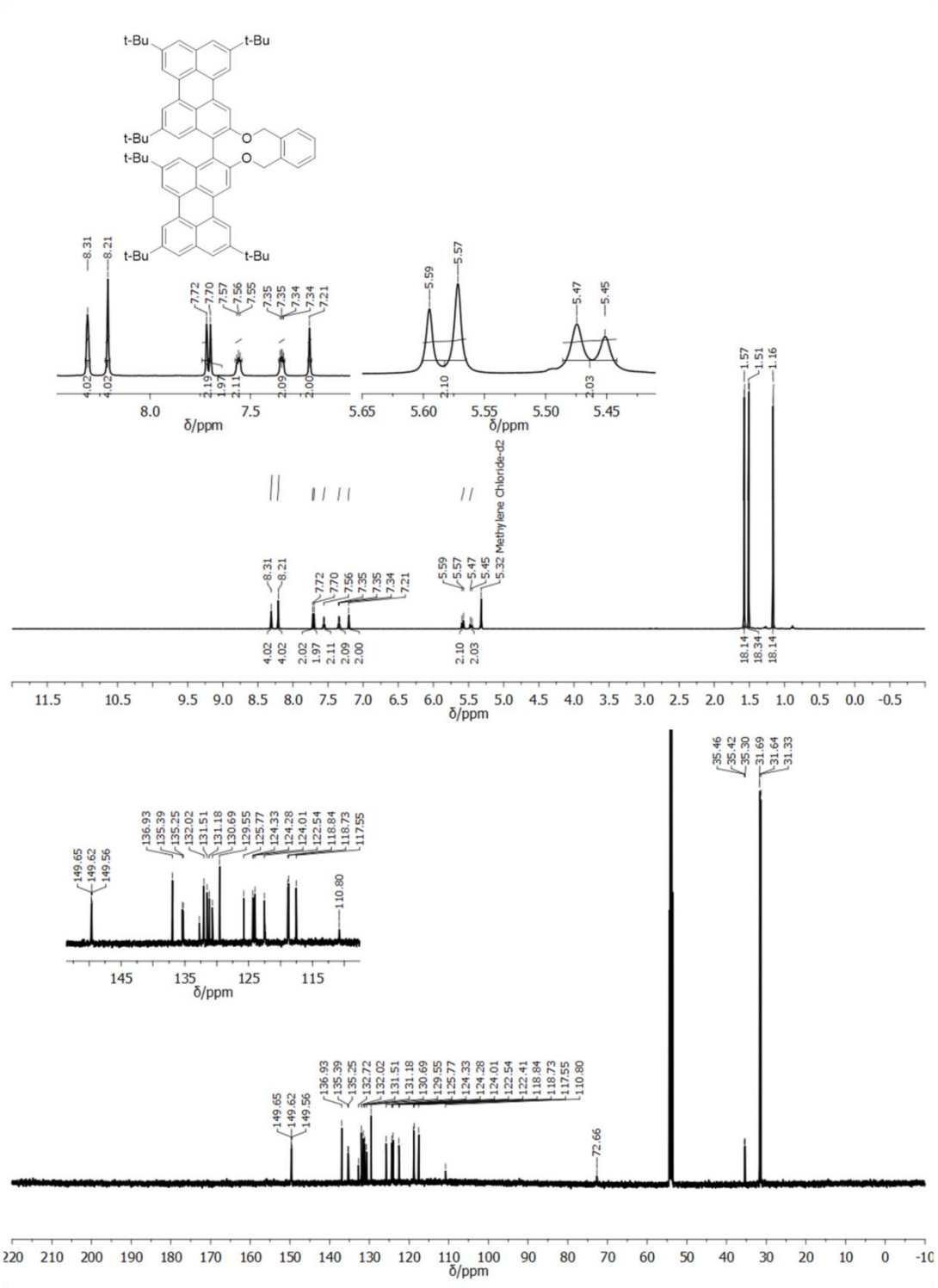

Figure A33. 500 MHz ^{1}H-NMR (top) and 125 MHz ^{13}C-NMR (bottom) spectra of **3-29** in CD_2Cl_2.

A2. Crystallographic data

Table A1. Crystallographic data and refinement details for compound **2-6a.**

Moiety Formula	$C_{50}H_{76}N_2O_2$	θ min,max (°)	1.4, 24.3
Sum Formula	$C_{50}H_{76}N_2O_2$	Resolution (Å)	0.85
Formula weight (Da)	737.12	Total refl. collctd	8303
Temperature (K)	100(2)	Independent refl.	4307 [R(int) = 0.1387]
Wavelength (Å)	0.700	Obs. Refl. [Fo>4σ(Fo)]	2986
Crystal system	Triclinic	I/ σ(I) (all data)	4.6
Space Group	*P* -1	I/ σ(I) (max resltn)	1.9
a (Å)	5.340(1)	Completeness (all data)	0.99
b (Å)	15.290(3)	Completeness	0.94
c (Å)	16.380(3)	Rmerge (all data)	0.042
α (°)	106.06(3)	Rmerge (max resltn,)	0.140
β (°)	94.75(3)	Multiplicity (all data)	1.9
γ (°)	90.44(3)	Multiplicity (max resltn)	1.8
V ($Å^3$)	1280.1(5)	Data/restraint/parameters	4307 /112/302
Z	1	Goof	0.921
ρ ($g \cdot cm^{-3}$)	0.956	R_1[a] [I>2.0σ(I)], wR_2 [a] [I>2.0σ(I)]	0.1252, 0.3150
F(000)	406	R_1[a] (all data), wR_2 [a]	0.1556, 0.3496
μ (mm^{-1})	0.055	(all data)	

[a] $R_1 = \Sigma\, ||Fo|-|Fc|| \,/\, \Sigma|Fo|$, $wR_2 = [\Sigma\, w\,(Fo^2 - Fc^2)^2 \,/\, \Sigma w\,(Fo^2)^2]^{½}$.

Table A2. Crystallographic data and refinement details for compounds **3-4**, **3-5^{Fur}**, **3-6^{Fur}**, **3-7^{Fur}** and **3-11**.

	3-4	**3-5^{Fur}**	**3-6^{Fur}**	**3-7^{Fur}**	**3-11**
CCDC Number	1424425	1424426	1424427	1424428	1424424
Moiety Formula	$C_{64}H_{70}O_2 \cdot 4CH_4O$	$C_{42}H_{40}O$	$C_{64}H_{68}O \cdot 1.5\, C_6H_{14}$	$C_{24}H_{14}O$	$C_{40}H_{50}B_2O_4$
Sum Formula	$C_{68}H_{86}O_6$	$C_{42}H_{40}O$	$C_{73}H_{89}O$	$C_{24}H_{14}O$	$C_{40.5}H_{52}B_2O_5$
Formula weight (Da)	999.36	560.74	982.62	318.35	640.44
Temperature (K)	100(2)	100(2)	100(2)	100(2)	100(2)
Wavelength (Å)	0.800	0.700	0.700	0.700	0.900

Crystal system	Triclinic	Monoclinic	Monoclinic	Orthorhombic	Trigonal
Space Group	*P* -1	*P* 2_1/c	*P* 2/c	*P* $2_12_12_1$	*R* -3
a (Å)	10.598(2)	11.049(5)	10.730(2)	5.633(1)	43.246(14)
b (Å)	15.177(2)	11.024(1)	12.406(3)	14.558(3)	43.246(14)
c (Å)	19.662(2)	25.124(4)	22.974(5)	18.397(4)	12.043(4)
α (°)	107.777(3)	90	90	90	90
β (°)	100.222(1)	93.41(5)	102.10(3)	90	90
γ (°)	96.282(6)	90	90	90	120
V (Å^3)	2918.2(7)	3054.8(15)	2990.3(11)	1508.6(5)	19506(14)
Z	2	4	2	4	18
ρ (g·cm^{-3})	1.137	1.219	1.093	1.402	0.981
F(000)	1084	1200	1072	664	6210
μ (mm^{-1})	0.090	0.068	0.060	0.081	0.105
θ min,max (°)	1.3, 30.8	2.0, 27.8	1.8, 27.8	1.8, 27.8	2.1, 28.6
Resolution (Å)	0.78	0.75	0.75	0.75	0.94
Total refl. collctd	21677	47029	25169	23893	23902
Independent refl.	12308, [R(int) = 0.0375]	7320, [R(int) = 0.0299]	7314, [R(int) = 0.0202]	3689, [R(int) = 0.0094]	5283, [R(int) = 0.0483]
Obs. Refl. [Fo>4 σ (Fo)]	11049	6222	6385	3669	4465
I/σ(I) (all data)	16.3	21.1	12.9	59.6	14.0
I/σ(I) (max resltn)	3.7	11.4	9.4	49.8	5.5
Completeness (all data)	0.96	0.98	0.99	0.99	0.98
Completeness	0.84	0.94	1.00	1.00	0.93
Rmerge (all data)	0.083	0.042	0.021	0.016	0.146
Rmerge (max resltn,)	0.091	0.108	0.054	0.019	0.063
Multiplicity (all data)	3.5	6.3	3.4	11.0	4.5
Multiplicity (max resltn)	1.6	6.4	3.3	10.4	4.4
Data/restraint/parameters	12308 /128/769	7320/0/429	7314/28/376	3689/0/226	5283/38/564
Goof	0.994	1.029	1.025	1.050	1.076

R_1[a] [I>2.0 σ (I)], wR_2 [a] [I>2.0 σ (I)]	0.1268, 0.3316	0.0599, 0.1517	0.0483, 0.1369	0.0305, 0.0835	0.1040, 0.2728
R_1[a] (all data), wR_2 [a] (all data)	0.1203, 0.3365	0.0530, 0.1457	0.0543, 0.1427	0.0306, 0.0837	0.1126, 0.2813

[a] $R_1 = \Sigma\,||Fo|-|Fc|| \,/\, \Sigma|Fo|$, $wR_2 = [\Sigma\, w\,(Fo^2 - Fc^2)^2 \,/\, \Sigma w\,(Fo^2)^2]^{½}$.

Table A3. Crystallographic data and refinement details for compounds **3-21**, **3-22**, **3-28** and **3-29**.

	3-21	**3-22**	**3-28**	**3-29**
Moiety Formula	$C_{60}H_{48}F_{12}O_{12}S_4 \cdot 2\,C_6H_6$	$C_{30}H_{26}F_6O_6S_2$	$C_{66}H_{72}O_2 \cdot 1.5\,CH_2Br_2$	$C_{72}H_{76}O_2 \cdot 0.5CH_2Cl_2$
Sum Formula	$C_{72}H_{60}F_{12}O_{12}S_4$	$C_{30}H_{26}F_6O_6S_2$	$C_{67.5}H_{75}Br_3O_2$	$C_{72.5}H_{77}ClO_2$
Formula weight (Da)	1473.44	660.63	1157.98	1015.79
Temperature (K)	100(2)	100(2)	100(2)	100(2)
Wavelength (Å)	0.700	0.700	0.700	0.700
Crystal system	Monoclinic	Orthorhombic	Monoclinic	Triclinic
Space Group	*P* $2_1/n$	*P nna*	*P n*	*P* -1
a (Å)	10.434(2)	15.365(3)	9.892(2)	10.879(2)
b (Å)	26.901(5)	27.584(6)	22.494(5)	15.599(3)
c (Å)	24.188(5)	27.782(6)	30.317(6)	17.643(4)
α (°)	90	90	90	101.08(3)
β (°)	99.83(3)	90	96.21(3)	94.26(3)
γ (°)	90	90	90	105.06(3)
V ($Å^3$)	6689(2)	11775(4)	6706(2)	2812.9(11)
Z	4	16	4	2
ρ ($g \cdot cm^{-3}$)	1.463	1.491	1.144	1.199
F(000)	3040	5440	2392	1090
μ (mm^{-1})	0.227	0.248	1.776	0.110
θ min,max (°)	1.7, 24.8	1.5, 25.2	1.1, 16.9	1.1, 24.8
Resolution (Å)	0.72	0.8	1.2	0.72
Total refl. collctd	56797	83323	8539	59665

Independent refl.	18423 [R(int) = 0.0601]	11978 [R(int) = 0.0527]	5171 [R(int) = 0.2529]	15447 [R(int) = 0.0884]
Obs. Refl. [Fo>4 σ (Fo)]	11750	8159	2353	8656
I/ σ (I) (all data)	8.9	11.3	9.6	5.9
I/ σ (I) (max resltn)	3.1	4.1	1.3	1.8
Completeness (all data)	0.98	1.00	0.80	0.98
Completeness (max resltn)	0.94	1.00	0.67	0.95
Rmerge (all data)	0.0565	0.0865	0.2549	0.0705
Rmerge (max resltn,)	0.2111	0.3542	0.5286	0.3880
Multiplicity (all data)	3.0	6.7	2.0	3.8
Multiplicity (max resltn)	2.8	6.1	1.6	3.0
Data/restraint/parameters	18423/1121/1215	11978/88/877	5171/673/581	15447/10/748
Goof	1.058	1.057	1.011	1.011
R_1[a] [I>2.0σ (I)], wR_2[a] [I>2.0 σ (I)]	0.1526, 0.2974	0.1125, 0.2890	0.2293, 0.4508	0.0653, 0.1703
R_1[a] (all data), wR_2[a] (all data)	0.1967, 0.3211	0.1490, 0.3244	0.3211, 0.5144	0.1285, 0.2139

A3. Device fabrication and characterization

Table A4. Photovoltaic parameters of the best performing devices, varying Spiro-OMeTAD (SP) and **f-SWNT-1** concentration.

HTM	J_{sc} (mA cm^{-2})	V_{oc} (V)	FF	PCE (%)
SP90 (90 mg/mL)	9.42	0.93	0.51	4.5
SP63 (63 mg/mL)	16.14	0.92	0.44	6.5
SP45(45 mg/mL)	15.27	0.87	0.43	5.8
SP45 **f-SWCNT-1** [0.8 mg/mL]	12.07	0.94	0.51	5.8
SP45 **f-SWCNT-1** [0.4 mg/mL]	11.63	0.95	0.59	6.4